UNIVERSIDAD DE BUENOS AIRES
Facultad de Ciencias Exactas y Naturales
Departamento de Física

Charged-particle distributions at low transverse momentum and a search for low-mass resonances decaying into two jets at ATLAS

Tesis para optar por el título de Doctora de la Universidad de Buenos Aires en el área Ciencias Físicas

María Roberta Devesa

Director de tesis:	Dr. Gustavo Javier Otero y Garzon
Consejero de estudios:	Dr. Fernando Lombardo
Lugar de trabajo:	Departamento de Física, FCEyN, UBA

Buenos Aires, Diciembre 2019

Charged-particle distributions at low transverse momentum and a search for low-mass resonances decaying into two jets at ATLAS

Abstract

The charged-particle multiplicity distributions are measured in pp collisions at a center-of-mass energy of 13TeV, with the ATLAS detector. The data are collected using a dedicated trigger for minimum bias data during 2015. The events are selected by requiring at least two stable charged particles with transverse momentum above 100 MeV and an absolute value of the pseudorapidity of $|\eta| < 2.5$. This region of phase space is interesting to explore as it is poorly described by models of soft QCD. Thus the charged particle multiplicity per event, the dependence of the number of charged particles on their transverse momentum (p_T) and pseudorapidity (η), and the average p_T are measured and compared with several Monte Carlo QCD-like models to better constrain their parameters.

In addition, a search is performed for localized excesses in the dijet mass distributions of low-dijet-mass events produced in association with a high transverse energy photon. The search uses up to $79.8 fb^1$, at a center-of-mass energy of 13TeV with data recorded during 2015–2017. Two variants are presented: one which makes no jet flavor requirements and one which requires both jets to be tagged as b-jets. The observed mass distributions are consistent with multi-jet processes in the Standard Model. Thus the data was used to set upper limits on the production cross-section for a benchmark *Z'* model and, separately, on generic Gaussian-shaped contributions to the mass distributions, extending the current ATLAS constraints on dijet resonances to the mass range between 225 and 1100 GeV.

keywords: ATLAS, Charged-particles distribution, mass resonance, ISR photon

Acknowledgements

I want to thank Heather Gray for been my guide during my first year at CERN. She have been always very kind and patient when I was new in a very big world.

Also, I want to thank to my colleges and supervisors that helped me to overcome all kind of problems, and for allowing me to work in the biggest collider.

To Carlo and Traian who have been there always helping me to improve myself, and for all that good times that we enjoy together.

A mi familia, que siempre esta ahí apoyandome en todo momento animandome a seguir para adelante.

Por último pero no menos importante a mis amigues, siempre estan ahí, a pie de cañon bancandome en todas! Les mejores Maxi, Mer, Mel, Gasti, Kari, Fer, Mi, Mica, Ilo, Emi, Ce. También a mis amigas no locales Ce, Sabri, Guada y Belen, que siempre me demuestran que la distancia es solo un factor relativo. Finally, to Simona, Arthur, Bora and Martin for shearing good times with me.

... Para Bia

y para la Ro del pasado que le parecía increíble como unas partículas podían colisionar y convertirse en otras totalmente diferentes (con alguna probabilidad y respetando los numero cuanticos...), y que soñaba con trabajar en el acelerador de mayor energía.

Contents

1 Introduction

The work presented in this thesis has been carried out within the ATLAS experiment, at the Large Hadron Collider. Two analyses are presented.

In the first one, measurements of charged-particle distributions in proton-proton collisions are presented. These are used to reflect the strong interaction with low momentum transfer. In this region, the charged-particle interactions are described by quantum chromodynamics (QCD) and thus, these measurements are essential for an accurate description of $p-p$ interactions and to constrain free parameters of Monte Carlo event generators. In particular, this analysis extends previous measurements to a new phase-space in the low momentum regime: p_T >100 MeV and $|\eta|$ <2.5. The data recorded from $p-p$ collision at a center-of-mass energy of 13 TeV recorded during 2015 and collected using a dedicated trigger for minimum bias data. The analysis strategy starts with raw charged-particle multiplicity distributions. These are corrected to take into account reconstruction inefficiencies. Furthermore, an unfolding procedure with a Bayesian method is applied to correct for the detector effects. The final distributions are then compared to several Monte Carlo generators.

The second analysis is a search for localized excesses in the dijet mass distributions of low dijet mass events produced in association with a high transverse energy photon. Searches for dijets resonances with masses of several hundred GeVs have been carried out by different experiments. However, these searches have been limited at lower masses by the large multi-jet background. At this regime, these events are produced at such high rates that would saturate the on-line selection and impose thresholds that limit the sensitivity of this analysis. The current analysis uses a different approach to overcome this limitation. It utilizes dijet events in association with a high-p_T initial-state radiation photon that can be used for triggering, allowing the resonance to be reconstructed from lower-p_T jets. Consequently, the subject of this analysis is a resolved final state consisting of two jets and one photon.

The search uses a luminosity up to 79.8 fb^{-1} and center-of-mass energy of 13 TeV during 2015-2017. Two variants are presented: one which makes no jet flavor requirements and one which requires both jets to be tagged as b-jets. The results of the mass distributions were consistent with multi-jet processes in the Standard Model. Therefore the data was used to set upper limits on the production cross-section for a benchmark Z' model and on generic Gaussian-shape contributions to the mass distributions, extending the current ATLAS constraints on dijet resonances to the mass range between 225 and 1100 GeV.

This thesis organizes as follows. Section 2 starts with a brief overview of the Standard Model and some limitations. It also presents an introduction to the Monte Carlos used through the analyses in Section 2.4. The LHC and the ATLAS detector and a summary of their performance are described in Section 3 and Section 4. Section 5 focusses on the different techniques used to reconstruct the objects used by the analyses. Section 6 presents the analysis of the charged-particles distribution and Section 6 presents the search for localized excesses in the dijet mass distributions. Finally, Section 8 presents a summary and the conclusions.

2 Theoretical Introduction

2.1 The Standard Model

The Standard Model (SM)[107][102][2] is the theoretical framework that best describes the composition and the interaction of the matter at a subatomic scale. Since it was developed in the 1960s, it has been strongly tested and it has been very successful in describing experimental observations.

The SM is a renormalizable quantum field theory based on the total invariance under the gauge group:

$$U(1)_Y \otimes SU(2)_L \otimes SU(3)_C \tag{1}$$

where $SU(3)_C$ is the symmetry group of the strong interaction and $U(1)_Y \otimes SU(2)_L$ corresponds to the electroweak interaction. The subindex L denotes that the left-handed fermions have isospin, a restriction imposed to reflect experimental observations. The subindex Y denotes the hypercharge and C denotes the color, explained in detail in Section 2.1.3

The SM describes the components of the matter, *fermions*, and the interactions between them by the force mediator, *bosons*. The former are divided into two groups, *quarks* and *leptons*, and both are sorted in families or generations, where each family has the same quantum numbers but different mass values.

In addition, each quark and lepton has an anti-particle, with the same mass and opposite quantum numbers. A summary of this particles is presented on Figure 1

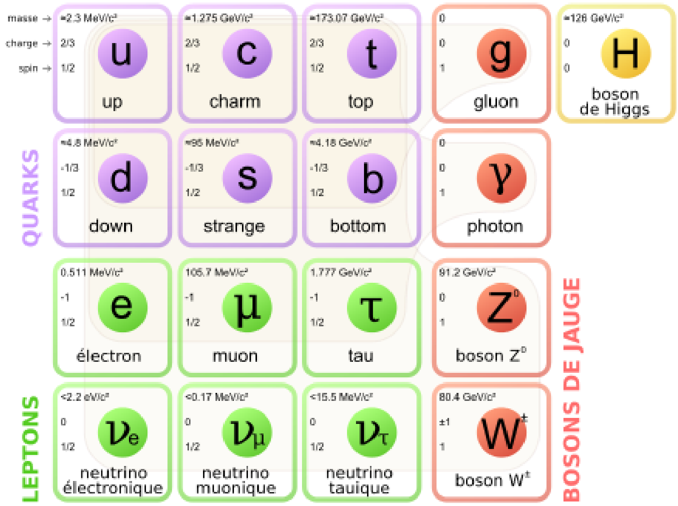

Figure 1: Diagram of the particles described by the SM.

The fermions with spin 1/2 are described by Dirac equation, That follows from the Lagrangian:

$$L = \bar{\psi}(i\gamma^\mu \partial_\mu - m)\psi \tag{2}$$

where ψ is the fermion field. γ^μ are the Dirac matrices and m is the mass of the fermion.

The Noether theorem states that if the Lagrangian is invariant under a transformation, then there will be a corresponding conservation law; i.e. there is a quantity that is constant. In this case, by imposing the Lagrangian to be invariant under local transformations of a given symmetry group, new (boson) fields appear.

The number of bosons is equal to the number of generators of the symmetry group. A summary of the bosons in the SM is shown on the right side of Figure 1. Bosons Z and $W^{\pm}$ are the weak force mediators; G are those for the strong interaction force mediator; γ, the electromagnetic force and the H boson is the responsable for the mass of particles. Each interaction will be described in the following Sections 2.1.1,2.1.2 and 2.1.3.

2.1.1 Electroweak Theory (EW)

In the SM, the electromagnetic and weak interactions are described together by Glashow-Weinberg-Salam theory [101][1] as the electroweak interaction, that satisfies $SU(2)_L \otimes U(1)_Y$ gauge symmetry group. The Lagrangian for the electroweak interactions is given by:

$$L_{EW} = \sum_{\Psi} \bar{\Psi}[i\gamma^{\mu} D_{\mu}]\Psi - \frac{1}{4} W_{\mu\nu}{}^{a} W_{a}{}^{\mu\nu} - \frac{1}{4} B_{\mu\nu} B^{\mu\nu} \tag{3}$$

$$D_{\mu} = \partial_{\mu} + igT^{a} W_{\mu}{}^{a} + ig' \frac{1}{2} T_{Y} B_{\mu} \tag{4}$$

where T^a are the generators of $SU(2)_L$ group. The generator of the $U(1)_Y$ group is represented by T_Y. And the coupling constants to the $W_{\mu}{}^{a}$ triplet and B_{μ} fields are g and g'. The subindex L denotes the fact that in nature the weak interacion only affects left handed (right-handed anti-particles) particles. Therefore Ψ is the fermion doublets for the left-handed and fermion singlets for right-handed. $\Psi : \begin{pmatrix} \nu_{l_i} & l_i \end{pmatrix}_L$ and $(l_i)_R$ for leptons, and $\begin{pmatrix} u_i & d_i \end{pmatrix}_L$, $(u_i)_R$ and $(d_i)_R$ for quarks. The subindex i runs over each family. However the down elements d_i are not those from Figure 1 but a mixture of them given by the Cabibbo-Kobayashi-Maskawa [90][87] unitary rotation $d_i = \sum_j V_{ij} d_j$.

Mass terms can not be added as $-m^2 f^2$ (for a field f) to the Lagrangian because it breaks the local gauge invariance. However this issue can be adressed properly by the Higgs mechanism, where the masses araise naturally by the symmetry breaking as it is described in Section 2.1.2.

2.1.2 The Higgs mechanism

In 1964 the Higgs mechanism was a proposed solution to the fact that weak gauge bosons in equation 3 are massless, which is in conflict with experiments.

The Higgs mechanism into the SM theory proposes a spin zero Higgs boson particle. In this model, the mass emerges from the interaction of the particles with the higgs field.

The minimal solution is a scalar field with four real components, arranged in a complex doublet $\Phi = (\phi^+ \ \phi^0)$. And the Lagrangian is given by:

$$L_H = |D_\mu \Phi|^2 - \mu^2 \Phi^\dagger \Phi - \lambda (\Phi^\dagger \Phi)^2 \tag{5}$$

The fields of the weak force are included in the Lagrangian through the covariant derivate D_μ as defined in Equation 4. The last two terms in L_H that define the potential, depend on μ and λ. Taking $\mu^2 \leq 0$ and $\lambda \geq 0$ the minimum of the Φ field potential is degenerated, with a fundamental vaccum value of $\Phi^\dagger \Phi = \frac{v^2}{2}$. The v is called the vacuum expectation value (VEV) of the neutral component of the Higgs doublet.

All these minimum configurations are connected by gauge transformations, that change the phase of the complex field Φ, without affecting its modulus.

Choosing one of the minimum configuration of the Φ field. The potential is no longer symmetric. This is called *spontaneous symmetry breaking*. However the Lagrangian is still invariant.

Expanding Φ around the minimum

$$\begin{pmatrix} \phi^+ \\ \phi^0 \end{pmatrix} = \frac{1}{\sqrt{2}} exp[\frac{i\sigma_i \Theta^i(x)}{v}] \begin{pmatrix} 0 \\ v + H(x) \end{pmatrix} \tag{6}$$

the phase can be removed by rotating with a $SU(2)_L$ gauge transformation

$$\Phi(x) \to \Phi'(x) = U(x)\Phi(x) = \frac{1}{\sqrt{2}} \begin{pmatrix} 0 \\ v + H(x) \end{pmatrix} \tag{7}$$

where $U(x) = \exp[-i\sigma_i \Theta^i(x)/v]$. This gauge choice is called *unitary gauge*. Three of four real scalar fields are "eaten" by the gauge transformation. However, these three degrees of freedom appear as mass terms (longitudinal components) for the three weak force boson fields. The remaining scalar field is the massive electrically-neutral Higgs boson [67] [71].

The mass terms for weak bosons arise from the kinetic part of the Lagrangian, through the covariant derivative.

$$\begin{aligned} (D_\mu \Phi^\dagger)(D_\mu \Phi) = & \frac{v^2}{2}(g_1 Y_w B_\mu + g_2 \frac{T}{2} {W^2}_\mu)^2 + \frac{v^2}{2}(\frac{T}{2})^2 g_2^2 ({W_\mu}^1)^2 \\ & + \frac{v^2}{2}(\frac{T}{2})^2 g_2^2 ({W_\mu}^3)^2 + \ non - quadratic \ terms \end{aligned} \tag{8}$$

This new terms assign masses to three fields for ${W_\mu}^1$ and ${W_\mu}^2$, which become ${W_\mu}^\pm$ bosons with a linear combination.

$$W^\pm = -\frac{1}{\sqrt{2}}(W^1 \pm iW^2) \tag{9}$$

And a slightly different linear combination for B_μ and ${W_\mu}^3$ that corresponds to Z and γ. Where an orthogonal linear combination is identified as a massless gauge boson, the photon.

$$\begin{pmatrix} \gamma \\ Z^0 \end{pmatrix} = \begin{pmatrix} cos(\theta_w) & sin(\theta_w) \\ -sin(\theta_w) & cos(\theta_w) \end{pmatrix} \begin{pmatrix} B \\ W^3 \end{pmatrix} \tag{10}$$

Where θ_w is the weak mixing angle. This also introduces a relationship between the mass of the Z^0 (M_Z) and the mass of the $W^{\pm}$ (M_w) particles.

$$M_Z = \frac{M_w}{cos(\theta_w)} \tag{11}$$

Also the expansion of Yukawa terms in the same basis gives mass terms for the fermions. Neutrinos instead do not get masses in this process due to the non right-handed component[68][111].

$$L_{fermions} = -y_l(\bar{\nu_l}, \bar{l})_L \begin{pmatrix} \phi^+ \\ \phi^0 \end{pmatrix} l_R - y_d^{ij}(\bar{u_i}, \bar{d'})_L \begin{pmatrix} \phi^+ \\ \phi^0 \end{pmatrix} d_{jR}$$

$$-y_u^{ij}(\bar{u_i}, \bar{d'})_L \begin{pmatrix} -\phi^0 \\ \phi^- \end{pmatrix} u_{jR} \ + \ h.c. \tag{12}$$

where y are the Yukawa coupling constants. Expanding the scalar doublet around the expectation value ($\phi^0 = \frac{v+h}{\sqrt{2}}, \phi^{\pm} = 0$), two terms survive for the lepton subsector:

$$L_{leptons} = -\frac{y_l v}{\sqrt{2}}\bar{l}l - \frac{y_l}{\sqrt{2}}\bar{l}lh \equiv m_l\bar{l}l - \frac{m_l}{v}\bar{l}lh \tag{13}$$

The first term gives the lepton mass and the second one reflects the coupling to the Higgs boson h, using $m_l = y_l v/\sqrt{2}$.

The quark subsector is more complicated due to the CKM mixing of down-type quarks ($d'_i = SumV_{ij}.d_j$), reflecting the fact that the EW eigenstates are a rotation of the Halmitonian eigenstates

2.1.3 Quantum Chromodynamics (QCD)

The description of the strong field interactions between quarks and gluons, called *partons*, originally developed Gellmann [86] and Zweig [72] in the 1960s to explain the huge amount of baryon resonances discovered during 1950s [92], evolved over the years into a renormalizable quantum field theory. The QCD Lagrangian of QCD within the SM is given by:

$$L_{QCD} = \sum_{\Psi} \bar{\Psi}_q[i\gamma^\mu(\partial_\mu - ig_s {A_\mu}^a T_a)]\Psi_q - \frac{1}{4}{F^a}_{\mu\nu}{F^{\mu\nu}}_a \tag{14}$$

where Ψ_q and ${F^a}_{\mu\nu}$ (field tensor) are defined by

$${F^a}_{\mu\nu} = \partial_\mu {A^a}_\nu - \partial_\nu {A^a}_\mu - g_s f_{abc} {A^b}_\mu {A^c}_\nu \ ; \ \Psi_q = \begin{pmatrix} {\psi^q}_{red} \\ {\psi^q}_{green} \\ {\psi^q}_{blue} \end{pmatrix}$$

The Lagrangian of QCD (Equation 14) is invariant under $SU(3)$ rotations. This local invariance requires the introduction of eight gauge fields, which correspond to eight mediators (gluons). And the quantum number conserved is the color, which can be red, green or blue.

The sum in Equation 14 runs over Ψ_q quark fields only. g_s is the strong coupling constant and ${A_\mu}^c$ are the eight ($c = 1, .., 8$) Lorenz vectors representing the massless gluon gauge bosons, and $T_{ab}{}^{c}$ are the generators of $SU(3)_c$ group with the property that $[T^a, T^b] = if_{abc}T^c$.

As in nature quarks and gluons are found only in uncolored states, they can not be as individual particles. Instead, they form groups called *hadrons*.

There are two families of hadrons: *mesons* and *baryons*. The first one is made with quarks and an anti-quarks, having opposite color they form colorless states. The second ones, are made with combinations of 3 quarks, each of them with a different color (r,g,b), forming again an uncolored state.

Expanding Equation 14 there are three types of vertices ggg and $q\bar{q}g$ proportional to g_s, and $gggg$ proportional to ${g_s}^2$ a tree level. The strength of the strong interaction is described by a coupling constant: $\alpha_s \equiv \frac{{g_s}^2}{4\pi}$, where g_s denotes the QCD coupling constant.

The interaction between gluons reflects the fact that they carry color charge. Also, it means that α_s depends of the scale of the interaction. It is the four-momentum transferred between the partons Q^2. If the interaction occurs with a large momentum transfer it is called *hard* and if not, *soft*.

At leading order the strength of the strong coupling is given by:

$$\alpha_s(Q^2) = \frac{12\pi}{(33 - 2n_f)ln((Q^2/{\Lambda_{QCD}}^2))} \tag{15}$$

where n_f is the number of quark flavors and Λ_{QCD} is the renormalization scale[1].

As Equation 15 shows, α_s decreases with the logarithm of the interaction strength. In the high energy regime the QCD interaction becomes weak. This phenomenon is referered to as *"asymptotic freedom"* [73] [93].

The opposite happens for lower energy, the value of α_s increases giving as result the *"confinement"* of quarks and gluons.

This phenomenon also means that if partons with color charge start to separate form each other, the potential energy increases to the point that it is energetically more convenient to hadronize creating a quark-anti-quark pair with opposite charge from the the vacuum. As a consequence, colored partons produced in high-energy interactions give place to a shower of hadrons.

Figure 2 shows the dependency between α_s and the energy scale.

QCD interactions are dominant at the LHC because α_s constant is much larger than the other coupling constants. Therefore a good description of the QCD process is needed, either to understand the hadronic process in itself or as background of other process of interest like the Higgs physics.

2.2 Hadronic collisions

An appropriate description of the physics processes in a *pp* collision may be complicated. A typical hadronic collision is illustrated in Figure 3. When two hadrons

[1] The contribution of all such diagrams across all orders provides a diverging infinite sum which can be overcome by using renormalisation: a set of parameters of the theory are rescaled to counteract the additions from the loops. The process of renormalisation always introduces a scale Λ_{QCD} at which the calculations for the rescaling procedure are made.

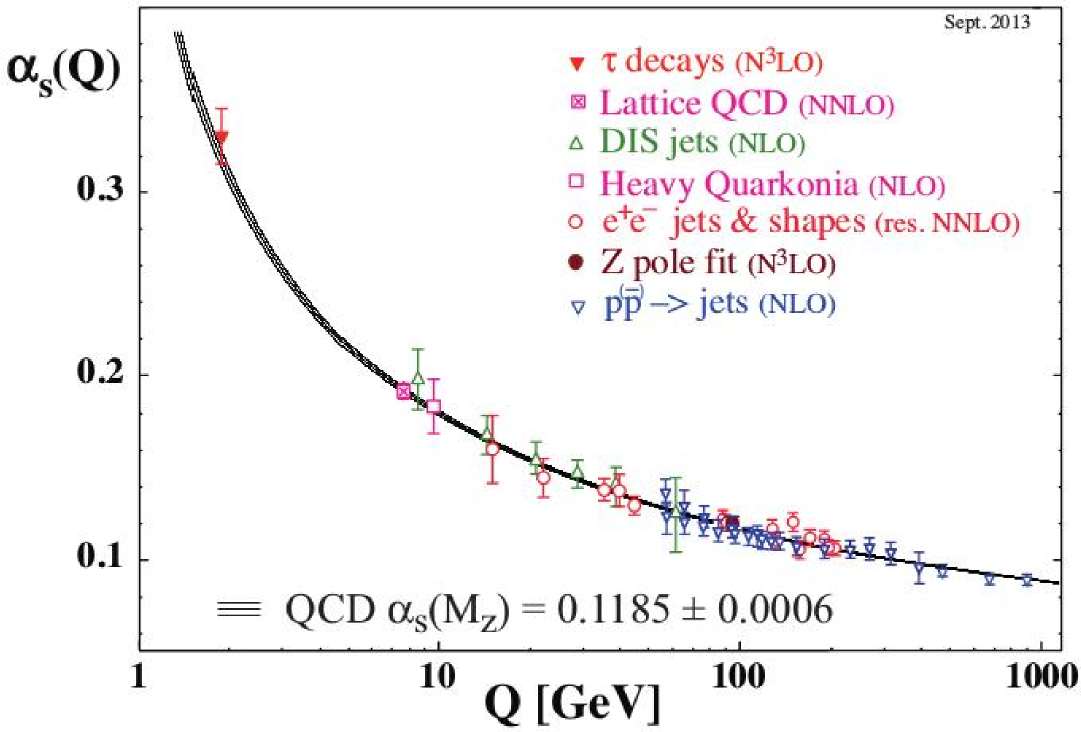

Figure 2: Combined measurements of α_s as a function of the scale Q for several experimental sources. NLO, NNLO etc indicates the order of perturbative QCD used in the calculation of the reported value [98]

collide, partons may interact and be scattered several ways. Either, the incoming or outgoing partons can radiate, and all outgoing partons hadronize.

Besides, the hadronization is a complex process and involves perturbative and non-perturbative QCD processes, described in Section 2.2.1.

In most cases of physics of interest, only particles coming from $high - p_T$ processes are studied and the contribution of soft interactions are typically negligible. These interactions are referred to as being part of the *underlying event*. However, for precision studies, as the measurement of the top quark mass, models used for the underlying event can have a significant impact [64].

2.2.1 Cross-section and Factorization Theorem

The computation of the cross-section contains both perturbative and non-perturbative behaviours simultaneously. The *factorization theorem* shows that the cross-section for a scattering process between hadrons A and B leading to the final state X can be calculated by separating the high-scale, perturbative part of the interaction from the low-scale, non-perturbative part and treating them independently [77].

It can be understood intuitively by considering the interaction between two relativistically moving hadrons with high momentum transfer, where the partons in them feel the asymptotic freedom. The time dilation kinematic variable of the rela-

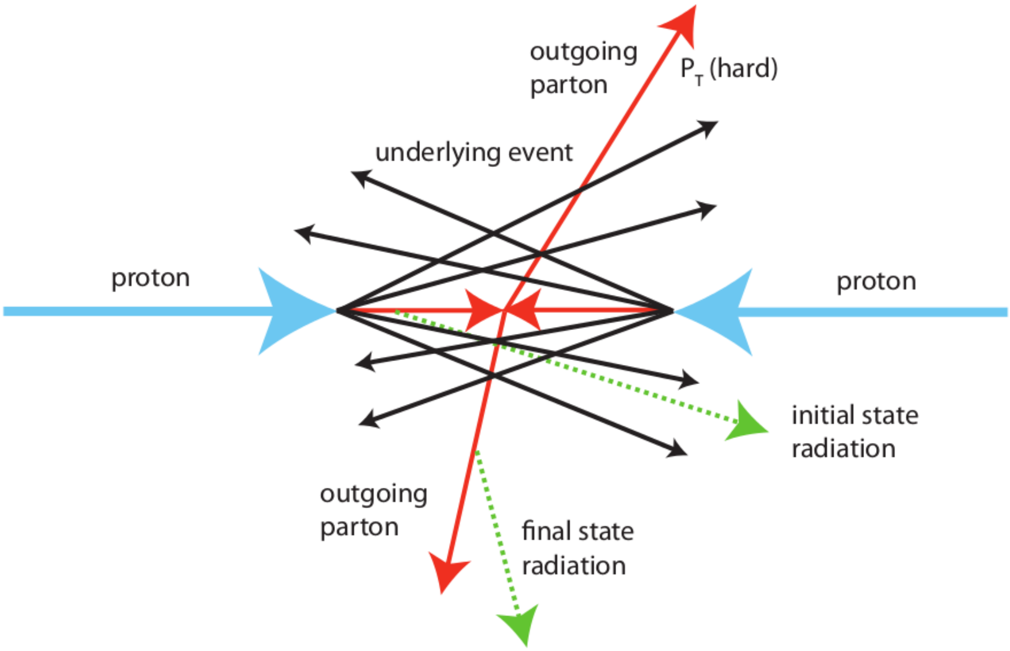

Figure 3: Illustration of components of a hard scattering process in a hadron-hadron collision. The incoming protons are shown in blue. The partons undergoing the hard scattering are shown in red. Possible initial and final state radiation is shown using dashed green lines. The particles participating in the underlying event are shown in black.

tivistic moving hadrons is sufficient that any virtual particles will be nearly constant during the collision and the parton momenta will not change substantially. Thus the hadrons interact not as single particles but rather as collections of free partons of fixed momentum [81]. The cross-section for the collision can then be computed using the cross-section for the single parton-parton interaction of interest, weighting it with the probability for each parton to carry a given proportion of the hadrons momentum, and then integrating over the possible combinations [79]

$$\sigma_{P_1 P_2 \to X} = \sum_{i,j} \int dx_1 dx_2 f_i(x_1, \mu^2) f_j(x_2, \mu^2) \hat{\sigma}_{i,j}(p_1, p_2, \alpha_s(\mu^2), Q^2/\mu^2) \tag{16}$$

where P_1 and P_2 are the four momenta of the incoming hadrons. A fraction of these two momenta goes to the partons which interact in the hard scattering are $p_1 = x_1 P_1$ and $p_2 = x_2 P_2$. The four momentum transferred between the partons in the hard scattering is Q. Then the parton distribution functions (pdf), $f_i(x, \mu^2)$, depend on the fraction of momentum carried by each parton and the choice of factorization scale, μ, which will be discussed later. And the cross-section for the partons is $\hat{\sigma}_{i,j}$. All the components of the cross-section are schematized in Figure 4.

Two partons (i, j) can collide under different types of “hard” scatter, giving as a result two or more final-state partons. Partons with a large transverse momentum (p_T) tend to radiate more partons generating as consequence a “spray” of partons.

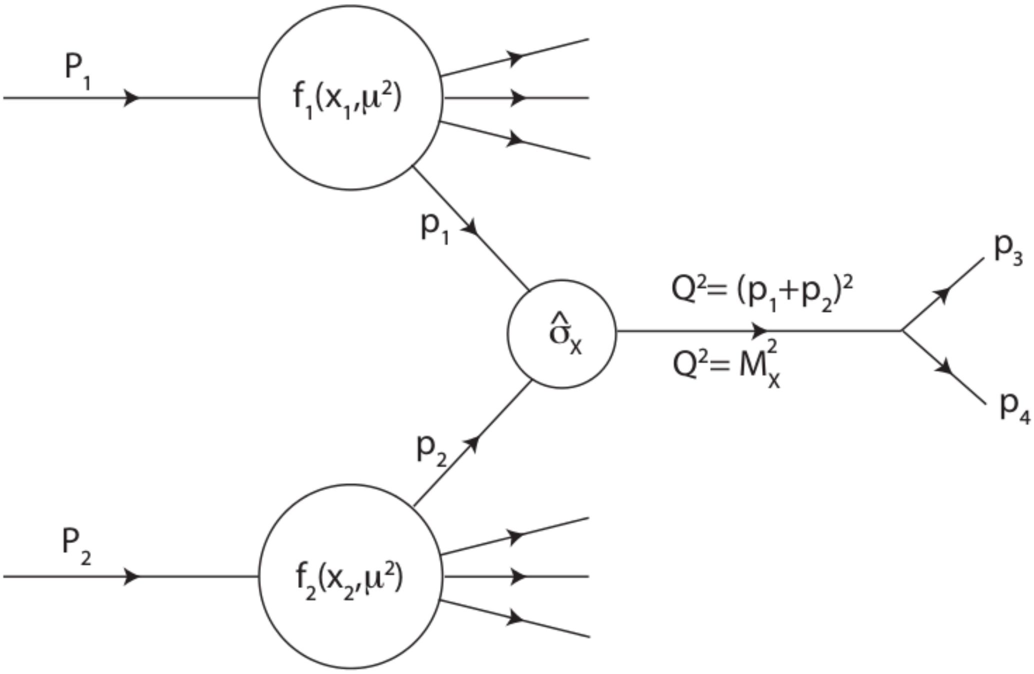

Figure 4: Scheme of the cross-section for the hard scattering of two hadrons with momenta P_1 and P_2. The *pdf* $f_i(x_i, Q^2)$ that gives the probability to have a parton with a fraction x_i of the proton momentum. And the cross-section for the parton interaction $\hat{\sigma_x}$

As the shower develops, each parton looses momentum, and the strong interaction becomes dominant over kinematics transforming single partons into hadrons. This phenomena is call *hadronization* and is a consequence of the color confinement principle[2]

A final state can also contain energy from processes that do not come from the hard scatter. Partons can irradiate, mostly, gluons and photons before the hard scatter occurs. This process is called *initial state radiation* (ISR). Other posibility is the case where there are multiple simultaneous parton interactions (MPI). Figure 5 is a representation of a hadron-hadron collision, and the main process described before.

2.2.2 Types of Inelastic Scattering

The total cross-section is the sum of the cross-sections of all possible *pp* interactions. These can be either elastic or inelastic. In the first case the both protons end intact and no additional particles are produced. Opposite to the Inelastic interaction, where at least one of the incoming protons is destroyed and therefore the out-coming particles differ from the incoming ones.

[2] The totality of the partons within the shower hadronize at the very neighborhood of the interaction point within a lenght of the size of a proton ($1fm$).

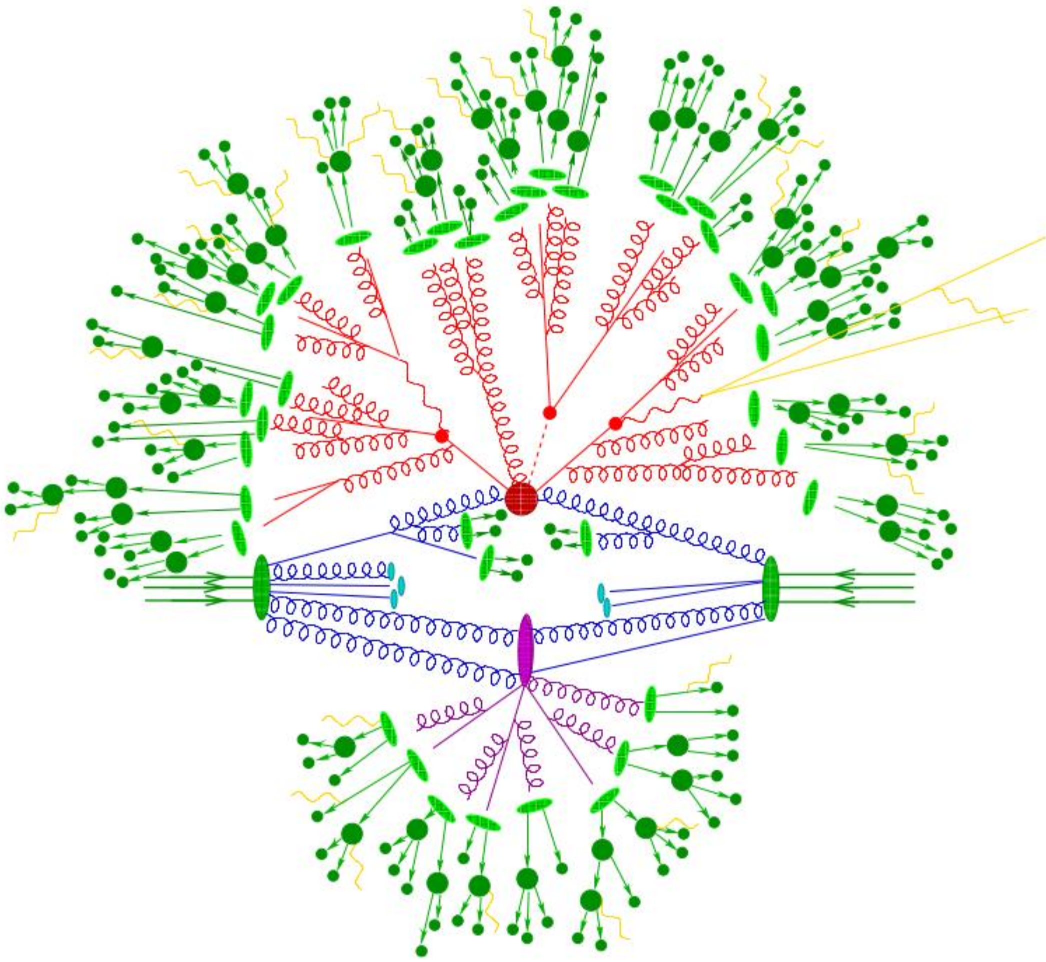

Figure 5: Simulation of a pp collision. Incoming partons are in blue. In red, the hard scattering process is represented by the large (red) circle, and the parton showering created by it. The underlying event interactions are shown in purple. Hadrons are indicated in green for both, the initial protons and those which begin to form once particles have lost sufficient energy that their QCD interactions are no longer perturbative [109].

There are three types of inelastic interactions as shown Figure 6. Inelastic interactions in which color charge is exchanged are referred to as non-diffractive (ND) interactions. In a single diffraction (SD) a particle is exchanged between the two protons and one of the incoming protons end in a diffractive system. In double diffraction (DD) the same happens but both of the protons form diffractive systems.

Non- single- and double- diffractive events have different topologies and multiplicities. In QCD non-diffractive events result in a large number of particles being produced at central rapidity. However, the multiplicity falls fast at forward rapidities. In a single-diffractive event, the proton which breaks up produces particles at high rapidity. The other incoming particle is essentially undisturbed and has the rapidity of the beam. In a double-diffractive event particles are produced sym-

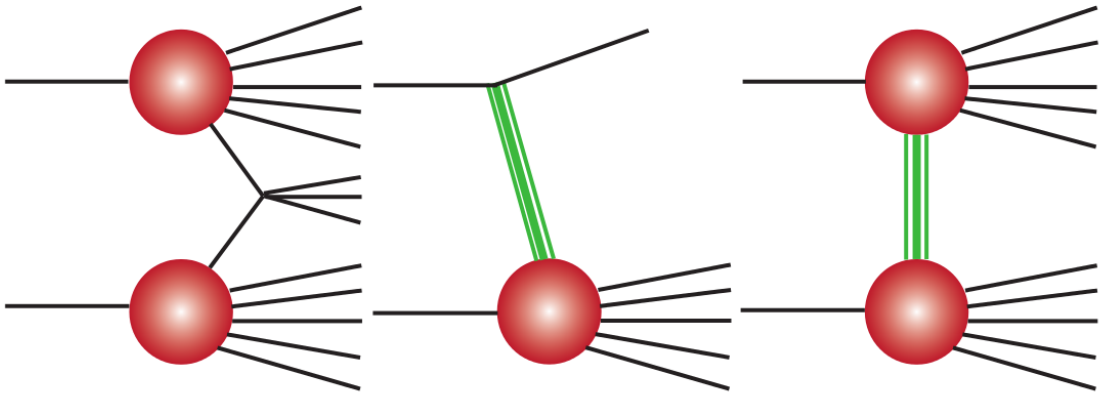

Figure 6: Different types of inelastic pp collisions. (a) Non-diffractive interaction , (b) single-diffractive diffraction and (c) double-diffractive diffraction.

metrically at positive and negative forward rapidity, with fewer particles produced in the central region. Both non-diffractive and double-diffractive interactions are symmetric around $\eta = 0$.

2.3 Beyond the Standard Model

The big goal is to find the Theory of everything, one single model that describes all aspects of the universe [66]. Physicists know that this model can not be the Standard Model. Even when it describes very successful several aspects of nature it can not be complete since, for instance, gravity can not be included in it. So far the Standard Model agrees with all confirmed experimental data from the accelerators and other several experiments, but this observed particle spectrum may not be enough to describe the matter composition of the universe. Some of the most important outstanding issues are described below.

Incomplete model...

There are several inconsistencies and facts that the SM does not explain. For instance, the value of the particle quantum numbers such as the electric charge (Q), weak isospin (T_3), hyper-charge (Y) and color charges. Also, the values of the masses for the quarks, leptons and some bosons are not provided by the theory, they depend on Yukawa couplings and the vacuum expectation value. In fact, there are 19 free parameters(+ 9 if we take into count the masses of the neutrinos responsible for the neutrino-flavor oscillation). These parameters *seem* too large to be considered an *elegant* theory.

All the points mentioned before constitute the fondations of the SM theory. But the SM does not explain the measurements of the galactic rotation speeds [112], neither the gravity. Also, the SM indicates that the amount of matter and antimatter should have been produced in equal quantities at the time of the Big Bang, however the big majority of the universe is made of matter.

Several theories attempt to understand and explain the issues mentioned before, some of the most popular are briefly commented below.

Dark matter (DM)

In 1970, measurements of galactic rotation speed provided clear evidence that additional mass was present around galaxies. This mass, is associated to what is called Dark Matter has to be invisible to telescopes but be present in order to explain the gravitational effects observed [117][88].

There is no appropriate DM candidate in the SM. Extremely heavy right-handed neutrinos are a possibility, but difficult to reconcile with the low masses and mixing requirements of the known neutrinos [115]. Thus a new particle not considered by the SM is expected to be a candidate for Dark Matter. Some properties are inferred from cosmological observations and previous collider results: It does not interact electromagnetically. otherwise, it could be detected with astronomical procedures. And must be stable since no SM decay products were observed.

Many DM candidates are proposed but weakly interacting massive particle (WIMP) is motivated to be a plausible candidate.

Supersimmetry (SUSY)

The supersymmetry theory incorporates a fermion-boson symmetry. It considers that for each particle of the SM model exists a supersymmetric partner, the spin of which differs by a half-integer.

A super-symmetrical extension to the Standard Model would solve some issues with the SM like cancelation of divergencies, candidates for DM and unification of interactions.

2.4 Monte Carlo Generators

Several processes, as the determination of the resolution, optimization or the estimation of the analysis background rates, require predictions based on Monte Carlo simulations (MC).

An event generator uses predictions like the QCD or QED models for *pp* collisions and simulates the rate of different outcomes. However, with the increasing number of outgoing partons, complexity in the calculations become challenging. Furthermore, these calculations do not provide the full hadronic level event description. So, an alternative approach is provided by the Monte Carlo programs.

Matrix element: To describe a 2$\rightarrow$ n process from the theory, a set of Feynman diagrams are evaluated. So, the matrix elements (ME) are calculated in powers of the strong coupling constant (α_s). It becomes hard to compute at high order, but it can be factorized into a simple core process (e.g. $2 \rightarrow 2$, convoluted with parton probabilities to mimic a higher-order process). Simulation programs, like PYTHIA [114], implement this approach using leading-order (LO) perturbative calculations, others like SHERPA [110], use next-to-leading-order NLO perturbation calculations intead.

Underlying event (UE): In addition to the hard interaction generated, also the interactions between the incoming proton remnants need to be taken into account. This is usually modeled through multiple extra $2 \rightarrow 2$ scatterings, occurring at a scale of a few GeV. The UE can include additional hard interactions and soft processes which can not be calculated perturbatively. These are modeled with adjustable parameters that are tuned to experimental data.

hadronization: As the shower reaches $Q^2 = \Lambda_{QCD}$, the coupling forces become significant and confinement takes place. This is no longer described by first principles and involves the transformation of the outgoing colored partons into colorless hadrons of a typical 1 GeV mass scale. The hadronization is commonly described by the Lund string fragmentation model [50]. It describes the color force by a linearly rising potential as charges separate. The potential energy stored increases as partons recede, so it may break up by the production of new quark-antiquark. Then, they may combine to produce hadrons. After the perturbative parton branching process, the remaining gluons are split into light $q\hat{q}$ pairs, and then neighboring quarks and antiquarks can be combined into color singlets (colorless "clusters"), with masses distributions peaking at low values and asymptotically.

Tune: The MC generators contain a number of free parameters due to the non-perturbative, and therefore incalculable, nature of much of the soft physics processes, like the shower approximations, hadronization, and underlying event. These different parameters are usually tuned with data from colliders. A specific set of chosen parameters for a MC generator is referred to as a tune. The most common used are the A14 tune [35] and the AU2 tune [31].

Detector simulation: To simulate the detector effects and reproduce events as may be measured by the ATLAS detector, the simulations must be passed by tools like GEANT 4 [97]. These simulators simulate the effects of the particles passing by the detector layers and is based on the geometry description, components, and magnetic field.The physics processes include ionization, Bremsstrahlung, photon conversions, multiple scattering, scintillation, absorption, and transition radiation.

Digitalization: The last step involves the digitalization, which simulates the detector outputs in the same format as the actual raw data.

3 The Large Hadron Collider

The Large Hadron Collider [55] (LHC) is the world's largest and more powerful particle collider built so far. It is located at the Conseil Europen pour la Recherche Nuclaire (CERN), at the France-Switzerland border area. There are four big experiments, all of them able to explore the tera-electronvolt (TeV) scale through proton (or heavier ion) collisions. However, they have a specific purpose. Two of them multi-purpose: ATLAS (A Toroidal LHC ApparatuS) [25] and CMS (Compact Muon Solenoid) [60]. And two dedicated experiments: LHCb (Large Hadron Collider beauty) [83] specialized on b quark physics and ALICE (A Large Ion Collider Experiment) [8] focused on studies of heavy ion collisions.

The LHC was installed in a 27-kilometer circular tunnel where a previous collider was, the Large Electron Positron (LEP) collider, at approximately 100 meters underground.

3.1 Machine design

The LHC was designed to produce pp collisions at a center-of-mass energy ($\sqrt{s}$) of 14TeV. However, during 2010-2011 it was operating at $\sqrt{s}$ =7TeV and $\sqrt{s}$ =8TeV during 2012 period. This period is known as Run1.

Between 2013 and 2014 the LHC entered in the first shutdown (LS1). It was necessary to modernize the infrastructure and prepare it for operations at higher energies. From 2015 until 2018 the LHC started the Run2 working at $\sqrt{s}$ =13TeV and with a double number of interactions per pp crossing.

Another significant feature is that the LHC is prepared to work with an instantaneous luminosity (descrived in Section 3.2) of $10^{34} cm^{-2} s^{-1}$, with the beams containing around 2000 bunches with 25ns interval time.

The LHC rincg is only the last element of the CERN accelerator complex as shown Figure 7. The first element is a bottle of hydrogen gas which works as the proton source once that the electrons are removed. Then, they are pulsed from it to a Linear Accelerator (Linac2) up to 100 microsecond per pulse. The Linac2 uses radio-frequency cavities to charge cylindrical conductors alternately positively or negatively. When protons pass through the conductors, are pushed ahead causing the acceleration. Small quadrupole magnets ensure that the protons are arranged in a tight beam. At the end of the Linac 2, the protons have an energy of 50 MeV and go at 31.4% of the speed of light.

Then, these protons enter to the Proton Synchrotron Booster which is made up of four superimposed synchrotron rings which accelerate protons up to 1.4GeV (91.6% of the speed of light)to be injected into the Proton Synchrotron (PS). It accelerates not only protons to the PS but also ions for the Low Energy Ion Ring (LEIR). It works with particles at energies up to 25 GeV (99.93% of the speed of light). After the protons pass to the Super Proton Synchrotron (SPS) which is the last step of the LHC. The SPS has a circumference of 7 km and it accelerates protons up to 450GeV.

Finally the LHC is the largest and most powerful accelerator. It uses superconducting magnets to boost the energy of the particles along a 27 Km ring. In

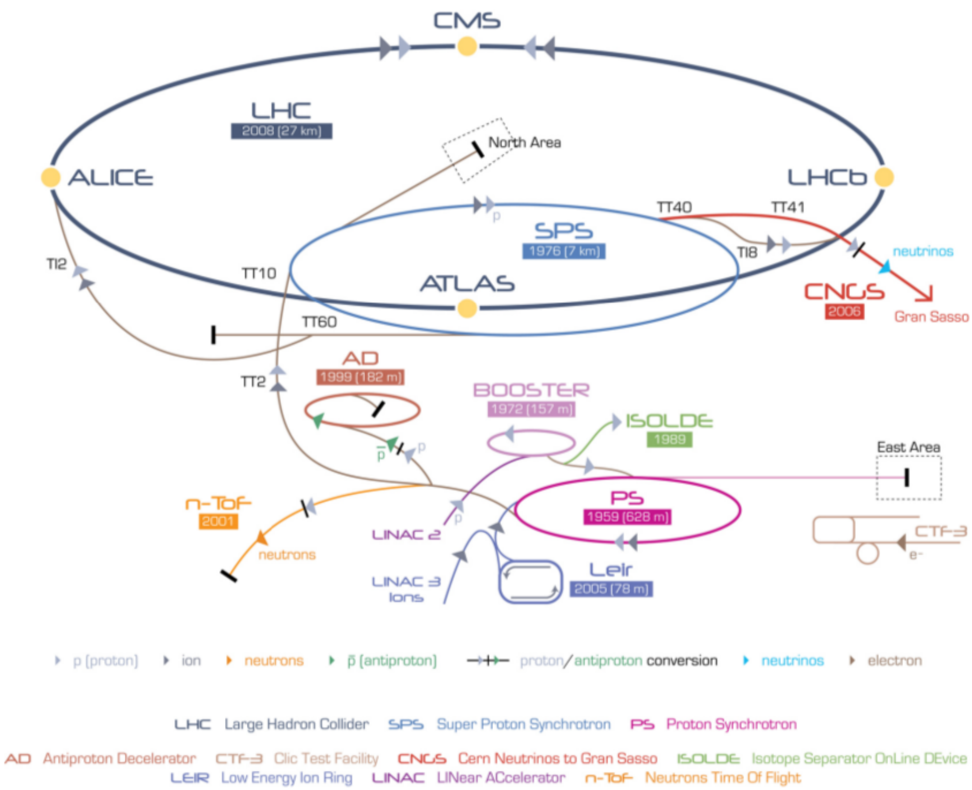

Figure 7: The CERN complex encompassing several accelerators. Image from Ref. [69].

it, two high-energy particle beams are accelerated to an energy of 7 TeV (nominal value) (99.9999991% of the speed of light). The beams travel in opposite directions in separate beams pipes (two tubes kept at ultra vacuum), guided with a magnetic field generated by superconducting electromagnets, which require a temperature of -271.3 C (lower than in the outer space!). To keep this temperature, the accelerator is connected to a distribution system of liquid helium, which cools the magnets and other supply services.

3.2 Running conditions in the 2015-2018 period

The number of events per second, N_{events}, generated in each LHC collision is $N_{events} = L.\sigma_{event}$, where L is the machine luminosity and σ_{event} is the cross-section of the process. The luminosity depends on the beam parameters and for a Gaussian beam distribution, it can be written as:

$$L = n_c f_{rev} \frac{N_1 N_2}{4\pi {\sigma^*}_x {\sigma^*}_y} \tag{17}$$

Where n_c is the number of colliding bunch pairs, N_b is the number of protons per bunch in the beam b, f_{rev} is the protons revolution frequency and ${\sigma^*}_{x,y}$ are the transverse sizes of the beam at the interaction point. Equation 17 shows how the instantaneous luminosity increases when the cross-section is reduced.

The time integrated luminosity $L^{int} = \int Ldt$ during 2015 to 2018 data taking periods is shown in Figure 8.

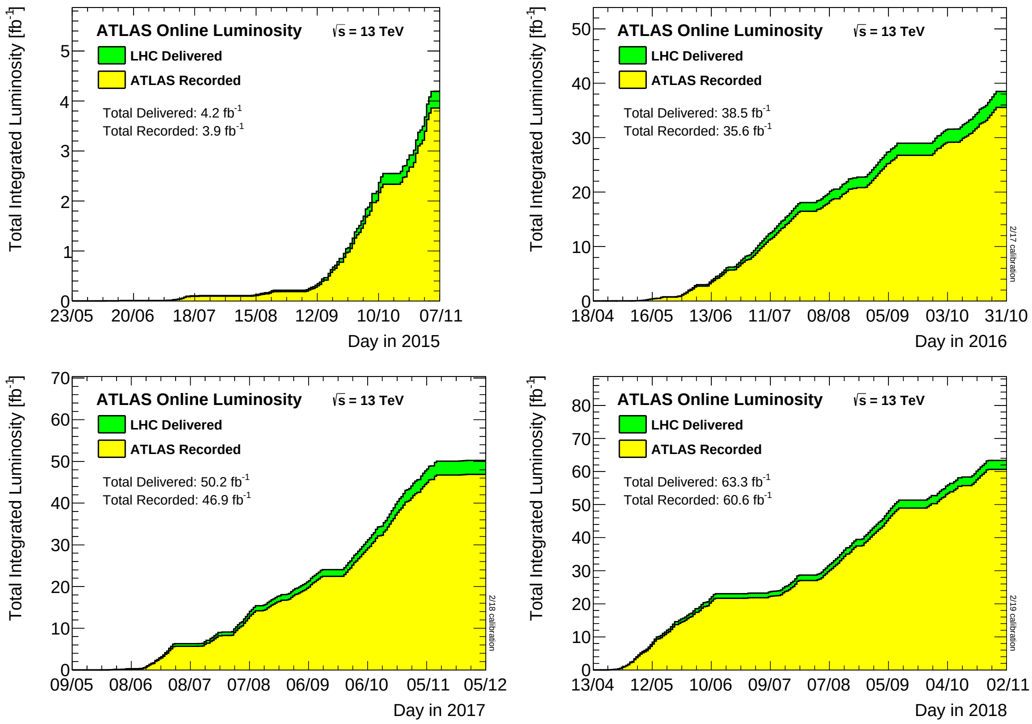

Figure 8: Cumulative luminosity as a function of time delivered to (green) and recorded by ATLAS (yellow) during stable beams for pp collisions at 13 TeV center-of-mass energy from 2015 to 2018. Images from Ref [22]

3.3 Pileup

As a consequence of the high luminosity several proton collisions can be recorded in a single event. This effect causes that the energy of other proton collisions can be interfering with the meansured energy of the hard scatter. This phenomena is called *pileup* and there are two principal sources for it:

- *In-time pileup:* when multiple particle collisions occur within a single bunch crossing and the products are recored in the same event.

- *Out-of-time pileup:* when particle collisions occur in different bunch crossings but the detector recoreds them within a single event due to the brief time between the two different collisions.

The pileup can be estimated from the running conditions as the average number of inelastic collisions per bunch crossing, μ:

$$\mu = \frac{L\sigma_{inelastic}}{n_b f_r} \tag{18}$$

Where n_b and f_r are the number and the frequency of bunches respectively, and $\sigma_{inelastic}$ is the inelastic cross-section for pp collisions [20].

As a consequence it can change depending on the beam optics and bunch parameters at the impact point across different periods of data taking. Therefore, the underlying Poisson distribution can be shifted towards higher or lower values of $< \mu >$ as shown in Figure 9 for 2015 to 2018 data.

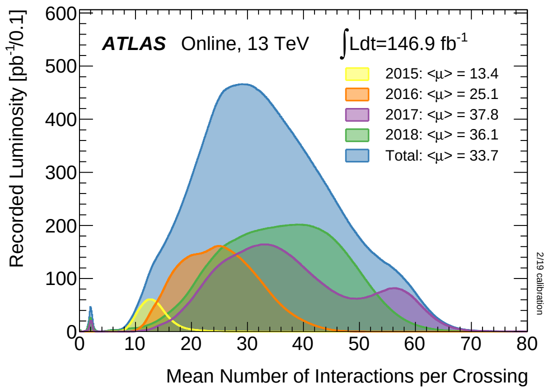

Figure 9: luminosity-weighted distribution of the mean number of interactions per crossing for 2015 to 2018 pp collision data at 13 TeV center-of-mass energy. All data recorded by ATLAS during stable beams is shown, and the integrated luminosity and the mean μ value are given in the figure. Image from Ref [28]

4 The ATLAS detector

ATLAS, A Toroidal LHC ApparatuS, is one of the two multi-purpose experiment at the LHC. It is a 7000 ton detector and has 44m in length per 25m in height. It is symmetric with respect to the interaction point at the center of the detector.

As shown on Figure 4, it is composed by different sub-systems each one with a specific purpose. The inner detector is located closest to the collision point with the goal of measureing the trajectories of the charged-particles, described in section 4.2. Surrounding the inner detector there are two calorimeters: the Electro-magnetic and the hadronic calorimeter. The Calorimeters determine the energy of the particles (neutral and charged particles) , both explained in Section 4.3. Finally the last detector is the muon spectrometer, which allows to measure the position and momentum of muons, described in Section 4.4. Besides, to compute the momentum of the particles two system of magnets are used to bend the trajectory of the particles, explained in Section 4.5.

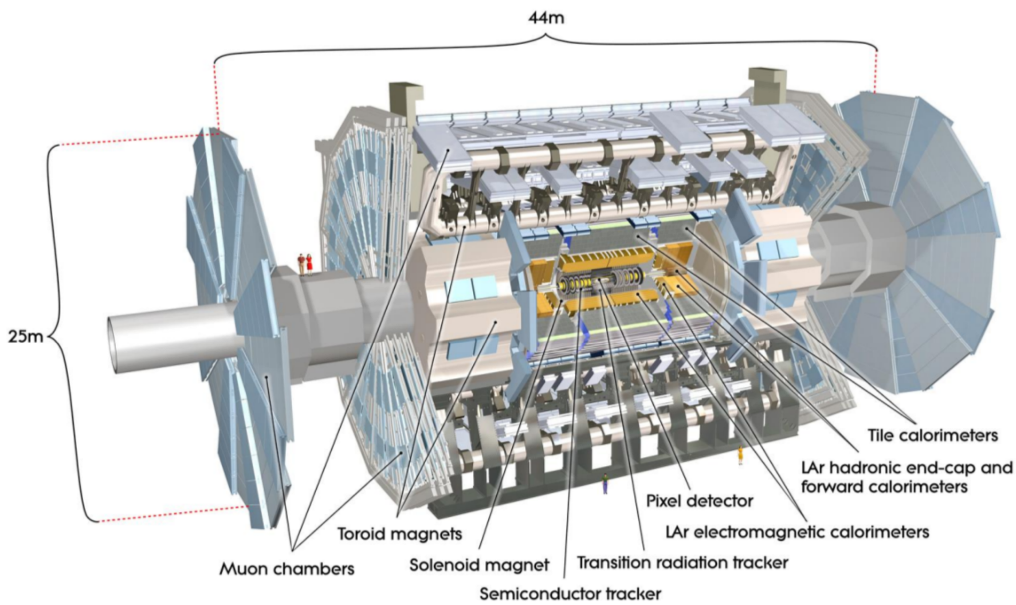

Figure 10: Diagram of the ATLAS detector and sub-systems. Image from Ref. [35]

4.1 System of coordinates and kinematic variables

The coordinates system used in ATLAS is the right-handed Cartesian system, centered at the geometric center of the detector, where the z-axis goes parallel to the beam pipe, the x-axis points to the center of the LHC ring and then y-axis points upwards. As the ATLAS detector has a cylindrical symmetry, it is easier to use ϕ and θ variables.

The azimuthal angle ϕ is measured around the beam axis. Thus $\Delta\phi$ is invariant under longitudinal Lorentz boosts. However it is not the same for the polar angle:

$\Delta\theta$ which depends on the boost of the system. Instead, it is more convenient to work with the rapidity y and the pseudo-rapidity η defined as:

$$y = \frac{1}{2} ln(\frac{E + p_z}{E - p_z}) \tag{19}$$

$$\eta = -lntan(\frac{\theta}{2}) \tag{20}$$

The pseudo-rapidity is equal to the rapidity for massless particles. Thus, for relativistic objects y is closely related to η.

4.2 Inner detector

The goal of the inner detector system (ID) is to reconstruct the path of the charged particles, to measure their momentum and the position of the hard scatter of the event.

A charged particle passing through the Inner detector deposits a minimum of energy, enough to reconstruct the path but not enough to affect the trajectory and the energy measurements in the calorimeters.

The ATLAS ID has three independent but complementary detector systems. From the inside out, the first one is the pixel detector (Pixel), then the Semiconductor Tracker (SCT) and the last one is the Transition-Radiation driff-tube Tracker (TRT). Figure 11 shows a diagram of each tracking system, which covers a region of pseudo-rapidity of $|\eta| < 2.7$.

The ID is immersed in a solenoid magnetic field, that deflects particles in the transverse plane, allowing a highest precision in the computation of the momentum measurement. A complete description of the magnetic field systems is presented in Section 4.5.

During the LS1, the ATLAS Inner Detector was upgraded, installing the new Innermost barrel layer of Pixel called the Insertable B-Layer (IBL) [16], as shown in Figure 12. The distances between each layer are show in Figure 13.

4.2.1 Silicon pixel detector

The silicon pixel tracker is the innermost detector of the tracking system. For Run2, It was improved by inserting the IBL. It was installed at a radius of $r = 33.5$ mm with respect to the beam line and it covers the pseudo-rapidity region of $|\eta| < 3.03$. The size of the pixel sensors is 50x250μm^2 . It improves the track reconstruction performance; for example, both the transverse and longitudinal impactparameter resolution improve by more than 40% in the best case of tracks with transverse momentum(p_{T}) around 0.5 GeV.

Following-up the IBL, There are three barrel layers of pixel detectors (PIX1,PIX2,PIX3) [17], and three end-cap disk-layers. The size of the pixel-sensor modules is 50μm ($r - \phi$)x400μm(z).

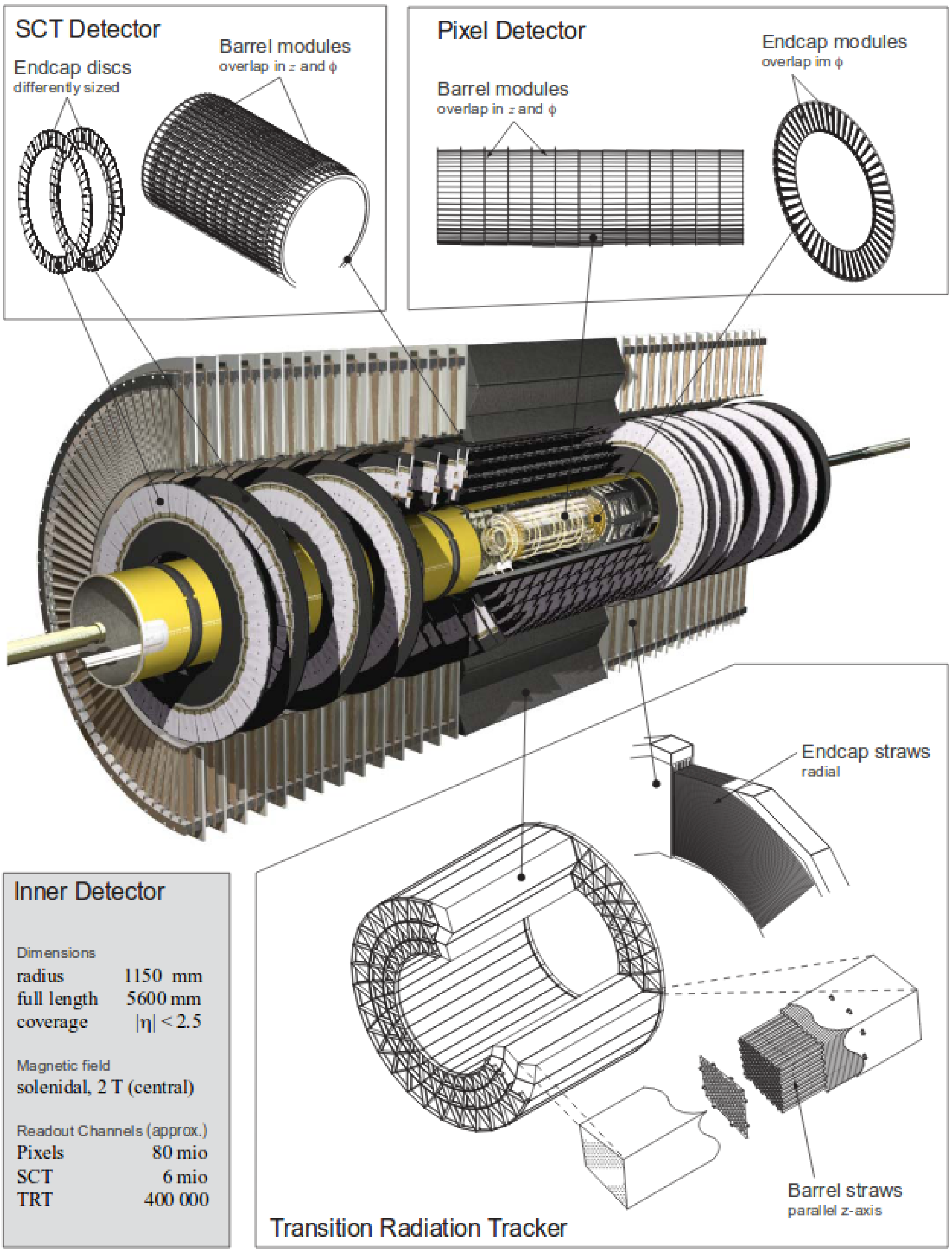

Figure 11: The ATLAS Inner Detector with the sub-detectors shown. Image from Ref [7].

4.2.2 Semiconductor Tracker

The Semiconductor Tracker consists of 4088 silicon strip modules, arranged in four barrel layers (referred to CVT1, SCT2, SCT3, SCT4 from inside to outside) and two end-caps. The Silicon strips are used instead of pixels because the particle density decreases with the radial distance from the interaction point. In this way fewer read-out channels are needed.

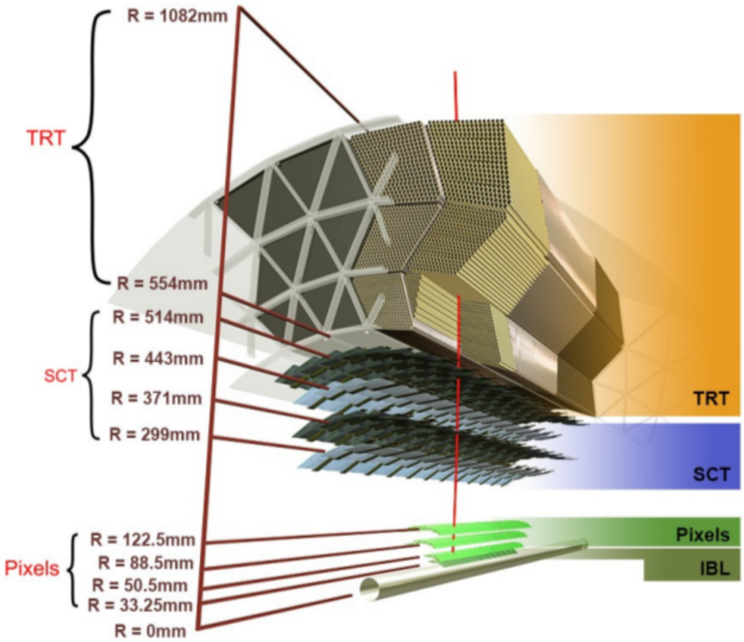

Figure 12: Sketch of the ATLAS inner detector showing all its components- , including the new insertable B-Layer (IBL). The distances to the in- interaction point are also shown. Image from Ref [40].

An SCT module is made up with two sensors glued back-to-back with a stereo angle of 40 mrad. The stereo angle allows a measurement to be made along the length of the strip.

In contrast to the pixel detector, the read-out of the SCT is binary so it does not provide information about the amount of deposited charge.

4.2.3 The Transition Radiation Tracker

The Transition Radition Tracker (TRT) surrounds the SCT detector. It is made of straw tubes with 4 mm of diameter. Each tube has an anode at the center and is filled with a $X_e/CO_2/O_2$ gas mixture. When a charged particle passes through a straw, the gas is ionized and the charge drifts to the anode. In consequence, the time that it takes the charge to reach the wire is used to measure the distance that the particle passes with respect to the wire.

The straws in the TRT barrel are 144cm long and are parallel to the beam axis. In the end-cap they are 37cm long and arranged radially in wheels. The TRT only provides information in the barrel in the $r - \phi$ direction with an accuracy of 130μm. To reconstruct the full trajectory the silicon detectors are needed in conjunction with the TRT. The straws are interleaved with fibers and foils so that an electron passing through produces photons through transition radiation. The photons are absorbed by the gas, producing a large amount of charge. The TRT read-out has two thresholds: a low one to measure ionization and a high one to identify these photons, which allows electrons to be identified using the TRT.

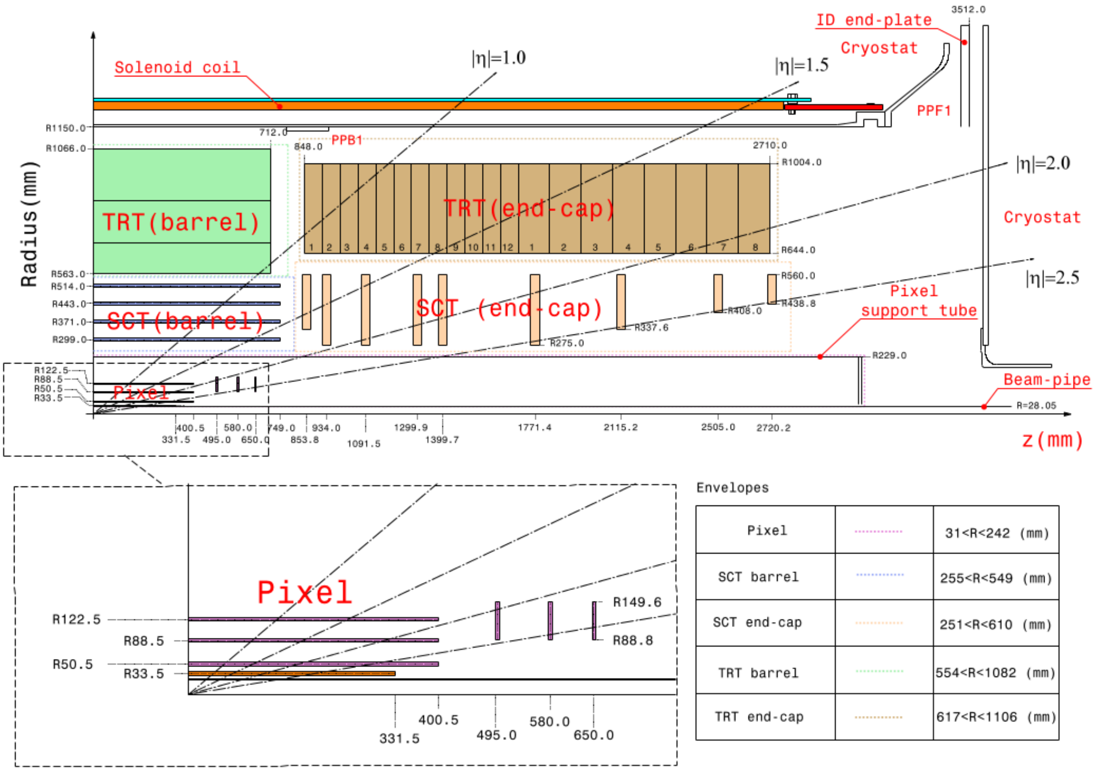

Figure 13: The rz view of the layout of the ATLAS ID. The top panel shows the whole inner detector, and the bottom-left panel shows a magnified view of the pixel detector region Image from Ref [37].

4.3 Calorimeter System

Sorroundng the ID there is the calorimeter system, whose goal is to measure the energy of the particles.

The ATLAS calorimeter system is composed by two different sub-detectors: the electromagnetic calorimeter and the hadronic calorimeter, both sample a full ϕ range and $|\eta| < 4.9$.

The detectors are made of layers intercalating absorbing and active material, to induce the parton showering and to measure their energy, respectively [70].

As the readout signal is proportional to the energy deposited only in the active media, it is a non-compensating system, part of the energy of nuclear collisions remains “invisible”. This creates a difference between the particles which interact strongly with the nuclei and the particles which interact by the electromagnetic force (EM). In the first case the measured energy is smaller, because, each kind of the particle shower involves different physics processes and develop differently in the detector [74].

The *electromagnetic showers* are energetic electrons that radiate photons by Bremsstrahlung processes, while these energetic photons going through the material can also convert to electron-positron pairs. These electromagnetic showers are originaly produced by electrons, positrons and photons.

To characterise the thickness of a material, the longitudinal depth of an EM shower is expressed in terms of the radiation length (X_0), the critical energy (E_c[3] and the initial energy (E_0) as:

$$X = X_0 \frac{ln(E_0/E_c)}{ln(2)} \tag{21}$$

The *hadronic showers* involve hadron production from nuclei interactions and hadron decays. In general, charged particles are produced by the hadronization process after the parton shower and hadron decay. Charged particles as pions and kaons are usually produced but one third of the energy dissipated in the hadronic shower is via neutral pions which decay to two photons ($\pi^0 \to \gamma\gamma$) and those produce an EM shower by electron Bremsstrahlung and e^+e^- pair production.

In addition, particles may interact with the nuclei in the absorber by several nuclear processes, that produce additional particles near the MeV scale. The longitudinal depth of the hadronic shower scales with the nuclear interaction length, as $\lambda \sim A^{\frac{1}{3}}$

The active material reacts when charge particles pass through. They are either plastic scintillators or liquid argon. In plastic scintillators the charged particles produce light via excitation followed by scintillation. The number of photons produced is proportional to the energy deposited by the incident particle and is guided to photomultiplier tubes (PMTs) by optical fibers. In the liquid argon medium the incident charged particles ionize the liquid, causing electrons and positive ions to drift (driven by a bias voltage) towards electrodes which measure the deposited charge.

Passive material consists of heavy absorber material which interacts with both charged and neutral particles but does not measure the deposited energy. Particles may interact by different mechanisms. Charged particles can radiate photons through Bremsstrahlung, which may pair-produce electrons and positrons that may themselves radiate further photons. Hadron-nucleon scattering can produce strongly interacting particles which can further interact with both the active and passive materials, again causing a shower of particles. Through this process the energy of charged and neutral particles is measured [80].

In ALTAS there are two calorimeters. The *electromagnetic calorimeter*, described in Section 4.3.1 and the *hadronic calorimeter* described in Section 4.3.2.

Resolution

To get an accuracy of the measurement of the particle energy is related to the resolution. Thus, precision can be improved by minimizing it. The fractional calorimeter resolution as a function of energy is described as Equation 22

$$\frac{\sigma_E}{E} = \frac{N}{E} \oplus \frac{S}{\sqrt{E}} \oplus C \tag{22}$$

[3] The critical energy E_c can be defined as the energy in which the bremsstrahlung and ionization rates are equal. A rough estimate is $Ec = 800MeV/(Z + 1.2)$

where N is a measurement of the noise, dominant at low energies, arising from background and electronics, S parametrizes the stochastic uncertainty due to the random sampling of the active and passive materials, and C is a constant term, dominant at higher energies arising from non-uniformities in the detector. All these terms are added in quadrature ($\otimes$) to derive the fractional resolution.

The target energy resolution for the ATLAS electromagnetic calorimeters as specified in the technical design report [13] is:

$$\frac{\sigma_E}{E} = \frac{17\%}{E} \oplus \frac{10\%}{\sqrt{E}} \oplus 0.7\%$$

4.3.1 Electromagnetic colorimeter

The electromagnetic calorimeter system consists of a central barrel (EMB) and two end-caps (EMEC). Both use liquid argon as an active material. Which is held in a liquid state at 89K by a cryostat. The EMB covers a region of $|\eta| < 1.475$ and the two EMEC cover a range of $1.375 < |\eta| < 3.2$.

The EMB is composed by three layers. The primary layer has a fine segmentation: $\Delta\eta \times \Delta\phi = 0.003 \times 0.1$ that permits a discrimination between single or two close by photon showers. A Second layer collects the largest fraction of the energy of the electromagnetic shower, in towers of $\Delta\eta \times \Delta\phi = 0.025 \times 0.0245$ which permits a detailed reconstruction of the showers. The third layer has half the granularity of the previous layer and measures the tail of the electromagnetic shower.

An accordion shape design was implemented for the electrodes and absorbers, because it allows full coverage in ϕ with no cracks and permits a high granularity. It is illustrated in Figure 14.

4.3.2 Hadronic colorimeter

The Hadronic calorimeter (HCAL) is a detector composed by both scintillating tile and liquid argon. Hadrons shower differently in matter than electromagnetic particles due to their strong force interactions. The scintillators in the calorimeter measure the energy via molecular excitation. Incoming particles excite molecules of a primary active material, which emit UV light on de-excitation.

Tile Calorimeter

It consists of a central barrel, in the central region ($0 < |\eta| < 1.0$) and two extended barrels ($0.8 < |\eta| < 1.7$) [24]. It samples a radii between 2288 and 4230 mm. The barrel has 64 modules made with scintillating tiles as the active medium embedded in a steel absorber. The barrel tile calorimeter has a granularity of $\Delta\eta \times \Delta\phi = 0.1 \times 0.1$ (and $\Delta\eta \times \Delta\phi = 0.1 \times 0.2$ in the third layer).

Hadronic end-cap (HEC) and forward (FCal) calorimeters

As the forward region of the detector has a higher particle flux, it must be instrumented with radiation-hard calorimeters. So it is built with liquid argon sampling

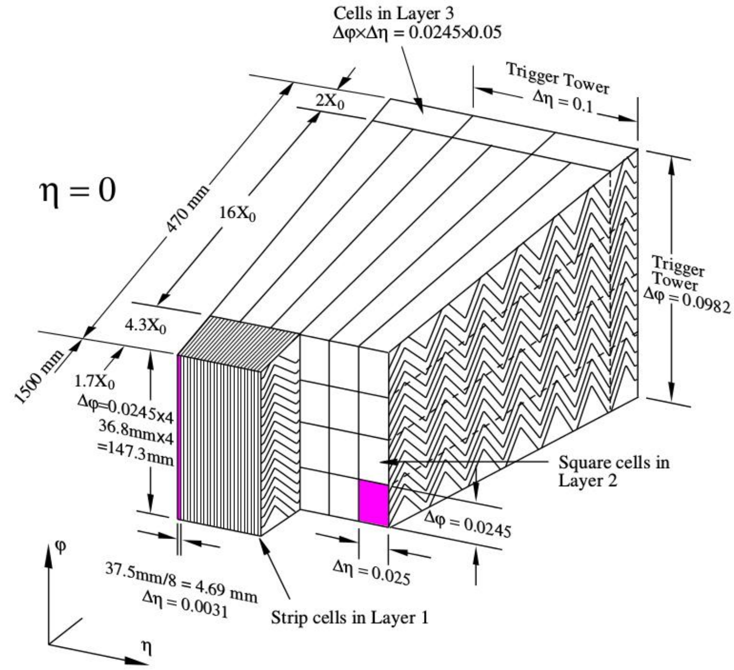

Figure 14: Diagram of a barrel module. The granularity in η and ϕ of the cells of each of the three layers and of the trigger towers are also shown. Image from Ref [26].

calorimeters. There are two sub-systems for this purpose: the hadronic end-caps (HEC) ($1.5 < |\eta| < 3.2$) and the forward calorimeter (FCal) ($3.1 < |\eta| < 4.9$). Both detectors operate in the same way as the electromagnetic calorimeter.

4.4 Muon system

The last detector of ATLAS is the muon spectrometer (MS). It is located sorrounding the toroidal magnets. A muon passing through is bent in $\pm z$ direction, The curved trajectory alows a precise measurement of the momentum with a resolution of $50\mu m$.

The muon spectrometer consists of four primary sub-systems, two precision muon trackers: the monitored drift tubes (MDT) and cathode strip chambers (CSC), and two triggering sub-systems: resistive plate chambers (RPC) and thin gap chambers (TGC). The layout of the muon system and the magnets are shown in Figure 16.

Precision muon trackers: built with drift tubes arranged in double layers of 3 or 4 tubes of $3mm$ diameter. Each of them have a central anode wire and are filled with argon, CO_2, and water vapor mixture.
Trigger chambers: are able to deliver a signal in less than 25 ns, thus providing the ability to tag at trigger level (see Section 6.5.1) and to recognise muon multiplicity. The trigger chambers measure both coordinates of the track, one in the bending (η) plane and one in the non-bending (ϕ) plane.

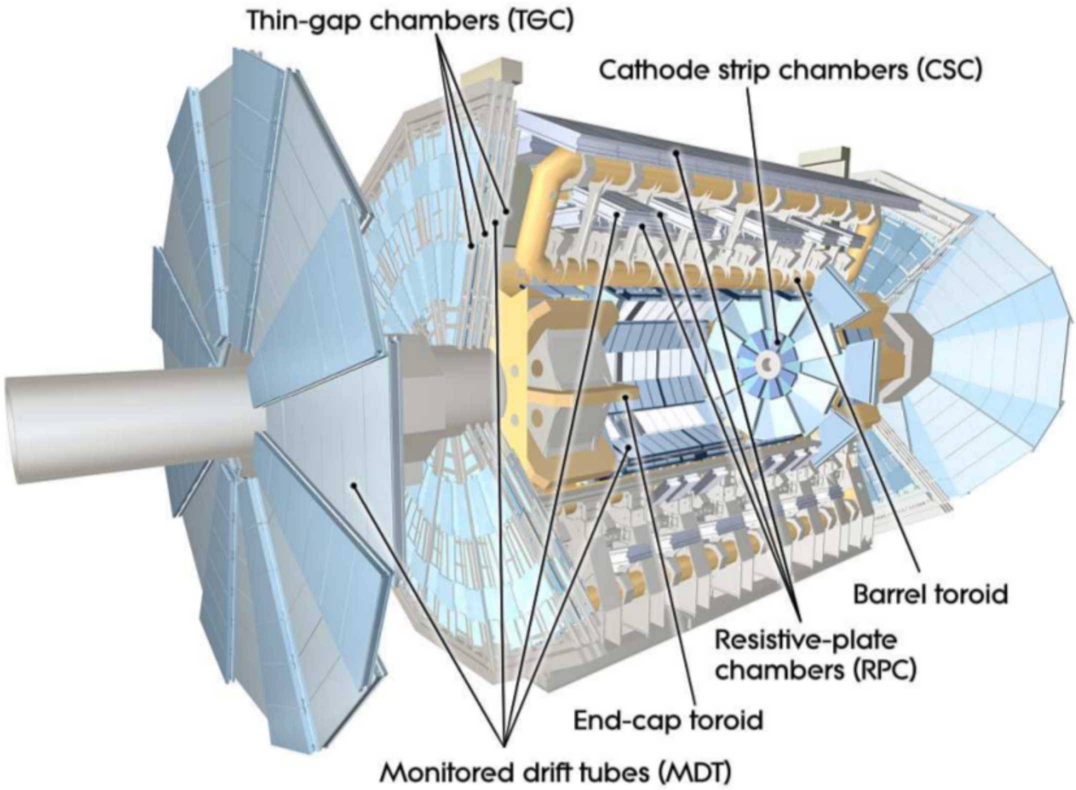

Figure 15: ATLAS muon system Image from Ref [26]

4.5 Magnet systems

The ATLAS detector uses four systems of magnets to bend the trayectory of charged particles. A central solenoid of $2T$ of axial magnetic field located around the Inner Detector, a barrel toroid of $0.5T$ of magnetic field and two end-caps of $1T$ in each one.

The solenoid is a single-layer coil made of a Niobium-Titanium superconductor and has a temperature of $4.5K$ with a current of $7.7kA$. The barrel and end-cap toroids are made from a $Nb/Ti/Cu$ conductor wound into pancake-shaped coils. The toroids operate at a temperature of $4.6K$ with a current of $20.5kA$.

4.6 Trigger System

The ATLAS detector is designed to work with proton crossing every 25 ns and the collisions are derived at a rate of 40 MHz in nominal operating conditions, which is more than can be saved. Furthermore, most of it will be domain by QCD and other physics processes well know, only a small fraction of it may contain physics of interest. Thus, ATLAS uses a *trigger system* to reduce the amount of information and to keep, as far as possible, only the events that reflect a particular topology indicating the potentiality new physics processes.

During Run2 the trigger system is divided into two levels. The first one, the *L1Calo* (L1) which is hardware-based, and the second one, the high-level-trigger

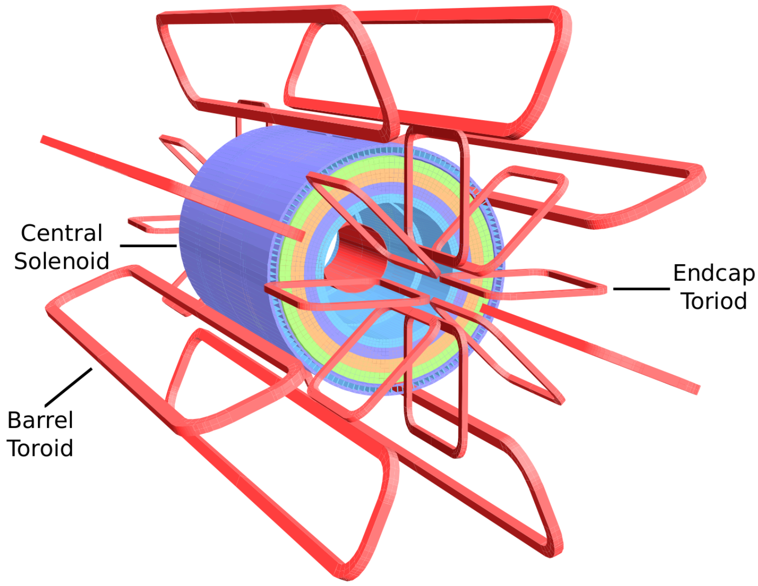

Figure 16: Geometry of magnet system. The eight barrel toroid coils, with the end-cap coils interleaved are visible. The central solenoid inside the calorimeter volume. Image from Ref [14]

(HLT) which is software-based.

The L1 reduces the rate to 75K events per second, taking quickly desitions using the information of the calorimeters and the muon spectrometer. It uses a rough estimation of the objects like jets, muons ,electrons, photons and τ decays. It can also estimate the large transverse energy and missing transverse signal.

The events which pass the L1 are filtered by the HLT level. It reduces the rate to 1kHz. The HLT has access to fine-granularity calorimeter information and also to the tracking information from the ID (not available at L1). It uses reconstruction algorithms and calibrations similar to those that are used later at the off-line level.

If an event is accepted by the HLT level, the information is stored to perform a full off-line event reconstruction. Since the luminosity of the proton beams decreases as collisions progress, data collection conditions change as a function of time. Therefore data is collected in time intervals of one minute, referred to as lumi-blocks. and each of it is assigned an integrated luminosity depending upon detector and beam conditions over that lumi- block. ATLAS provides lists of lumi-blocks of good data for each data taking period known as Good Run Lists (GRL).

5 Objects reconstruction in ATLAS

In ATLAS, the different objects: tracks, vertices, jets, taons (τ), photons (γ), electrons ($e^{\pm}$), muons (μ) and missing E_T, allow us to identify individual particles in the event. Each of them is measured using a variety of algorithms, that use the information collected from the detector.

The flowing sections present the principal algorithms used in ATLAS. Section 5.1 describes the algorithms used to build the tracks and vertices. Section 5.3 presents the principal jet reconstruction algorithms and their calibration. Also, Section 5.2 describe the algorithms used for the identification of electrons and photons.

5.1 Tracks and Vertices in ATLAS

Tracks symbolize the trajectories of charged particles and are a fundamental component of the event reconstruction. These objects are reconstructed using the measurements of the inner detector.

The vertices are made up using the information of the tracks and represent interaction points.

5.1.1 Track reconstruction

The Track reconstruction algorithm has two stages: *the pattern recognition*, that search for track candidates, and *the track fitting* which gives an estimation of the parameters that describe the particle trajectory. Both require a detailed description of the detector and a parametrization to describe the trajectories.

As mentioned in Section 4.2, charged-particles passing through the detector deposit energy due to the ionization process. The charge collected in the ID is read out by the electronics as *hits*.

Pattern recognition proposes to identify a collection of hits corresponding to a single particle trajectory. Then, the hit collection is processed by the track fitting algorithms to estimate the parameters than describe the trajectory of the particle. These algorithms have to discern the hits coming from noise or hit from other charged particles and wrongly associated, these are called *fake hits*, which must be avoided. Moreover, there are *expected hits* which are not found and are referred as *holes*[4].

The quality of track reconstruction algorithms is defined by two criteria. What fraction of tracks are reconstructed, the *track reconstruction efficiency*, and how well the track parameters represent those of the charged particles, the *track parameter resolution*. These two criteria are not fully independent. For instance, disassociated hits will decrease the quality of the track parameters.

The track reconstruction algorithm used by ATLAS is known as New Tracking or NEWT [108]. It includes different configurable algorithms that run sequentially. The process starts with *inside-out* algorithm, which reconstructs tracks from the center of the detector to outwards. It begins with seeds, that are found from groups

[4]Holes are estimated by following the track trajectory and comparing the hits on a track with the modules that the track passes through. Inactive modules or channels such as edge areas on the silicon sensors are not counted as holes.

of three space points in the silicon layer. Then, the seeds are used to build roads to find more hits moving forward. These hits could be attached to multiple tracks candidates. The ambiguity is solved rejecting poor track candidates. Then, the silicon track candidate is fit and an extension to the TRT is probed. Finally, a track fit is performed to provide the final estimate of the track parameters. A deeper description is presented in Section 5.1.1.2.

5.1.1.1 Impact Parameters

A charged particle passing through a uniform magnetic field follows an approximately helical trajectory[5] which can be parametrized by a set of five parameters schematized on Figure 17:

The longitudinal impact parameter d_0 is the distance of closest approach of the trajectory, to the reference point in the xy plane and the transverse impact parameter z_0 is the closest the approach of z coordinate of the track. The polar angle θ is the angle the track makes in the rz plane. and the azimuthal angle ϕ defined between the track and the tangent at the point of closes. And the curvature parameter q/p where q represents the electric charge of the particle and p is the momentum.

[5] The assumption of a perfect helical track model ignores effects from multiple scattering and energy loss, which depend on the particles energy and the amount of material the particle has traversed. These effects are taken into account in the track fit and the propagation of the track parameters.

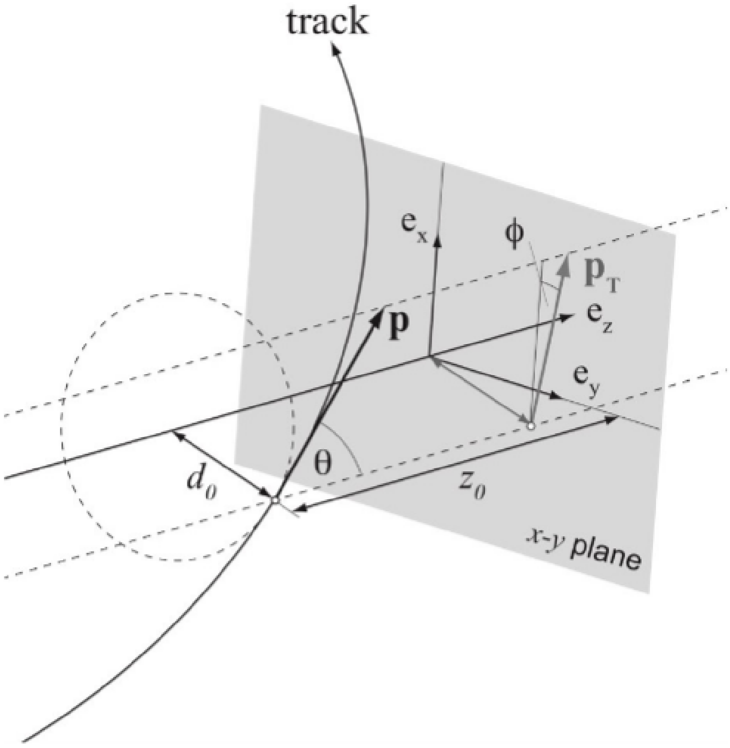

Figure 17: ATLAS track parameterization. The local expression of the point of closest approach is given by the signed transverse impact parameter d_0 and the longitudinal impact parameter z_0. The momentum direction is expressed in global coordinates ϕ using the azimuthal angle that is defined in the projected plane $x-y$ and the polar angle θ, which is measured to the global z axis. Image from Ref [3].

The impact parameters can be calculated for different reference points. The three commonly used are the nominal interaction point (0,0,0) in the ATLAS coordinates system (d_0, z_0), the reconstructed primary vertex (d_0^{PV}, z_0^{PV}) or the beam spot (d_0^{BS}, z_0^{BS}), where the beam spot is calculated by averaging the reconstructed primary vertex over a short data-taking period.

5.1.1.2 Track reconstruction algorithms

The first step for track reconstruction is the creation of three-dimensional space points group. The Pixel clusters provide directly 3D points from the silicon hits information. Two come from the pixel cluster position and the third one from the layer (known as radius). This is not the case for SCT clusters as they provide only one direction. So the space points are formed by combining the information of a pairs of clusters.

Track seeds are created using these space points as follows. The pattern recognition creates groups of points compatible with a single track.A default minimum of three points is needed, this requirement can change however this value that optimize the number of possible combinations being enough to provide a momentum estimated for the track. Also, a minimum distance between the points is required to avoid multiple points coming from the same layer.

Furthermore, cuts for the impact parameter and the transverse momentum are applied to limit the combinations and to optimize the execution speed. However as a track seed is only a collection of space points, they do not provide a parameterization of the track parameters. Thus a crude estimate is made by assuming a perfect helicoidal track model in a constant magnetic field. The seed impact parameter can not be calculated for the primary vertex since at this stage the tracks are not yet ceated and the primary vertex reconstruction algorithm has not been executed. The been spot is used instead.

The second step is the window search, applied in the seed propagation. Any hits within the road window are collected and a track candidate is built using a combinatorial Kalman filter [96]. Seeds can fail to become a track candidate for different reasons; for instance, if the road fails to find sufficient hits. Approximately more than a quarter of the seeds become track candidates. A full description can be found on [76].

The final step is to probe the information of the TRT for a possible extension. TRT hits are found using the propagation of the reconstructed track from the silicon detectors. The TRT requires at least 15 hits to be considered a successful extension. The extension of a track into the TRT improves the transverse momentum due to the increase in the length of the track. However, the impact parameters do not change significantly. Since the distance of these points from the reference point hardly change the impact parameter resolution.

5.1.1.3 Matching probability and track reconstruction efficiency

To mensure the track *reconstruction efficiency*, first an asociation between the reconstructed tracks and the *primary*[6] (or *secondary*[7]) particles is computed from simulation using a hit-based track-to-truth particle association [42]. It is done via the clusters, each one is connected to the truth particle which has the largest energy deposition in the MC simulation. The clusters are weighted according to their importance in the track reconstruction: if the clusters are from the pixel detector (including IBL) the weight is set to 10 for each cluster. If they are from the SCT, the weight is set to 5 and if they are from the TRT, the weight is set to 1 [118].

The matching probability P_{match} is defined as the ratio between the number of hits which are in common for a given track and the corresponding truth particle (N^{common}), and the number of hits of the track (N^{track}).

$$P_{match} = \frac{10.{N^{common}}_{Pixel} + 5.{N^{common}}_{SCT} + 1.{N^{common}}_{TRT}}{10.{N^{track}}_{Pixel} + 5.{N^{track}}_{SCT} + 1.{N^{track}}_{TRT}} \tag{23}$$

A reconstructed track with P_{match} >0.5 is asociated to a truth particle.

[6] are defined in MC, as charged particles with a mean lifetime $\tau > 300$ ps. These can be produced, either, directly in *pp* interactions or from subsequent decays of directly produced particles with $\tau < 30$ ps.

[7] *Secondary particles* are those produced from decays of particles with $\tau > 30$ ps.

Then, the track reconstruction efficiency $\epsilon_{trk}(p_T, \eta)$ is measured as a function of $p_{\mathrm{T}}$and ηas:

$$\epsilon_{trk}(p_T, \eta) = \frac{N^{matched}{}_{rec}(p_T, \eta)}{N_{gen}(p_{\mathrm{T}}, \eta)} \tag{24}$$

Where $N^{matched}{}_{rec}(p_T, \eta)$ is the number of recontracted tracks matched to a given generated charge particle and $N_{gen}(p_{\mathrm{T}}, \eta)$ is the number of generated charge particles.

The fake [8] rate $r_{fake}(p_T, \eta)$, is measured following Equation 25. It gives a magnitude of how many tracks are disassociated with particles. Fake tracks can have several sources, most common are due to the interaction with the matter and a bad performance in the track reconstruction process.

$$r_{fake}(p_T, \eta) = \frac{N^{unmatched}{}_{rec}(p_T, \eta)}{N_{gen}(p_{\mathrm{T}}, \eta)} \tag{25}$$

5.1.2 Vertex reconstruction

The vertices are reconstructed using the track information in an *iterative vertex finder* algorithm [95], which uses only tracks with a small IP $d_0 < 4mm$ well-measured, meaning $\sigma(d_0) < 5mm$ and $\sigma(z_0) < 10mm$. Also, a minimum number of 4 hits in the SCT and 6 hits for all the silicon detectors combined is required.

The algorithm finds the vertex seeds by looking for the global maximum of the z_0 distribution of the tracks. Then, further tracks are iteratively added and weighted according to their compatibility with the current vertex position estimate. The process finishes when there are no more tracks to be associated. All vertices are required to have at least two tracks with a nominal p_{T}value of 0.5 MeV.

Once all primary vertices are created, the algorithm chooses as event vertex that one with the highest $\sum (p_T{}^{tracks})^2$. Thus the number of primary vertices (PVs) is a measure of additional activity and can be used as an estimator of the average interaction per band-crossing (μ).

5.2 Photons and electrons

The ATLAS experiment uses the information of the calorimeters and the ID to identify and tag electrons ($e^{\pm}$) and photons (γ). This process is performed by reconstruction algorithms, that analyze the electromagnetic shower shape in the EM calorimeter and the associated tracks from the ID.

5.2.1 Reconstruction algorithms

The reconstruction algorithm analyzes the local depositions of energy in the electromagnetic calorimeter. In it the topological clusters are seeded by calorimeter cell in the second and third layers of it, where the enery deposited is greater than four standard desviations above the expected noise level of that cell. Once seed cells are defined, neighboring cells in which the energy deposited is greater than two

[8]The *Fake tracks* are tracks which do not match any particle or have $P_{\mathrm{match}} < 0.7$.

standard deviations above the expected noise level of that cell are iteratively added to the cluster. Lastly the neighboring cells surrounding the defined topocluster are included.

After the topocluster have been defined, they are matched to tracks from the ID. The candidate track is extrapolated to the EM calorimeter to asses the compatibility with the topocluster. Then it is defined as matched if it satisfies the following criteria: $|\Delta\eta| < 0.05$ and $-0.10 < q \times (\phi_{track} - \phi_{cluster}) < 0.05$ where q is the charge of the candidate charged particle, it means that the projected track must hit close to de location of the energy deposit. Both electrons and positrons will be identify a deposit of energy in the EM calorimeter with one asociated track. On the other hand unconverted photons carry no charge, these are photons which have converted in an alectron-positron pair in the detector volume (due to the interactions with the detector material). They appear as two clusters, each with an associated track (with oppositely-charged), and generally have a reconstructable conversion vertex. In addition, converted photons may be reconstructed from tracks with no hits in the innermost layer. The reconstruction algorithm takes into account the fact that some photons are classified as electrons (converted photons) and the other way around (due to miss associated tracks).

In Run 2, the reconstruction of photons and electrons has been improved by usining the superclusters, which allow energy from secondary showers (such as from a Bremsstrahlung photon) to be captured and factored into energy reconstruction. The topoclusters mentioned before are used as seeds to the superclaster. To be defined as a supercluster seed for an electron (photon), It must have at least 1 GeV (1.5 GeV) of energy deposited. In addition the topoclusters are defined as satellites of a supercluster seed if they fall within a window of $\Delta|\eta| \times \Delta\phi = 0.075 \times 0.125$ of the seed.

Ones all topoclusters have been assigned, the combined seed and satellites are defined as a supercluster, which is limited to maximum side of $\Delta\eta < 0.075$ in order to reduce the impact of pileup.

In addition an ofline identiication algorithm is applied. It reduce the amount of “fake” photon candidates, which are primarily charged jets mis-reconstructed as photons.

There are three primary identification working points: *loose, medium* and *tight.* The *loose* photon identification requirements is based on the electromagnetic shower produced in the hadronic calorimeter and in the shower shape in the second layer of the EM calorimeter.

The loose requirement uses the following variables:

- R_{had}: Ratio between the transverse energy deposited in all layers of the Hadronic calorimeter over the energy deposited in the cluster in the EM calorimeter, for $0.8 < |\eta| < 1.37$.

- R_{had1} Same but only considering transverse energy deposited in the first layer of the Hadronic calorimeter.

- R_η The ratio of the energy deposited in a $3 \times 7(\eta \times \phi)$ cell rectangle to that deposited in a 7×7 cell rectangle, where both rectangles are centered on the cell with the most depositedenergy

- $w_{\eta 2}$ The lateral shower width calcuated in a $3 \times 5(\eta \times \phi)$ cell rectangle.

The mediun requirement uses the same variable as before and also the E_{ratio}. It is defined as the ratio of the difference in energy deposited between the maximum deposit and thesecond largest deposit within a cluster to the sum of the energy in those two deposits.

The tight selection includes the requirements of thelooseworking point, and it adds information from the finely segmented strip layer of the calorimete. Overall, the tight selection provides a better fake photon rejection, while keeping the same identification efficiency.

5.3 Jets in ATLAS

Jets are definitions of the experimental production of the partonic showering. It is the manifestation of the hadronization of particles carrying a color charge. However, it is important to highlight that, in practice, there is not a double implicate between the jet and the parton. For instance, one parton may be reconstructed as multiple experimentally observed jets, and multiple parton showers may end up forming part of a single jet.

Jets are defined through several algorithms, where each of them can use a variety of objects at the tracking or calorimeter level. Furthermore, jets in Monte Carlo simulations can be defined using the parton showering or particle information.

The jets defined using track information are called *track jets*, in general, used for calibration purposes. There are also *true jets* , only defined in simulations, using particle level information as inputs. Lastly, the *calorimeter jets* are constructed using calorimeter measurements. ATLAS uses a high-level object called Topological cluster. These objects are a group of neighboring cells that have significant energies compared to the expected noise. Topological clusters are built using a 4-2-0 clustering scheme optimized to find efficiently low energy clusters without being overwhelmed by noise [119]. The topocluster formation algorithm starts from a seed cell, whose signal-to-noise (S/N) ratio is above a threshold of $S/N = 4$. The noise is estimated as the absolute value of the energy deposited in the calorimeter cell divided by the RMS of the energy distribution [9]. Cells neighboring (laterally and longitudinally) the seed which has a signal-to-noise ratio of at least $S/N = 2$ are then iteratively added. Finally, all nearest neighbor cells are added without any threshold to the cluster.

Incoming particles usually deposit their energy in many calorimeter cells, both in the lateral and longitudinal directions. Thus, the topoclusters may have different sizes and a variable number of cells depending mostly on the energy of the incoming particle: more energetic particles produce larger showers and thus larger clusters. A topocluster ends up formed, on average, by approximately 250 calorimeter cells.

Section 5.3.1 describes the principal jet algorithms used in ATLAS and Section 5.3.2 presents the jet calibration process made.

[9]RMS of the energy distribution is measured in events triggered at random events

5.3.1 Jet algorithms

There is not a unique jet definition. It can be adapted for a particular application or experimental conditions to reconstruct better the hard scattering process. However, the jet definition must satisfy the following criteria:

- Applicability in both experimental analyses and theoretical calculations;
- Yield reliable (finite) results at all orders in perturbation theory;
- Infrared and collinear (IRC) "safe";
- Experimentally "safe". It means not strongly affected by contamination from hadronization remanents and other underlying soft events like pileup or noise;

This criteria is an extension of the "Snowmass accord" [78] [100], created to facilitate the comparison through all jet physics results, which still provide a common ground for the development of modern jet algorithms. The most common definition adopted by ATLAS comes from the family of *sequential recombination* algorithms [99]. These are specifically designed to be insensitive to the presence of soft (Infrared) and collinear gluon emission. Thus are usable for calculations in perturbation theory. Recombinations algorithms work iteratively trying to reverse the pattern of QCD parton showers and multi-gluon radiations characterized by softer emissions as the shower evolves [65]. For this, the algorithm defines a distance d_{ij} between entries, particles or energy deposits, and d_{iB} between the entity i and the "beam" as is shown below:

$$\begin{aligned} d_{ij} = min({p_{T_i}}^{2p}, {p_{T_j}}^{2p})\frac{{\Delta R_{ij}}^2}{R^2} \\ d_{iB} = {p_{T_i}}^{2p} \end{aligned} \tag{26}$$

The ΔR_{ij}^2 is the angular distance between to points defined as $\Delta R_{ij}^2 = \Delta\eta^2 + \Delta\phi^2$; p_T is the transverse momentum of the entity i; and the parameter p and R regulate the evolution of the clustering. The algorithm identifies the smallest of the distance, and if it is d_{ij} then it combines the four-momentum of entries i and j, while if it is d_{ib}, it defines entity i as a jet and removes it from the list of the entries. Later, distances for the rest of the inputs are calculated and the procedure goes on until no inputs are left.

As it was mentioned, there are different algorithms to reverse the shower:

The k_t algorithm for $p = 1$ [100], where the distance used induces soft radiation particles to be merged first. This introduces a strong sensitivity to small fluctuations of the energy density of the particle shower.

The *Cambridge-Aachen (C/A)* algorithm for $p = 0$ [120] [89] works only with the angular component, sorting emissions by omitting the transverse momentum from d_{ij}

The $anti\!-\!k_t$ algorithm for $p = -1$ [84]. Here the soft particles will tend to cluster with hard ones long before the cluster among themselves, reducing the sensitivity to fluctuations of the parton shower. So, if a hard particle has no hard neighbors within a distance $2R$, then it will accumulate all the soft particles within a circle of radius R. The stability of the jet area facilitates the experimental calibration (as shown in Section 5.3.2), eliminating some parts of the momentum resolution loss caused by, for instance, pileup contamination. This is the default algorithm in ATLAS, and the one used in this thesis.

5.3.2 Jets calibration

The reconstructed jets may not have the true energy of the original parton. Not only because the topoclusters are calibrated at the electromagnetic scale, and therefore would reflect the energy deposited by an electromagnetic shower but do not properly for hadronic showers. There are other factors affecting the jet reconstruction algorithms. Some of them are listed below:

- *Dead material*: Some of the energy of a jet may land in non-responsive parts of the detector.
- *Leakage*: Some energy may fall outside the calorimeter
- *Out of jet cone*: Particles which fall outside the reconstructed calorimeter jet are a source of energy loss due to the jet reconstruction process.
- *Thresholds and reconstruction efficiency*: Part of the jet energy could be missed by the reconstruction. For instance, falling below the noise threshold requirements for cluster formation.

At this level, two jet collections of jets are performed. One with the EM-scale topoclusters called electromagnetic jets (EM), and the other one made with a preliminary calibration at the topocluster level called local cell signal weighting jets (LCW). The LCW calibration uses the shape of the shower depth and the energy density to assign a weight to the topoclusters. Both collections have to go through a four-step process of calibration, with the aim of restoring the energy scale of the reconstructed jet to that of the true jet. Each step is briefly described below:

1. *Pileup correction*: This effect is generated by additional energy deposits as was explained in Section 3.3. These extra deposits of energy need to be subtracted. Thus, a correction derived from MC simulations and applied in bins of y and p_T takes into account the number of primary vertices (N_{PV}) and the average number of interactions per bunch crossing ($<\mu>$), which is sensitive to the out-of-time pile-up.
2. *Jet origin correction* The four-momentum of the jet is adjusted to the interaction vertex instead of the nominal center of the ATLAS detector. The interaction vertex is one with the largest value of $\sum(p_T{}^{track})^2$, where the scalar sum is taken over all tracks associated with the vertex as is described in Section 5.1.2.
3. *Jet energy and η corrections*: This step returns the jet energy and η to the scale of truth MC jets. The calibration to be applied is derived as follows

[33]. Calorimeter jets from a MC sample are matched to a truth jet and the EM-scale jet energy response is computed as:

$$R_{EM}{}^{jet} = \frac{E_{EM}{}^{jet}}{E_{truth}{}^{jet}} \tag{27}$$

The response is calculated for all such jets and binned in truth jet energy and η_{det}. Within each $(E_{truth}{}^{jet}, \eta_{det})$ bin, the $R_{EM}{}^{jet}$ distribution is fitted with a Gaussian function. Then the mean is used to determine the R that bin ($< R_{EM}{}^{jet} >$). This quantity depends on the mean reconstructed jet energy $< E_{EM}{}^{jet} >$ in the same E_{true} bin and so varies with the jet energy. This distribution is fitted using de following function:

$$F_{calib}(E_{EM}{}^{jet}) = \sum_{i=0}^{N_{max}} a_i (lnE_{EM}{}^{jet})^i \tag{28}$$

where a_i are free parameters and the number of terms in the function N_{max} can be up to 6 depending on the goodness of the fit. So, for a measured EM jet of a given η_{det} and $E_{EM}{}^{jet}$ the energy can be corrected by dividing it by the value of F_{calib} in that η_{det} bin as:

$$E_{EM+JES}{}^{jet} = \frac{E_{EM}{}^{jet}}{F_{calib}(E_{EM}{}^{jet})|_{\eta_{det}}} \tag{29}$$

4. *Residual in situ calibration*: Takes into account the differences between data and MC. It corrects the jet energy form the conservation of the transverse momentum using a well-measured set of objects as a reference.

   In the central region ($|\eta|$ <1.2), the direct p_T balance between a jet and a Z boson can estimate the remaining jet correction up to p_T =200GeV. Up to 800 GeV, a photon can be balanced against the total recoil of the jet and the proton remnant. Finally, for jets up to the TeV scale, a very high-p_{T}jet can be balanced against a group of lower-p_{T}jets already calibrated with the preceding two methods. For jets in the forward calorimeter regions, the transverse momentum balance method draws a comparison to well-calibrated central jets, and thus the calibration is extended across the full detector range. The same balance techniques are applied on data and MC and the difference between the two is taken as the residual in situ correction and applied to the data [34]:

$$Correction = \frac{1}{R(p_T{}^{jet}, \eta)} = \frac{< p_T{}^{jet}/p_T{}^{red} >_{MC}}{< p_T{}^{jet}/p_T{}^{ref} >_{data}} \tag{30}$$

As an example, the Figure 18 shows the relative jet energy resolution $\sigma_{p_{\mathrm{T}}}/p_{\mathrm{T}}$ as a function of $p_{\mathrm{T}}$for anti-kt jets with a radius parameter of $R = 0.4$ and inputs of EM-scale topoclusters calibrated with the EM+JES scheme followed by a residual in situ calibration and using the 2017 dataset. The expectation from Monte Carlo simulation is compared with the relative resolution as evaluated in data.

The error bars on points indicate the total uncertainties on the derivation of the relative resolution in dijet events, adding in quadrature statistical and systematic components. The result of the combination of the in situ techniques is shown as the dark line. The band indicates the total uncertainty resulting from the combination of in situ techniques, and includes the statistical and systematic components added in quadrature, although the statistical component is found to be negligible.

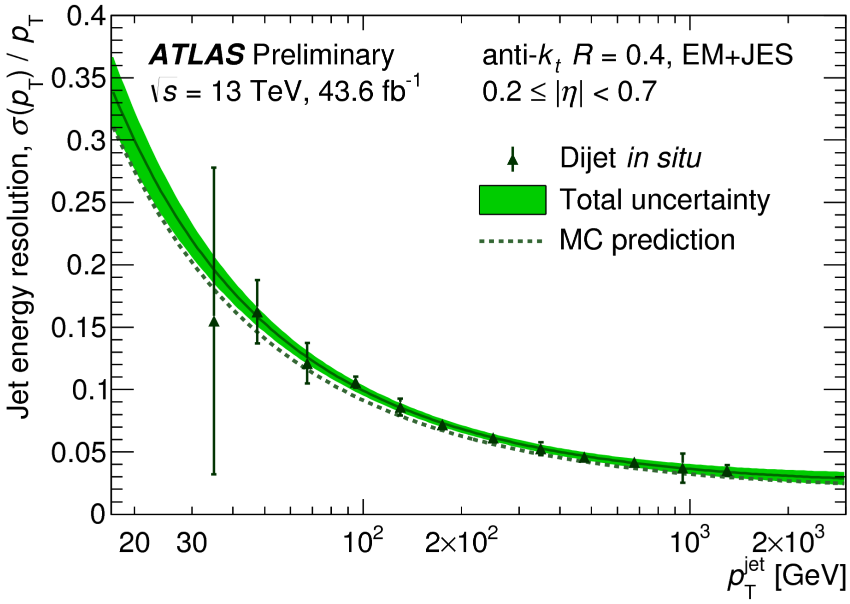

Figure 18: Relative jet energy resolution as a function of $p_{\mathrm{T}}$for anti-kt jets with $R = 0.4$. performed with inputs calibrated at the EM-scale. For a ηbin of 0.2< $|\eta^{det}|$ <0.7. The dark line represents the in situ techniques. The dot line represents the MC prediction and in green the statistical and systematic components added in quadrature. Image from Ref [21].

6 Charged particle multiplicities in pp interactions with $p_T \geq 100$ MeV

6.1 Motivation and analysis strategy

A description of low-energy processes is not possible within a perturbative framework. Thus, the measurements of charged-particle distributions in pp collisions provide an inside view by reflecting the strong interaction with low momentum transfer. Many of the MC event generators are inspired by QCD-like models, and the measurements are used to constrain their free parameters. Therefore, a description of low-energy strong interaction processes is essential for simulations of pp interactions and the effects of multiple pp processes in the same bunch crossing.

This analysis strategy is inspired by previous results from ATLAS [27] [29]. The aim is to measure the charged-particles distributions listed below and compared them with respect to MC predictions.

$$\frac{1}{N_{ev}} . \frac{dN_{ch}}{d\eta} \tag{31}$$

$$\frac{1}{N_{ev}} . \frac{1}{2\pi p_T} . \frac{d^2N_{ch}}{d\eta dp_T} \tag{32}$$

$$\frac{1}{N_{ev}} . \frac{dN_{ev}}{dn_{ch}} \tag{33}$$

$$< p_T > \ as\ a\ function\ of\ n_{ch} \tag{34}$$

where p_T is the transverse momentum of track to the beam direction, η is the pseudorapidity, n_{ch} is de number of primary charged-particles in an event and N_{ch} the total. N_{ev} is the number of events with $n_{ch} \geq 2$, selected as minimum bias events[10] , and $< p_T >$ is the average p_T for a given number of charged-particles.

The charged-particle density as a function of η $(\frac{1}{N_{ev}} . \frac{dN_{ch}}{d\eta})$ is sensitive to the fraction of energy of the collision converted into soft particles. When the collision energy increases, the number of multiple parton interactions per collision rises too. This increases the density at central η .

The distribution of the average momentum as a function of the number of charged-particles was recently introduced because it becomes useful to constrain the color reconnection parameters in Pythia, Section 2.4.

The Monte Carlo simulations are used in several stages of the analysis. Therefore a brief summary of the samples used is presented in Section 6.2.

[10]Events triggered by a minimum bias trigger whose requirement is to have at least one colision

The analysis uses the events that fire the MinBias trigger described in Section 6.5. Then, it measures the n_{sel}, η and p_T data raw distributions[11] for the tracks that pass the event and the track selection criteria described in Section 6.3.

Then an event weight and a track weight are applied to correct inefficiencies of the detector reconstruction processes. The first one corrects for the trigger and vertex reconstruction efficiency. And the second one for the tracking efficiency and it also subtracts secondaries particles, out-of-kinematic-range particles, and strange baryons.

Finally, weighted distributions are corrected for the migration bins (due to the resolution) by unfolding them with a bayesian method to deconvolute the detector effects. The correction process is described in Section 6.8.

Throughout all this process the reconstructed tracks and vertex used are described in Section 6.4.3 and Section 6.4

The final results and comparisons to different MC generators are presented in section 6.13.

6.1.1 Some definitions before...

Although a first introduction to the different objects in ATLAS was presented in Section 5.1. This analysis requires a deeper description of the objects used. So, a brief "dictionary" of the most common terms is introduced below:

Primary and secondary particles The *primary particles* are defined in MC, as charged particles with a mean lifetime $\tau > 300$ ps. These can be produced, either, directly in pp interactions or from subsequent decays of directly produced particles with $\tau < 30$ ps. In the same way, *secondary particles* are those produced from decays of particles with $\tau > 30$ ps. Both, primary and secondary particles have a minimum p_{T} requirement of 100 MeV applied.

Primary tracks (secondary tracks) *Primary (and secondary) track* particles are tracks that ate matched with primary (and secondary) particles. The matching criteria is that P_{match} has to be larger than 0.5. With the matching probability (P_{match}) described in Section 5.1.1.3.

Fake tracks The *Fake tracks* are those which do not match any particle $P_{\mathrm{match}} < 0.5$.

Strange baryons These particles have a mean lifetime of $30 < \tau < 300$ ps and decay after a short flight length inside the tracking volume. Therefore they have a very low tracking efficiency and are excluded from the primary particle definition in this analysis[12]

[11]Distributions after the event and track selection

[12] These objects are excluded in this analysis but not in older iterations of the analysis at lower center-of-mass energies

6.2 Data and MC Samples

The data used was recorded during a period with a special configuration of the LHC with low beam currents and reduced beam focusing. This leads to a low expected mean number of interactions per bunch crossing $\langle\mu\rangle$=0.005.

For MC generators, the PYTHIA 8 A2 [113] and EPOS LHC [94] event generators are used in this analysis. As tune for the PYTHIA 8 A2 generator, the ATLAS minimum-bias A2 [19] tune is used. It is based on the MSTW2008LO PDF [104] and provides a good description of minimum bias events and the transverse energy flow data.

The comparison to the unfolded data distribution is done for these two generators, also, all results are compared to the QGSJET-II [91] generator and the PYTHIA 8 A2 generator using the Monash [106] tune instead of the dedicated ATLAS tune. It is based on the NNPDF23LO PDF [51]. For EPOS LHC and QGSJET-II an LHC tune is provided from the appropriate authors. Table 1 shows the list of used MC models.

Generator	Version	Tune	PDF	Focus	Data	From
Pythia 8	8.185	A2	MSTW2008LO	MB	LHC	ATLAS
Epos	3.4	LHC	-	MB	LHC	Authors
Pythia 8	8.186	Monash	NNPDF23L0	MB/UE	LHC	Authors
QGSJET-II	II-04	LHC	-	MB	LHC	Authors

Table 1: Details of the MC models used. It should be noted that the tunes use data from different experiments for constraining different processes, but only the data which had the most weight on each specific tune are shown. Here LHC indicates data taken at $\sqrt{s}$ =7 TeV, although $\sqrt{s}$ =900 GeV data were also included in ATLAS tunes, with much smaller weight. Some tunes are focused on describing the minimum-bias (MB) distributions better, while the rest are tuned to describe the underlying event (UE) distributions, as indicated here.

6.3 Event and Track Selection

The present analysis uses an event and a track selection designed to reduce background events and non-primary tracks contributions. The events have to satisfy the following criteria:

- The analysis uses the events that fired the *MBTS* trigger. A description and the performance of it is described in Section 6.5.
- It has to contain a primary vertex, reconstructed with at least two tracks with a p_T above of 100 MeV as descrives Section 6.4.3.
- Not contain a second vertex to avoid events with more than one interaction per bunch crossing

Then, tracks used for the analysis must satisfy the followings requirements:

- The p_T of the tracks should be grater than 100MeV and $|\eta| \leq 2.5$. Tracks with lower p_T values tend to be closed tracks and do not pass through the inner detector. The η requirement comes from the coverage of the ID detector.
- The tracks have to be built with at least one *pixel hit*. If a hit is expected in the innermost layer (IBL), then one is required. If a track passes through an inactive IBL module, then a hit is required in the next layer if one is expected. This requirement aims to avoid secondary tracks.
- In the same way the track has to be built with at least 2, 4 or 6 *SCT hits* for $p_T \leq 300MeV$, $\leq 400MeV$ or $\geq 400MeV$ respectively. This requirement makes the analysis less sensitive to differences in the number of dead modules.
- *The transverse impact parameter* (d_0) calculated with respect to the LHC beamline has to be smaller than 1.5 mm, and *the longitudinal impact parameter* (z_0) calculated with respect to the primary vertex is such that $|z_0 sin\theta| \leq 1.5mm$. Both requirements are to avoid secondaries tracks.
- If the track p_T is larger than 10 GeV, the track χ^2 probability must be larger than 0.01 to suppress mismeasured tracks.

6.4 Track reconstruction efficiency

The tracking reconstruction efficiency for primary particles is based on simulation and uses the tracks built with the algorithms described in Section 5.1.1.2 that pass the selection defined in Section 6.3. It is used to correct for the detector effects and is based on simulations.

To compute this efficiency, first, the generated particles are associated with the reconstructed tracks which pass the selection cuts. This process is done by the track-to-true particle association algorithm described in Section 5.1.1.3. Previous studies [23] show that the measured efficiency is independent of the number of generated particles and also of the trigger and vertex requirements.

The tracking efficiency for the selected primary tracks is shown in Figure 19 as a function of p_{T} and η . The components of the uncertainty on the track reconstruction efficiency are discussed in Section 6.4.1.

The low-efficiency values in $|\eta| > 1$ are due to the increasing amount of detector material that the particles have to pass through. And the soft increasing of the efficiency for $|\eta| > 2$ is associated with the fact that in this case the particles pass by a larger number of sensitive layers.

6.4.1 Systematic uncertainties on the track reconstruction efficiency

The systematic uncertainties come from the understanding of the compatibility of the detector geometry model in data and MC, and the cuts applied on the reconstruction process.

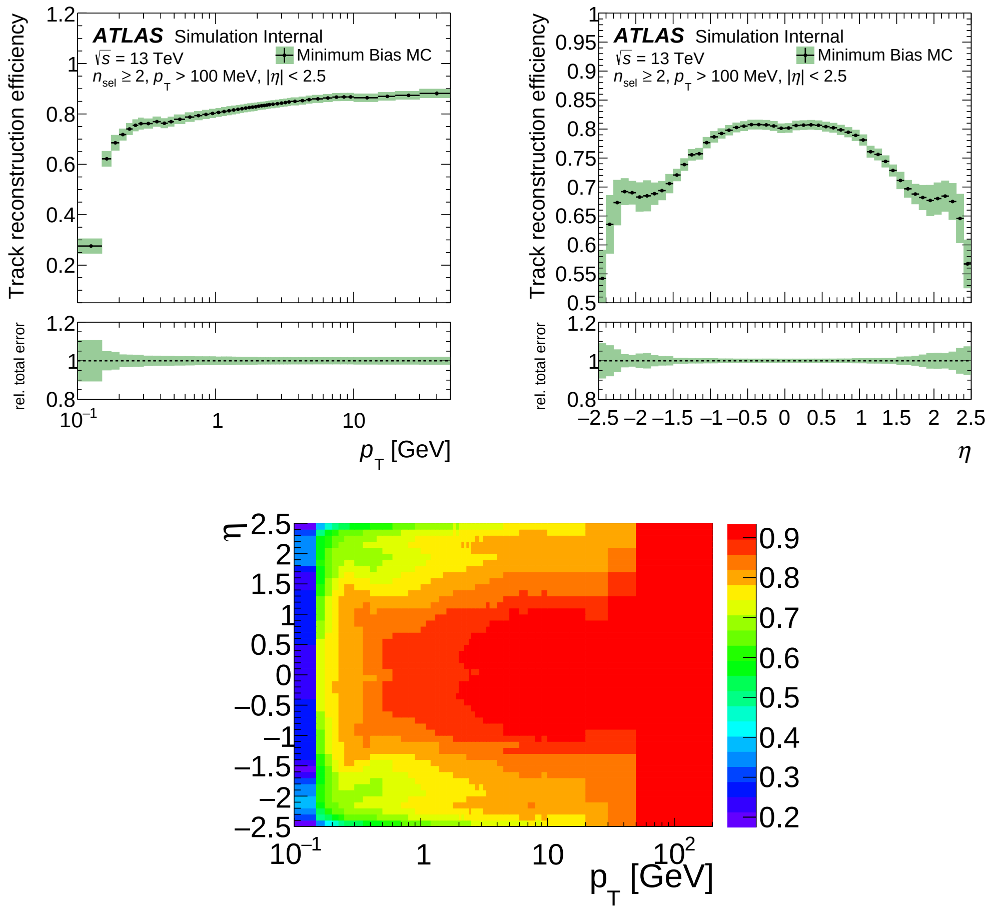

Figure 19: The primary track reconstruction efficiency integrated over p_T (top left), integrated over η (top right) and as a function of p_T and η (bottom). The green shaded error band includes the total systematic and statistical uncertainty.

Each systematic uncertainty on the track reconstruction is described below. The results are summarized in Table 2.

Systematic Uncertainty	Size	Region
Track Selection	0.5%	flat in p_T and η
χ^2 probability	0.2-7%	increasing for p_T
Material	1-9%	decreases for p_T ; increases for $\lvert\eta\rvert$

Table 2: The systematic uncertainties on the track reconstruction efficiency. All uncertainties are quoted relative to the track reconstruction efficiency.

Track selection systematic uncertainty Even when the detector conditions in MC simulations are well described, there are small differences in the number of hits counted in MC and data. In order to remove the dependence on the kinematics of tracks (η , p_T), a two-dimensional re-weighting of the MC is used. The systematic uncertainty is estimated by comparing the efficiency of each cut in data and MC, defined as:

$$\varepsilon(p_T, \eta) = \frac{N^{\text{tracks}}_{\text{all cuts}}(p_T, \eta)}{N^{\text{tracks}}_{\text{N-1 cuts}}(p_T, \eta)} \tag{35}$$

where $N^{\text{tracks}}_{\text{all cuts}}(p_T, \eta)$ is the number of reconstructed tracks with all cuts applied and $N^{\text{tracks}}_{\text{N-1 cuts}}(p_T, \eta)$ is the number reconstructed thacks with a hit requirement removed.

The track selection uncertainty is flat and goes to 0.5% for $|\eta| < 2.5$ and p_T as shown in Figure 20.

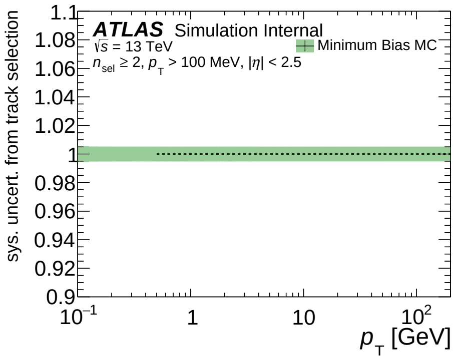

(a)

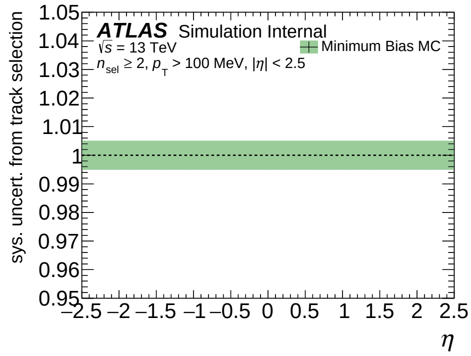

(b)

Figure 20: Relative systematic uncertainty from track selection on the primary tracking efficiency integrated over p_T (20(a)) and η (20(b))

χ^2 probability cut systematic uncertainty Badly measured low momentum charged particles are sometimes reconstructed as a high momentum tracks. Even when the fraction of this badly measured tracks is small at low p_T, for high p_T it becomes a significant fraction due to the falling p_T spectrum.

These bad measurements are caused by interactions of the tracks with the material which causes multiple scattering. This produces tracks with a bad χ^2 fit probability.

In order to suppress these tracks, a cut on the χ^2 probability of $P(\chi^2, \text{n}_{\text{dof}}) > 0.01$ is applied for tracks with p_T >10 GeV. The corresponding systematic uncertainty is performed as in previous analyses [23], the absolute difference between the fraction of tracks removed by the χ^2 cut is used and added in quadrature to the statistical uncertainty. It is less than 0.2% at 10 GeV rising up to 7% above 50 GeV as shown in Figure 21.

Material correction and systematic uncertainty The track reconstruction efficiency is strongly dependent on the material distribution in the detector. Previous studies [15] indicate the accuracy of the material measurements in the detector. It is a 5% uncertainty on the material in the entire inner detector plus an additional 10% uncertainty on the IBL material plus a 50% uncertainty coming from the PP0[13]

[13] The patch panel-0 (PP0) of the Pixel services are the service areas where is the optical-electrical signal conversion boards to reduce ionizing radiation dose and to facilitate access for maintenance.

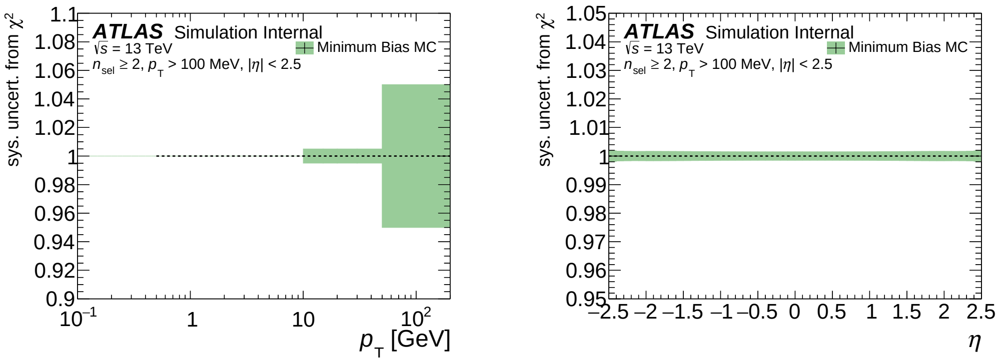

(a) (b)

Figure 21: Relative systematic uncertainty from χ^2 prob. cut on the primary tracking efficiency integrated over p_{T} (21(a)) and η (21(b)).

region ($|\eta| > 1.5$). The total uncertainty is taken as the cuadratic sum of the uncertainties. This leads to a total systematic uncertainty due to the material of 1-9%, which decreases with p_{T} and increases with $|\eta|$. The impact of the various components of the tracking efficiency systematic can be seen in Figura 22.

Total systematic uncertainty The total systematic uncertainty on the primary tracking efficiency is shown as a function of η and p_{T} in Figure 23. The statistical uncertainty is included here, but it is negligible.

It is located between the ID and the end-cap calorimeters far from the interaction point.

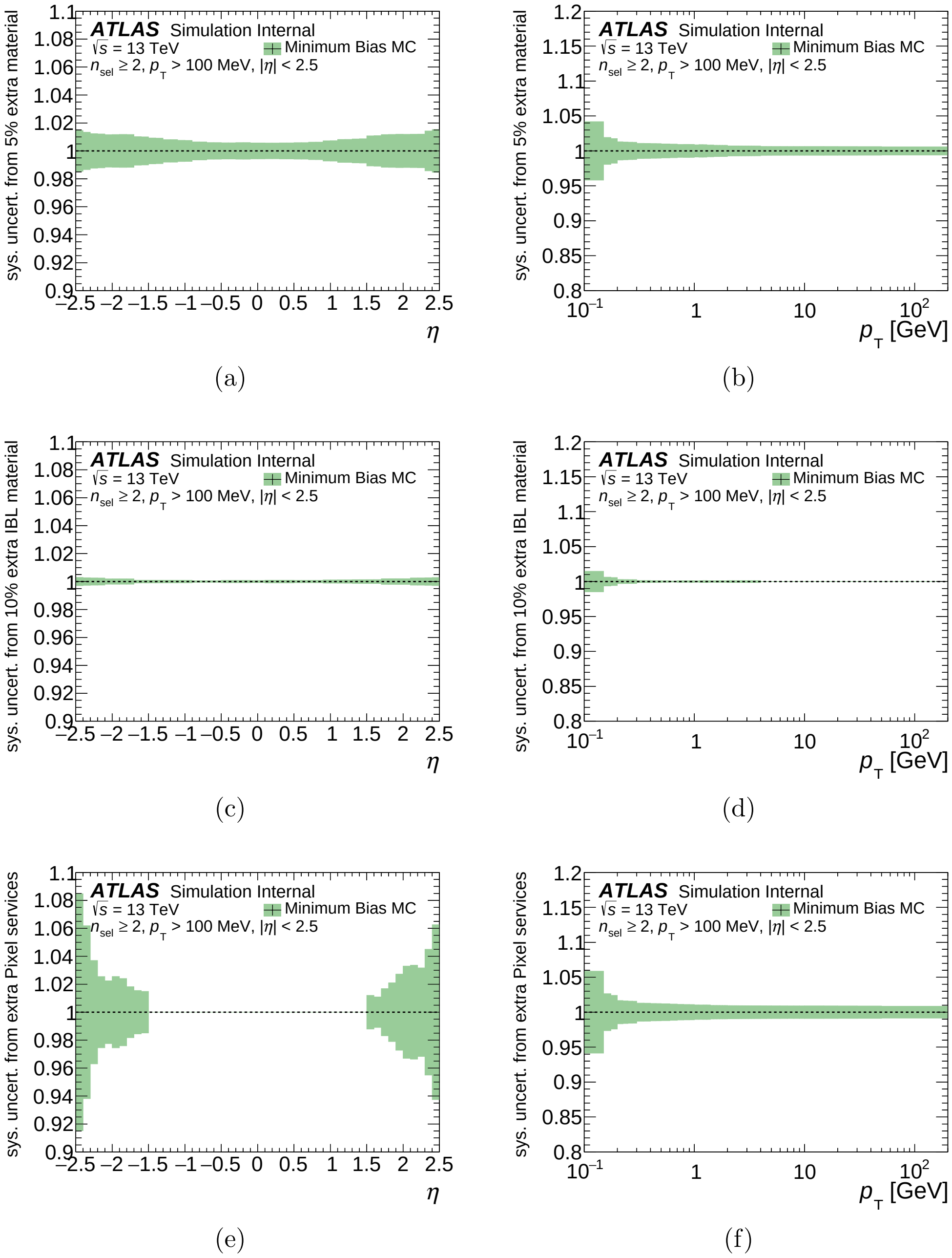

Figure 22: Relative uncertainty due to material in the inner detector on the primary tracking efficiency integrated over p_{T} (on the left) and η (on the right). 22(a) and 22(b) are the systematic uncertainty from 5% extra material; 22(c) and 22(d) are the systematic uncertainty from 10% extra material in the IBL; 22(e) and 22(f) are the systematic uncertainty from extra material in the patch panel region $|\eta| > 1.5$

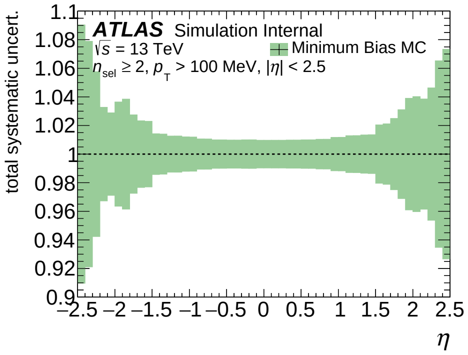

(a)

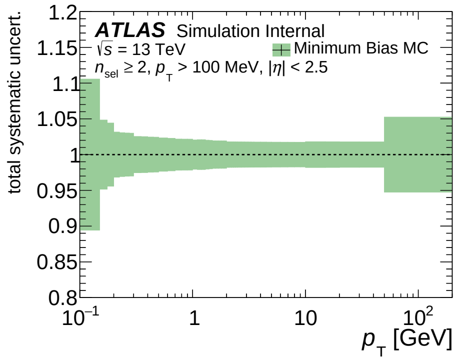

(b)

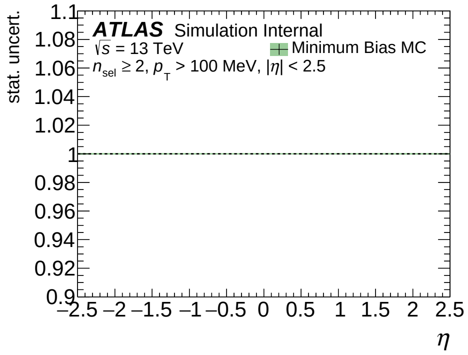

(c)

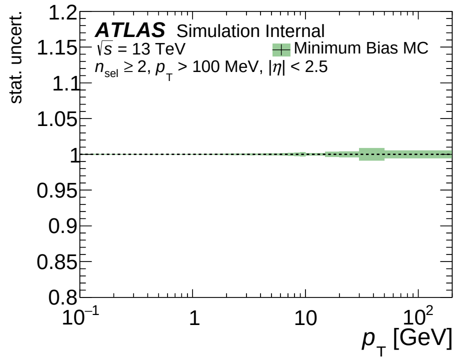

(d)

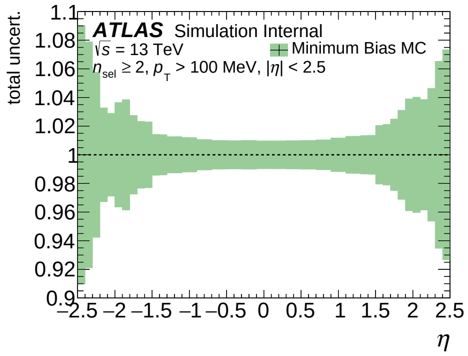

(e)

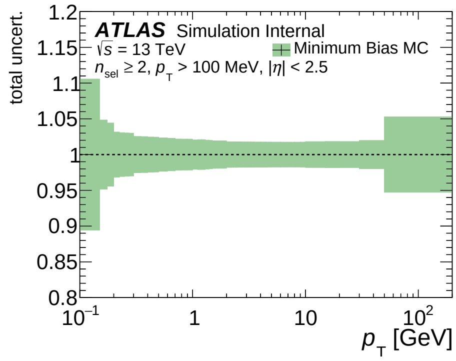

(f)

Figure 23: Relative uncertainty on the primary tracking efficiency integrated over p_{T} and η . The statistical uncertainty is included here, but it is negligible.

6.4.2 Low-p_{T} Tracks

The analysis of charges-particles-multiplicity measurements at low-p_{T} requires modifications of the nominal parameters used for the track reconstruction algorithms. The most significant is the minimum transverse momentum for tracks, which was lowered from 500 to 100 MeV. And the number of silicon hits lowered accordingly from 6 to 5. The optimal values used for this track selection was determined by studying the effects on the efficiency and the fake rate for different track reconstruction parameters.

Figure 24 compares the transverse momentum of the primary track distributions with different setup in the reconstruction algorithm. First, the *default*, uses a p_{T} threshold of 400 MeV. Second, called *MinBias*, uses a p_{T} threshold value of 100 MeV. And the last one, caled *MinBiasLowPt* uses a value of 50 MeV. In all cases the tracks were reconstructed using a minimum of 6 hits.

Figure 25 shows the efficiency of primary particles for the three configurations and Figure 26 shows the fake rate, for both cases, as a function of p_{T} and η.

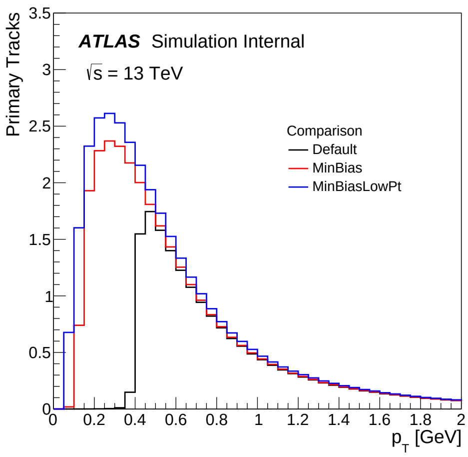

Figure 24: Number of primary tracks as a function of p_{T} . Different lines corresponds to diffent track reconstruction configurations; "default" for p_T >400MeV, "MinBias" for p_T >100MeV and "MinBiasLowPt" for p_T >50MeV.

Figure 25 shows that "MinBiasLowPt" curve reaches higher values of efficiency, however, Figure 26 also shows that the fake rate goes up to 25% for high η . This effect is expected considering the fake rate is correlated with the amount of material in the detector, which increases at high η . As a consequence of this effect, the p_{T} threshold was set at 100 MeV in the analysis. Another parameter value analized is the number of silicon hits (Si). Figure 27 and Figure 28 show the track efficiency for primary and secondary tracks as a function of p_{T} (left) and η (right); for different values of minimum number of Si hits and p_{T} threshold of 100 MeV. Figure 29 shows the same for fake tracks where its rate is. Figure 29 shows that the fake rate is under 3% and Figure 27 and Figure 28 show that the efficiency is slightly better at low p_{T} using 5 Si hit; so this value is chosen.

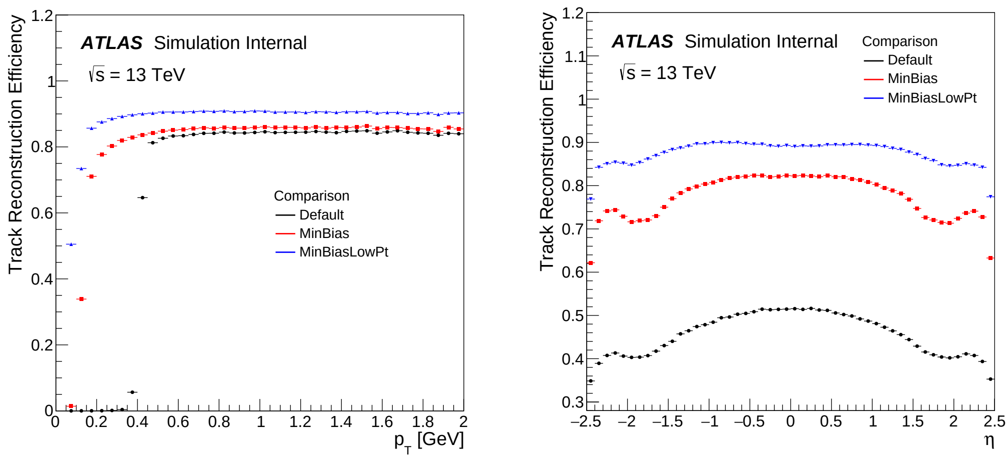

(a) (b)

Figure 25: Reconstruction efficiency of primary tracks as a function of p_{T} 25(a) on the left and as a function of η 25(b). Different lines corresponds to diffents track reconstruction configurations; "default" for p_T >400MeV, "MinBias" for p_T >100MeV and "MinBiasLowPt" for p_T >50MeV.

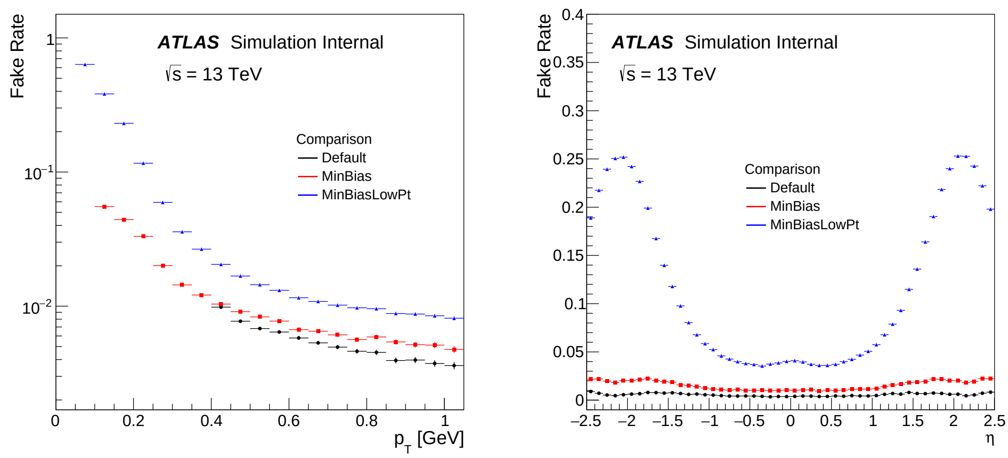

(a) (b)

Figure 26: Fake rate as a function of p_{T} 26(a) and as a function of η 26(b). Different lines correspond to diffents track reconstruction configurations; "default" for p_T >400MeV, "MinBias" for p_T >100MeV and "MinBiasLowPt" for p_T >50MeV.

Therefore the reconstruction setup used for the analysis is the same as for the standard track reconstruction except the p_{T} threshold with goes from 400 MeV to 100 MeV and the number of Si hits, reduced from 6 to 5.

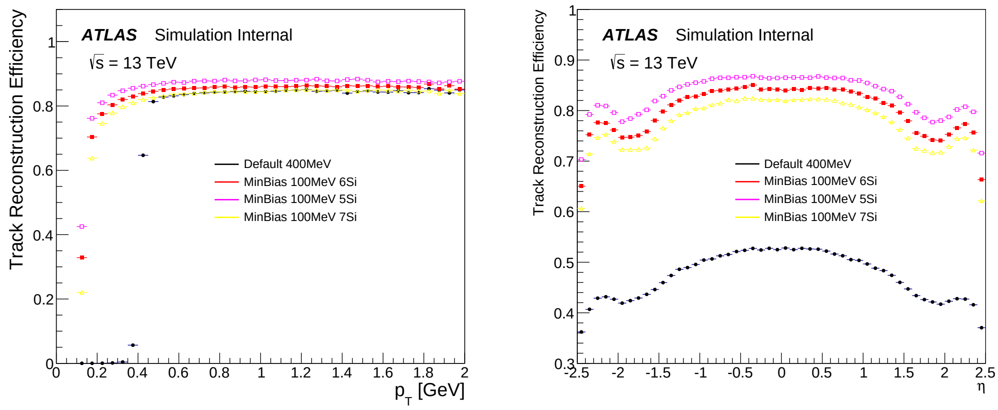

(a) (b)

Figure 27: The reconstruction efficiency of the primary track as a function of generated p_{T} (27(a)) and η (27(b)) for different values of Si required.

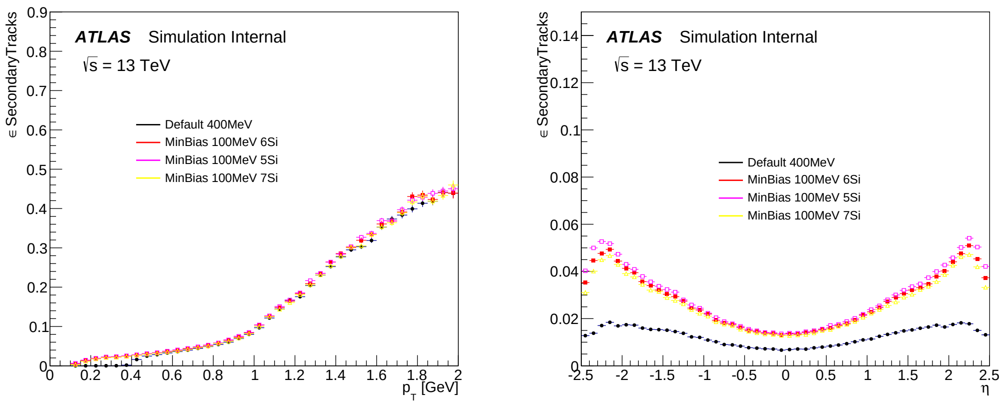

(a) (b)

Figure 28: The reconstruction efficiency of the secondary track as a function of generated p_{T} (28(a)) and η (28(b)) for different values of therequired number of Silicon hits (Si).

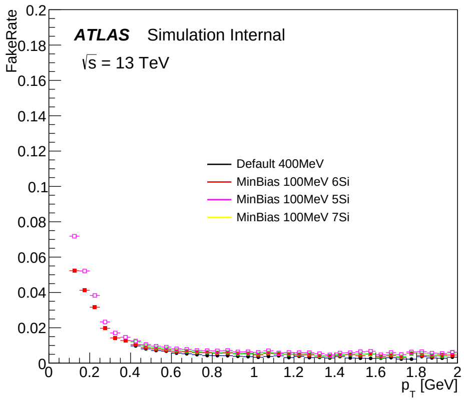

(a)

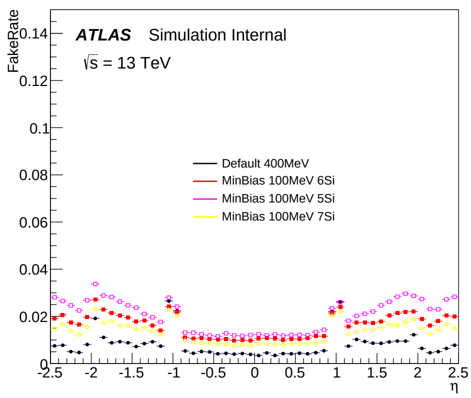

(b)

Figure 29: Fake rate as a function of generated p_{T} (29(a)) and η (29(b)) for different values of the required nuber of Silicon hits (Si).

6.4.2.1 Low-p_T tracking performance in Run2

To check the performance of track selection, the distributions of the number of tracks as a function of the number of hits in the IBL, SCT layer and Pixel layer are compared between data and MC, as shown in Figure 30. In each distribution, the event and track selection (from Section 6.3) are applied, except the cut that is shown in each plot. The differences, as seen in the number of IBL hits distribution, come from differences in the disabled modules between simulation and data and the agreement is consistent with previous studies [18].

Figure 31 shows the number of tracks as a function of d_0 (31(a)) and $z_0 \sin(\theta)$ (31(b)).

The agreement of both distributions in Figure 31 is only good in the central region. In the outer region, the agreement gets worse. This is expected as for larger impact parameter the number of secondary tracks is larger. Section 6.6 describes a correction to the rate of secondaries, that uses a scale factor which improves the modelling of the tails.

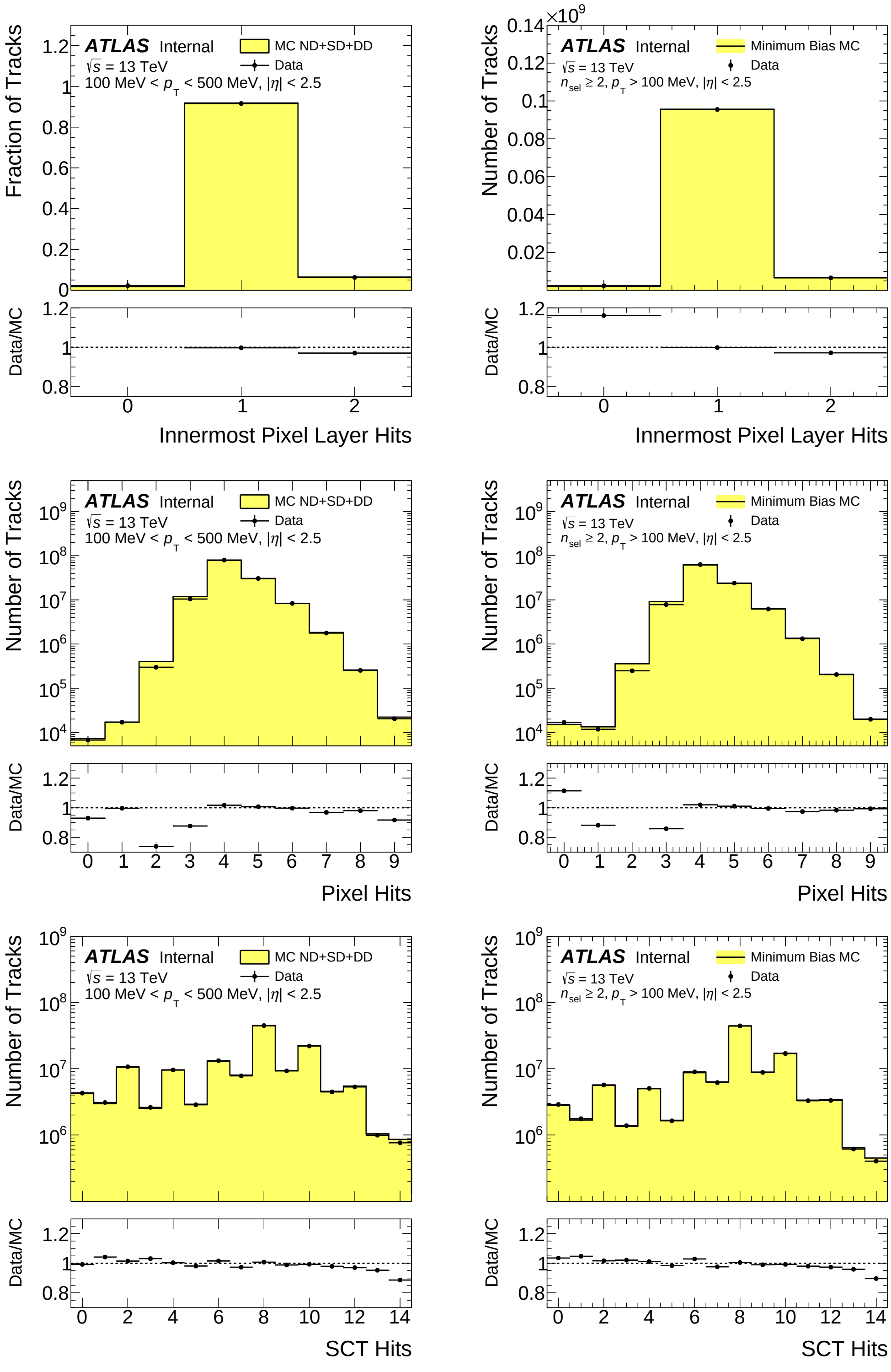

Figure 30: Number of tracks with different number of IBL hits (top); the number of tracks with a different number of Pixel layer hits (middle); the number of tracks with a different number of SCT hits (bottom). On the left-hand side for 100 GeV$<p_{\mathrm{T}}$ $<$500 GeV and on the right-hand side for the full phase-space with $p_{\mathrm{T}} > 100$ GeV. The p_{T} and η distribution of the tracks in MC is re-weighted to match the data and the number of tracks is scaled to data.

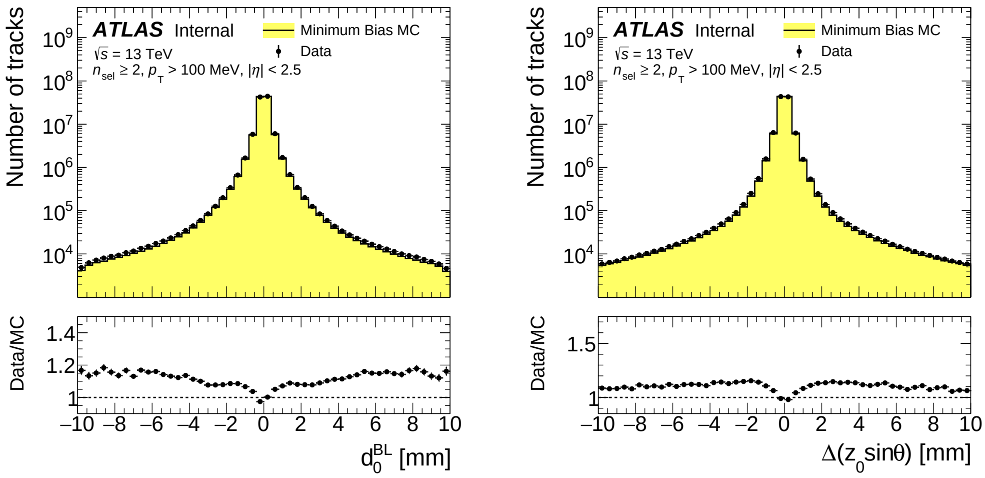

(a) (b)

Figure 31: Number of tracks as a function of d_0 on the left and $z_0 \sin(\theta)$ on the right. The p_T and η distribution of the tracks in MC is re-weighted to match the data and the number of tracks is scaled to data. No secondary scale-factor is applied here.

6.4.3 Vertex Efficiency

The vertex reconstruction efficiency, ϵ_{vtx}, is build from data as the ratio between the number of triggered events with at least two selected particles and a reconstructed vertex, over the total number of triggered events with at least two selected particles, as is defined in Equation 36

$$\epsilon_{vtx} = \frac{events\ passing\ MBTS_1\ \&\ n^{no-z}{}_{sel} \geq 2\ \&\ having\ a\ vertex}{events\ passing\ MBTS_1\ \&\ n^{no-z}{}_{sel} \geq 2} \tag{36}$$

The efficiency is then calculated as a function of the number of selected tracks $\mathrm{n}^{\text{no-z}}_{\text{sel}}$, tracks with all the selection cuts applied, but not the cut for z_0. The exclusion of the z cut is to relax the condition and increase the efficiency.

Events with only two tracks are corrected using a Δz_{tracks} (the distance between the two selected tracks in the event at the beamline) dependent correction because dependence on the separation was observed for events with low track multiplicity. This means that for events with only two tracks, the vertex efficiency is computed as a function of the Δz_{tracks} as shown in 32(b). For events with more than two tracks, the vertex efficiency is computed as a function of the number of selected tracks, as shown in the 32(a).

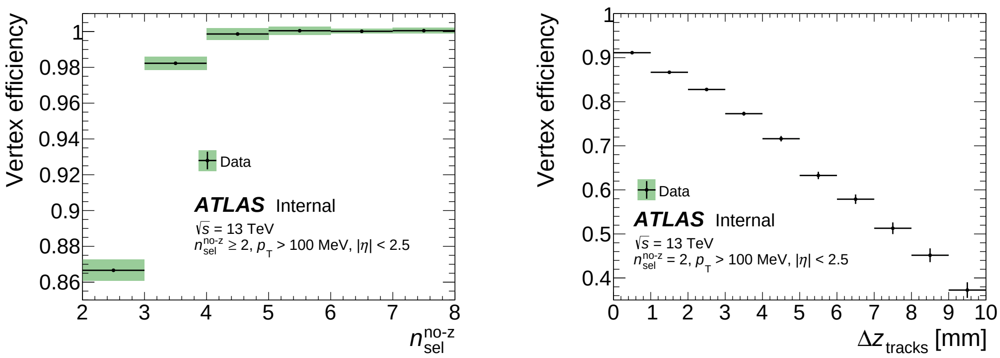

(a) (b)

Figure 32: Vertex efficiency in data with respect to the event selection as a function of the number of reconstructed tracks (left) and as function of Δz_{tracks} for exactly two selected tracks (right). The statistical errors are shown as black lines, the total errors as green shaded areas, which are very small and only hard to see for the right plot. The plot shows the efficiency in data at 13 TeV for $\mathrm{n}^{\text{no-z}}_{\text{sel}} \geq 2$, $p_{\mathrm{T}} > 100$ MeV, $|\eta| < 2.5$. The systematic errors are from the subtraction of the non-collision beam background.

The systematic uncertainties are treated in previous studies [23] by analyzing the non-collision beam (NCB) background that can be reconstructed as collisions within the ATLAS detector. Thus the difference in the vertex reconstruction efficiency with and without beam background removal is assigned as a systematic uncertainty.

6.5 Trigger

Events are collected from colliding proton bunches where the MBTS trigger recorded one or more counts on either side.

6.5.1 Trigger efficiency

The trigger efficiency (ϵ) is measured from a data sample selected using a randomly-seeded control trigger. It is defined as the ratio between events in which the control trigger also accepts the event and the total number of events in the control sample.

The control trigger selects events from a randomly filled bunch crossing on the L1 level and filtered at the HLT level. The First step of filtering asks for at least two pixel hits and at least three SCT hits. Then, a track reconstruction is applied in the event filter and only one track (with $p_{\mathrm{T}} > 200$ MeV) is required. The trigger efficiency is expected to be very high in events with two or more tracks even if the requirement $p_{\mathrm{T}} > 100$ MeV uses a bit lower threshold. The control trigger may fail only if all tracks in the event have $p_{\mathrm{T}} < 200$ MeV. Anyway, the efficiency of the control trigger was tested using a random sample containing 7861 events with at least two tracks with $p_{\mathrm{T}} > 100$. In this sample 200 events with $n_{\mathrm{sel}} = 2$ were found. All events collected this way were also accepted by the control trigger thus it is calculated efficiency is always equal to 100%, while the statistical error in $n_{\mathrm{sel}} = 2$ bin is $\sim$0.005. As the overall impact of the trigger efficiency uncertainty is negligible in this analysis.

The resulting trigger efficiency as a function of the number of selected tracks is shown in Figure 33 for selected tracks with a transverse momentum of p_{T} >100 MeV. For events with more than six reconstructed tracks, the trigger is fully efficient.

The systematic uncertainties on the trigger efficiency are calculated by varying the track selection. The variation is as follows: First, the restriction on the transverse impact parameter is removed, increasing the number of tracks and generating a migration of events to higher n_{sel}^{BL} bins, leading to a decrease of trigger efficiency at low multiplicities. Last, For tracks in events with a primary vertex, a cut on the z coordinate with respect to the primary vertex is applied reducing the number of accepted tracks, and causing a migration of events to lower n_{sel}^{BL} bins. The difference between the efficiency obtained and the default is less than 1%.

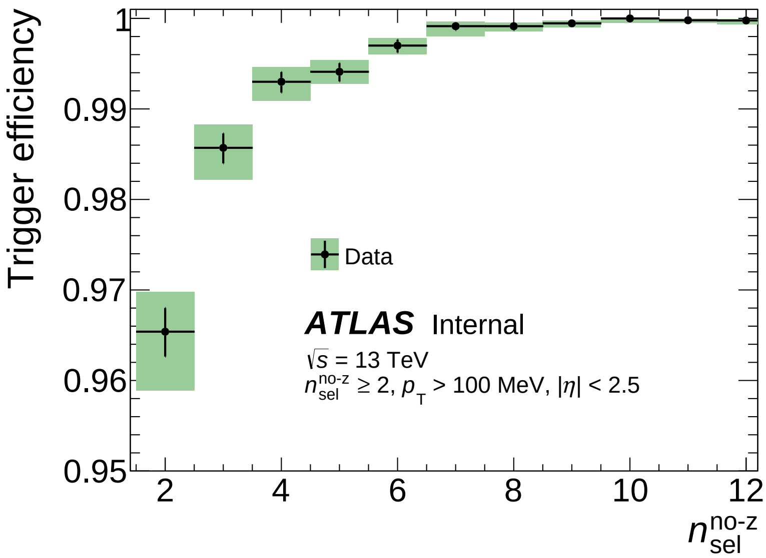

Figure 33: Trigger efficiency with respect to the event selection as a function of the number of reconstructed tracks (n_{sel}) with p_{T} > 100 MeV and $|\eta| < 2.5$, which are compatible with the beam line ($d_0^{\mathrm{BL\ no\text{-}z}} < 1.5$ mm). A reconstructed vertex is not required. The statistical errors are shown as black lines, the total errors as green shaded areas.

6.6 Backgrounds

Backgrounds must be subtracted from the raw distributions. There are two types of background. First, the *event background* related to non-collision events as proton interactions with residual gas molecules in the beam pile and cosmic ray interactions. And the second type is the *background to primary tracks*, such as hadronic interaction products, resulting in secondary tracks or fake tracks. Also events with more than one interaction in the same bunch-crossing (pileup events)

The first contribution is evaluated by considering events that pass the full event selection but occur when only one of the two beams is present. This contribution is less than 0.01%, and considered negligible. Also, the expected rate of cosmic ray events is less than 0.001 Hz which is irrelevant concerning the event readout rate (2 kHz) therefore it is neglected. The pileup contribution is avoided by the vertex condition, events with more than one vertex are excluded.

The amount of fake tracks was analized after the full event selection. Figure 35 shows the fraction of fake tracks as a function of $p_{\mathrm{T}}$and η. I can be seen that the fraction of fake tracks is less than 1%. Neverless them are subtracted. The uncertanty on the fake rate contribution is assumed to be 50% of the rate following the tracking group recomendations.

The contribution of secondary tracks comes from three sources: tracks created through hadronic interactions with the detector material, decay products of long-lived particles as k^0 and Δ^0, and photon conversions[14] which is the principal background for very low p_{T} tracks (100-250 MeV). Figure 35 shows the rate of secondary

[14]Creation of a pair of charged particles from a photon decay

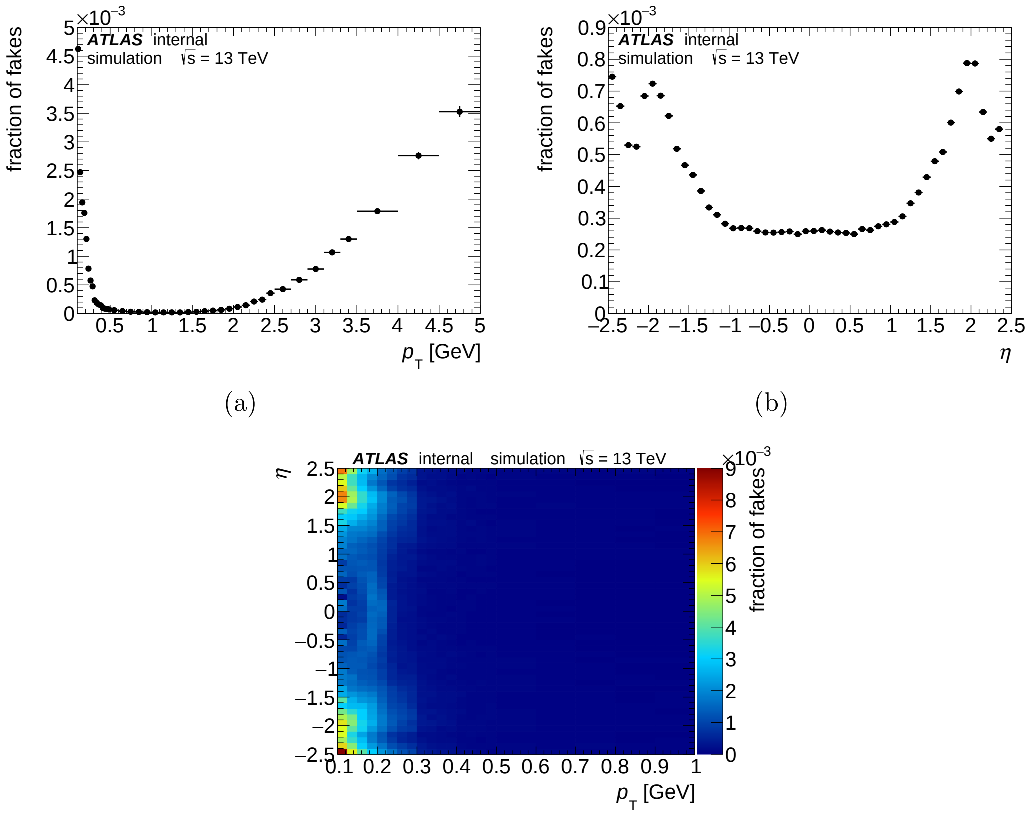

(a)

(b)

(c)

Figure 34: The fraction of fakes after applying the full event selection as a function of p_{T}(34(a)) or η (subfig:fakeeta) and the two-dimensional dependency of $p_{\mathrm{T}}$and η (subfig:fakepteta). The fraction is below 1negligible for the analysis

particles background.

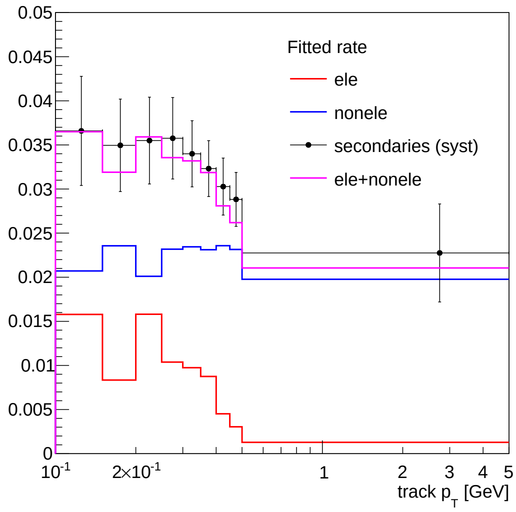

Figure 35: Secondary rate from Pythia sample

The procedure to determine the contribution of non-primary reconstructed tracks is fully described in [23]. The d_0 distribution is computed after applying the track selection except the transverse impact parameter d_0 cut. These distributions are fitted in the side-band regions to the distributions in data to find scaling factors for the rate of secondary tracks. The distribution before and after applying the fitted scale factor is shown in Figures 36, 37 and 38. The fit is performed in a range of $|d_0|$ from 4mm to 9,5mm. The lower limit is such that the primary rate is suppressed versus the secondary rate and the upper limit due to the cut in the pattern recognition. The process is done for differents p_{T} bins but for $p_T >$ 500 MeV, a single template is sufficient.

The systematic error on the fit method is obtained by varying, for the fit, the simulation with different amount of material, and the widow fit (from 3mm to 6mm in steps of 1mm). For p_{T}between 100 MeV and 150 MeV, this results in relative errors of 6.8% and 4.5%.

The difference in the generators of the ratio of secondaries in the fit region and the selected tracks are used as the systematic error which leads to a relative error of 5.18% in the 100 MeV $< p_T <$ 150 MeV bin. More details on systematic studies in all p_{T} bins can be found in Appendix A.1

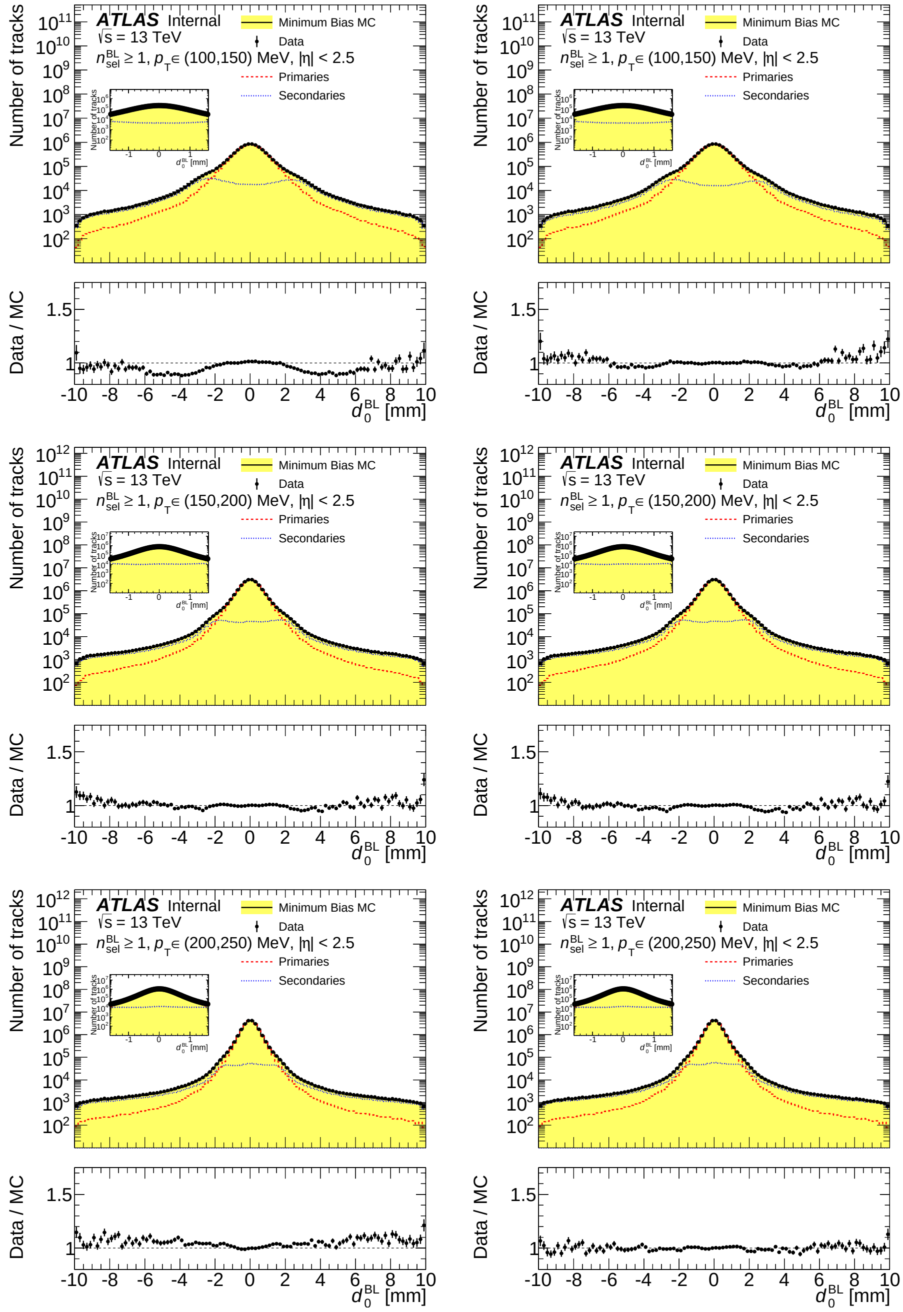

Figure 36: Impact parameter distribution d_0 for data compared to Pythia8 A2 tune without (left) and with (right) the data-fitted secondaries scale factor applied to the background from secondary tracks. The distribution of primary tracks is shown with a dashed line and the secondary background as a solid line.

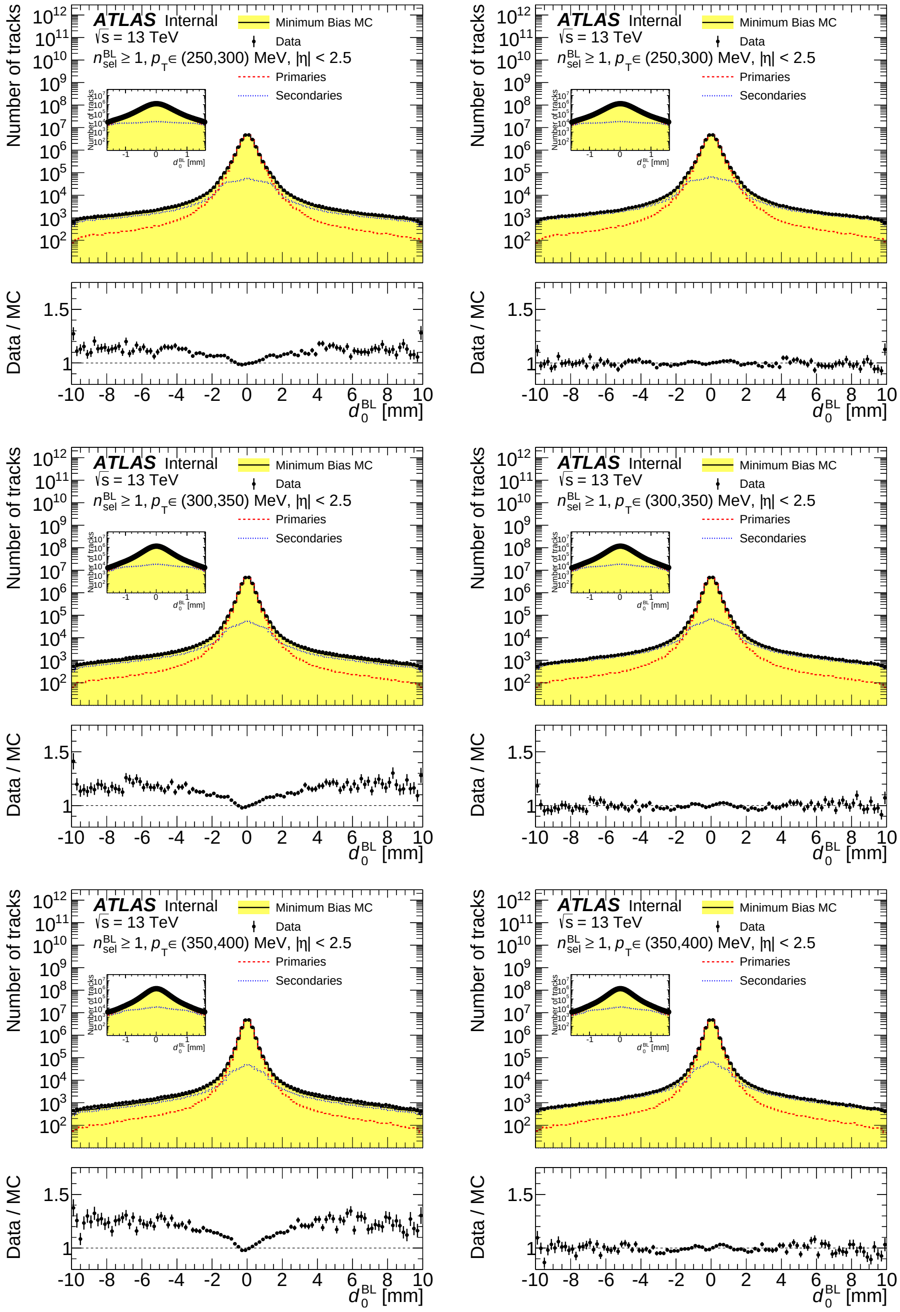

Figure 37: Impact parameter distribution d_0 for data compared to Pythia8 A2 tune without (left) and with (right) the data-fitted secondaries scale factor applied to the background from secondary tracks. The distribution of primary tracks is shown with a dashed line and the secondary background as a solid line.

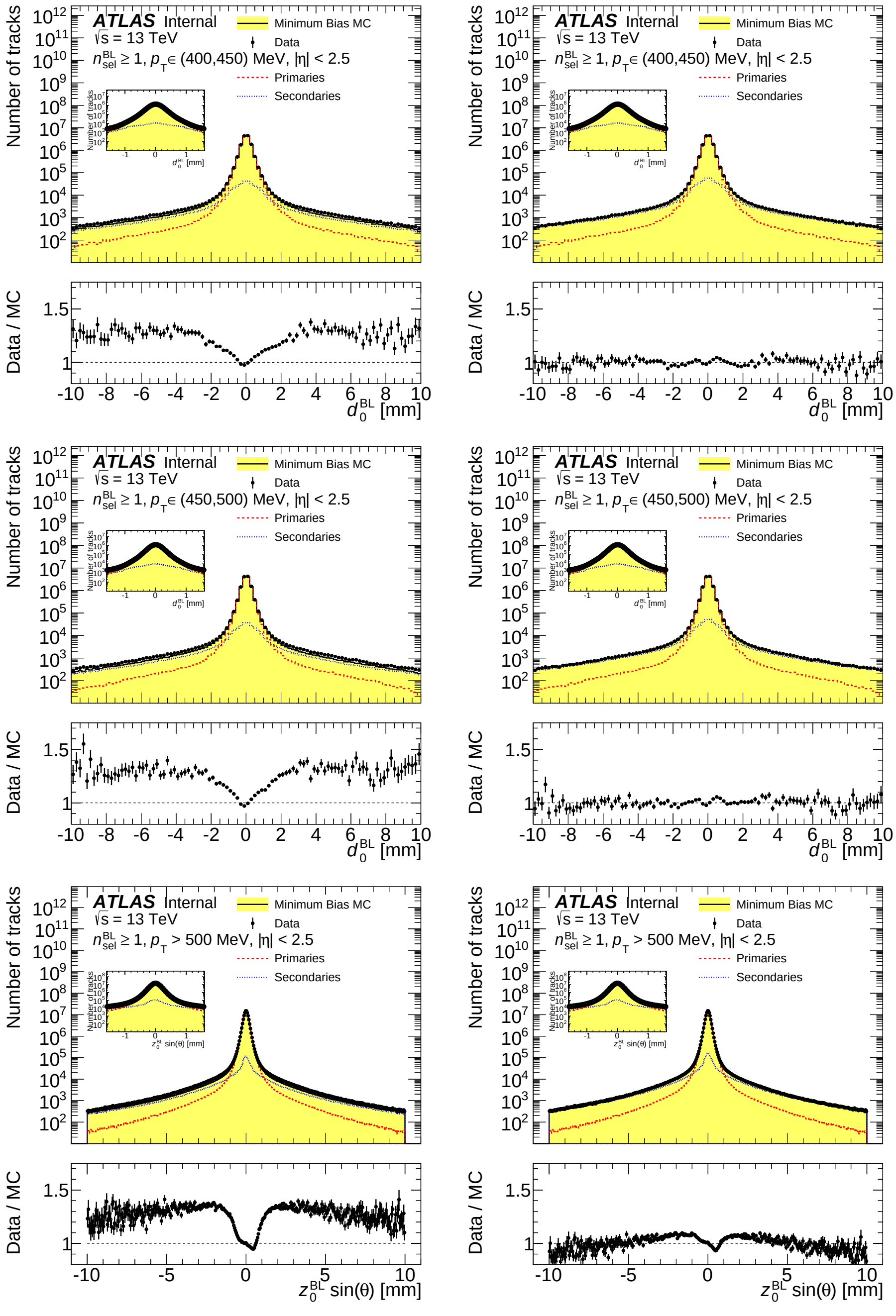

Figure 38: Impact parameter distribution d_0 for data compared to Pythia8 A2 tune without (left) and with (right) the data-fitted secondaries scale factor applied to the background from secondary tracks. The distribution of primary tracks is shown with a dashed line and the secondary background as a solid line.

6.7 Out of phase-space correction

There is a fraction of reconstructed selected primary tracks that migrates from outside to the inside of the kinematic range. It is estimated from different MC samples for comparison and in each case separately for η and p_{T}.

Figure 39 shows the η migration. On the left, the fraction of selected tracks originating from particles with $|\eta|$ >2.5 and on the right the migration to the region 2.4< $|\eta|$ <2.5 for the different samples.

Figure 40 shows the migration in p_{T} .The left plot shows the number of primary tracks originating from particles from p_T <100 MeV, after subtracting the number of particles migrating out of acceptance (from p_T >100 MeV to p_T <100 MeV) and normalized to the number of selected tracks. On the right the difference in residual p_{T} migration in the region 100 MeV< p_T <125 MeV.

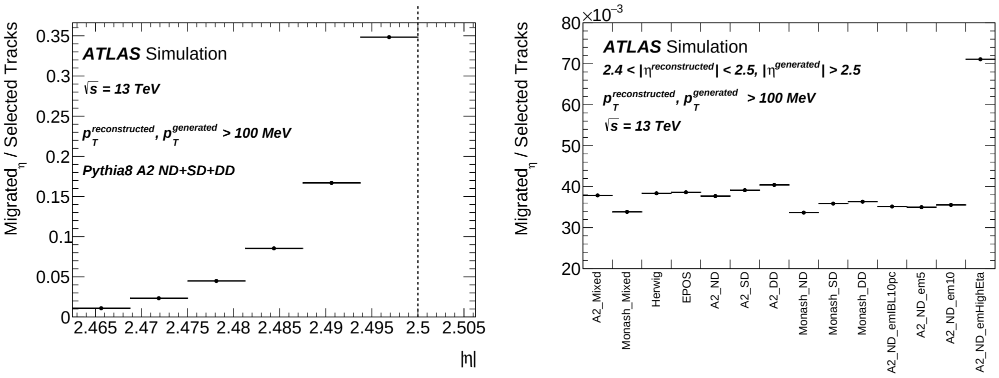

Figure 39: Primary particles migrating from $|\eta|$ >2.5 to be reconstructed as tracks with $|\eta|$ < 2.5. (a) Fraction of selected tracks originating from particles with $|\eta|$ > 2.5. (b) Sample comparison for η migration

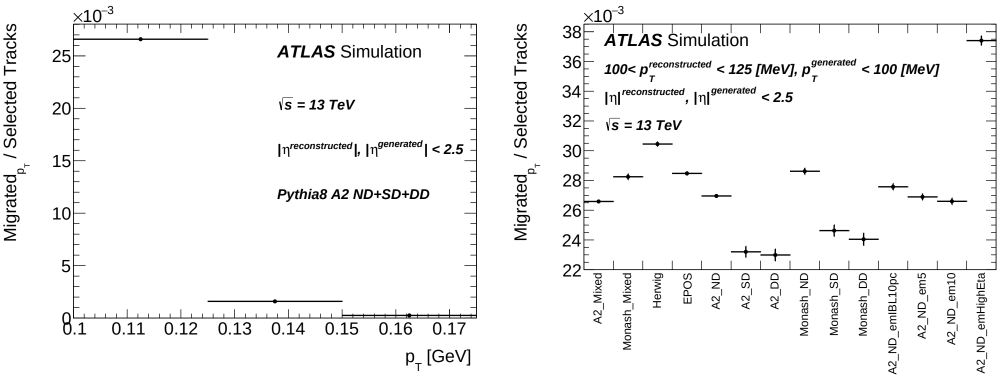

Figure 40: Primary particles migrating from $|p_T|$ <0.1 GeV to be reconstructed as tracks with $|p_T|$ >0.1 GeV. (a) Residual p_{T} migration (number of particles migrating in minus the number of particles migrating out) for the pythia 8 A2 mixed sample. (b) Sample comparison for p_{T} migration mixed sample

Both cases η and p_{T} right plots reflect the fact that the biggest changes in the number of migrated tracks are caused by material distortions.

A systematic uncertainty is considered to take into account the migration difference in the total migration between the samples. It is computed as the absolute value of the difference in migration fractions in the $2D$ distribution ($|\eta|$ vs p_{T}). The different contributions are added up in quadrature, and the relative sizes are in Table 3.

Systematic uncertainty	Calculated as difference between samples	Fraction of total uncertainty (p_{T})	Fraction of total uncertainty (η)
Generator	herwig++ pythia 8 Monash	19%	12%
Inner Detector extra material	5% extra ID material and Pythia8 ND	1%	4%
IBL corrected material	10% extra IBL material and Pythia8 ND	4%	4%
High η extra material	2×10% extra ID material ($|\eta| > 2.2$) and Pythia8 ND	76%	80%

Table 3: Summary table of the systematic uncertainties on the corrections applied to tracks originating from outside of the kinematic region (p_{T} and η acceptance)

Figure 41 shows, on the left, the total size of the out-of-phase-space correction as a function of η and p_{T}, and on the right, the resulting relative systematic uncertainty histogram. The correction is largest for the lowest p_{T} and highest η bin, but the relative uncertainty is still less than 4.5%

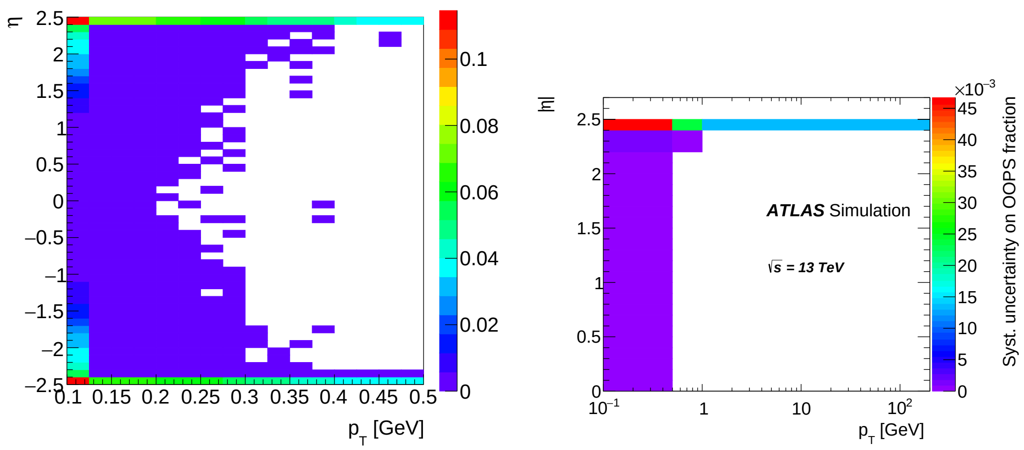

(a) (b)

Figure 41: The out of phase space correction in p_{T} and η bins (41(a)) and the systematic uncertainty on the out of phase space correction fractions (41(b))

6.8 Correction Procedure

The data must be corrected to obtain the inclusive spectra for charged primary particles satisfying the phase-space requirement ($|\eta|$ <2.5 and $p_T \geq$ 100MeV). These corrections include inefficiencies due to the trigger selection (ϵ_{trig}) and vertex requirement (ϵ_{vtx}). Therefore the number of events lost are corrected by an event-by-event weight:

$$\mathrm{w}_{\text{ev}}(n_{\text{sel}}, \eta\ ) = \frac{1}{\epsilon_{\text{trig}}(n_{\text{sel}}^{\text{no-z}})} \cdot \frac{1}{\epsilon_{\text{vtx}}(n_{\text{sel}}^{\text{no-z}}, \Delta \mathrm{z}_{\text{tracks}})} \tag{37}$$

where $n_{\text{sel}}^{\text{no-z}}$ is the multiplicity of selected tracks with the relaxed selection (no cut on the vertex and hence no cut on the longitudinal impact parameter). The calculation of the trigger efficiency is explained in Section 6.5.1 and the vertex efficiency is in Section 6.4.3.

Also, to correct for the inefficiencies in the track reconstruction, the p_{T} , η , and mean p_{T} distributions of the selected tracks are corrected with a track-by-track weight. It uses the tracking reconstruction efficiency (ϵ_{trk}) and removes the fractions for non-primary particles (f_{nonp}), for strange baryons (f_{sb}) and for particles outside the kinematic range (f_{okr}), as shows Equation 38:

$$\mathrm{w}_{\text{trk}}(p_{\text{T}}\ , \eta) = \frac{1}{\epsilon_{\text{trk}}(p_{\text{T}}\ , \eta)} \cdot (1 - f_{\text{nonp}}(p_{\text{T}}\ , \eta) - f_{\text{okr}}(p_{\text{T}}\ , \eta) - f_{\text{sb}}(p_{\text{T}}\ , \eta) - f_{\text{fake}}(p_{\text{T}}\ , \eta)) \tag{38}$$

In addition, a cross-check was developed only for the unfolding procedure with a completely independent code based on RooUnfold tools [5].

The correction procedure for each of the measured distributions ($\frac{1}{N_{ev}} \cdot \frac{dN_{ch}}{d\eta}$, $\frac{1}{N_{ev}} \cdot \frac{1}{2\pi()p_T} \cdot \frac{d^2 N_{ch}}{d\eta dp_T}$, $\frac{1}{N_{ev}} \cdot \frac{dN_{ev}}{dn_{ch}}$ and $< p_T >$) is presented separately in the following sections.

The inicial raw distributions of the variables of interest (n_{sel}, p_{T} , η) are shown in Figure 42. The main contribution is from non-diffractive (ND) events with around 80%, single (SD) and double diffractive (DD) events contribute around 10% each. This composition is very similar to the one seen in [29].

6.8.1 Summary of the systematics uncertanties

A summary of all systematics uncertanties is presented in Table 4. The systematic uncertainties due to the vertex reconstruction and the trigger efficiency are neglected as they are an order of magnitude smaller than the systematic uncertainties due to the tracking efficiency.

The systematics applied to each distribution are described in the respective sections.

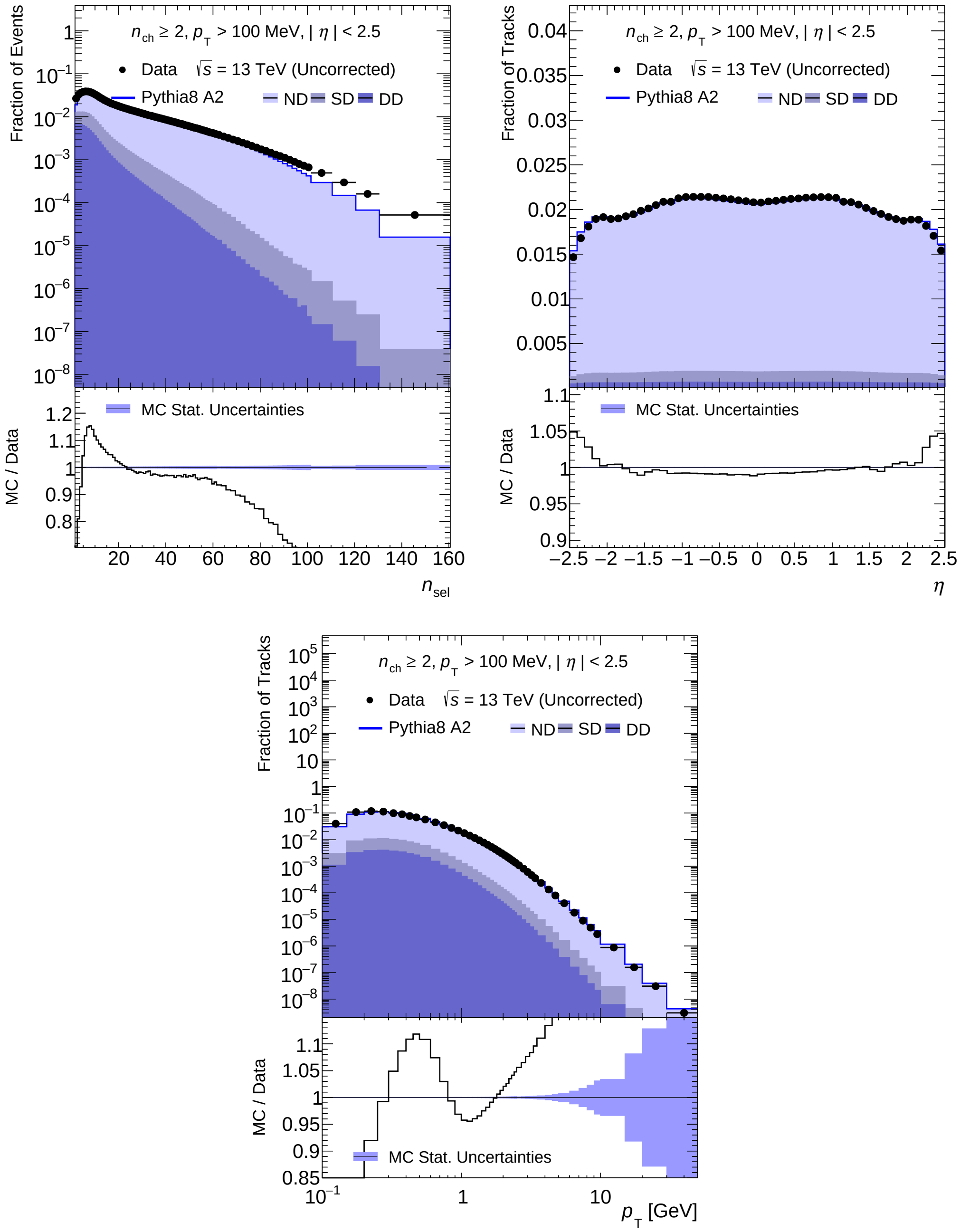

Figure 42: Raw distributions of the fraction of events/tracks in each bin. The distributions are split for the MC expectation into single diffractive (SD), non-diffractive (ND) and double diffractive events (DD).

6.8.2 Correction to $\mathrm{d}N_{\mathrm{ev}}/\mathrm{d}n_{\mathrm{ch}}$

In order to remove the detector effects in the final results, one needs to express the multiplicity distribution in terms of the number of charged primary particles n_{ch} instead of the number of selected charged tracks n_{sel}. For that purpose a *Bayesian unfolding* procedure[23] is implemented. Then, the distribution of pri-

Distribution	Systematic uncertainty	max. size
all	material	10%
all	secondaries	5%
all	strange baryons	2%
all	effect of badly measured tracks	7%
all	out-of-kinematic-range	0.5%
n_{ch}	propagation of stat uncert. due to unfolding matrix	<1%
p_{T}	propagation of stat uncert. due to unfolding matrix	4% for p_{T} <10 GeV <30% for p_{T} <14 GeV >40% for p_{T} >14 GeV
n_{ch}, $< p_T >$	p_{T} spectrum	<1%
	non-closures	
n_{ch}	4,2,2,2% in n_{ch}=2,3,4,5 cover vtx, trigger syst	
η	0.4% for the full range, 1% for the first and last bin	
p_{T}	1% for p_{T} ≤10 GeV, 3% for p_{T} >10 GeV	
$< p_T >$	2% in n_{ch} ≤15 and 0.5% else	

Table 4: List of systematic.

mary particles are gotten by the probability relation given by the Bayes theorem $P(n_{ch}).P(n_{sel}|n_{ch}) = P(n_{ch}|n_{sel}).P(n_{sel})$ over n_{sel}:

$$N_{ev}(n_{ch}) = \sum_{n_{sel}\geq 0} P(n_{ch}|n_{sel}).N_{ev}(n_{sel}) = \frac{1}{\epsilon^{miss}(n_{ch})} \sum_{n_{sel}\geq 2} P(n_{ch}|n_{sel}).N_{ev}(n_{sel}) \quad (39)$$

The second relation factorizes the contribution of events that are lost due to track reconstruction inefficiencies but would pass the particle level phase-space cuts, i.e. those with $n_{\mathrm{ch}} \geq 2$ but $n_{\mathrm{sel}} = 0$ or 1. The correction applied is written in Equation 40.

$$\varepsilon^{miss}(n_{\mathrm{ch}}) = 1 - (1-\epsilon_{trk})^{n_{\mathrm{ch}}} - n_{\mathrm{ch}}.\epsilon_{trk}.(1-\epsilon)^{(n_{\mathrm{ch}}-1)} \quad (40)$$

Where the ϵ_{trk} is the mean tracking efficiency in the first n_{sel} bin. The correction is significant in the first n_{ch} bin, with significantly smaller contributions in higher bins. The procedure assumes that the mean tracking efficiency is constant as a function of n_{ch}. In table 5, the mean tracking efficiencies are listed for the different samples which are used in this analysis.

Sample	mean trk. eff.
Data	0.71941
PYTHIA 2	0.71337
EPOS LHC	0.72951

Table 5: Mean tracking efficiency in the first n_{sel} bin for all different samples which are used for this analysis. The tracking efficiency is used in order to calculate the so-called miss-factor for the out-of-phase-space correction.

The condicional probability $P(n_{ch}|n_{sel})$ of observing an event with true n_{ch}, given the observed n_{sel} is unknown. Therefore, the idea is to get an estimate for $P(n_{ch}|n_{sel})$ form MC using a Bayesian unfolding, and improve it by iterations:

$$P(n_{ch}|n_{sel})^{r+1} = P(n_{sel}|n_{ch})\frac{{N_{ev}}^{r}(n_{ch})}{N_{ev}(n_{sel})} \tag{41}$$

Where $P(n_{sel}|n_{ch})$ is the *resolution function* and ${N_{ev}}^{r}(n_{ch})$ and ${N_{ev}}^{r}(n_{sel})$ are the distributions of primary particles and of selected tracks, respectively. Only for $r = 0$, these are the *prior* from MC.

The unfolding matrix is made up with the PYTHIA 2 MC sample and is applied to the data distribution to obtain the observed n_{ch} distribution. The resulting distribution is used to re-populate the matrix and the correction is re-computed. This procedure is repeated and converges after 5 iterations in data. The unfolding matrix from Equation 41 is shown in Figure 43. It shows several events with low n_{sel} but high n_{ch}. These events are caused by the tracking inefficiencies where no tracks were found.

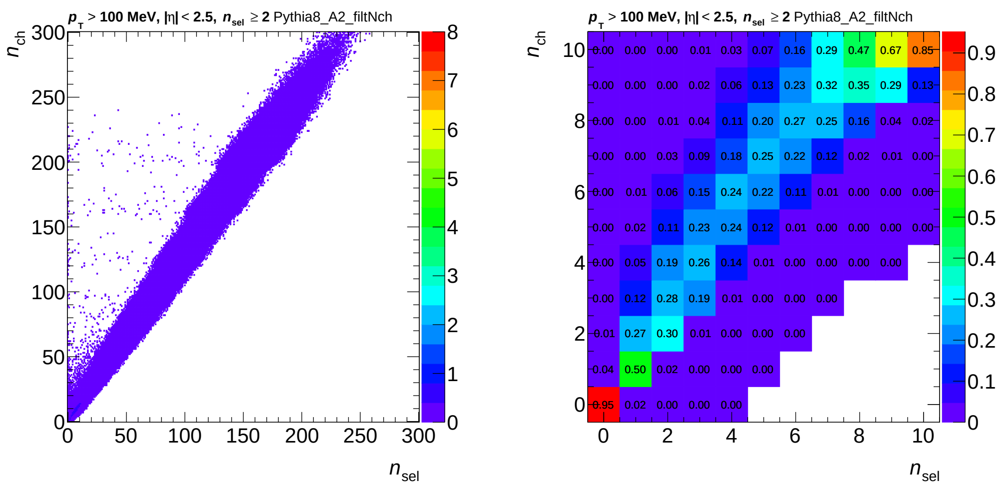

Figure 43: Migration matrix derived from PYTHIA 2. On the left hand side is the full matrix, on the right hand side the rows are normalized to one. The matrix is shown for the first iteration.

6.8.2.1 Closure test for $\mathrm{d}N_{\mathrm{ev}}/\mathrm{d}n_{\mathrm{ch}}$

Different closure tests were performed for the unfolding procedure. They are divided into two groups, one that uses the unfolded matrix generated with PYTHIA 2 and the second that uses EPOS LHC instead.

For both groups, two distributions are tried as inputs: the first one uses PYTHIA 2 and the second one uses EPOS LHC. If the distribution is generated with a different generator than the matrix then it works as pseudo-data. Both closure groups are shown in Figure 44 and Figure 45, and Figure 47 and Figure 46 respectively.

The closure test shows the n_{ch} distribution and an additional comparison is done for events with $n_{\mathrm{sel}} \geq 2$ which do not migrate outside the detector phase-space. These are labeled “visible” in the plot and correspond to the unfolded distribution without applying the correction factor ϵ_{miss} (cf. eq 40). Therefore it probes especially the matrix-based step of the correction. The unfolding works very well for this test, as the ratio from the unfolded distribution to the truth distribution is always at one (blue line in the ratio plot).

Figure 45(a) shows that the number of used iterations is 5. The best number of iterations is selected by finding the iteration with the lowest difference between the expected and the resulting distribution. The right-hand plot shows the improvement of the result with an increasing number of iterations. Also for this closure test, the ratio is again around one and shows that the correction procedure works well.

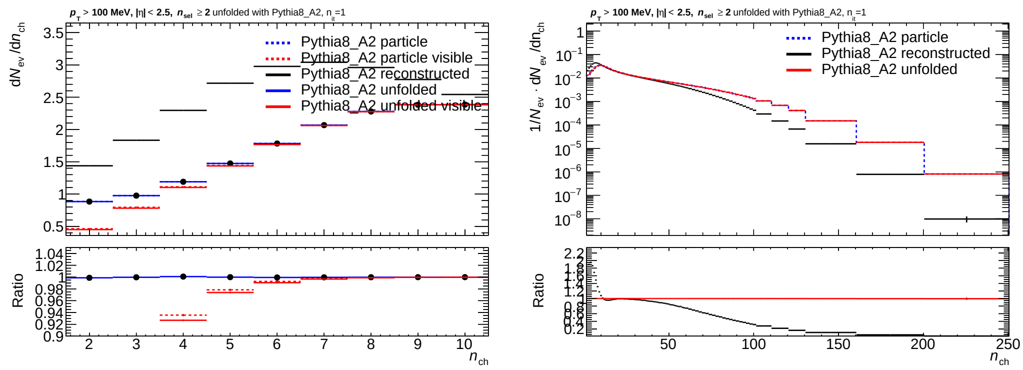

Figure 44: Closure test using PYTHIA 2 for the input distribution and the construction of the unfolding matrix. The label ”visible” is used for the subset of events with $n_{\mathrm{sel}} \geq 2$ that do not migrate outside the detector phase-space. The closure test is shown for a zoom to low multiplicity (left) and for the full range (right).

The cross check using RooUnfoldBayes tool was done using PYTHIA 2 for the matrix determination. Figure 48 shows PYTHIA 2 unfolded with PYTHIA 2 on 48(b) for the full range and on48(b) for the first bins. Figure 49 shows the closure test for unfolding EPOS LHC with the PYTHIA 2 matrix, for the full range on the left and for the first bins on the right side. As well as for the main method, the closure gets better when increasing the number of iterations. The ratio is within 5% for 5 iterations. This is slightly larger than using the main method.

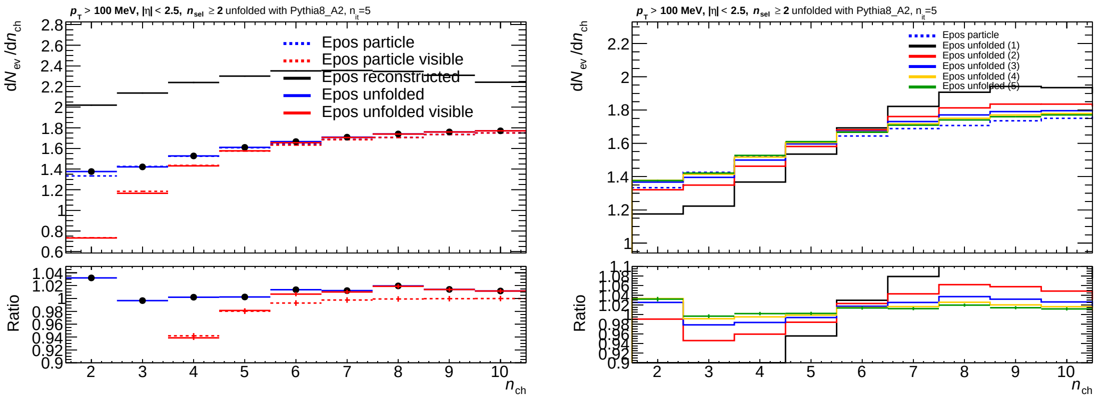

(a) (b)

Figure 45: Closure test using EPOS LHC for the input distribution and PYTHIA 2 for the construction of the unfolding matrix. The 45(b) shows how the results improve with increasing number of iterations.

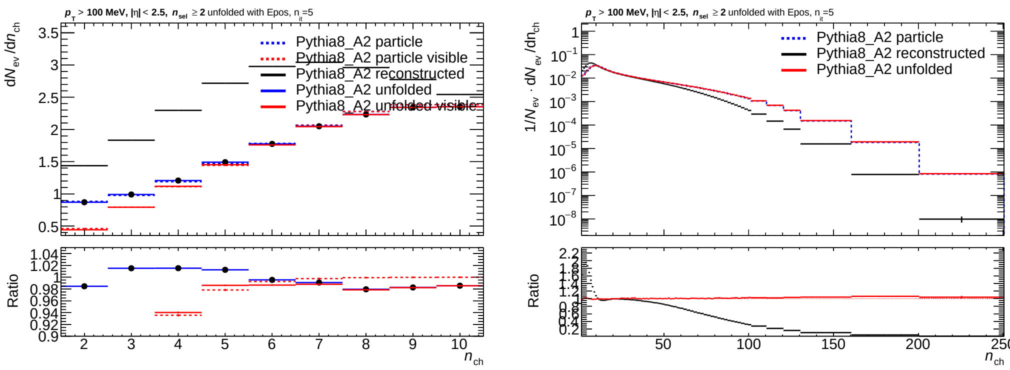

Figure 46: Closure test using PYTHIA 2 as the input distribution and EPOS LHC generator to construct the unfolding matrix. The label "visible" is used for the subset of events with $n_{\mathrm{sel}\geq 2}$ that do not migrate outside of the detector phase-space.

6.8.2.2 Unfolded data distribution and the systematics uncertainties

The data distributions are undolded following the same procedure as described above. In this case the number of iterations to achieve a good convergence in the n_{ch} distribution is small thanks to the relatively good modeling of the multiplicity distribution. The MC deviates from data for $n_{\mathrm{sel}} > 70$. The results can be seen in Figure 50 using different MC inputs as model for the unfolding matrix. This demonstrates a good stability of the unfolding procedure.

Figure 51 shows the data unfolded with the PYTHIA 2 matrix using RooUnfoldBayes, and the ratio on the bottom shows the agreement between the unfolded distributions using this method and using the main method.

The systematic uncertainties on the unfolded distributions are obtained by modifying the input distributions to be unfolded. And the results are compared to the

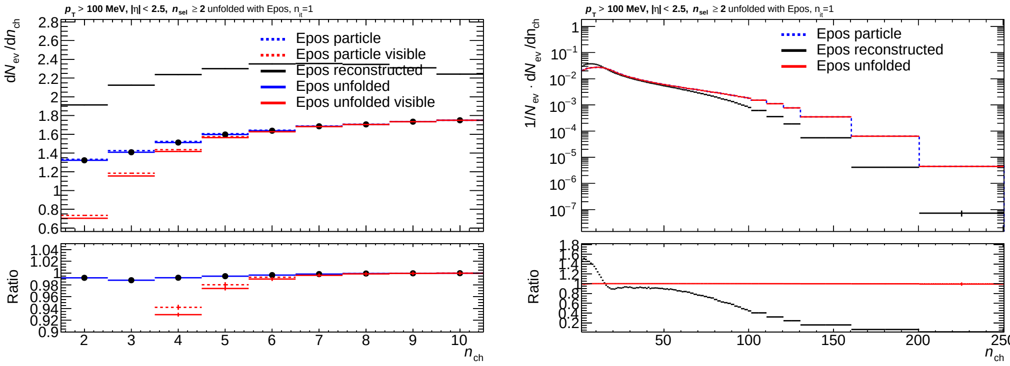

Figure 47: Closure test using EPOS LHC for both the input distribution and the generator to construct the unfolding matrix. The label ”visible” is used for the subset of events with $n_{\text{sel}\geq 2}$ that do not migrate outside of the detector phase-space.

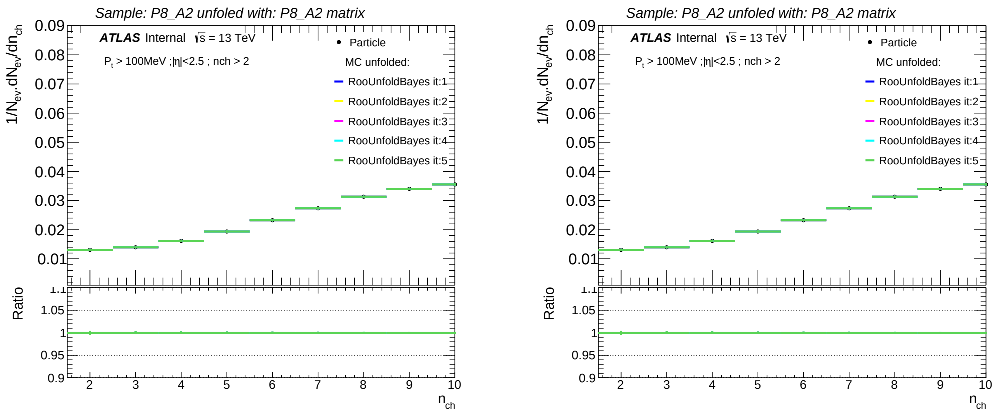

(a) (b)

Figure 48: Closure test using PYTHIA 2 for the input distribution and the construction of the unfolding matrix. 48(b) for the full range and 48(b) for the first bins.

unfolded nominal distribution. Previous studies [29] show that if the matrix is varied by the systematic uncertainties intead of the input distributions, similar results are obtained.

The systematic uncertanties are propagated starting from the observed n_{sel} spectrum in data and randomly adding and removing tracks. There are three systematic for the unfolded n_{ch} distribution. Each of them described bellow.

- *Track weight uncertainties* are added or removed tracks depending on the p_{T} and η of the existing tracks and their associated track reconstruction efficiency uncertainty $(\Delta\epsilon_{trk}(p_{\mathrm{T}}\ , \eta))$. For each track a random number is added(/removed), and if it is less/more than $\Delta\epsilon_{trk}(p_{\mathrm{T}}\ , \eta)$, n_{sel} is increasead/ decreased by one.

  The down variation is underestimated for low multiplicities because it is not

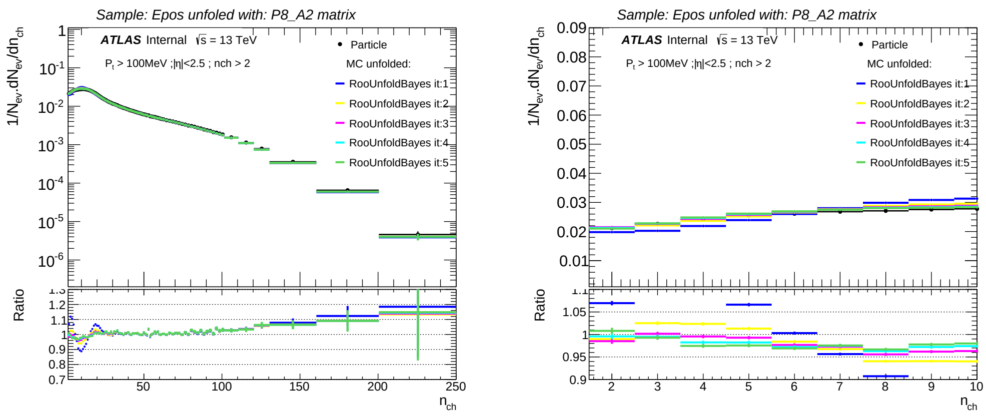

(a) (b)

Figure 49: Closure test using EPOS LHC for the input distribution and PYTHIA 2 for the construction of the unfolding matrix.49(a) for the full range and 49(b) for the first bins.

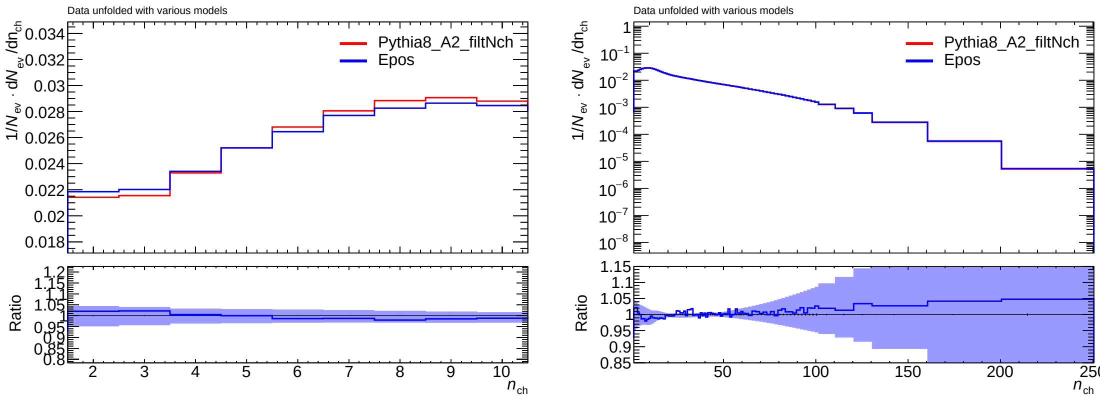

(a) (b)

Figure 50: Comparison for unfolding data PYTHIA 2 and EPOS LHC on 50(a) side for a zoom into the low n_{ch} and on 50(b) hand side for the full range.

possible to create tracks from $n_{sel} \leq 1$. Hence, the uncertainties created for the "up" variation is symmetrized.

This procedure is also used to propagate the uncertainties of the strange barions, secondaries tracks and out-of-kinematic-space tracks.

It is performed by adding or removing tracks depending on the p_{T} and η of the existing tracks and their associated track reconstruct efficiency uncertanty $(\Delta\epsilon_{trk}(p_{\mathrm{T}}\ ,\eta))$. For each track a random numer is added(/removed), and if it is less/more than $\Delta\epsilon_{trk}(p_{\mathrm{T}}\ ,\eta)$, n_{sel} is increasead/ decreased by one.

the "down" variation is under estimated for low multiplicities because it is not posible to create tracks from $n_{sel} \leq 1$. As a consecuence the uncertaty created

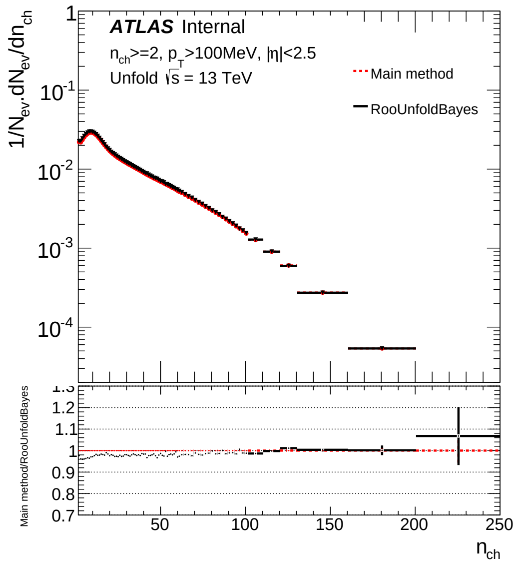

Figure 51: Data unfolded with PYTHIA 2 matrix using RooUnfoldBayes.

for "up" variation is symetrizated.

This procedure is also used to propagate the uncertainties of the strange barions, secondary tracks and out-of-knematic-space tracks.

Then, all the different components are added in quadrature, by asumming positive and negative desviations from the nominal values.

The systematic uncertainty due to de difference between data and MC is obtained by the variation of the tracking weight in the n_{sel} distribution. The variation is obtained using the difference in the average tracking efficiencies in data (delivered from the $p_{\rm T}$ spectrum) and MC.
The average tracking efficiency is the ratio of the sum over all reconstructed tracks in data and all true tracks. The denominator can be expressed by the sum of reconstructed tracks weighted by the track reconstruction efficiency ϵ_{trk}.

$$\bar{\epsilon_{trk}}(n_{sel}) = \frac{n(n_{sel})}{\sum_{i\epsilon_{sel}} \frac{1}{\epsilon_{eff,i}}}$$

and the ϵ_{trk} can be computed by, either integrationg over the $p_{\rm T}$ -spectrum in data or MC, considering the shape difference of the $p_{\rm T}$ -spectrum between them.

The average tracking efficiency is calculated as a function of $n_{\rm sel}$. This is shown in Figure 52 on the left hand side for data, PYTHIA 2 and EPOS LHC. As EPOS LHC is in between these two distributions, the difference between data and PYTHIA 2 was calculated and is shown on the right hand side. The difference went nearly up to 1% for large multiplicities and the absolute difference is taken as a systematic uncertainty for all n_{ch} dependent final distributions (n_{ch} spectrum and the mean p_{T} vs. n_{ch} distribution).

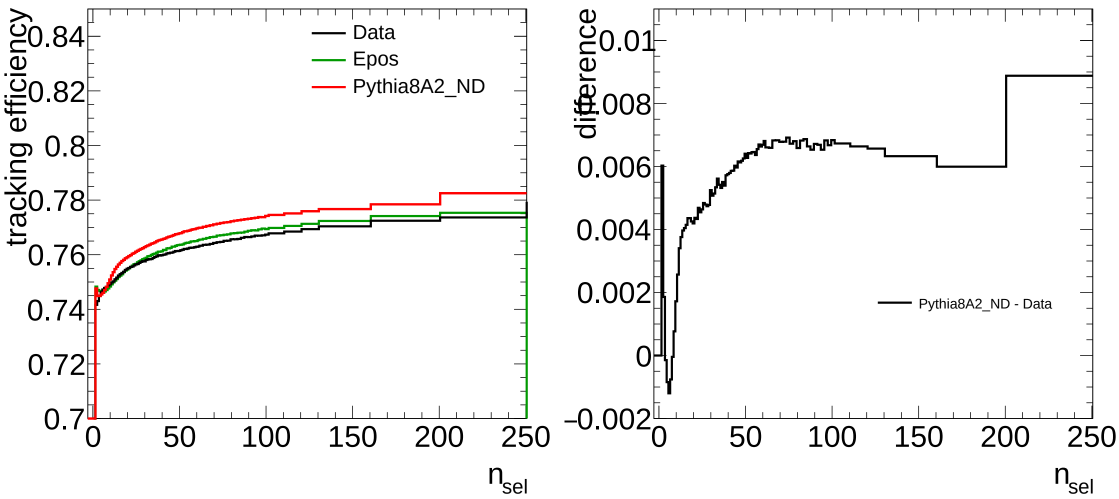

(a) (b)

Figure 52: Comparison of the average track reconstruction efficiency (as derived from MC and parametrised by p_{T} and η) of all tracks in data and MC as a function of $n_{\mathrm{sel}}$of the event from which the tracks are taken (52(a)). The difference of this average track reconstruction efficiency between PYTHIA 2 and data (52(b)).

- *Non-closure*
  A systematic uncertainty due to the non-closure is added: 4,2,2,2% in n_{ch}=2,3,4,5 respectivly

In Figure 53, one can see on the left hand side the breakdown of all the different systematics for unfolding data and using PYTHIA 2 as input model. On the right hand side, the total uncertainty and the contribution of the statistical uncertainty from the unfolding matrix are shown. The uncertainty band is not symmetric as the up and down variations from the various systematics have different influence on the shape of the n_{ch}distribution. The dominant systematics come from the material and the secondaries.

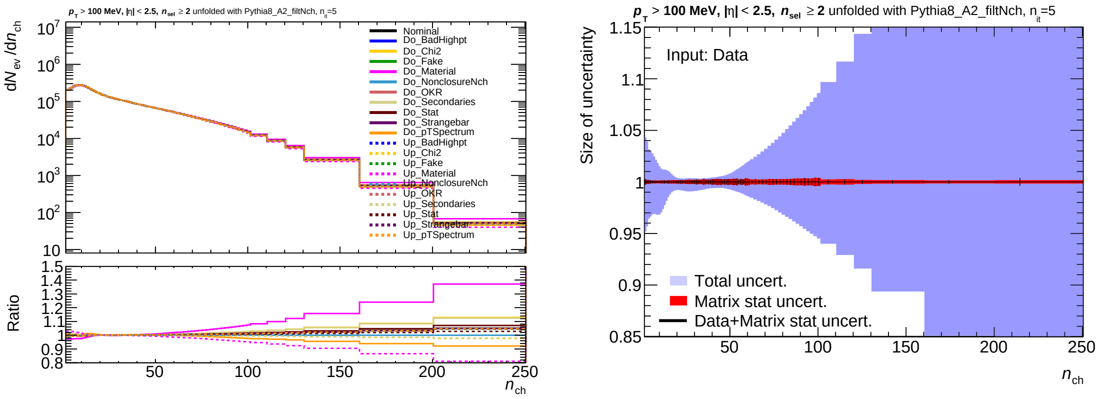

(a) (b)

Figure 53: Breakdown of all systematic uncertainties on 53(a). Uncertainty on 53(b) side show the contribution from the statistical uncertainty due to the unfolding matrix.

6.9 Correction to N_{ev}

The total number of events N_{ev} is defined as the integral of the n_{ch} distribution after all corrections are applied. Figure 54 shows the data unfolded distribution with the total systematics as a function of $n_{\mathrm{ch}}^{\mathrm{min}}$, denoting the selection on the particle multiplicity.

6.9.1 Unfolded data distribution and the systematics uncertainties

The systematics are obtained in the same way as for the n_{ch} distribution. Only the out-of-phase-space correction has an impact on N_{ev}. Figure 54 shows the total systematic error on the total number of events N_{ev} ($n_{\mathrm{ch}} > n_{\mathrm{ch}}^{\mathrm{min}}$).

The total number of events after unfolding is $N_{\mathrm{ev}} = 9.5 \cdot 10^6$ for the phase-space with a transverse momentum ≥ 100 MeV and $n_{\mathrm{ch}} \geq 2$ with a relative uncertainty of 0.5%.

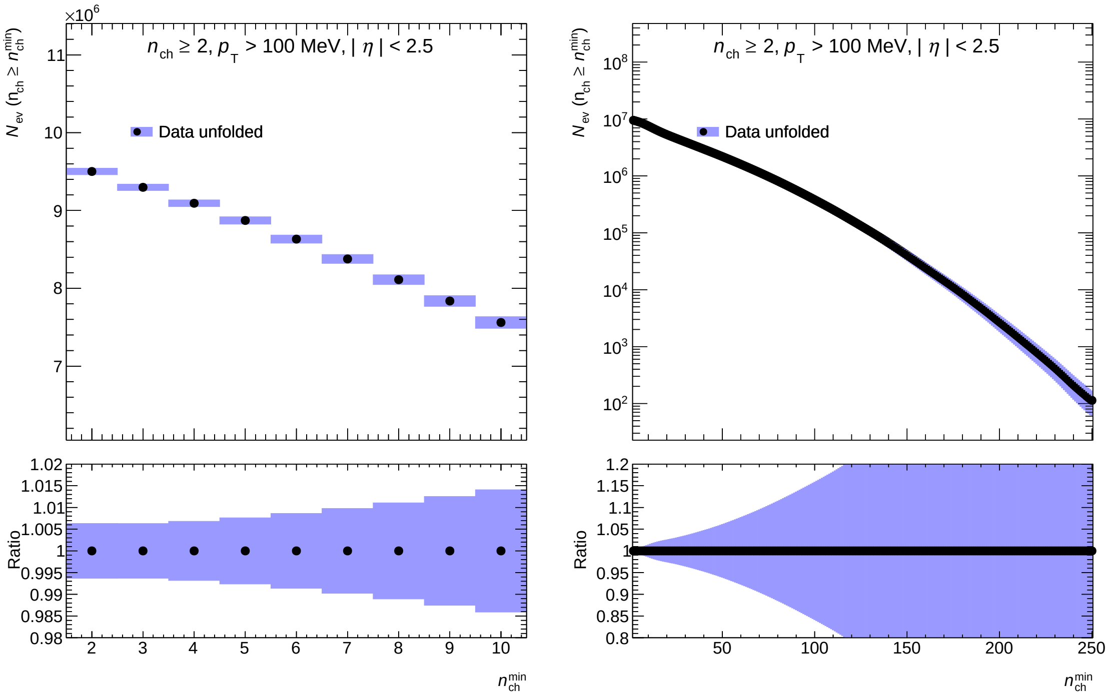

Figure 54: Total systematic error for $n_{\mathrm{ch}} > n_{\mathrm{ch}^{\mathrm{min}}}$ zoomed to low multiplicity (left) and for the full range (right).

6.10 Correction to $\frac{1}{N_{\mathrm{ev}}} \cdot \frac{\mathrm{d}N_{\mathrm{ch}}}{\mathrm{d}p_{\mathrm{T}}}$

First, the event weight is applied and the track are corrected by the track weight. Afterward, the unfolding procedure is performed using an unfolding matrix computed with PYTHIA 2 and 5 iterations were required to converge. The matrix is shown in Figure 55.

6.10.1 closure test for $\frac{1}{N_{\mathrm{ev}}} \cdot \frac{\mathrm{d}N_{\mathrm{ch}}}{\mathrm{d}p_{\mathrm{T}}}$

Two sets of closure tests were performed for the unfolding procedure on the p_{T} distribution. One uses the PYTHIA 2 sample to build the matrix and PYTHIA 2 and EPOS LHC for the p_{T} distribution to unfold. And the second one uses EPOS LHC to build the matrix and the same two generators for the p_{T} distributions. Figures 56 and 56 shows both cases respectively.

The general agreement is good. The overall non-closure comparing all closure tests gives a difference of 1% for the low p_{T} part and 3% for p_{T} >10 GeV which is then also used as additional systematic uncertainty for this distribution.

The same closure tests were performed in the cross-check procedure using RooUnfoldBayes. They are shown in Figure 58. On the left-hand side, the same generator is used for the matrix and for the input distribution. while on the right side PYTHIA 2 and EPOS LHC are used for the unfolding matrix and the distribution. Figure 58 shows a closure within 5% except for the first bin and lower than 2% for the other bins.

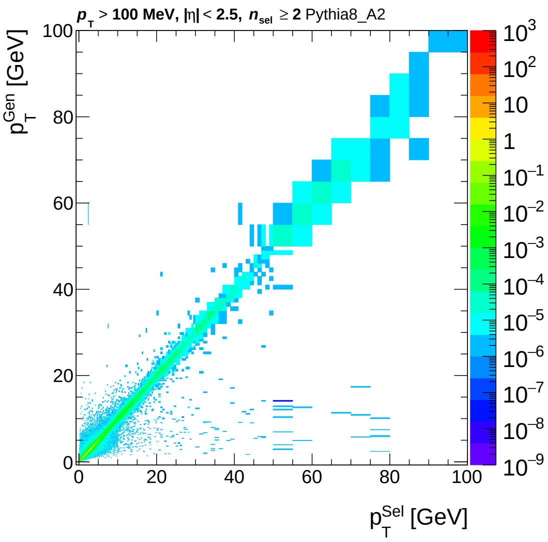

Figure 55: Unfolding matrix for p_T filled using PYTHIA 2.

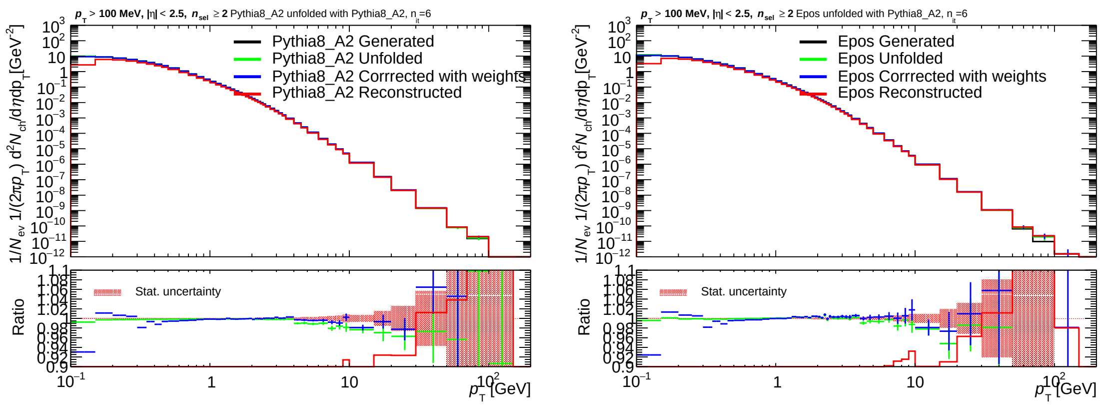

(a) (b)

Figure 56: Closure test derived using PYTHIA 2 for both the input and the matrix (56(a)). Closure test derived using EPOS LHC for the input and PYTHIA 2 for the matrix (57(a)). Track wise corrections are derived from PYTHIA 2 in both cases.

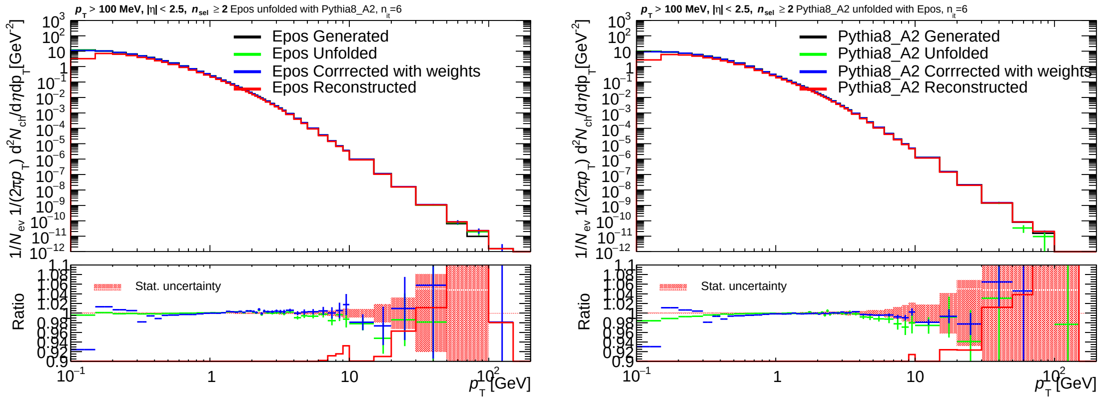

(a) (b)

Figure 57: Closure test using EPOS LHC as the input distribution and PYTHIA 2 generator to construct the unfolding matrix (57(a)) and PYTHIA 2 as the input and EPOS LHC as generator to construct the unfolding matrix (57(b)).

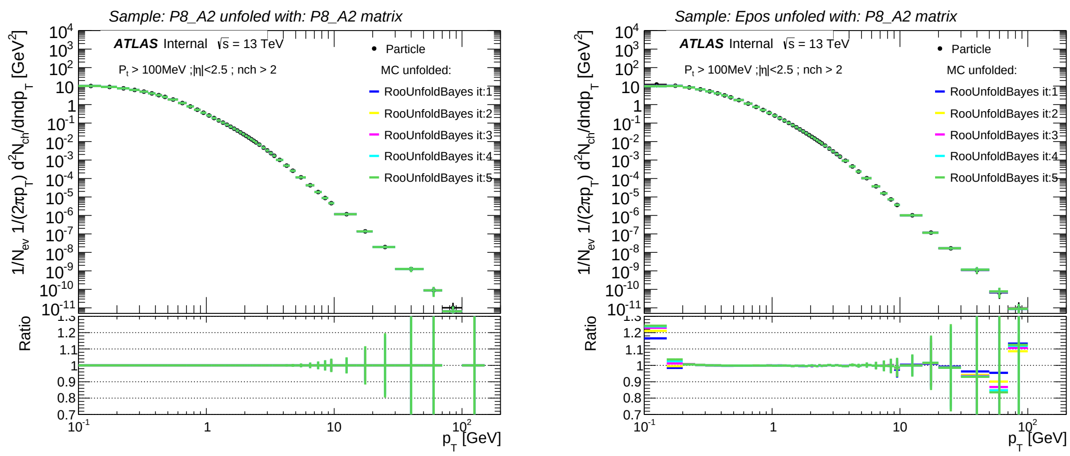

Figure 58: Closure test using PYTHIA 2 for both the input and the matrix on the left side. Closure test using EPOS LHC for the input and PYTHIA 2 for the matrix on the right side.

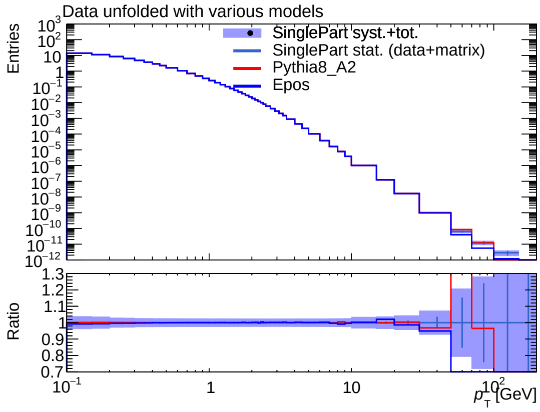

Figure 59: Data unfolded with PYTHIA 2 and EPOS LHC

6.10.2 Unfolded data distribution and the systematics uncertainties

The systematic uncertainties are computed modifying the input distribution with a variation of the tracking weights.

Then, for each variation, the p_T distribution obtained is used as input for the unfolding process. Finally, the differences with respect to the nominal distribution are used as systematic uncertainty.

Figure 59 shows the corrected data as a function of p_T. They are unfolded using different MC samples for the construction of the unfolding matrix. The agreement between the different distributions shows again a good stability of the unfolding procedure as the results are within the statistical error band when data are unfolded with PYTHIA 2.

The breakdown of the systematics is shown for the p_T distribution in Figure 60 on 60(a). The 60(b) shows the unfolded distribution with the systematic and the statistical uncertainties combined. For the low p_T region, the material systematic is again the most dominant. For high p_T , the total uncertainty comes mostly from the statistical uncertainty.

As it was done for the n_{ch} data distribution, Figuer 61 shows data unfolded with PYTHIA 2 matrix using RooUnfoldBayes as a function of p_T . The ratio on the bottom shows the agreement between the unfolded distributions using the RooUnfoldBayes method and using the main method.

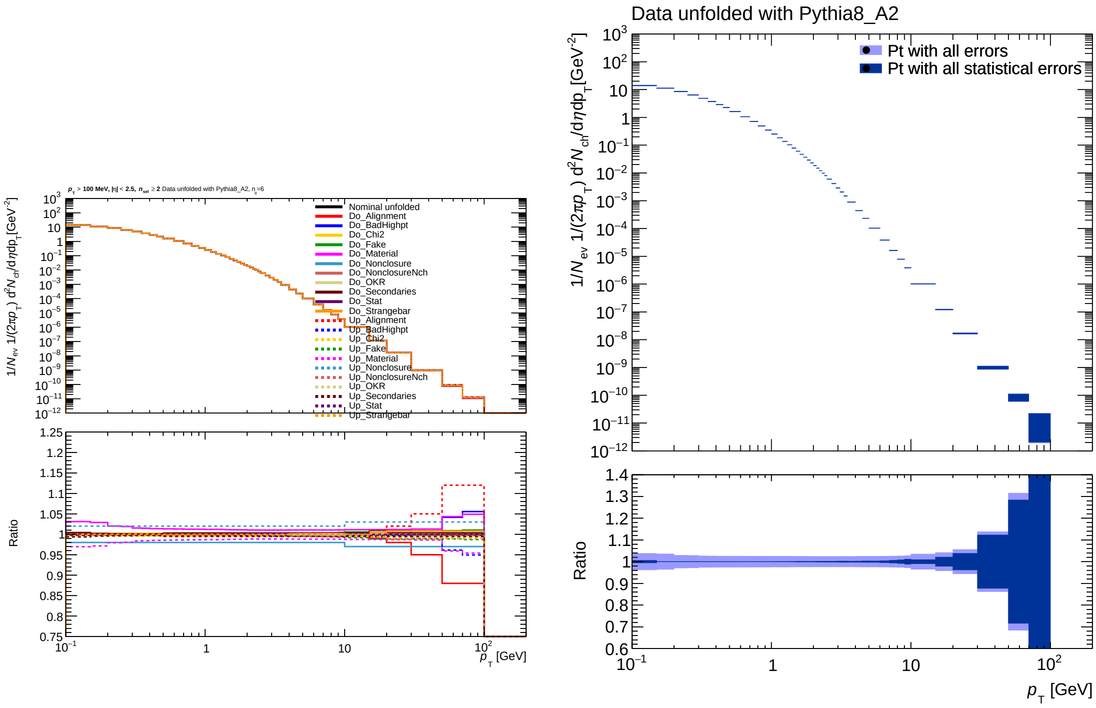

(a) (b)

Figure 60: Breakdown of different systematic variations of the tracking efficiency for the unfolded spectrum (60(a)) and unfolded distribution with the statistical and total systematic uncertainty (60(b)).

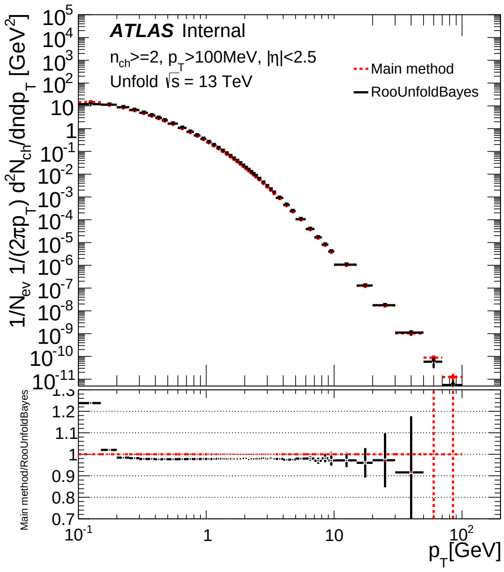

Figure 61: Data unfolded with PYTHIA 2 matrix using RooUnfoldBayes.

6.11 Correction to $\frac{1}{N_{\mathrm{ev}}} \cdot \frac{\mathrm{d}N_{\mathrm{ch}}}{\mathrm{d}\eta}$

As well as before, the event inceficiences are corrected by the event weight (Equation 37). Then, the tracks are corrected for the track reconstruction inefficiencies, the adition of non-primary tracks, the remamining strange barions and the out-of-kinematic range factors (Equation 38).

Afterwards, the η distribution is normalized by N_{ev} obtain in Section 6.9.

The unfolding procesure is not needed since the bin-to-bin migration is small due to a high η resolution.

The mean particle density at $\eta = 0$ is calculated as an average over 4 bins at the center of the distributions with a bin width of $\Delta\eta = 0.1$. The obtained charge particle density in the range $|\eta| < 0.2$ gives:

$$\frac{1}{N_{\mathrm{ev}}} \cdot \frac{dn_{\mathrm{ch}}}{d\eta}\bigg|_{\eta=0} = 6.422 \pm 0.002(\mathrm{stat.}) \pm 0.096(\mathrm{syst.})$$

6.11.1 Closure test

The closure test for the number of charged particles as a function of η was performed using PYTHIA 2 and EPOS LHC for the input distributions and to derive the tracking efficiency. The test shows a 1% of non-closure for the first and the last η bins and 0.4% for the central region. The results are shown in Figure 62.

6.11.2 data and the systematic uncertainties

The systematic uncertainties of the η distribution are estimated by the variation of the weights acording to their systematic uncertanties. For each systematic uncertainty, the distribution is normalized by N_{ev}, which is calculated for the same systematic vatiation.

On the left hand side of Figure 63, the breakdown of all relevant systematics is shown for the η distribution. The main systematic is again the material uncertainty, which has some bumpy features for high η . These are caused by the uncertainty coming from the PP0 region. The right hand side shows the corrected data distribution with the total systematic uncertainty.

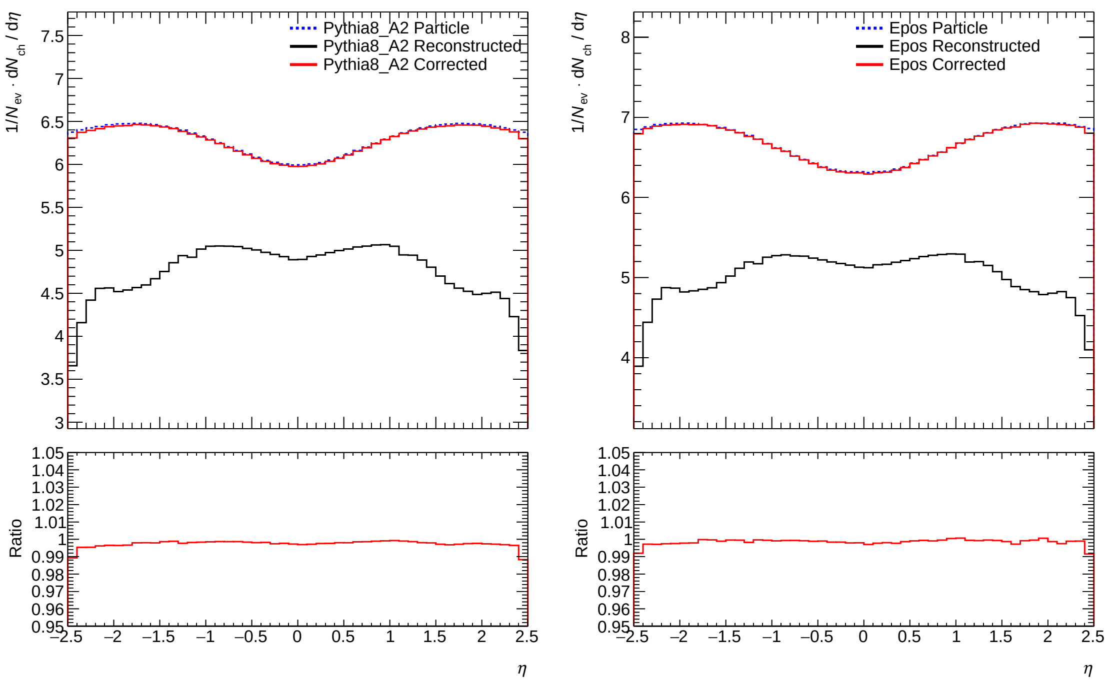

(a) (b)

Figure 62: Closure test for the η distribution using PYTHIA 2 (62(a)) and EPOS LHC (62(b)) as generator.

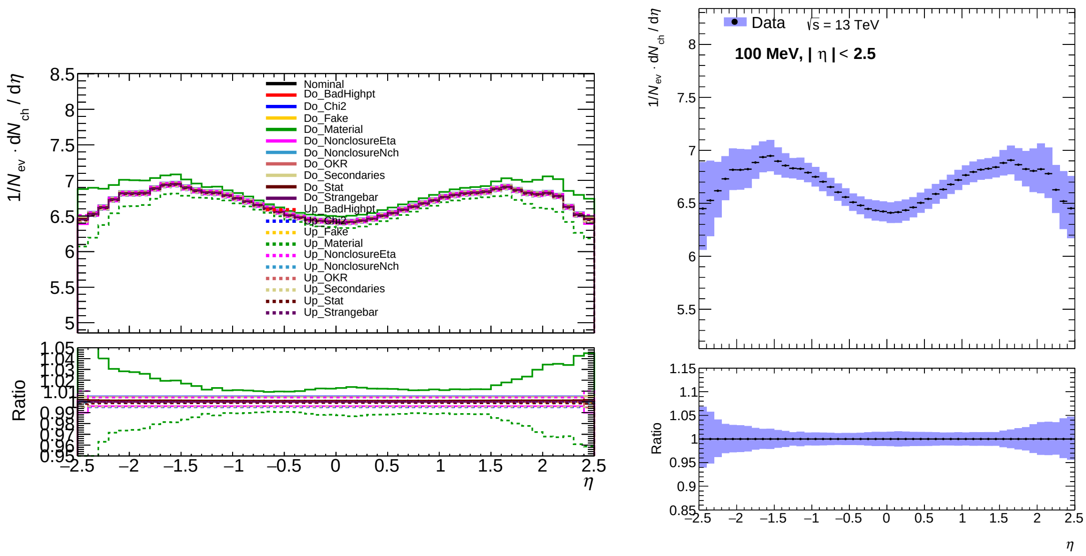

Figure 63: Breakdown of all different systematics for the η distribution (left), and the corrected data with the total systematic uncertainty (right).

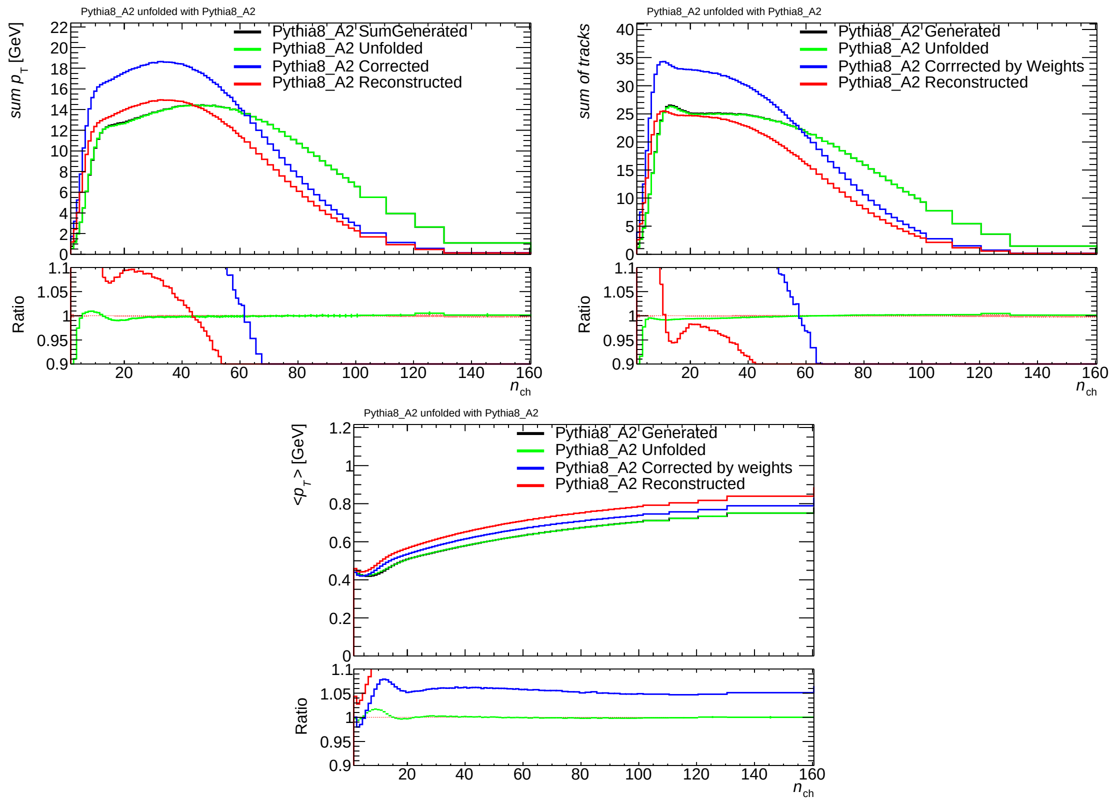

Figure 64: Closure test for $\sum_{\text{tracks}} p_{\text{T}}$ vs. n_{ch} and $\sum_{\text{tracks}} 1$ vs. n_{ch} as well as for $\langle p_{\text{T}} \rangle$ vs n_{ch} using PYTHIA 2 as input distribution and unfolding matrix.

6.12 Correction to $\langle p_{\text{T}} \rangle$ as a function of n_{ch}

The correction for the $\langle p_{\text{T}} \rangle$ vs. n_{ch} distribution is done separately for the two components $\sum_i p_{\text{T}}$ vs. n_{ch} and $\sum_i 1$ vs. n_{ch}. The sum is over all tracks and all events; the second sum represents the total number of tracks in each bin of n_{ch}. These two distributions are then divided to get the unfolded $\langle p_{\text{T}} \rangle$ distribution.

6.12.1 closure test

For the $\langle p_{\text{T}} \rangle$ vs. n_{ch} distribution, the closure test is first done for the two individual distributions. These and the resulting ratio are shown in Figure 64 using PYTHIA 2 for the input distribution and the construction of the unfolding matrix. In the resulting ratio plot, one can see that the unfolded distribution matches relatively good with the truth distribution. In the very first bins, 5< n_{ch} <15 one can see some differences up to 2%. The other closure tests confirm the difference of around 2% for n_{ch} <15. For higher multiplicity the ratio is flat and show very good closure.

6.13 Results

All corrected and unfolded distributions discussed are compared to several MC samples. These MC samples are PYTHIA 2 PYTHIA *Monash*, EPOS LHC and

QGSJET-II . The theoretical predictions are obtained by running RIVET. In the same way as for the tracking efficiency, strange baryons are excluded in the primary definition.

The unfolded distributions are shown in Figures 65, 66, 67 and 68.

The different MC generators do not present a good description of the n_{ch} unfolded data distribution. The best agreement between the unfolded data and the MC prediction comes from EPOS LHC generator. Same behavior as [29]. The agreement for η is good except for PYTHIA 2.

For the p_{T} distribution similar discrepancies as for the n_{ch} distribution can be seen for both analyses. The best description comes from the EPOS LHC generator. The agreement for the $\langle p_{\text{T}} \rangle$ vs. n_{ch} distribution shows similar agreement for EPOS LHC but larger disagreement for PYTHIA 2 and PYTHIA *Monash*. The description from QGSJET-II is very poor.

In order to compare the mean particle density with previous ATLAS measurements and other measurements, it is necessary to extrapolate the measured mean particle density at $\eta = 0$ in order to include the contribution of the strange baryons. For this the extrapolation factor is taken from the EPOS LHC generator and is 1.0121 $\pm$ 0.0002. The systematic uncertainties of the extrapolation factor is taken as the largest observed difference of PYTHIA 2 with respect to EPOS LHC where the extrapolation factor for PYTHIA 2 1.0086 $\pm$ 0.0002. This results to the following mean particle density:

$$\left.\frac{1}{N_{\text{ev}}} \cdot \frac{dn_{\text{ch}}}{d\eta}\right|_{\eta=0} = 6.500 \pm 0.002(\text{stat.}) \pm 0.099(\text{syst.})$$

Figure 69 shows the mean particle density including several ATLAS measurements only for the low p_{T} phase-spaces. Figure 70 shows the same distribution for all available ATLAS measurements so far. The uncertainty includes the statistical as well as the systematic uncertainty for the measured density and for the extrapolated factor which are added in quadrature.

Overall the agreement for PYTHIA 2 does not seem as good as it was studied in the baseline analysis. From this plot, the modeling of QGSJET-II and EPOS LHC seems quite well described even if there are description problems for other distributions as seen from the mean transverse momentum distribution.

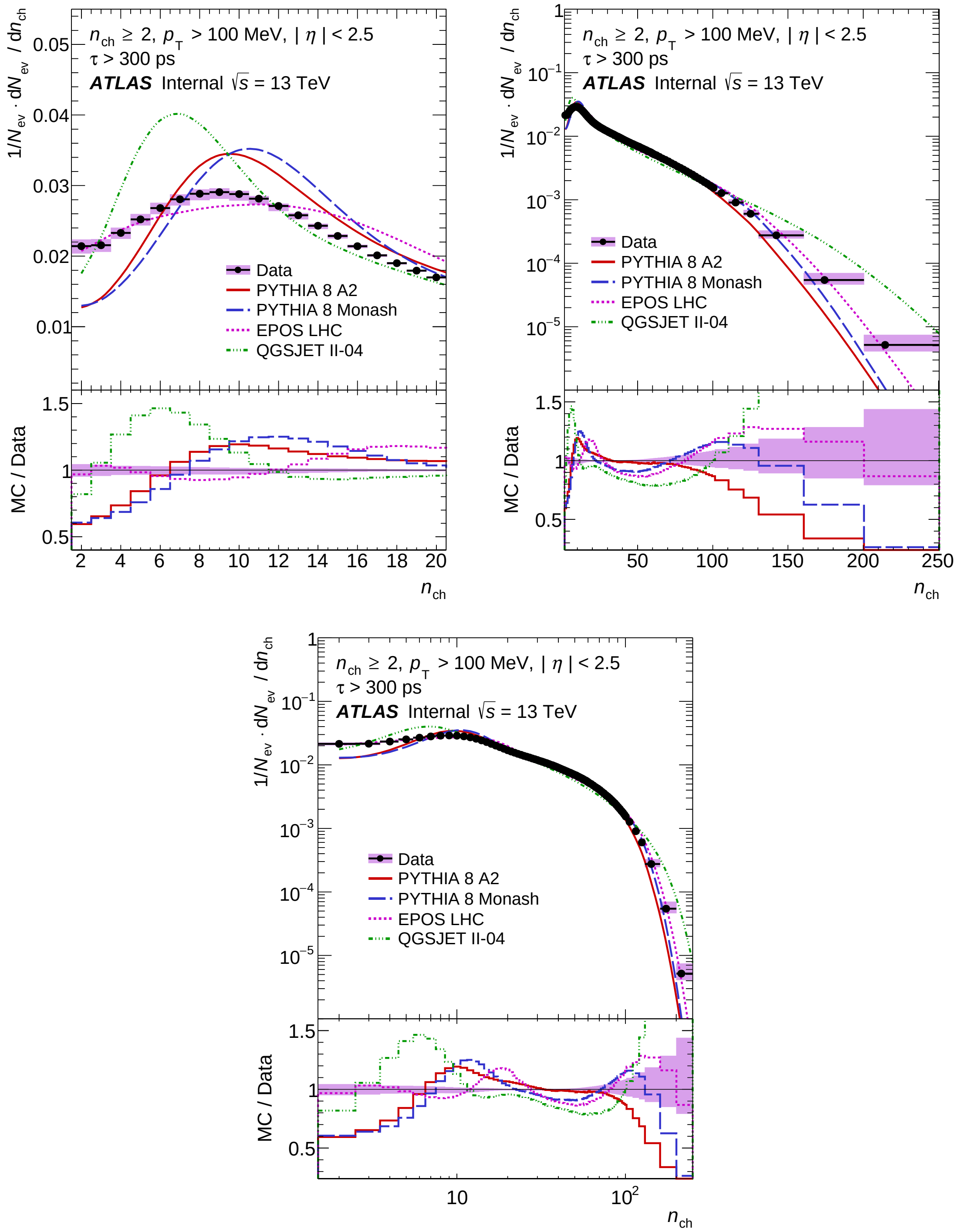

Figure 65: Multiplicity distribution of primary charged particles for a zoom into low multiplicities up to 20 (top left), for higher multiplicities up to 140 (top right) and for the full range used in the analysis (bottom).

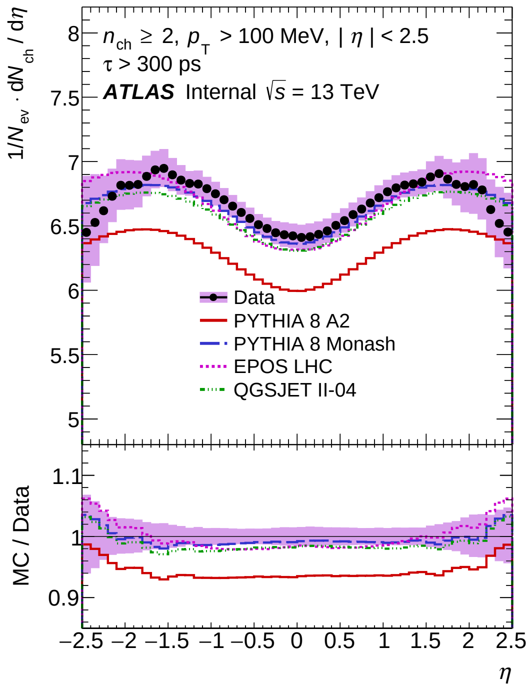

Figure 66: Pseudorapidity dependence of the charged particles.

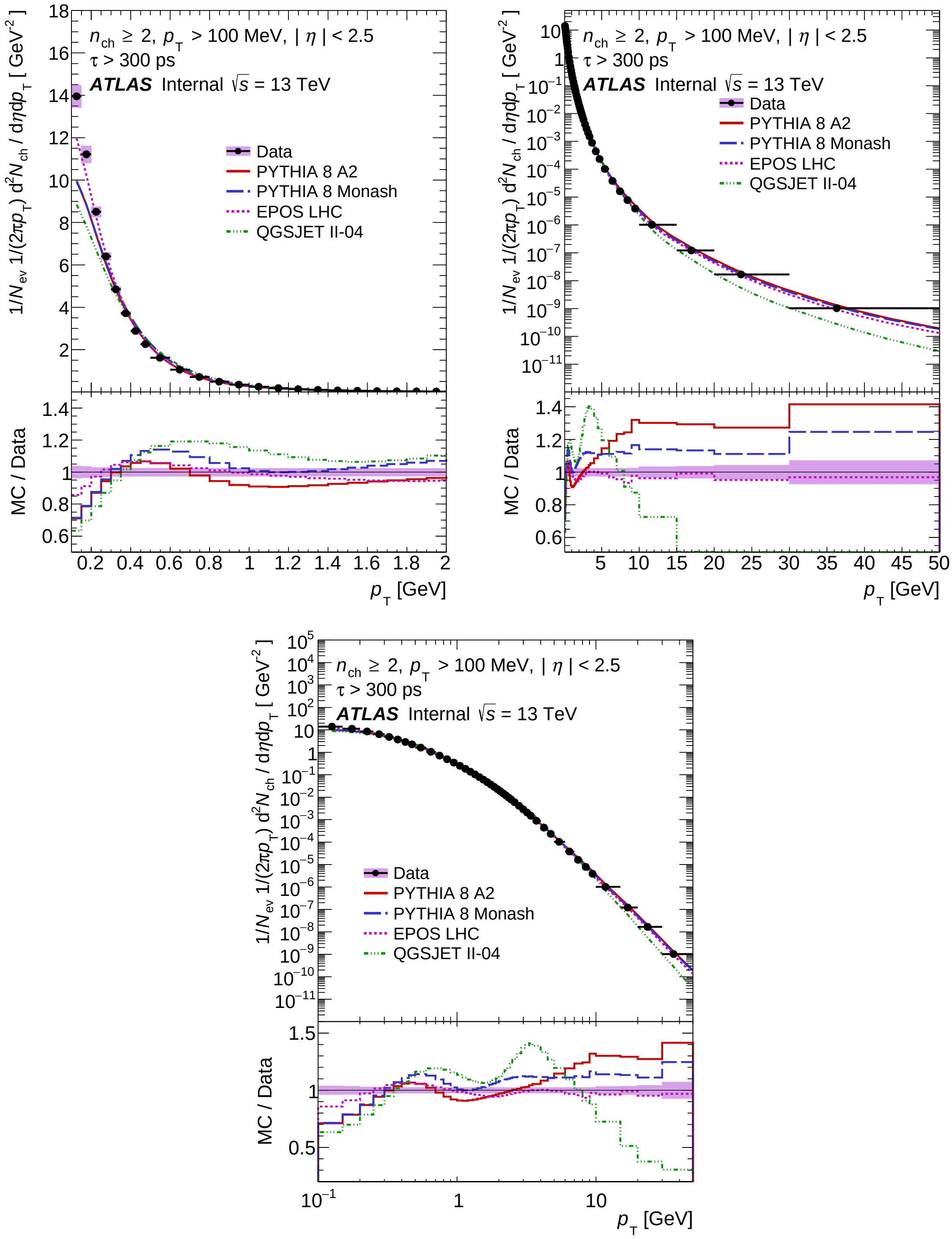

Figure 67: The rate of charged particles as a function of transverse momentum for a zoom into the low p_T region up to 2 GeV (top left), for transverse momentum for up to 50 GeV (top right) and for the full range used in the analysis (bottom).

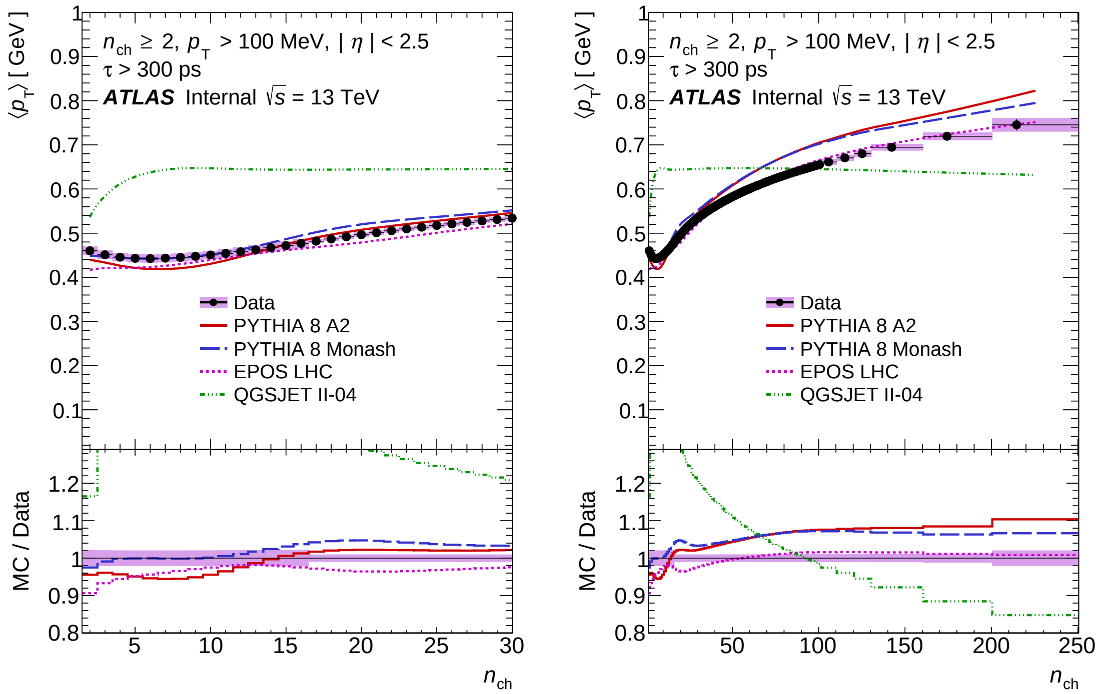

Figure 68: Mean transverse momentum per event as a function of event multiplicity for a zoom into the low n_{ch}region up to 30 (left) and for the full range (right).

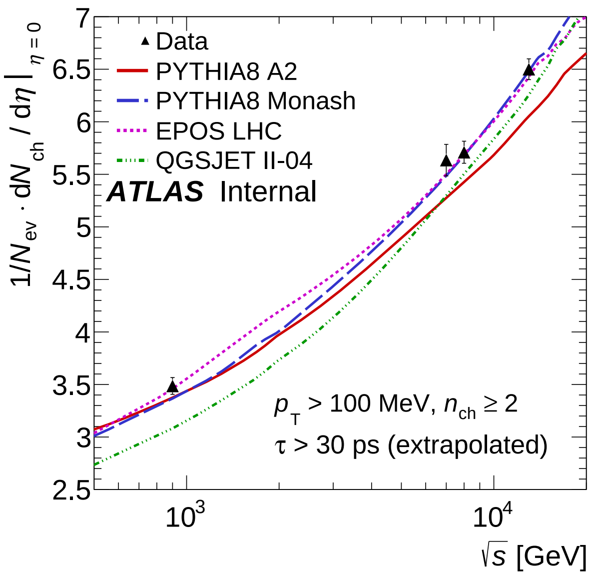

Figure 69: Summary plot of mean particle density at $\eta = 0$ including several ATLAS measurements for low p_{T} at different $\sqrt{s}$ energies. The 13 TeV result is extrapolated by a factor of 1.012 which is the fraction of strange baryons predicted by EPOS LHC.

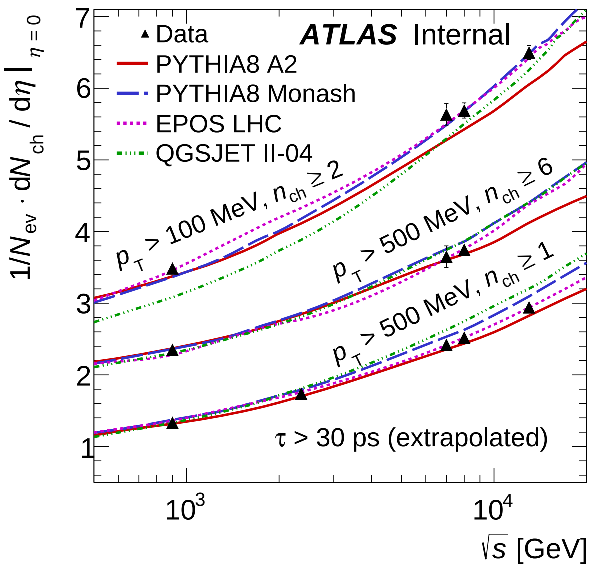

Figure 70: Summary plot of mean particle density at $\eta = 0$ including several ATLAS measurements for different phase-spaces at different $\sqrt{s}$ energies. The 13 TeV result is extrapolated by a factor of 1.012 which is the fraction of strange baryons predicted by PYTHIA *Monash*.

7 Search for resolved dijet resonances

7.1 Motivation and analysis strategy

ATLAS and CMS have engaged in a program of complementary searches of new particles decaying to pairs of jets [75]. Any strongly interacting new particle directly produced via quarks and gluons and later decaying to them, will generate a pair of jets. Thus the dijet signatures are a simple way to search for several possible new physics models. The increasing collision energy allows searches to access higher mass ranges for possible new physics. However, higher energies comes at a cost; lower masses and smaller hypothesised couplings are particulary chalenging due to the trigger prescales required to control increasing instantaneous luminosities. Dijet searches at 13 TeV have excluded resonances beginning at a mass of 1.2 TeVto 5.2 TeV [46, 47], 0.2TeV to 6 TeV [48], and an 8 TeV dijet search [38] beginning from 250 GeV to 950 GeV was strongly limited by these same trigger prescales. The trigger-level analysis (TLA) evades trigger bandwidth restrictions by recording only minimal event information but at a very high rate [43].

The presented analysis has a diferent approach. It uses events produced in asociation with a high-p_{T} initial-state radiation photon, that can be used for triggering. This allows the resonance to be reconstructed from lower-p_{T} jets that would not pass an unprescaled single-jet trigger. This analysis considers then, two jets and one photon for the final state (see Figure 71).

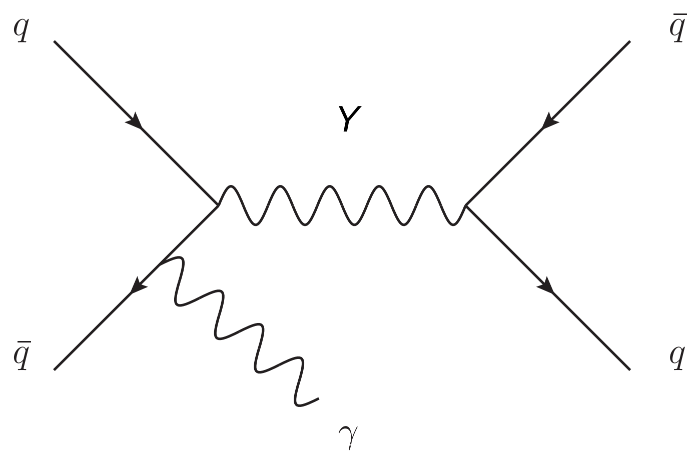

Figure 71: Example Feynman diagram for a generic new resonance Y produced in association with a photon and decaying to two jets.

A leptophobic axial-vector mediator Z' particle is used as a benchmark for interpretation [62]. For some models of Beyond the Standard Model (BSM) [82, 53, 54], new particles are expected to preferentially decay to third-generation quarks. Sensitivity to such models can be dramatically improved by requiring that one or both of the jets from the resonance decay be *tagged* as originating from a b . The *b-tag* channel was not present in the previous studies [45].

This study uses data collected with the ATLAS detector during 2015–2017 at a centre-of-mass energy of 13 TeV. The invariant mass distribution of a selected pair of jets (M_{jj}) in each event is compared to a smooth SM-only background prediction taken from a fit. A model-nonspecific search phase compares the data to the expected background. In case the search phase does not show any significant excess, limits are then set on the benchmark Z' models for signal masses and on generic gaussian shaped hipotesis.

The analysis is presented as follows. It starts with a description of the datasets used and the Monte Carlo samples used for background and signal in Section 7.2. The object reconstruction and calibration are explained in Section 7.3, while Section 7.6 details the event selection. The *b-jet* tagging procedure is described in Section 7.7, including studies of the choices made for this analysis. In addition various kinematic checks on the dataset after selection and a comparison between data and each MC period is shown in Appendix B.3. Section 7.8 shows studies of the signal kinematics and the impact of selection and morphing on the template shapes. The background modelling procedure with all relevant studies is presented in Section 7.9, while all systematic uncertainties are explained in Section 7.10. Finally, Section 7.11 gives the results of the analysis.

7.2 Data and Monte Carlo samples

Data collected between 2015 and 2017 as well as simulated events from a range of Monte Carlo generators were used.

7.2.1 Data

Collected data form *pp* collision at the ATLAS detector during 2015 and 2017 inclusive; with a centre-of-mass energy of 13 TeVwas used for the analysis. Two selections are used (see Section 7.6), one corresponding to a luminosity of 79.8 $fb^{-1}$and the other of 76.6 fb^{-1}. After removing the events with unsuitable beam conditions or some inactive portions of the detector using Good Runs List[15] During 2016 and 2017, the topoclustering thresholds and pileup conditions changed. This modified the pileup profile for these year datasets (see Section 3.3). Hence, various cross-checks comparing 2016 to 2017 data, as well as both datasets to corresponding MC campaigns are include in Appendix B.3.

7.2.2 Monte Carlo samples

The Monte Carlo samples corresponding to background processes are only used for the studies of the analysis before unblinding, to optimize the analysis selection and to determine the reported limits.

All MC samples used in this analysis are produced with a GEANT 4-based simulation, with additional pile-up interactions in each simulated event modeled by adding multiple soft *pp* collisions generated by Pythia 8.165 [105] with the MSTW2008 LO PDF and AU2 tune [32]. After event generation and the addition of pile-up, the response of the ATLAS detector to particles passing through

[15] Aplication used in ATLAS to select the well beviour runs

the detector elements is simulated with the GEANT4 toolkit [6] and events are reconstructed using the same software used to reconstruct events in data.

Background processes

Background processes with a photon and 1, 2, or 3 jets were simulated using SHERPAgenerator. The details of these samples are described in Table 6.

Generator	DSID	Simulation details
SHERPA	361039–361062	FS, NLO, MC16a+MC16d

Table 6: Simulated samples used for background studies.

Signals

The main benchmark model is a Z' axial-vector mediator signal consistent with recent recommendations from the ATLAS-CMS Dark Matter (DM) Forum [4].

This benchmark signal is used in the search and limit-setting phases of the analysis and for testing the sensitivity of potential resonant signals on the search phase.

The choice of this benchmark signal is motivated by the role that searches for dijet resonances play in constraining possible interactions between dark matter, or a "dark sector", and the Standard Model. In this analysis, we consider a pure axial-vector leptophobic Z' model in the specific scenario [57], where the searches are in regions of parameter space where the decay of the Z' to invisible particles is kinematically suppressed.

In this model, the Z' arises from a simple extension of the Standard Model (SM) with an additional $U(1)$ gauge symmetry and a Dirac fermion Dark Matter particle that has charges only under this new group. Assuming that some SM particles are also charged under this group, the Z' can mediate interactions between the SM and DM. The DM particle χ has a mass m_χ. The spin-1 Z' has mass M_{med}.

The Dark Matter Forum [63] report models with vector or axial-vector couplings between the spin-1 mediator Z' and SM and DM fields, with the corresponding interaction Lagrangians:

$$\mathcal{L}_{\text{vector}} = g_{SM} \sum_{q=u,d,s,c,b,t} Z'_\mu \bar{q}\gamma^\mu q + g_{DM} Z'_\mu \bar{\chi}\gamma^\mu \chi$$

$$\mathcal{L}_{\text{axial-vector}} = g_{SM} \sum_{q=u,d,s,c,b,t} Z'_\mu \bar{q}\gamma^\mu \gamma^5 q + g_{DM} Z'_\mu \bar{\chi}\gamma^\mu \gamma^5 \chi.$$

The parameters in the model are thus

$$\{\ g_{SM},\ g_{DM},\ m_\chi,\ M_{med}.\} \tag{42}$$

where g_{SM} is the coupling of the Z' mediator to quarks, g_{DM} is its coupling to the Dark Matter fermion, m_χ is the mass of the Dark Matter fermion and M_{med} is the Z' mass.

The two most relevant parameters of this model in the dijet search are the coupling of the Z' to quarks as it drives the intrinsic width of the resonance and the Z' mass. These two parameters are scanned to obtain the signal grid used for the limit setting. The Dark Matter mass is fixed at 10 TeV and the coupling to DM to 1.5. Changing the DM-related parameters has no effect on the width of the resonance in this search since with this choice the mediator cannot decay directly to DM. Nevertheless, a dijet search can still probe a dark interaction even though the DM particle is inaccessible to colliders.

The signal samples have been generated for 5 mass points. These have been produced with at least 20,000 events with coupling constant $g_{SM} = 0.1, 0.2, 0.3$ and 0.4. Given that this analysis is sensitive to samples with $g_{SM} \sim 2$, higher couplings than the ones produced are not necessary since the corresponding mass points would be already excluded.

The signal samples have been generated using the Madgraph generator[10] with the NNPDF2.3 LO PDF [52] and the A14 tune [35], and hadronic showers are produced with PYTHIA 8. To further increase statistics, a truth-level filter is applied to the photon p_{T}. Two sets of samples are produced: one set with this filter set at $p_{\mathrm{T}}^{\gamma} = 100$ GeV and a second with the filter at $p_{\mathrm{T}}^{\gamma} = 50$ GeV. These are used with the two different analysis triggers (see Section 7.6) to ensure high statistics for each mass point while keeping all appropriate events. The simulated Z' signals used can be found in Tables 19 and 20. As the tables show, only one coupling value was generated with the 50 GeV filter. The width is calculated as:

$$\Gamma_{\mathrm{Med}} = \Gamma_{\mathrm{DM}} + \Gamma_{\mathrm{SM}} \tag{43}$$

where:

$$\Gamma_{\mathrm{SM}} = \sum_{q \in (m_q < \frac{m_{\mathrm{Med}}}{2})} \frac{3 m_{\mathrm{Med}} g_{SM}^2}{12\pi} \times \left(1 - \frac{(2m_q)^2}{m_{\mathrm{Med}}^2}\right)^{3/2} \tag{44}$$

and

$$\Gamma_{\mathrm{DM}} = \begin{cases} \frac{m_{\mathrm{Med}} g_{\mathrm{DM}}^2}{12\pi} \times \left(1 - \frac{(2m_{\mathrm{DM}})^2}{m_{\mathrm{Med}}^2}\right)^{3/2}, & \text{if } m_{\mathrm{DM}} < \frac{m_{\mathrm{Med}}}{2} \\ 0, & \text{otherwise} \end{cases} \tag{45}$$

Figures showing signal width in the reconstructed samples, as well as cross sections, can be found in Section 7.8. This analysis is sensitive to couplings at the level of 0.2 and will only set limits in the regime where the width is less than 15% of the resonance mass. Larger widths are not possible to fit within this framework based on previous experience. Signals with larger widths cannot be discovered by the search phase, and attempting to fit for these larger signal can potentially bias the background fit. A similar effect is seen in other di-jet searches ([47] and [43]). For much wider signals, it would also be necessary to account for interference with the standard model.

7.3 Objects selection

This analysis works with two objects: photons and jets. The reconstraction requirement of each one are described below.

Photon

The photons used for the analysis are reconstructed following the ATLAS standard procedures and calibrated using the recommendation from the EGAMMA group. They have to satisfy the following criteria:

- Photon $p_{\mathrm{T}} > 10$ GeV and $|\eta| < 2.37$, and at least one photon of $p_{\mathrm{T}} > 95$ GeV to ensure trigger efficiency descrived in Section 7.4
- The *tight* working point is used for photon identification in accordance with the recommendations [11].
- The photon passes the standard object quality cuts defined by the EGamma group recomentations.
- The photon must pass an isolation requirement. This specifies that the sum of energies of all EM-scale topoclusters in a $\Delta R < 0.4$ cone around the photon must satisfy the following: `topoetcone40` < 2.45 GeV $+ 0.022 \cdot E_{\mathrm{T}}^{\gamma}$. An additional requirement is placed on tracks such that the sum of track p_{T} in a $\Delta R < 0.2$ cone around the photon must be a small fraction of the total photon p_{T}: `ptcone20`$/p_{\mathrm{T}}^{\gamma} < 0.05$

Jet

Anti-kT R =0.4 jets are used for the analysis and are calibrated following recomendations of the JetEtMiss group.

Jets are retained which pass the following criteria:

- Jet p_{T}> 25 GeV, falling within the region typically considered well-calibrated
- Jet $|\eta| < 2.8$, ensuring that the most forward jets stay fully contained within the HCAL endcap
- All jets selected by the above must pass *loose* jet cleaning requirement [39] which is designed to provide an efficiency of selecting jets from pp above 99.5% for p_T >20 GeV.
- Jets with 25 GeV $< p_{\mathrm{T}} < 60$ GeV and $|\eta| < 2.4$ must pass the recommended jet vertex tagging (JVT) selection. This removes jets with a large fraction of tracks originating from pileup vertices. Details can be found in [36].

7.4 Trigger studies

Several triggers were studied in this analysis, however only those that present the best performance are discused here. For an easier description we will divide them into two groups: the single-object and the multi-object triggers. For both cases, the aim is to increase the sensitivity and the inclusion of a larger M_{jj} range.

The trigger studies were done in two stages, before and after the optimization of the cut selection[16].

In addition, all the turn-on curves were fitted by an *error function* (Equation 46) of three free parameters (p_0, p_1 and p_2) to get the point where it reaches the 99% of the efficiency from the fit.

$$p_0 \cdot (1 + erf(\frac{x - p_1}{\sqrt(2)p_2})) \tag{46}$$

single-object trigger

The lowest unprescaled single-photon trigger across 2015, 2016 and 2017 datasets, was the `HLT_g140_loose`. Thus, their efficiency with respect to the off-line transverse momentum of the leading photon is studied by bootstrapping from the `HLT_g60_loose` trigger. This means that the efficiency is determined by taking the ratio of events passing both triggers from those that passed only the reference trigger, which is fully efficient for isolated photons passing tight identification and $p_\mathrm{T} > 70$ GeV.

As the thresholds of this trigger did not change at any point in 2015–2017, and as this photon trigger is relatively pileup insensitive, the performance was found to be essentially identical for the three years and the turn-on curve for this entire period is shown in Figure 72(a).

The trigger efficiency was computed again after optimizing the y^* [17] cuts and determining a lower M_{jj} boundary from the fitting procedure. In this way the most accurate evaluation of trigger efficiencies were made by looking only at the events which are relevant to the analysis. The trigger efficiency for the single-photon trigger with analysis cuts applied is presented in Figure 72(b).

multi-object trigger

The lowest unprescaled multi-object trigger studied in this analysis were `HLT_g75_tight_3j50noL1_L1EM22VHI`, for 2016, and `HLT_g85_tight_L1EM22VHI_3j50noL1`, for 2017. These triggers require at least three HLT jets with $p_\mathrm{T} > 50$ GeV and one photon with $p_\mathrm{T} > 75$ or 85 GeV respectively, passing the tight identification criteria (descrived in Section 5.2), at the on-line level.

The efficiency of the trigger with respect to the offline reconstruction is studied by bootstrapping from the `HLT_g60_loose` trigger. which is fully efficient for the full set of events passing the multi-object ("compound") trigger. The efficiency was studied as a function of the transverse momentum of the leading isolated photon passing tight identification. It is important to highlight that this kind of trigger requires two types of objects: photons and jets, therefore their efficiencies are related to the respective thresholds. The jet component of the trigger reaches a plateau when the subleading jets have a $p_\mathrm{T} > 65$ GeV. So, this condition is also required to build the

[16] Off-line selection cuts defined to optimize the relationship between signal and background, see Section 7.6

[17] y^* is defined as the diference in the pseudo-rapidity between the leading and the sub-leading jets, it is described in Section 7.5

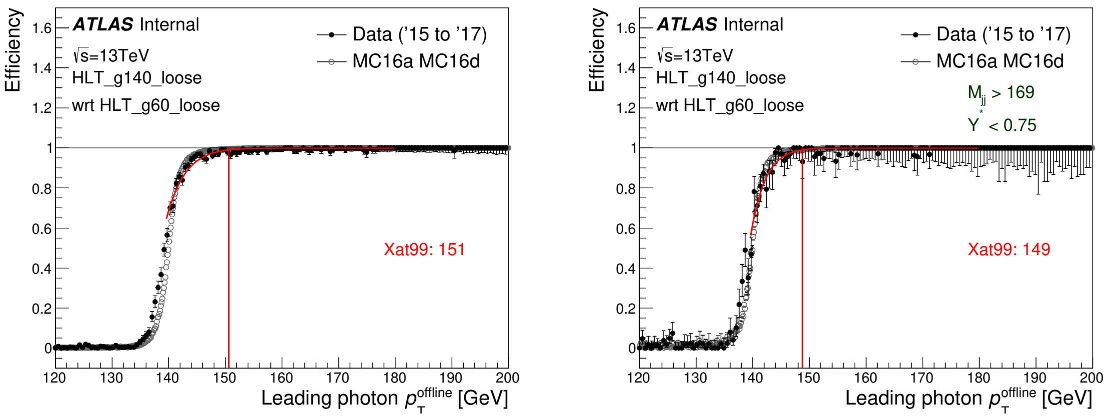

(a) before analysis selection

(b) after analysis selection

Figure 72: 72(a) shows the turn-on curve in 2015–2017 data for the `HLT_g140_loose` trigger. The efficiency is found with reference to the prescaled `HLT_g60_loose` trigger, which is fully efficient within the p_{T}range considered. `HLT_g140_loose` is found to be $> 99\%$ efficient for leading photon $p_{\mathrm{T}} > 151$ GeV. Same for 72(b) but with all the analysis cuts are applied. It is reaches the plateau for leading photon $p_{\mathrm{T}} > 149$ GeV.

efficiency (A deeper description of the combined trigger requirements can be found in Appendix B.4).

Figure 73(a) shows the efficiency after requiring that the subleading jet p_{T} is greater than 85 GeV. As this trigger requiers two types of objects, photon and jets, it's efficiency depends on these objects reching their respective plateau.

As well as before, the turn-on curve versus photon p_{T} was re-checked after application of the final analysis cuts and the results are shown in Figure 73(b).

A similar behaviour is observed for the `HLT_g85_tight_L1EM22VHI_3j50noL1` trigger in the 2017 dataset, so the same procedure was developed. Figure 74(a) shows the efficiency of this trigger with no kinematic selection and Figure 74(b) shows the turn-on curve versus photon p_{T} after applying all analysis selection cuts.

To combine 2016 and 2017 data, a single unified set of cuts is defined such that both triggers will be on their plateaus. This requires an off-line isolated photon of $p_{\mathrm{T}} > 95$ GeV passing tight identification and two jets of $p_{\mathrm{T}} > 65$ GeV. Nonetheless it is clear from Figure 74(b) that the analysis selection does not achieve truly full efficiency even after application of these jet and photon p_{T} cuts. To account for this, an uncertainties is estimated by looking at trigger efficiency as a function of M_{jj} . For details on this uncertainty see Section 7.10.

Figure 75 compares the shapes of the background distributions using a single-photon triggering strategy versus the multi-object triggering strategy. The sensitivities of the two analysis strategies are shown in Figure 76 (details in Section 7.7). Two key points are illustrated by these plots:

1. The single-photon triggering strategy leads to a sharper M_{jj} distribution

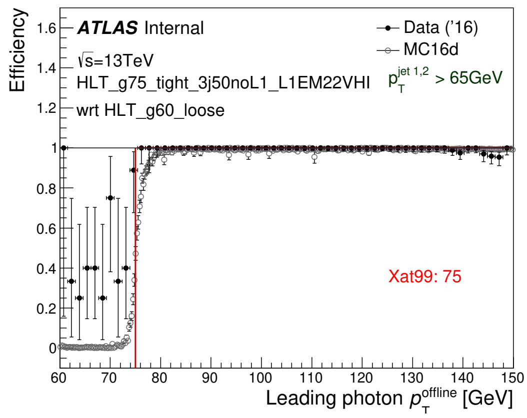

(a) before analysis selection

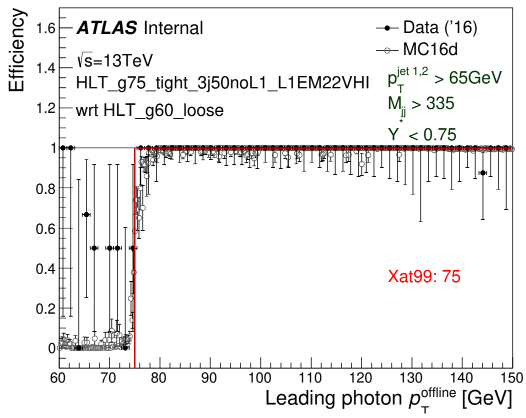

(b) after analysis selection

Figure 73: 73(a) shows the efficiency of the dijet+γ trigger as a function of leading isolated photon passing tight identification criteria. The subleading jet p_{T} is required to be above 65 GeV. The efficiencies in 2016 data and mc16a are shown. Full efficiency occurs at 80 GeV. 73(b) same but with all the final analysis cuts in y^* and M_{jj} are applied.

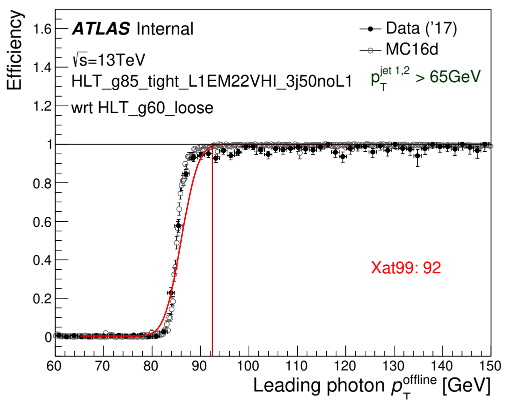

(a) before analysis selection

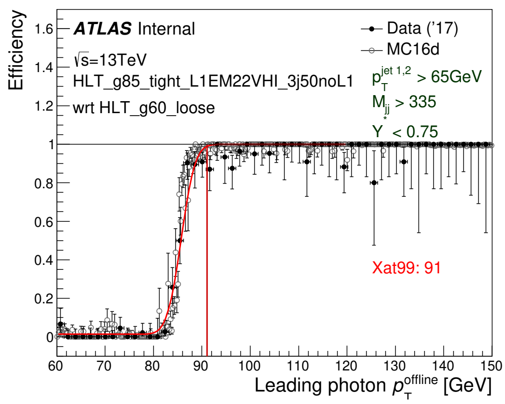

(b) after analysis selection

Figure 74: 74(a) shows the efficiency of the dijet+γ trigger as a function of leading isolated photon passing tight identification criteria without any kinematic selection. The efficiency in 2017 data is shown. The dashed line corresponds to full efficiency. 74(b) same ,but after the analysis selection

which could be fit from a lower mass, while the multi-object triggering strategy leads to a distribution with a noticeable shoulder which could not be fitted until $\sim$ 300 GeV higher in M_{jj} .

2. The multi-object triggering strategy provides better analysis sensitivity than the single-photon triggering strategy.

As the present analysis sets limits on signal masses as low as 200 or 250 GeV . The

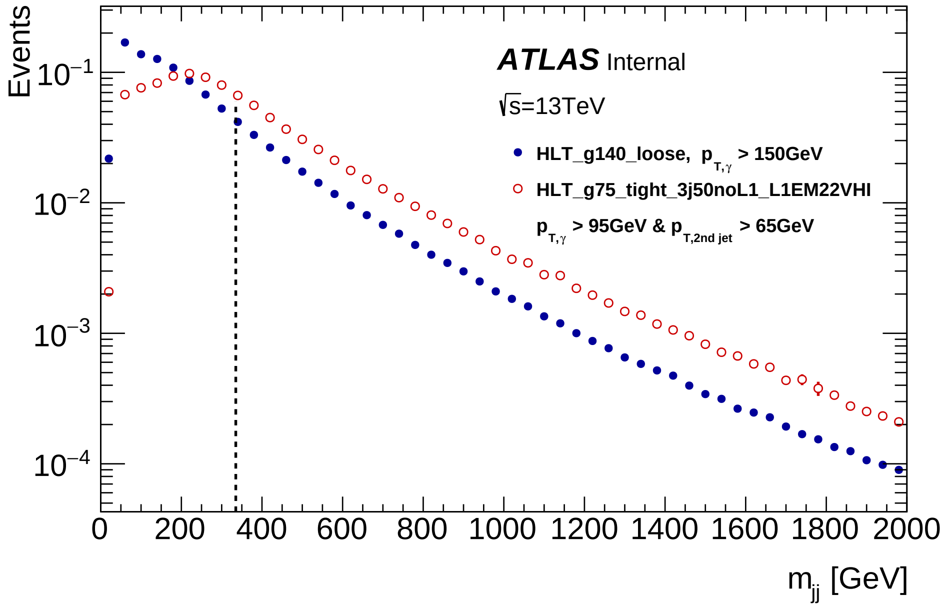

Figure 75: Invariant mass distribution for Sherpa multijets requiring on one side events to pass `HLT_g140_loose` trigger and leading photon $p_T > 150$ GeV (single-photon trigger); and on the other hand, events to pass `HLT_g75_tight_3j50noL1_L1EM22VHI` trigger, leading photon $p_T > 95$ GeV and two leading jets $p_T > 65$ GeV (multi-object trigger) . No y^* cut is applied.

single-photon trigger is included for the low values of the mass range. However, in order not to lose sensitivity gained by the multi-object trigger, this analysis therefore uses both selections. A spectrum was created with each triggering strategy and fitted independently. For masses where the multi-object trigger selection can be fitted and used to constrain signal points, those will be the nominal results. Where this spectrum is not yet smoothly falling, the single-photon trigger result will be used. This conclusion is summarised and the relevant luminosities for each selection are recorded in the Event Selection discussion later in this Section (see Table 10).

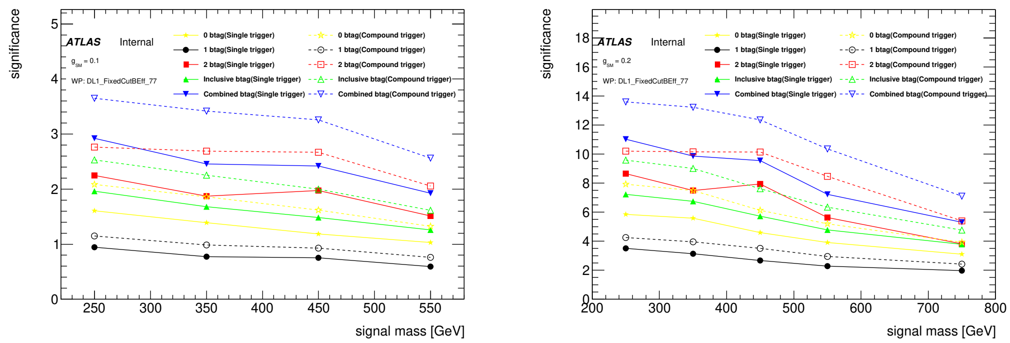

(a) $g_q = 0.1$

(b) $g_q = 0.2$

Figure 76: Comparison of analysis sensitivity (based on the definition in Equation 47) to a benchmark Z'with couplings $g_q = 0.1$ (76(a)) and $g_q = 0.2$ (76(b)) for a multi-object trigger strategy versus a single photon trigger strategy. For the doubly *b-tag* result, the DL1 tagger at the 77% fixed efficiency working point is used (see Section 7.7.1). The luminosities are scaled to represent the full Run II dataset including the 3 fb^{-1} loss from the multi-object trigger strategy. These results show that for masses where both triggering strategies can be fitted, the multi-object trigger strategy provides improved analysis sensitivity, even when accounting for the loss of the 2015 dataset.

7.5 Optimization cuts

To optimize the number of events that may contain physics of interest with respect to the background events, several discriminant variables were studied. The significance of these variables gives a relationship between the number of signal events related to the amount of background. It is computed as $S/\sqrt{B}$, where S corresponds to the signal distribution and B to the background. The maximum of the significance provides an appropriate cut selection.

The cut values determined may also have an impact on the smoothness of the M_{jj} range that would be properly fit, thus it is important to check that the M_{jj} shape does not get distorted by a specific cut.

Four target mass points were studied: 250 GeV, 350 GeV, 450 GeV and 550 GeV, each with a range of ±50 GeV. The study searches for selection cut values that are identical for all mass ranges. Also, only the trigger requirement and a cut on the p_T value where it reaches the 99% the efficiency are applied.

The signal and background distributions for different discriminant variables were studied. A brief description of them is presented below.

***Asymmetry* :** The asymmetry in p_T between the two signal jets: $A = \frac{(|p_{T,1}|-|p_{T,2}|)}{(|p_{T,1}|+|p_{T,2}|)}$. This is expected to be smaller on average for signal than for background.

ΔR : The difference in η, ϕ location between the ISR object and the nearest signal jet. In a signal event with a reasonably boosted resonance these are expected to be roughly back-to-back.

$\Delta R_{M_{jj}}$: Same as before but with respect to the invariant jet mass.

y^* : A key discriminating variable for dijet analyses, y^* is a measure of rapidity difference between the two signal jets. Specifically, $y^* = \frac{y_1 - y_2}{2}$. Signal should be produced roughly isotropically, but multijet production preferentially generates forward jets. Therefore, the requirement that the two selected jets are relatively central in their centre-of-mass frame makes y^* an effective discriminant[18].

Unfortunately, many of the candidate variables have poor discrimination power. These distributions can be found in Appendix B.5.

The y^* and the asymmetry presented better discrimination power, see Figure 77, a multivariate analysis using `TMVA` was attempted. The methods tested were Fisher, Likelihood, and Cuts. The first two multivariate discriminant methods provide a new variable to cut on that, unfortunately, has different optimal values for each mass range, which effectively results in different variables for different ranges. Because of this fact, this study only focuses on the third method which determines optimal cuts on variables without the necessity of introducing new composite variables for which their optimal performances are different across mass ranges.

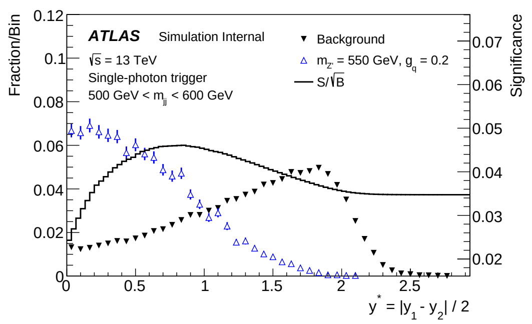

(a) y^*

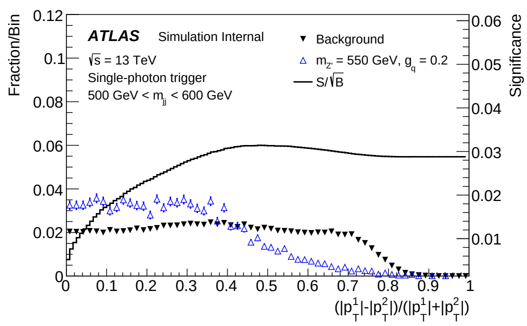

(b) Asymmetry between ISR and reconstructed jet

Figure 77: Signal (S) and background (B) distributions of the discriminant variables (asymmetry, and y^*), along with the distribution $S/\sqrt{B}$, for the two leading jets in photon+jet events in the 500 GeV to 600 GeV mass range.

Results for this study are summarised in Table 7 which shows the maximum value of the significance normalized to a luminosity of $1/pb$ on each mass range, computed for different sets of variables.

It was found that the variables were largely correlated, thus almost no additional sensitivity was gained by using multiple variables instead of simply the more powerful

[18]Future iterations of the analysis would do well to study this variable or equivalents in the context of $2 \rightarrow 3$ processes, as its use has been developed and mostly informed by $2 \rightarrow 2$ process searches like the dijet analysis.

Mass range [GeV]	Only y^*	Only Asymmetry	Asymmetry and y^*
$200 \leq M_{jj} \leq 300$	0.033	0.029	0.034
$300 \leq M_{jj} \leq 400$	0.066	0.051	0.066
$400 \leq M_{jj} \leq 500$	0.055	0.040	0.055
$500 \leq M_{jj} \leq 600$	0.046	0.031	0.047

Table 7: Maximum value of the significance $s/\sqrt{b}$ for each mass range, for different combinations of variables

of them: y^* . It was therefore concluded that a multivariate technique offered no additional power over a rectangular cut based technique.

The goal is then to determine a cut value in y^* which maximizes the significance across all mass ranges. The criteria employed is to use the cut value that optimizes the mass range with the lowest significance value, and verify that it does not significantly reduce the significance value for the other mass ranges. Tables 8 and 9 show the significance value for each mass range when selecting a cut value using the method mentioned above.

Mass range [GeV]	Max. $s/\sqrt{b}$ optimized for each mass range (and y^* cut used)	Max. $s/\sqrt{b}$ for $y^* \leq 0.75$
$200 \leq M_{jj} \leq 300$	0.067 (y^* ≤0.81)	0.0676
$300 \leq M_{jj} \leq 400$	0.066 (y^* ≤0.78)	0.0658
$400 \leq M_{jj} \leq 500$	0.0554 (y^* ≤0.78)	0.0553
$500 \leq M_{jj} \leq 600$	0.0460 (y^* ≤0.85)	0.0458

Table 8: Maximum value of the significance $s/\sqrt{b}$, optimized for each range (left) and for $y^* \leq 0.75$ as used in the analysis (right). The `HLT_g140_loose` trigger and relative selection are shown.

Mass range [GeV]	Max. $s/\sqrt{b}$ optimized for each mass range (and y^* cut used)	Max. $s/\sqrt{b}$ for for $y^* \leq 0.75$
$200 \leq M_{jj} \leq 300$	0.0319 (y^* ≤0.81)	0.0317
$300 \leq M_{jj} \leq 400$	0.0294 (y^* ≤0.81)	0.0293
$400 \leq M_{jj} \leq 500$	0.0249 (y^* ≤0.78)	0.0247
$500 \leq M_{jj} \leq 600$	0.0202 (y^* ≤0.78)	0.0202

Table 9: Maximum value of the significance $s/\sqrt{b}$, optimized for each range(left) and for $y^* \leq 0.75$ as used in the analysis (right). The `HLT_g85_tight_3j50noL1_L1EM22VHI` trigger and relative selection are shown.

The cut of $y^* \leq 0.75$ was introduced very early in the analysis when a second channel (jet ISR) was still considered, to homogenize the cut selection. The value of 0.75 was taken after checking the loss in the significance from 0.78 to 0.75, as it was less than 1% the selection of $y^* \leq 0.75$ defined and applied in the rest of the analysis.

7.6 Event selection

The events used in the analysis are required to pass the following event selection:

- pass the trigger listed in Table 10
- satisfy the jet cleaning criteria [39], after applying the jet-vertex-tagging (JVT) to avoild pileup events.

In addition the data have to satisfy:

- the run has to be included in an appropriate good runs list (GRL).
- to have a primary vertex reconstracted with at least 2 tracks with p_T >500 MeV.

The following triggers are used in each of the specified cases, in accordance with the studies presented in Section 7.4. The total luminosity result is thus 76.595 fb^{-1} for $M_{jj} < 335$ GeV (“compound” trigger) and 79.826 fb^{-1} for $M_{jj} >$ 335 GeV (“single photon” trigger).

Channel	Year	High-level Trigger	Lumi.[fb^{-1}]
	2015	–	–
“Compound trigger”,M_{jj} > 335 GeV	2016	`HLT_g75_tight_3j50noL1_L1EM22VHI`	33.009
	2017	`HLT_g85_tight_L1EM22VHI_3j50noL1`	43.586
“Single photon trigger”, M_{jj} < 335 GeV	2015 – 2017	`HLT_g140_loose`	79.826

Table 10: Triggers used for each channel and each year’s datasets. An additional signal region using single-jet triggers allows an extension of the search range to lower masses, albeit at lower sensitivity.

Analysis selection

The analysis selection is described in Table 11. The jet and photon multiplicity and p_{T} cuts are necessary to ensure each trigger is fully efficient. Optimal cuts in y^* were determined as described in Section 7.5. The M_{jj} cuts are determined by the shape of each spectrum and are chosen such that the spectrum can be described by a smooth fit above the cut. The data cutflows and yields for both channels are in Tables 22 and 24, also the cutflows for MC are given in Appendix B.2.

Cut	Single-photon trigger	Compound trigger
Number of jets	$n_{\mathrm{jet}} \geq 2$	$n_{\mathrm{jet}} \geq 2$
Number of photons	$n_\gamma \geq 1$	$n_\gamma \geq 1$
Lead γ p_{T}	$p_{\mathrm{T}}^{\gamma} > 150$ GeV	$p_{\mathrm{T}}^{\gamma} > 95$ GeV
Lead & sublead jet p_{T}	$p_{\mathrm{T}}^{j} > 25$ GeV	$p_{\mathrm{T}}^{j} > 65$ GeV
Centrality	$y_{12}^* < 0.75$	$y_{12}^* < 0.75$
Invariant mass	$M_{jj} > 169$ GeV	$M_{jj} > 335$ GeV

Table 11: Analysis search region cuts

Cut	Single photon trigger		Compound trigger	
	Events remaining	% remaining	Events remaining	% remaining
Total	6443085312	–	5227867136	–
GRL	111929303	1.7%	103846024	2.0%
Trigger	93589345	83.6%	34203232	32.9%
Cleaning	93424536	99.8%	34149788	99.8%
$n_{jets} \geq 2$	89115138	95.4%	33409444	97.8%
$n_{\gamma} \geq 1$	19199687	21.5%	16350066	48.9%
Lead γ p_{T} cut	5249652	27.3%	9174245	56.1%
Lead jet p_{T}cut	5249652	100%	8712658	95.0%
Sublead jet p_{T}cut	5249652	100%	5633026	64.7%
$\lvert y^{*} \rvert < 0.75$	3093280	58.9%	3478528	61.8%

Table 12: Cutflow for data 2015+2016. Percentages remaining are relative to the previous cut, and all values are relative to the objects remaining in the ntuple: thus all jets pass the leading and subleading jet cut, since only jets above 25 GeV are kept in the ntuple. Please note that there was not compound trigger used in 2015, so all events there originate in the 2016 dataset.

Cut	Single photon trigger		Compound trigger	
	Events remaining	% remaining	Events remaining	% remaining
Total	5002680320	–	5002680320	–
GRL	139551621	2.8%	139551621	2.8%
Trigger	109049835	78.1%	42646980	30.6%
Cleaning	108878354	99.8%	42593952	99.9%
$n_{jets} \geq 2$	104090372	95.6%	41596064	97.7%
$n_{\gamma} \geq 1$	24898568	23.9%	20861906	50.2%
Lead γ p_{T} cut	6325551	25.4%	12916492	61.9%
Lead jet p_{T}cut	6325551	100%	12125213	93.9%
Sublead jet p_{T}cut	6325551	100%	7380192	60.9%
$\lvert y^{*} < \rvert 0.75$	4014393	63.5%	4552562	61.7%

Table 13: Cutflow for data 2017. Percentages remaining are relative to the previous cut, and all values are relative to the objects remaining in the ntuple: thus all jets pass the leading and subleading jet cut, since only jets above 25 GeV are kept in the ntuple.

7.7 b-Jet tagging

As it was briefly mentioned before, the analysis is divided into two searches, one inclusive in jets, and one using only events where the two jets, candidates for the resonance, are tagged as *b-tag* .

This section explores the choice of tagging criteria, justifies the addition of the b-tagged channels, and shows the consequences for the resulting spectra.

7.7.1 Tagger and working point selection

This analysis explores two official taggers: `MV2c10` and `DL1`, folowing the recomentations of the tagging group[19].

The optimal choice of tagger and working point was determined by comparing signal sensitivity for each choice across the full range of Z' mass points. The significance was defined as follows [61]:

$$Z = \sqrt{\sum_i^{bins} Z_i^2}\,,\ \text{where } Z_i = \sqrt{2\left[(s+b)\log(1+\frac{s}{b}) - s\right]} \tag{47}$$

The full analysis selection was used in the nominal MC samples. In Addition, the two jets forming the candidate Z' have to pass the relevant tagging requirements.

Figures 78, 79 compare the significance for a range of taggers and for all available working points, with hybrid[20] and fixed[21] conditions, respectively. In all cases, the Z' with a coupling constant $g_{SM} = 0.2$ was used for the tests. However, the Appendix B.5 shows the full set of plots for all taggers, working points, and coupling values.

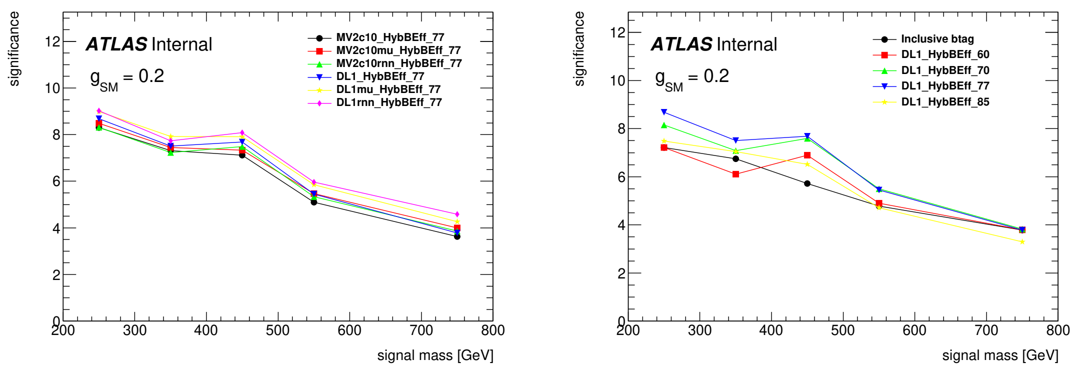

(a) Comparison of taggers at 77% hybrid WP (b) Comparison of hybrid WPs for `DL1` tagger

Figure 78: Signal significance in two-*b-tag* channel for 78(a) various taggers at the same hybrid working point and 78(b) various hybrid working points for the most promising supported tagger. The selection corresponds to the single-photon trigger. Signals with a coupling of $g_q = 0.2$ are shown.

For all mass points, the `DL1` tagger outperforms the `MV2c10` tagger. Thus, it was chosen.

[19] Originaly six official taggers were studied to determine the optimal choice for this analysis: `DL1rnn`, `DL1mu`, `DL1`, `MV2c10rnn`, `MV2c10mu`, and `MV2c10`. However in January 2018 the tagging group set only two of them: `MV2c10` and `DL1`

[20] Hybrid condition refers to use a mix of Fixed condition below a p_{T}cutoff value, and a Flat Efficiency confition above it. And Flat Efficiency condition means that different DL1 cut values are use to hold efficiency at a cerntain value in each pT sub-region.

[21] Fixed condition refers to set the average value of the b-tagging efficiency to a certain value

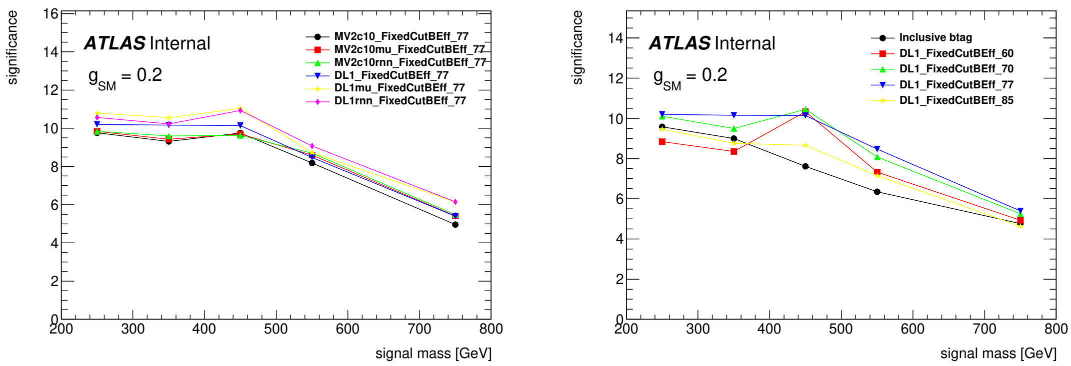

(a) Comparison of taggers at 77% fixed WP (b) Comparison of fixed WPs for `DL1` tagger

Figure 79: Signal significance in two-*b-tag* channel for 79(a) various taggers at the same fixed working point and 79(b) various fixed working points for the most promising supported tagger. The selection corresponds to the compound trigger. Signals with a coupling of $g_q = 0.2$ are shown.

The right plot in Figure 78 and Figure 79 reflects that the significances change significantly across the mass range for various working point. Taking this into account, it was found that the optimal hybrid efficiency working point is 77% and the optimal fixed efficiency working point is also 77%. Nevertheless, the decision still needs to take into account the possibility of introducing features or sharp changes in the composition of the M_{jj} spectrum, as discussed in the following section.

Tagging efficiencies and mis-tag rates

To ensure that the final tagged spectra can be fitted properly, the *b-tag* efficiencies and fake rates must vary smoothly as a function of mass. Otherwise, it could lead to localized excesses and deficits in the data spectrum and It may generate challenges to the fit, generating then fake signals.

Figure 80 shows tagging efficiencies for the 77% hybrid efficiency working point for the signal jets using the single-photon trigger as an example.

The efficiency presents some structure visible around 200 GeV. As a result, a comparison of the efficiencies between the optimal hybrid and fixed working points was performed to choose that one with smoother performance.

Also, the miss c and l tag rates were consider. If it was too high, it could mean than c or light quarks may be tagged as b very often. In the same way, a smooth behavior is expected for those distributions.

Figures 81, 82 and 83 show the b-tagging efficiency, c-jet miss tag rate, and light jet miss tag rate for the same signal jets for both the 77% hybrid efficiency WP and the 77% fixed efficiency WP. Both fixed and hybrid working points are problematic for p_{T}< 200 GeVbecause they are not smooth distributions. For the hybrid working point, these features are most visible in the *b-tag* efficiency and the *c*-jet mistag rate, while for the fixed working point the features are most visible in the light jet mistag rate. However, the light jet mistags rate for the fixed efficiency working point is

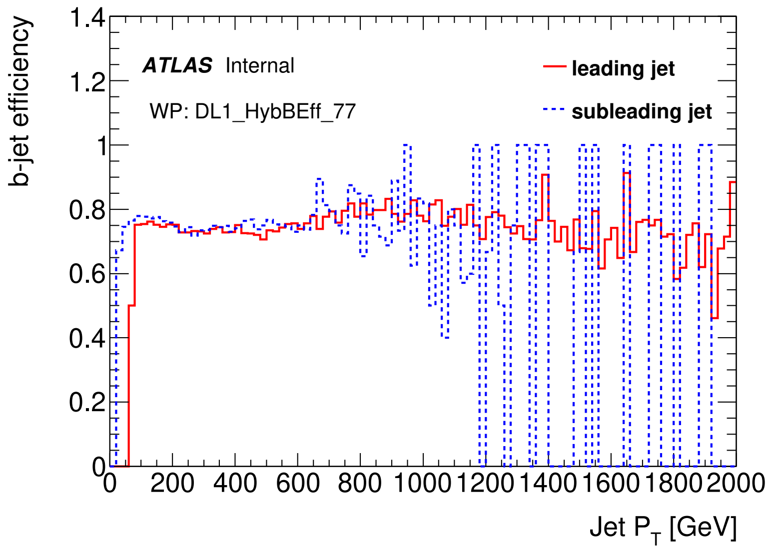

Figure 80: Efficiency of *b-tag* using the `DL1` tagger at 77% hybrid efficiency WP. The full analysis selection is applied to the nominal background MC samples, and the leading and subleading jets are shown.

very small for low p_{T}jets resulting in a low contribution of mistagged rates in this part of the spectrum. A detailed study of the impact of non-smooth efficiencies and mistag rates on the final M_{jj} spectrum shape suggests that non-smoothnesses on this scale do not cause future issues on the M_{jj} distribution (see Appendix B.8 for details). Therefore, the safest choice between the two performant working points is to use the fixed efficiency WP at 77% efficiency.

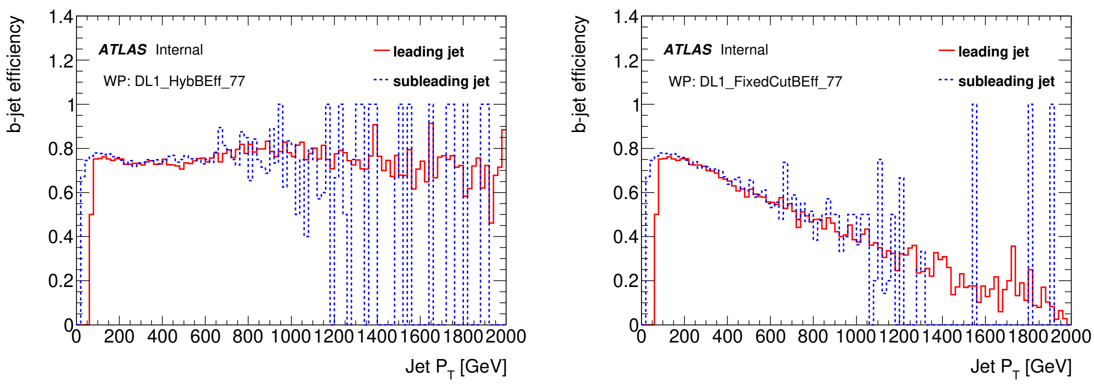

(a) Hybrid WP

(b) Fixed WP

Figure 81: Efficiency of *b-tag* in the for the 77% hybrid efficiency working point (81(a)) and the 77% fixed efficiency working point (81(b)). In each case, the full analysis selection is applied to the nominal background MC samples.

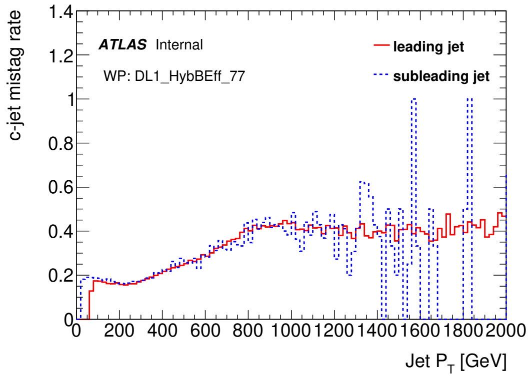

(a) Hybrid WP

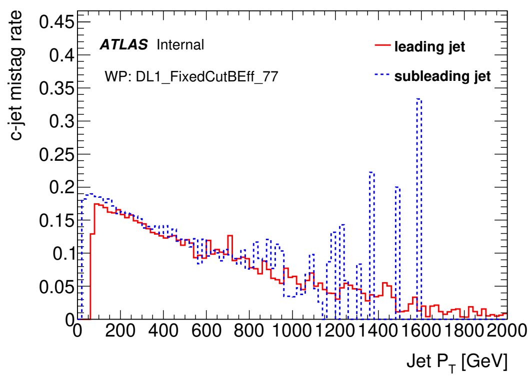

(b) Fixed WP

Figure 82: Mistag rate for c jets for the 77% hybrid efficiency working point (82(a)) and the 77% fixed efficiency working point (82(b)). In each case, the full analysis selection is applied to the nominal background MC samples.

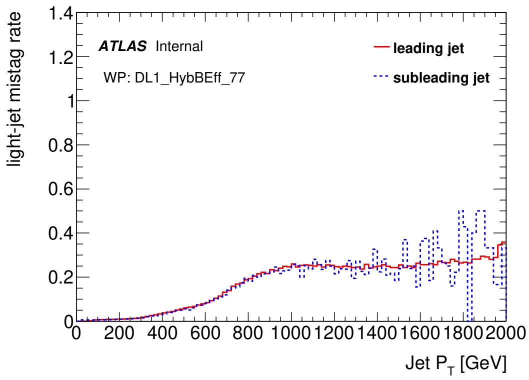

(a) Hybrid WP

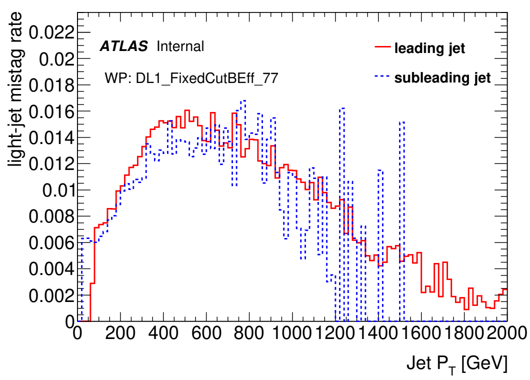

(b) Fixed WP

Figure 83: Mistag rate for light jets for the 77% hybrid efficiency working point (83(a)) and the 77% fixed efficiency working point (83(b)). In each case, the full analysis selection is applied to the nominal background MC samples.

7.7.2 Defining the analysis selection

There is not a unique tagging choice. This analysis explores five tagging choices defined bellow:

Inclusive No tagging requirements are made in the selection

0-tag Explicitly require that neither jet from the candidate resonance is *b-tag*

1-tag Require that exactly one jet from the candidate resonance is *b-tag*

2-tag As in the optimisation studies, require that both jets from the candidate resonance are *b-tag*

Combined A simple combination is performed between the 0, 1, and 2-tagged channels:
$Z_{comb} = \sqrt{Z_0^2 + Z_1^2 + Z_2^2}$

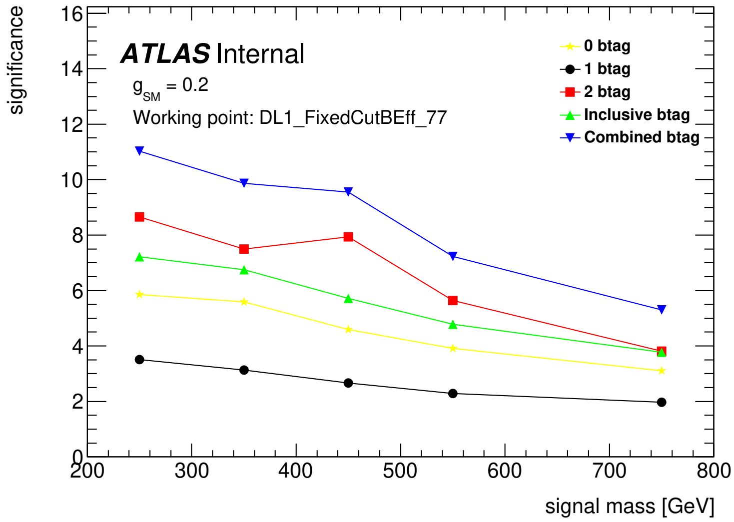

Figure 84: Signal significance versus mass in the inclusive, 0-tag, 1-tag, and 2-tag channel as well a combination of 0, 1, and 2-tags. The DL1 tagger is used at the 77% fixed efficiency WP. Z'signals with coupling $g_q = 0.2$ are used.

Figure 84 compares the significance of each tagging case. The 2-tagged selection offers a noticeable increase in sensitivity over the inclusive channel.

The inclusive spectrum is the most general case and is the simplest option for reinterpretation. The 2-tagged channel provides additional information particularly interesting for some models which decay preferentially to heavy flavours. On another hand, the combined would only be re-interpretable if all three exclusive tagging channels (0, 1, and 2) were provided, since the branching ratios can vary from model to model, and a simpler result is preferred. Therefore, the option of showing only two results in each channel (inclusive and 2-tagged) is preferred for the current iteration of the analysis.

Conclusion for b-tagging in the selection

To summarise the outcomes of the three preceding sections, the analysis will be presented in two channels per trigger selection:

- Photon ISR, inclusive
- Photon ISR, 2-tagged

For the 2-tagged channels, the `DL1` tagger at the 77% fixed efficiency working point is used. Both the leading and subleading jets are required to pass this tagging requirement.

7.7.3 Impact of the tagging choices on the spectra

Figure 85 shows the M_{jj} distribution in Sherpa mc16d after all analysis cuts in the inclusive and 2-tagged cases. The selection corresponds to the single-photon trigger, and the spectra are broken down by flavor, to illustrate changes in the composition as a function of M_{jj} . The inclusive spectrum is dominated by light jets in roughly equal proportions for all masses. The 2-tagged spectrum illustrates the decrease in *b-tag* performance as a function of mass, with a higher proportion of true di-b events at lower masses and a composition dominated by miss-tagged light jets at higher masses. These plots use the `DL1` tagger at the 77% fixed cut working point. Additional plots of the compositions of various jet kinematic distributions can be found in Appendix B.6.

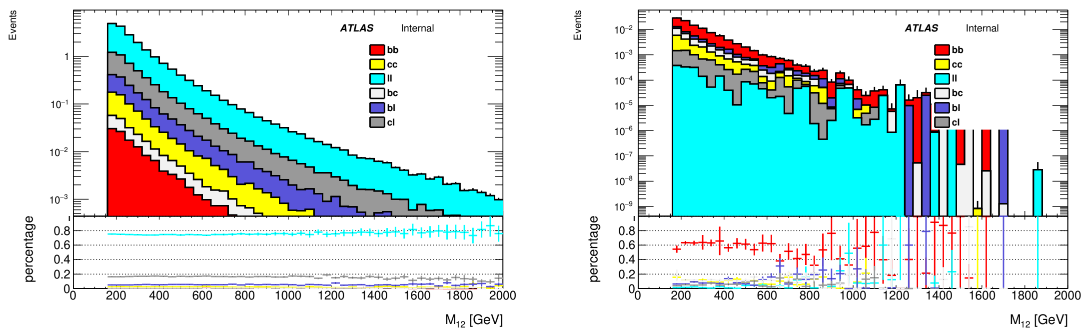

(a) Inclusive selection

(b) 2-tagged selection

Figure 85: Flavour composition breakdown of the M_{jj} spectrum in Sherpa mc16d for the inclusive selection 85(a) and for the 2-tagged selection 85(b). The fraction represented by each flavour pairing is shown in the ratio plot. The single photon trigger signal region is used.

The understanding of the composition of the tagged spectra is essential to know if it will be possible to describe it with a fit-based background estimate. A smooth variation in the flavor composition helps prevent the formation of sharp corners in the tagged spectrum. These plots show that changes in composition are smooth within the statistical uncertainties of the MC samples.

Another concern is the appropriateness of using a fit-based background estimate for a large mass range when the composition may change. If the background distribution is not made up of the same type of events through all mass ranges, use a function that forces a correlation on these events such that the background estimate at high mass values may depend on that at low masses. This concern is addressed by changing the background estimate strategy from a single global fit to a *sliding window* fit (see Section 7.9 for details). As long as each sliding window fit is not wider in range than a few hundred GeV, then over the range of a single fit, the composition changes only slightly and smoothly.

7.8 Signal shapes, cross-sections and acceptance

All signal MC samples used in the analysis are plotted in Figures 86 through 88. These show the peak visible in M_{jj} for each sample at the reconstructed level after passing all analysis cuts. The three figures show three different g_q coupling values for the Z' model. A Bukin fit [56] is performed to each peak to determine its width, and the results are found to range from around 13% for the lowest masses to 8% for the narrowest and highest masses. As all of these are within 15% width to mass ratio, this benchmark is appropriate for this fitting and bump-hunt based search.

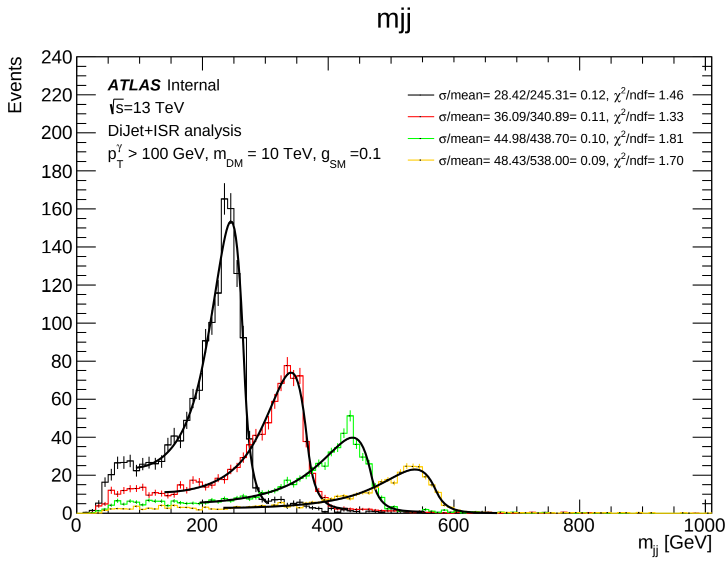

Figure 86: Fits to signal masses in simulated Z'samples with $g_q = 0.1$. The signals have nominal masses of 250, 350, 450, and 550 GeVfrom left to right.

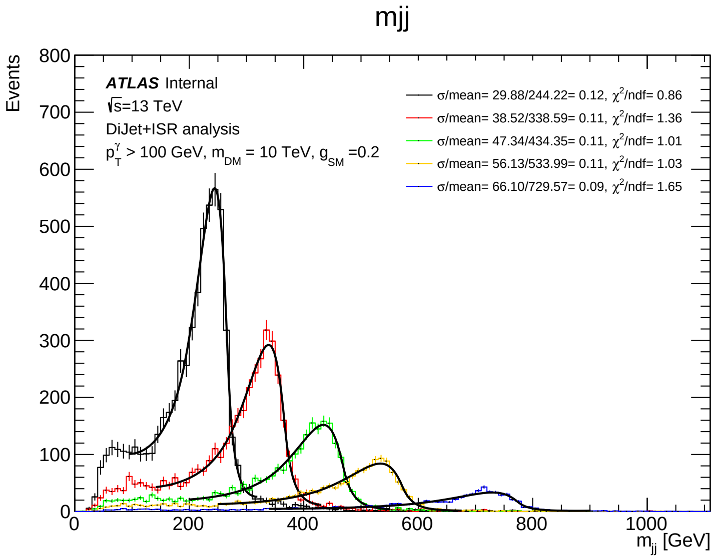

Figure 87: Fits to signal masses in simulated Z'samples with $g_q = 0.2$. The signals have nominal masses of 250, 350, 450, 550, and 750 GeVfrom left to right.

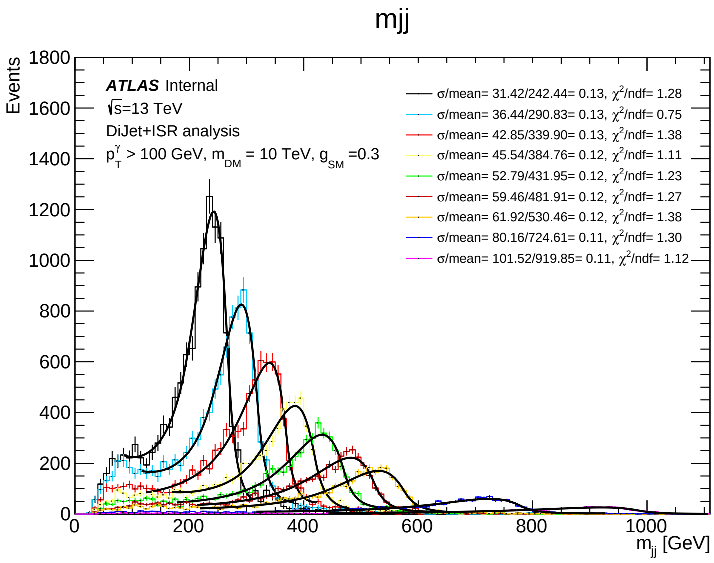

Figure 88: Fits to signal masses in simulated Z'samples with $g_q = 0.3$. The signals have nominal masses of 250, 300, 350, 400, 450, 500, 550, 750, and 950 GeVfrom left to right.

Cross-sections

The cross-sections for the Z' benchmark signal samples are shown in units of picobarns in Figure 89. It reflects the fact that smaller coupling values of the signal to standard model quarks mean smaller cross-section for the simulated process, $pp \ \rightarrow Z' + \gamma \ \rightarrow \ q\ q\ \gamma$.

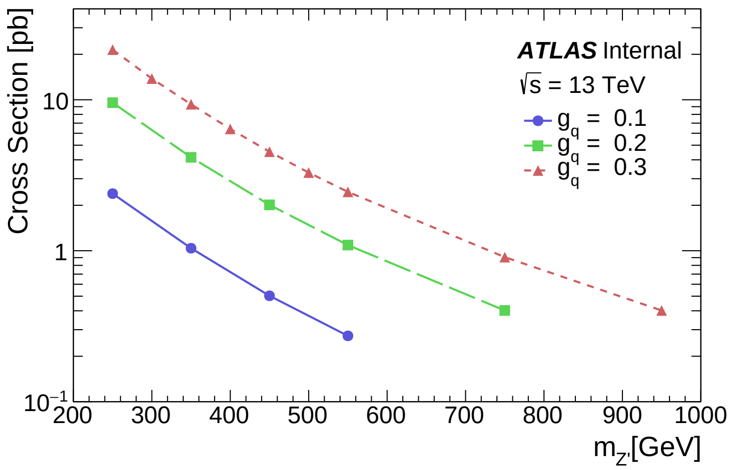

Figure 89: Cross-sections of Z'benchmark model for all coupling values used in the analysis. Values displayed are in picobarns.

Acceptance

The number of signal events due to a new process can be expresed by the Equation 48 as follows:

$$N_{sig} = \mathcal{L} \cdot \sigma \cdot \mathrm{BR} \cdot A \cdot \epsilon \tag{48}$$

This shows, the relevant efficiencies (ϵ) and acceptances (A) must be taken into account to get the amount of signal expected for a model with a given cross-section (σ). The relevant factors which affect this analysis are briefly described below:

Kinematic acceptance Fraction of events at truth level which pass analysis selection cuts, $a_{\mathrm{kin}} = n_{\mathrm{truth}}/n_{\mathrm{tot}}$

Photon efficiency Efficiency of photon identification and reconstruction. This factor is included in the reco-level efficiency.

Jet efficiency Efficiency of jet reconstruction. This is 1 in ATLAS for all practical purposes.

B-tagging efficiency Number of jets surviving the *b-tag* process. This is a function of both tagging efficiency for real *b-jet* and mistag rate for light and *c*-jets, and is included in the reco-level efficiency.

Trigger efficiency Efficiency of the photon reconstruction in the trigger. This factor is included in the reco-level efficiency.

Each of them does not need to be computed individually, instead can be measured as two quantities, a single acceptance and a single efficiency per signal point and channel.

The acceptance is measured as the fraction of events that pass the kinematic analysis selection cuts (that is, excluding trigger requirement) at the truth level.

Mass points below 450 GeVare shown using the samples with filter cut at photon $p_T = 100$ GeV and the single-photon trigger selection, while mass points above 450 GeVare shown using the samples with filter cut at photon $p_T = 50$ GeV and the compound trigger selection.

It is important to highlight that these acceptances of the single-photon trigger selection and compound trigger selection can not be directly compared with one another in this way because the filter efficiencies for the two samples differ substantially (see Tables 19 and 20 in AppendixB.1). Thus, to remove the ATLAS MC-specific generator dependence of these numbers and compare the true kinematic-level acceptance, the curves are multiplied by the filter efficiency of each sample. The resulting ATLAS-independent acceptance curves are shown in Figure 90.

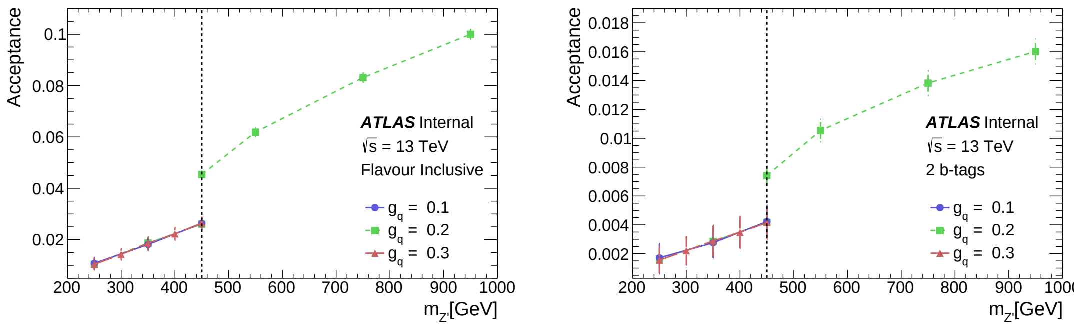

(a) Inclusive selection

(b) 2-*b*-*tag* selection

Figure 90: Kinematic acceptance of the Z' benchmark model for all coupling values considered in the analysis. The acceptance quantities are multiplied by the filter efficiency for each sample to remove the otherwise hidden impact of the different photon p_T cuts at generator level. The single photon trigger selection and appropriate samples are used below 450 GeVwhile the compound trigger selection and appropriate samples are used above that point.

The efficiency is defined as the fraction of the reconstruction-level events that passed all analysis requirements over the number of truth-level events that passed the kinematic requirements. So it accounts for the trigger, ID, and tagging efficiencies. These quantities are shown for each signal point in Figure 91.

The visible cross section for the Z' model is then given by $\sigma \cdot k \cdot \epsilon_{\text{filter}}$ multiplied by the two acceptance and efficiency values from the relevant plot at each mass point. The branching ratio is incorporated in the cross section value in this case, since only events resulting in a jet final state are generated. An interpolation between the points is performed logarithmically in Z' mass and appears as straight lines in the figures.

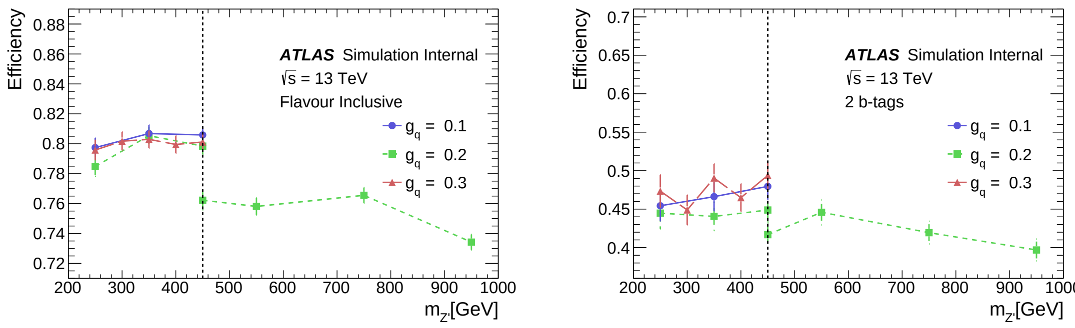

(a) Inclusive selection

(b) 2-*b-tag* selection

Figure 91: Efficiency of the Z'benchmark model for all mass points and coupling values considered in the analysis.

7.9 Background modelling

The background estimate for this analysis is performed using a parametric fitting procedure. The method fits the observed dijet mass distribution using a few-parameter function over the complete search range. The background to be modeled consists of QCD processes with a complex mixture of PDFs, parton showering, and the effects of the detector response and kinematic selection.

The functions used to moderate the background are presented in Table 14. These have been studied in various spectra relevant to the analysis, composed of both ve been carriedMC and subsets of data, as detailed in Section 7.9.2. The three-parameter dijet function has proven insufficiently flexible, so the studies focus on the other three: the four and five parameter dijet functions and the UA2 function. Each offers benefits in particular situations. The analysis strategy is to create the nominal background estimate from whichever function performs the best in real data and will define an uncertainty on that function selection using the second-best of the three functions. This is described in more detail in Section 7.9.3.

Functional form	Citation	Label
$f(x) = p_1(1-x)^{p_2}x^{p_3}$	[46]	`our3param`
$f(x) = p_1(1-x)^{p_2}x^{p_3+p_4 \ln x}$	[38]	`our4param`
$f(x) = p_1(1-x)^{p_2}x^{p_3+p_4 \ln x * p_5 \ln x^2}$	[38]	`our5param`
$f(x) = \frac{p_1}{x^{p_2}}e^{-p_3 x - p_4 x^2}$	[116]	`UA2`

Table 14: Functional forms explored for fitting the QCD background, with citation to previous results in which they have been used to fit similar distributions and label for reference in the rest of the text.

7.9.1 Motivation for a sliding window fit

Historically, the resonance searches in dijet channels have been carried out by looking for a localized excess above a smooth background, which is obtained by fitting the entire dijet mass spectrum with ad-hoc functions. But, with increasing data, the fitting procedure with a global fit becomes increasingly challenging. In particular, when the data increase several orders of magnitude. For this reason, the presented analysis adopted a sliding window fit, as described as in [103]. It is a background estimation method that looks for localized excesses by sliding over the data spectrum of a given half-width (corresponding to a number of bins termed as window-half-width or "whw" in the following) in small, overlapping windows. This allows the analysis to move away from an assumption that low and high ranges of M_{jj} can predictably be strongly correlated.

The unblinding strategy considers the possibility of a global fit and, if the fit quality is too low, will move to a sliding window fit and iteratively narrow the window until the background can be adequately described.

As an example, a case in which a global fit would be insufficient is shown in Figure 92. For this spectrum, created to simulate the shape of the 2-tagged spectrum, a global fit with the five-parameter function cannot satisfactorily describe the whole range in M_{jj} . Both the $p-value$ of 0.0 and the sinusoidal shape evidenced in the fit residuals demonstrate that the fit is not acceptable. In contrast, a sliding window fit with a window half-width of 13 bins performs better. A reasonable $p-value$ is obtained and the sinusoidal residuals are reduced. Even when this may not be the final choice for the window width, it demonstrates increased flexibility of the sliding window fit.

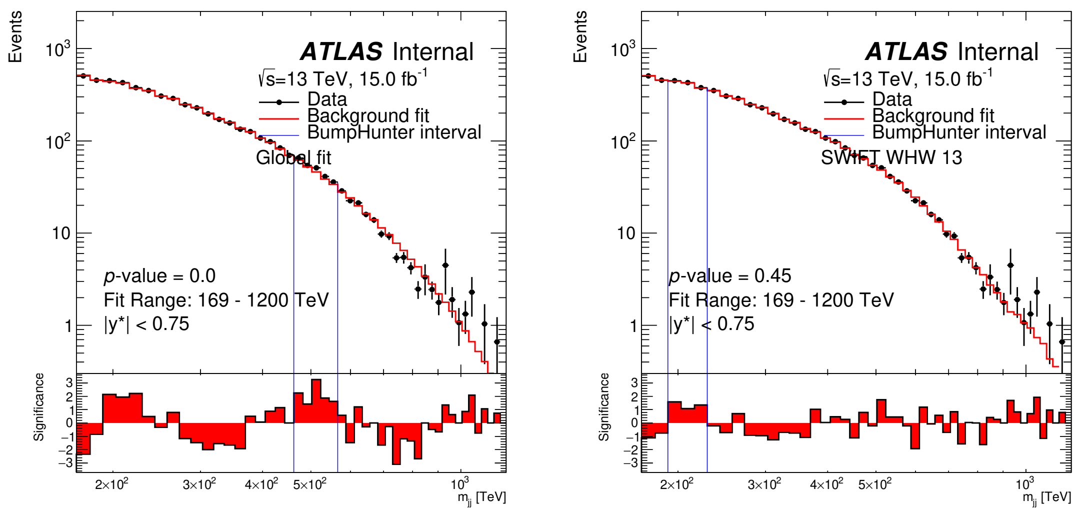

(a) Global fit (b) Sliding window fit

Figure 92: Fits to a spectrum derived from the inclusive single-photon trigger channel using an ABCD method[22] to estimate to represent the 2-tagged result. Figure 92(a) uses a global fit while Figure 92(b) uses a sliding window fit with window half-width of 13 bins. In both cases the five-parameter dijet function is shown. The spectra corresponds to use 15 fb^{-1}of real data.

The sliding window fits, however, may generate potential issues for analyses due to their increased flexibility. If the window width is too narrow, the fit is more flexible and loses sensitivity [44]. Thus the widest window still able to fit the spectrum shape is used. The optimization of the window width is discussed in the following sections.

7.9.2 Selection of parameters for the sliding window fit based on goodness-of-fit and signal injection

There are two parameters to be defined for the fitting procedure: the maximum and the minimum usable window width.

The *minimum acceptable window width* is determined via signal injection tests, as is fully descrived in Section 7.9.2.2.

The *maximum usable window width* can be found by fitting the Monte Carlo spectra, where there is no signal and can also be complemented by tests in a dataset equivalent to that used for the 2015+2016 data[23], which give a null result [45]. To do so, the window half-width is increased one bin at a time until a pre-determined fit quality criterion reaches a certain threshold. Following previous studies [43], the criterion is such that the background estimation to have a χ^2 $p-$value above 0.05, and if it is necessary, after excluding the window containing the largest excess.

Also, the tests on data are useful to reduce the set of fit functions and to exclude window widths that are too large for a dataset that is smaller than the full dataset used for the analysis. In the sense that if they already give a χ^2 $p-$value below 0.05 on a 15fb^{-1}spectrum, they will not be sufficiently flexible to fit the full dataset spectrum.

The statistic of the MC and the data is not representative of the statistic of the full dataset used in this analysis, thus, the actual *sliding window size* is determined directly on data as described in Section 7.9.3. Nevertheless, Appendix B.9 shows the results of fits on the 15 fb^{-1}and MC spectra for the inclusive single photon-triggered and compound-triggered signal regions. These results give us an initial determination of the maximum possible window.

All the following tests were performed before unblinding the analysis and therefore used 303 GeVas the starting point for the fit in the compound trigger spectrum. This value was later improved following the procedure described below in Section 7.9.3 and led to the value of 335 GeVquoted elsewhere.

7.9.2.1 Tests of fitting in statistically non-sensitive dataset

To test the background estimation method, the fitting procedure was applied over a dataset that is equivalent to the one from the last public result (2015+2016), where no signal was found.

The `UA2`, `our4param` and `our5param` functions were tested, using different values of window half-widths starting from half the spectrum and ending at 12 bins. To

[23] This dataset corresponds to approximately 15 fb^{-1}.

simulate the unblinding procedure, we first show the results of the global fit. If the χ^2 p-value of the overall background is below 0.05, then the procedure moves to SWiFt with a half-window width equivalent to half the spectrum. If the χ^2 p-value is still below 0.05, the half-window width is reduced by one bin and the fit is performed again. This procedure stops whenever the overall background χ^2 p-value is above 0.05 or when a half-window width of 14 is reached (see Section 7.9.2.2 for studies of the minimal signal width). this test is useful to gather a first idea on the maximum possible window that can be used for the sliding window fit, with about a quarter of the dataset. Figure 93 shows the results of the widest possible window and the results of the fit with the largest window where the χ^2 p-value is above 0.05, for each of the channels and each selection of the functions.

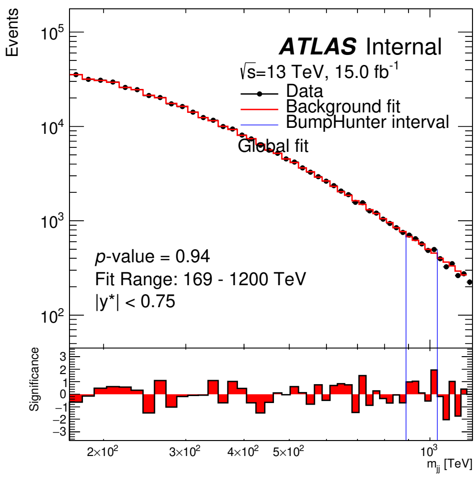

(a) photon ISR, inclusive single photon trigger, global

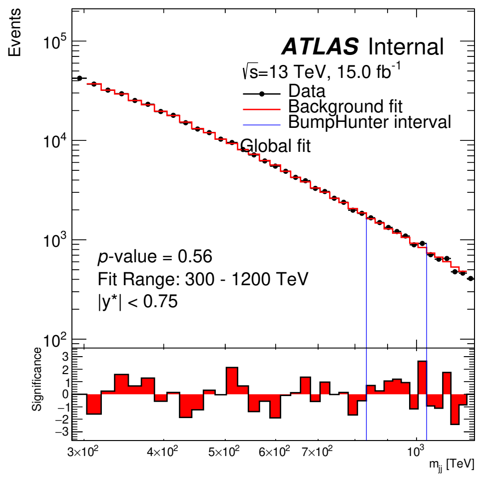

(b) photon ISR, inclusive photon + dijet trigger, global

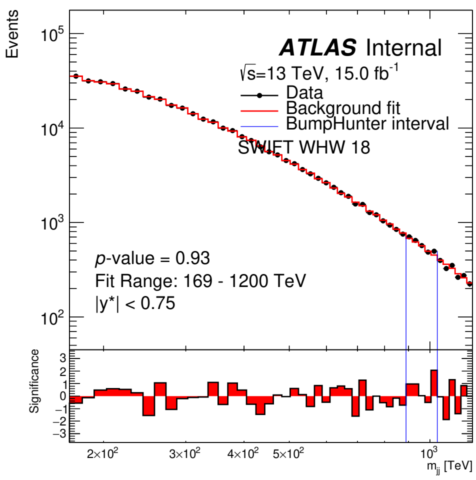

(c) photon ISR, inclusive single photon trigger, SWIFT

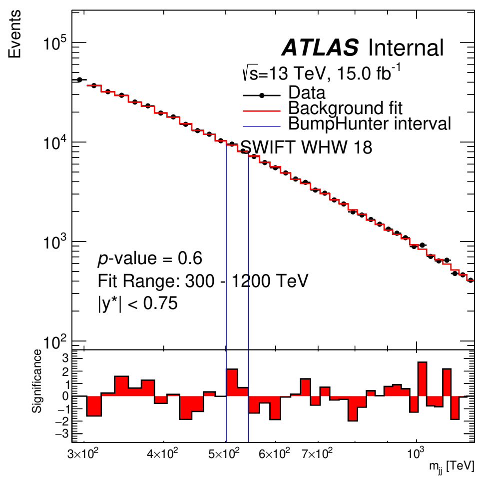

(d) photon ISR, inclusive photon + dijet trigger, SWIFT

Figure 93: Global fits and example sliding window fits in 15/fb of data for the inclusive selection, using the `our4param` function.

Functional form	Channel (inclusive)	Fit type	χ^2 $p-value$	BH $p-value$
`our4param`	Compound trigger	SWiFt, whw=18	0.052	0.60
`our5param`	Compound trigger	SWiFt, whw=18	0.052	0.49
`UA2`	Compound trigger	SWiFt, whw=16	0.056	0.58
`our4param`	Single photon trigger	global	0.85	0.94
`our5param`	Single photon trigger	global	0.86	0.94
`UA2`	Single photon trigger	global	0.079	0.35

Table 15: Summary of the fitting tests in data, showing the χ^2 and BumpHunter $p-value$for different fitting configurations.

The $p-value$ printed on each plot is the `BumpHunter` [58] $p-value$: this is used to determine the presence or absence of a signal, but is not the primary determinant of fit quality: for that, the χ^2 $p-value$ is used.

All functions already provide a good description of the 15 fb^{-1}data for the single-photon trigger with a global fit. The example shown uses the dijet four-parameter function, but the other two provide comparable results. If the full dataset behaves similarly to the smaller dataset, there will be no need to use a sliding window fit. For the compound trigger spectrum, a sliding window fit is needed and an acceptable χ^2 $p-value$ is reached with all function starting from a half-window width of 16 for the `UA2` function and increasing to 18 bins for the other two functions. This is despite the acceptable `BumpHunter` $p-value$ at larger window widths. The various $p-value$ and test results are summarized in Table 15.

Since this dataset does not include any b-tagging selection, as that signal region is still unexplored and blind, an ABCD method was needed to reweight the inclusive sample; It is described in Appendix B.11. The selected dataset has a luminosity of approximately 14.5 fb^{-1}(labeled in the following plots as 15 fb^{-1}for simplicity) and corresponds to data 2016 periods B, C, E, G, and K. Figure 94 demonstrates the closure of the method in Sherpa MC. It can be seen that the statistics of the Sherpa 2-tagged spectrum is not sufficient to bring any statistically firm conclusion. There is a not good closure of the method starting from 600 GeV. This is a possible explanation of why the fitting tests are not successful on the full range up to 1.2 TeV, and we have to restrict the fit range to 800 GeV and 1 TeV. Nevertheless, in data, we will use the full range and follow the unblinding procedure.

The results in Figure 95 and Table 16 for two different background estimation ranges (1 TeV and 800 GeV) show that we would have at least two functions with a window width above 14 bins of half-width.

Functional form	Channel (ABCD "tagged")	Fit type	χ^2 $p-value$
`our5param`	Single photon trigger	SWiFt, whw=17, fit range $m_{jj} < 1$ TeV	0.137
`UA2`	Single photon trigger	SWiFt, whw=14, fit range $m_{jj} < 1$ TeV	0.116
`our5param`	Single photon trigger	SWiFt, whw=15, fit range $m_{jj} < 0.8$ TeV	0.123
`our4param`	Single photon trigger	SWiFt, whw=15, fit range $m_{jj} < 0.8$ TeV	0.186
`UA2`	Single photon trigger	SWiFt, whw=14, fit range $m_{jj} < 0.8$ TeV	0.094

Table 16: Summary of the fitting tests in an ABCD-scaled 2-tagged spectrum derived from data, showing the χ^2 $p-value$for different fitting configurations.

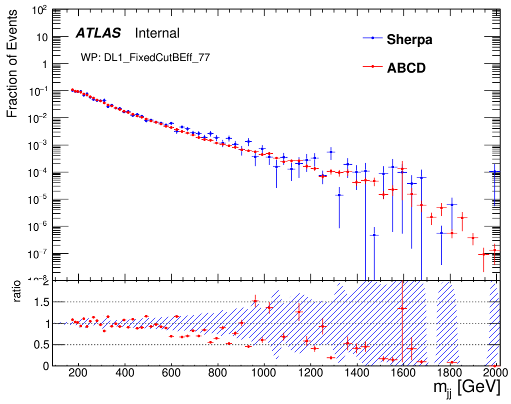

Figure 94: Closure results of the ABCD method using sherpa samples for the single photon trigger selection. The two spectra are normalized to 1 to compare the shapes.

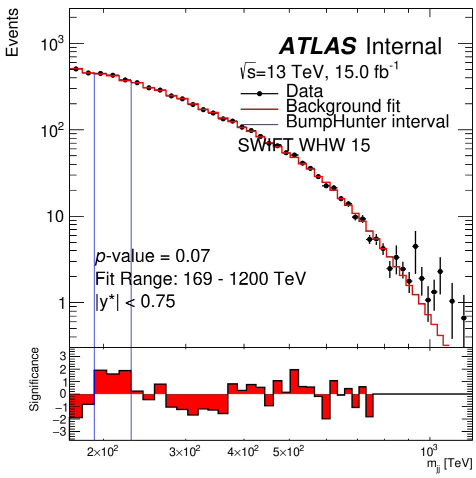

(a) photon ISR, inclusive single photon trigger, ABCD 2-tagged spectrum, end point 800 GeV, `our4param`

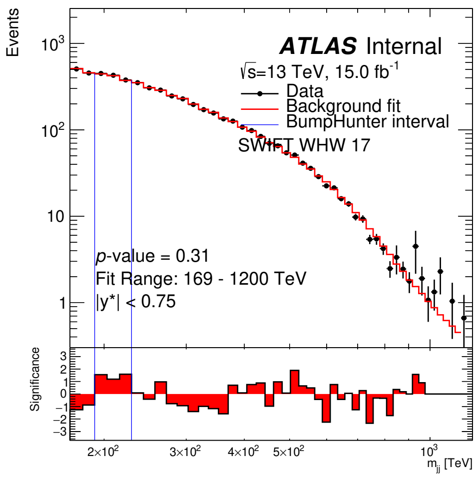

(b) photon ISR, inclusive photon + dijet trigger, ABCD 2-tagged spectrum, end point 1 TeV, `our5param`

Figure 95: Examples of fits in 15/fb of data in an ABCD-scaled 2-tagged spectrum, using the `our4param` and `our5param` functions.

7.9.2.2 Signal injection and spurious signal test

The robustness of the fit-based-background estimation technique is given by the following requirements:

- The background estimation must not exhibit localized excesses or deficiencies due to differences between the QCD shape and background estimation;
- If the background estimation is significantly affected by the presence of a signal, it must be identified and the signal window excluded;
- If the signal is present but at low levels such that it is not identified, the predicted background values must not be significantly affected, neither in the

region neighboring the signal nor globally.

All the studies performed across this section use the minimum window half-width obtained from the MC studies, as well as with neighboring smaller and larger window half-widths to understand the trends. Instead, the starting point for the half-width obtained in data will be only available after unblinding as discussed in Section 7.9.3.

A true spurious signal test can not be produced because of the lack of MC statistics for background samples. Therefore, instead of an MC-based spurious signal test, the analysis performs the signal injection studies described to prove that the background estimate will not be biased by the presence of a signal.

The background estimation procedure is tested in the presence of injected gaussian signals to study the dependence of the signal sensitivity in the search phase on the SwiFt window width and to validate the robustness of the background fit.

The injected signals have a relative width of 5% to 15% and are injected at all tested mass points in the fit mass range. In this study, the signal normalization is iteratively tuned to exceed the BumpHunter p-value threshold (0.01) set to remove the interval of the highest excess of the mass spectrum from the fit.

The background is derived from pseudo-experiments from a smooth fit to the 15/fb data spectra, drawing pseudo-data with statistics equivalent to the statistics of the full dataset. The signal-plus-background distribution is then fitted using the SWiFt algorithm with different window widths. The shape of the fitted background with signal injected is then compared to the shape of the background without any signal injected, allowing to understand the bias given by the possible signals against the statistical uncertainties.

As an example, in Figure 96, the curves in the main panel indicate the ratio to the background without any signal injected, for the case in which the signal normalization is below the BumpHunter 0.01 p-value threshold for removal of the window corresponding to the excess (”just above”, green graphs) and in the case when it does not (”just below”, blue graphs). The bottom panels show the bin-by-bin significance of pseudo-data vs background estimation in the two cases, with the light red area superimposed representing the significance from a fit to the pseudo-data without any signal injected.

The ”just below” case represents the bias to the background from having a signal-like fluctuation without being able to discover any signal, while the ”just above” case represents the case where the signal is found and removed, and the pseudo-data distribution is then refitted. We expect the bias from the ”just above” case if a signal is found and the corresponding window removed to be smaller than for the case where the window is not removed, so we decide on the minimal acceptable signal window using the ”just below” case. We consider the bias in the ”just below” case acceptable when contained within 3 sigma of the statistical uncertainties. In the example in Figure 96, we show one case in which the bias is not acceptable (Figure 96(a)), in the case of a wide signal close to the start of the fit range (400 GeV mass vs 300 GeV for the fit’s starting point), and one case in which the bias is acceptable (Figure 96(b)), in the case of a narrow signal in the middle of the fit range (750 GeV mass vs 250 GeV for the fit’s starting point).

We perform this test for all SWiFt half-window widths from 22 bins to 12 bins, for all signal mass points considered in the analysis (250 GeV to 1100 GeV) and for

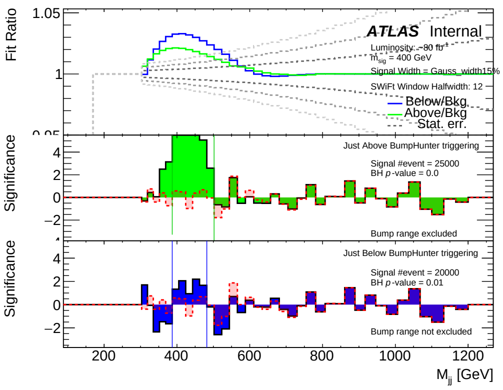

(a) Photon + dijet trigger, width=15%

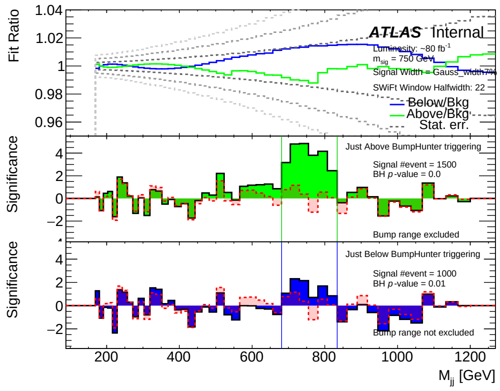

(b) Single photon trigger, width=7%

Figure 96: Comparisons of the fit in cases of inclusion/exclusion of the bump region for different Gaussian signals injected at the 400 GeVmass point for the photon + dijet trigger (left) and 750 GeVmass point for the single photon trigger (right). The green and blue curves on the top panel represent the ratios between background without any signal injected to the background with signal injected, in the green case after removing the most discrepant bins in all SWiFt fits and in the blue case without bin removal, mimicking the case in which the signal is just below the discovery threshold. The bottom two panels show the significance of signal+background with respect to the estimated background in the two cases (with and without signal exclusion, respectively). The significance of the deviations of the (pseudo-)data with respect to the background estimated starting from a distribution where there was no injected signal is overlaid in red, showing the intrinsic statistical fluctuations of the dataset.

the three Gaussian widths of 7%, 10% and 15%, and for each of the two inclusive channels. This test was not performed for the b-tagged channel as we did not unblind the data, and the MC statistics was insufficient, but since the statistics of the background is much lower we expect that it will be easier to fit the distribution using a global fit, which is more robust than SWiFt. Not all mass points are available, but we can draw conclusions by looking at the general trends in Figure 97 and Figure 98.

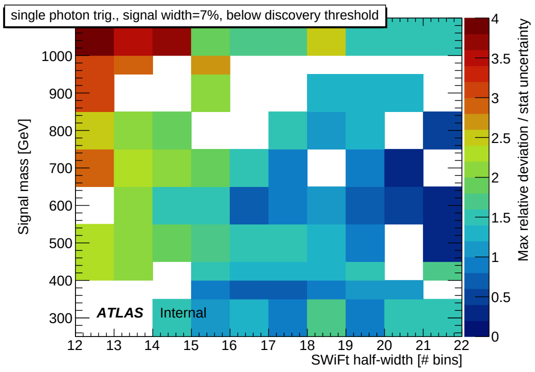

(a) Signal width 7%

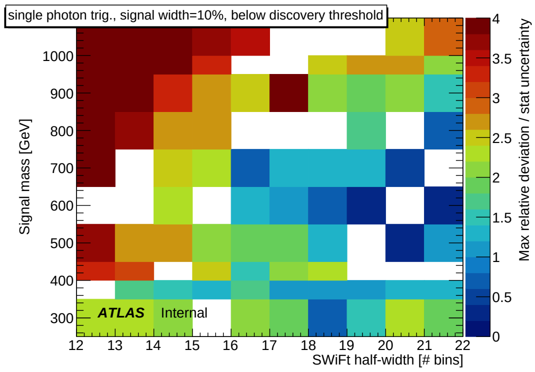

(b) Signal width 10%

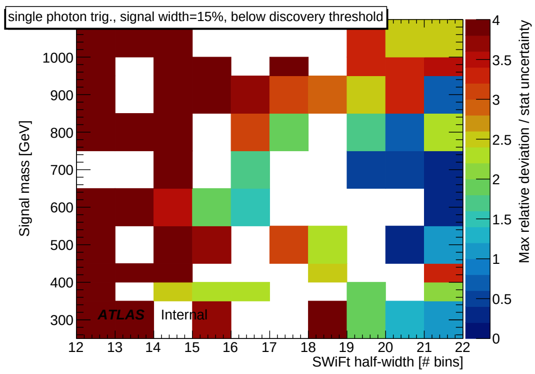

(c) Signal width 15%

Figure 97: Maximum possible background fit bias from a signal just below the discovery threshold within the dijet mass range 200 GeV - 1200 GeV, divided by the statistical uncertainty in the same bin. The plots show the results for single photon trigger using the three Gaussian widths of 7%, 10% and 15%.

In each bin of the plots in Figures 97 ands 98, the z-axis value is the ratio between the blue ”just below” curve and the grey statistical uncertainty line in the bin where the bias due to signal injection is largest; i.e. where the blue curve is at its peak. This therefore represents the number of standard deviations by which the fit is pulled at its maximum. The conclusions drawn from these plots affect both search and limit setting phase, since the presence of a non-detectable signal biasing the background estimation would mean a model-independent search is not sensitive to it. Based on Figures 97 and 98:

- we set the minimum acceptable SWiFt window half-width to 14 bins, as that

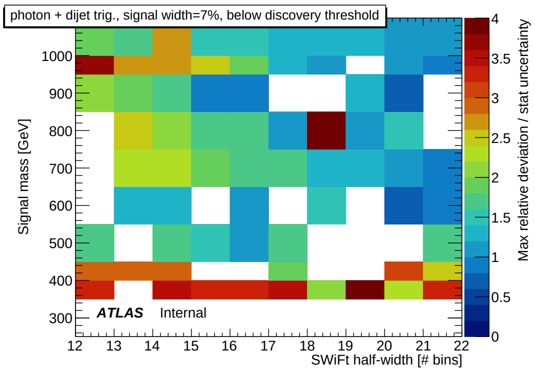

(a) Signal width 7%

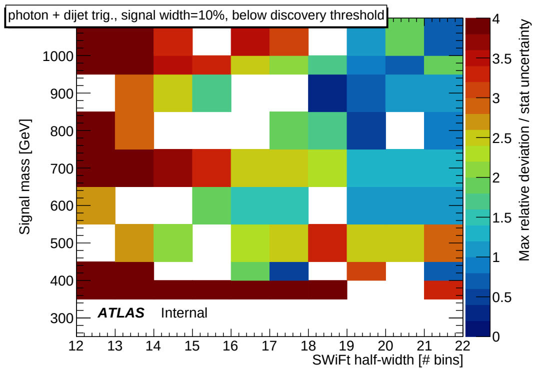

(b) Signal width 10%

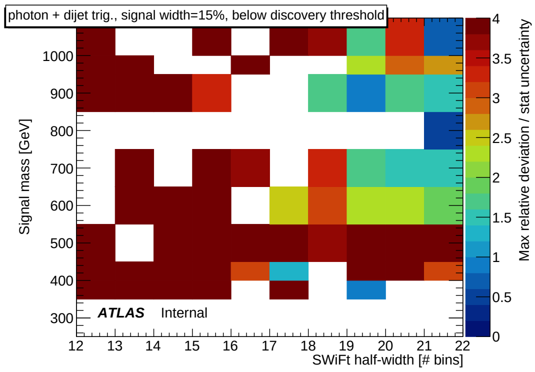

(c) Signal width 15%

Figure 98: Maximum possible background fit bias from a signal just below the discovery threshold within the dijet mass range 200 GeV - 1200 GeV, divided by the statistical uncertainty in the same bin. The plots show the results for the photon + dijet trigger using the three Gaussian widths of 7%, 10% and 15%.

ensures that the bias for signals of 7% and 10% in each of the two trigger selections remains below the threshold.

- If the SWiFt window half-width is smaller than 19 bins, we will not set Gaussian limits for widths of 15% for the single photon trigger, and we will not set Gaussian limits for widths of 15% for the dijet + photon trigger region.
- If the minimum acceptable SWiFt window half-width of 14 bins is reached, we will restrict the search region and the signals probed to 1 TeV rather than 1.2 TeV;

7.9.3 Unblinding procedure

All the studies shown in Section 7.9 indicates that the unblinded spectra can be well described using a sliding window fit with one of the selected functions and either a global fit or a window half-width of at least 14 bins. Nonetheless, a good-specification of the procedure is needed to define the parameters of the background estimation during the unblinding.

The unblinding procedure is defined as follows

1. The spectrum is fit using a global fit from the lowest starting points considered viable (169 GeV for the single-photon trigger spectra, and 335 GeV for the spectra triggered by the compound trigger), and subsequently, a sliding window fit (SWiFt), for the 5-parameter, 4-parameter, and UA2 functions. For the sliding window fit, start with a window with a wide half-width, ideally, the largest which the data and MC tests indicate might be useable, but necessarily one which gives a χ^2 $p-value$ above 0.05 in the tests (17).

2. In the case of the global fit, check whether two fit functions converged. In case of the sliding window fit, check whether the individual sliding window fits converged for at least two of the functions. If not, reduce the window size and start over.

3. For the fit functions that converged, check whether the global data-background χ^2 $p-value$ is above 0.05.

    - if yes, refit allowing for window exclusion and proceed with regular search and limit setting phase (BumpHunter $p-value$, if above a threshold of 0.01 proceed to set limits)
    - if not, we need to distinguish between a bad background description and an excess, so we refit excluding the most discrepant window and let the background for that window be estimated using the sidebands. Then we check the BumpHunter$p-value$ considering the whole spectrum, and the χ^2 and BumpHunter $p-value$ for the compatibility of the data and estimated background excluding the most discrepant window

At this point the procedure branches into two cases:

If the $p-value$ of both χ^2 and BumpHunter for the spectrum excluding the most discrepant window are above the predefined thresholds of 0.05 and 0.01, and the BumpHunter $p-value$ including the window is below 0.01, then there is an indication of an excess.

In this case, the next step is to proceed with applying systematic uncertainties to the background in the search phase. The description and validation of the systematic uncertainties are presented in Section 7.10.

If the $p-value$ of both χ^2 and BumpHunter for the spectrum even excluding the most discrepant window are still below the predefined thresholds of 0.05 and 0.01, they are the indication of a bad background estimation. So, the window half-width is decreased by one bin, and the procedure repeated. The procedure continues until two functions satisfy the criteria above (with the same window width). The fit function with the largest χ^2 $p-value$ is chosen as nominal. If the window half-width becomes too narrow that the sensitivity to the signals sought is lost as shown from the signal injection tests, then the procedure is repeated removing one bin from the lowest mass region at a time. The reason for requiring at least two functions to pass the criteria for a good fit when unblinding is that the alternate description of the background is available. The uncertainty will be defined from it, as described in Section 7.10.

7.10 Systematic uncertainties

This section presents all the uncertainties used in the analysis. The uncertainties due to the jet energy scale must be applied only to the background or to the signal, but not to both, in order to properly estimate their impact. Thus, only uncertainties relevant to the fitting procedure are applied to the background estimate and all uncertainties referred to Monte Carlo are applied to the signal samples.

7.10.1 Uncertainties applied to the background estimate

There are two systematic uncertainties are related to the background estimation method: one due to the fit function choice and other associated to the fit quality. The latter is related to the statistical uncertainty of the dataset being fitted, and is the dominant of the two uncertainties. The details of each uncertainty are as follows:

Function choice: As discussed in Section 7.9.3, the function with the best χ^2 $p-value$ in the unblinding procedure is taken as the nominal function and at least two more functions are required to pass the criteria. From those two, that one with worst perform is then taken as an alternate.

The difference between the nominal and alternate fit functions is used to define an uncertainty that is permitted to change between the fit function and the alternative one maintaining a directionality, even if the nominal and alternate functions cross. A detailed description of how the fit function uncertainty is implemented in the limit setting can be found in [12].

Fit quality: Ideally, the uncertainty associated with the quality of the fit would be determined by the covariance matrix of the fitted parameters. However, there are cases where the likelihood function has a badly-behaved maximum, so it is not possible to compute this covariance matrix.

Thus a different method is required. Since the confidence interval on a function is meant to represent the 1σ region within which the fit would fall in the large-number limit of repeated trials, it can also be found by throwing pseudo experiments and fitting each. This method does not need an accurate estimation of the parameter errors; instead, the pseudo experiments are generated using Poisson statistics based on H_0 so only the fit itself is required. Here, as before, H_0 is defined from the nominal fit; that is, the fit to the real data. A large number of these pseudo-datasets are generated, each is fit using the same starting conditions as the observed data, and the error on the fit in each bin is defined to be the RMS of the function value in that bin for all the pseudo experiments.

Figure 99 shows the two uncertainties for a sliding window fit with window half-width of 23 bins. The demonstration plot uses the 15 fb^{-1} sample dataset with the inclusive selection and the compound trigger. In this example, the nominal fit is taken from the dijet 4-parameter function, while the UA2 function is taken as the alternate. The statistical uncertainty (fit quality uncertainty) is dominant across the M_{jj} range. There are noticeable variations in the function choice uncertainty for different mass ranges; this is an expression of the average differences between the fit functions in different regions of M_{jj} .

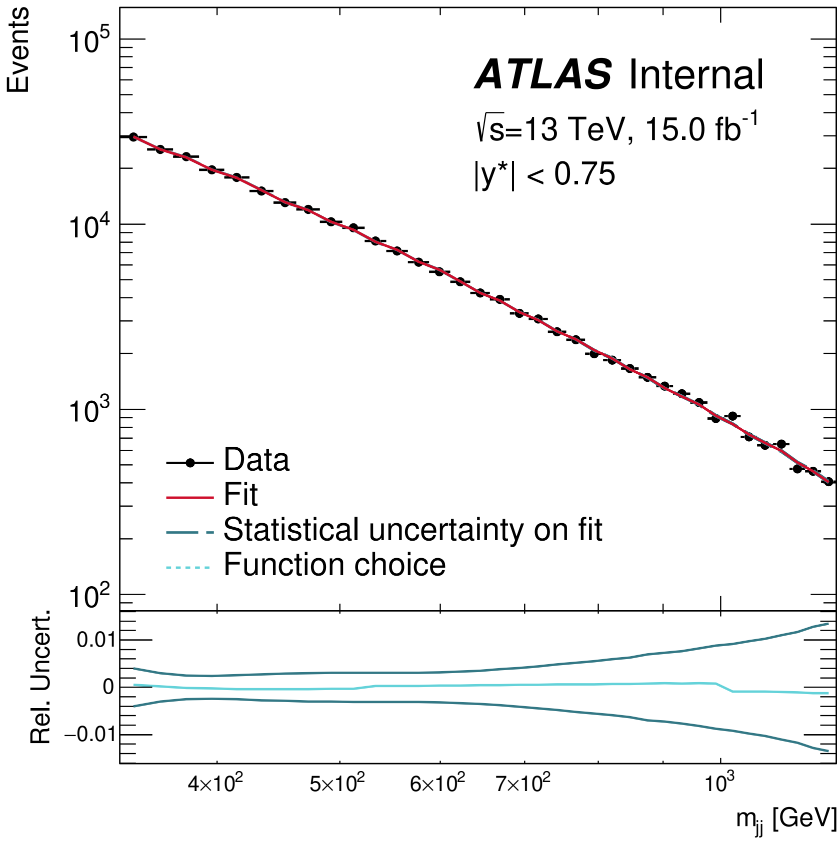

Figure 99: Fit quality uncertainty (dark blue) and fit function choice uncertainty (light blue) in an example fit to a statistically non-sensitive data sample using the compound trigger and inclusive selection. The fit quality uncertainty is symmetric while the fit function choice uncertainty is treated as asymmetric to preserve the directionality when the two fits cross one another.

7.10.2 Uncertainties applied to the signal

The systematic uncertainties applied to the signal are the jet energy scale (JES); jet energy resolution (JER); photon ID, energy scale, and resolution; *b-tag* scale factor uncertainties; luminosity; and PDF parameter choice. Details of each are given below.

Jet energy scale and resolution

JES
A jet energy scale (JES) uncertainty is applied to the signal templates, following the JetEtMiss group recommendations. The number of uncertanties regarding the JES is the strongly-reduced to 4 nuisance parameters. The JES uncertainty ranges from around 8% for jets of $p_{\mathrm{T}}\sim$ 25 GeV to 1% for jets of $p_{\mathrm{T}}\sim$ 750 GeV.

An example of the variation due to each nuisance parameter is given in Appendix B.10.1. All the uncertainties act not on the acceptance but rather on the peak location, moving it to higher or lower M_{jj} as events move between bins. This effect is accounted for in the limit setting procedure by using MC templates for $\pm1, 2, 3\sigma$ in each of the uncertainties and allowing all four to be marginalized independently.

This approach is only valid for the Z' model-dependent limits; the Gaussian limits require an approximation of this effect which is discussed in Section 7.10.3.

JER
The uncertainty on the jet energy resolution (JER) is also estimated by varying signal templates according to JetEtMiss recommendations. Unlike the JES, the effect is not to change the signal peak location, but rather to widen the peak somewhat. The impact is hard to see bin-by-bin, as the statistics of affected bins are quite low and the fluctuations vary dramatically. Instead of using the variation between the templates and propagate very statistically dependent effects, average trends are examined to look for a single treatment that can be applied across samples. The Appendix B.10.1 shows the effects of varying the JER on two signal sample templates.

For this procedure, the binning is increased to 50 GeV and the weighted average effect between all samples is taken as the value in each bin. This is sufficient to reduce the statistical fluctuations and extract the size of the underlying uncertainty. A linear fit is performed to the resulting distribution. Based on the fits, a flat 3% JER uncertainty will be applied in both channels.

Photon ID, energy scale and resolution

The *photon energy scale* and *resolution uncertainties* are determined following the recommendations of the EGamma CP. Both of these uncertainties can affect signal acceptance by determining whether or not a photon passes the trigger-based offline p_{T} requirement, but it does not affect the shape of M_{jj} . The impact on a representative Z' point (450 GeV, $g_q = 0.2$) is shown in the Appendix B.10.1, it can be seen that the effects alter the normalization of the sample but not the peak shape or location.

As the uncertainties evaluated in each sample are statistically limited, a method was explored for deriving a value of the uncertainty which could be applied to all signal samples. Instead of relying on the differences between MC templates, the variation in each signal point due to the systematics were plotted together to understand the overall behavior and determine if it could be used to derive a statistics-robust evaluation of the uncertainty as a function of M_{jj} . The results are shown in the Appendix B.10.1. No difference is expected for the doubly *b-tag* selection, but the statistics are smaller, so the inclusive selection is used to derive the uncertainty.

The *photon ID scale factor* uncertainty affects the MC weights of the events which have passed the selection, thus only the normalization of the signal templates may change. As a consequence, it shows less statistical fluctuation than the energy scale and resolution uncertainties, which vary in which events pass selection rather than their weights. They are nevertheless evaluated using the same technique as the previous uncertainties to determine a single consistent treatment across the signal samples.

Thus the effects of photon energy scale, resolution, and ID scale factor are treated purely as acceptance uncertainties, with a single fixed-size covering all three uncertainties of 2% for the single-photon trigger and 1.4% for the compound trigger. One parameter will be used to scale the number of events in the signal template.

Trigger efficiency

From the studies in Section 7.4, it was noticeable that the compound trigger never reaches a perfect plateau of 100% efficiency even after all analysis cuts are applied. To determine how the trigger inefficiency uncertainty should be applied, the trigger efficiency as a function of M_{jj} is calculated. The same curve is computed for the single-photon trigger for comparison. In both cases, all analysis cuts except for minimum M_{jj} are applied, including relevant photon and jet p_{T} cuts as well as the y^* cut.

The trigger efficiency versus M_{jj} for each trigger can be found in Appendix B.10.1, overlaid with a horizontal line fitted to the data points in each. No obvious dependence of the efficiency on M_{jj} is visible; the apparent approach to full efficiency at high mass is an effect of the decreasing statistics. Based on these fits, an uncertainty of 3% is applied in the compound trigger channel to account for trigger inefficiency. No such uncertainty is applied for the single-photon trigger where the efficiency is essentially 100%.

b-tagging scale factors

The b-tagging efficiency for b, c, and light-jets uses simulated event samples that have applied around 25 scale factors to compensate for differences between data and simulation. The uncertainties of those scale factors are provided by the flavor-tagging CP group.

To take into account these uncertainties, the signal templates were produced variating each of these scale factors. As all of them were very small, a conservative simplification was made by taking the sum in quadrature of all of them and applying the result parameterized by a single nuisance parameter. It was then determined using a similar method to that of the photon energy uncertainties:

1. first, the impact on each signal sample was estimated to ensure it changed only normalization and not shape.

2. next, the impact bin by bin of each scale factor uncertainty was plotted for all signal samples, to ensure the size of the effect depended only on M_{jj} and not

on the individual sample being considered.

3. finally, the quadrature sum of the impact of all 25 uncertainties was averaged across the signal samples and a parameterization found for it which could be used on each sample, thereby producing an uncertainty robust against statistical fluctuations in the individual samples.

The overlay of bin-by-bin uncertainty sizes for the four largest uncertainties can be found in Appendix B.10.1. In some cases a substantial dependence of the uncertainty on M_{jj} is visible, but in all four cases, the size of the uncertainty does not depend significantly on the signal sample being examined. The same pattern is seen for the remaining 21 smaller uncertainties. This demonstrates that it is safe to use the collective information of all the signal samples to derive a single uncertainty robust to statistical fluctuations which can be applied to all individual samples.

The total uncertainty is relatively flat until about M_{jj} of 300 GeVwhen it begins to increase in a fairly linear way. To evaluate this M_{jj} dependence in more detail, a weighted average of the values in each bin is plotted, and a linear fit is performed from 300 GeVto 1200 GeV. A flat value of 5% can be used from 170 GeVto 300 GeV. Thus the total *b-tag* uncertainty used in both single photon trigger and compound trigger 2 *b-tag* channels is 5% for $M_{jj} < 300$ GeV and $0.0001115(M_{jj} - 300) + 0.05$ for 300 GeV $< M_{jj} < 1200$ GeV.

Luminosity

The uncertainty on the integrated luminosity is handled as a single normalization uncertainty applied to the signal templates following the recommendations of the ATLAS luminosity working group. For the single trigger photon channels, its value is taken to be $\pm 2.0\%$. and for the compound trigger photon channels is $\pm 2.3\%$. In both cases, the luminosity uncertainty is applied as a scale factor on the signal sample.

PDF choice and parameters

PDF uncertainties principally affect the normalization of the signal rather than the shape of the distributions. To determine the effect, events are generated using the ensemble of PDFs provided by the NNPDF group. The differences in acceptance are calculated for each member of the ensemble and, following the physics modeling group recommendation, the standard deviation of all acceptance variations is assigned as a systematic uncertainty. For this purpose, the mass distribution after the analysis selection and all relevant weights as a function of mediator mass is calculated for each pdf variation (see Appendix B.10.1). The results showed that the systematic uncertainty is less than 1% everywhere. Thus a 1% flat systematic was applied on the signal normalization.

7.10.3 JES uncertainty for model-independent limits

Most of the uncertainties on the background estimate are unchanged between model-dependent and model-independent limits. The acceptance uncertainties due to JER, photon energy scale and resolution, b-tagging scale factors, and luminosity can all be applied to Gaussian-shaped signals in the same way as to the Z'samples. Not the same for the PDF uncertainty, which is not applied to Gaussian limits since it is a theory-dependent uncertainty.

To simulate the effects of JES on a real signal for use with the Gaussians, the impact on the M_{jj} value of the signal peak due to the uncertainty must be measured and can then be applied to move the mean of the Gaussian template. To this end, a Gaussian fit is performed to the core of each signal template as well as to the $\pm 3\sigma$ variations in each JES uncertainty component.

The equivalent fit is repeated for each point and the resulting shift in the fitted mean location is added in quadrature across the four independent nuisance parameters. The Z' coupling values with the largest number of mass points are shown, but the other couplings behave similarly. The fits are less reliable in the 2 *b-tag* channel due to the very low statistics, and in particular tend to fail for the $+3\sigma$ variations due to the shape of the signal. Thus the larger shifts in the -3σ direction should be taken as the more reliable estimate of the uncertainty size. In every case, the shift in the mean is found to be $\leq 2\%$. Therefore this value is chosen for use in the model-independent Gaussian limits.

7.10.4 Summary of uncertainties

A summary of all uncertainties for each channel is presented in Table 17.

Uncertainty	Inclusive, single γ trig.	Inclusive, compound trig.	2 *b-tag* , single γ trig.	2 *b-tag* , compound trig.
Fit statistics	0.5% - 10% of background, depending on channel and M_{jj}			
Fit function choice	0.5% - 10% of background, depending on channel and M_{jj}			
JES	Templates for Z', 2.0% shift in Gaus. mean for model-independent limits			
JER	3.0%	3.0%	3.0%	3.0%
Photon related	2.0%	1.4%	2.0%	1.4%
Trigger efficiency	–	3.0%	–	3.0%
b-tag SFs	–	–	~5.0%-15.0%	~5.0%-15.0%
Luminosity	2.0%	2.3%	2.0%	2.3%
PDF	1.0% Z', none for model-independent limits			

Table 17: Summary of all uncertainties used in limit setting, by channel.

7.11 Results

The search phase results for the 4 analysis spectra: inclusive using the single-photon trigger, inclusive using the compound trigger, 2 *b-jets* using the single-photon trigger, and 2 *b-jets* using the compound trigger are shown in Figure 100. No evidence of new physics is observed in any channel. The BumpHunter $p - value$ for the four channels range from 0.59 to 0.97 as specified in the plots and in Table 18. The lower panel displays the difference between data and the fit calculated from Poisson statistics and converted to a number of standard deviations following the convention described in [59].

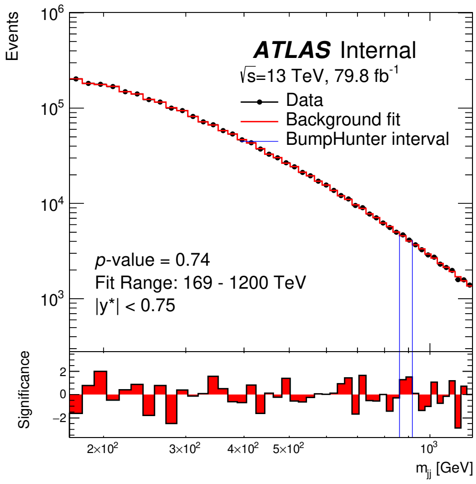

(a) Inclusive, single photon trigger

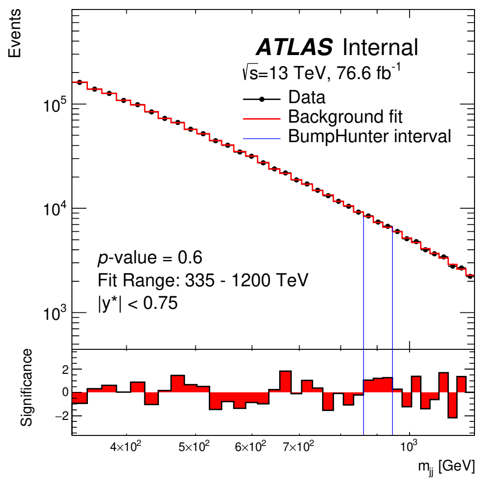

(b) Inclusive, compound trigger

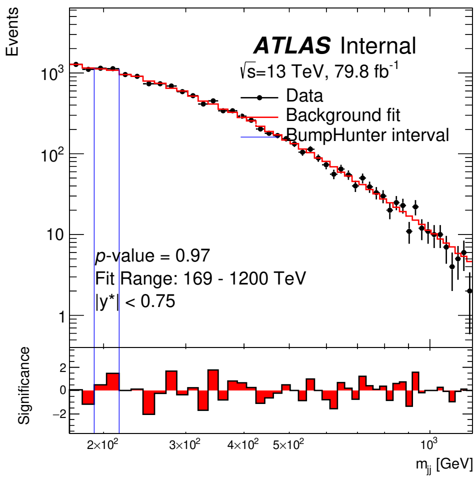

(c) 2 *b-jets* , single photon trigger

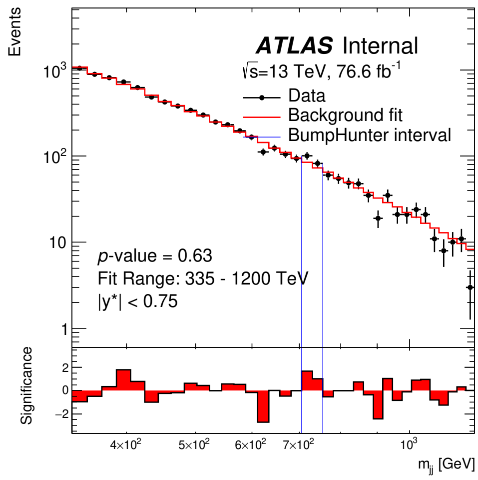

(d) 2 *b-jets* , compound trigger

Figure 100: Search phase results for the four analysis channels: inclusive using the single photon trigger (100(a)), inclusive using the compound trigger (100(b)), requiring two *b-jets* with the single photon trigger (100(c)), and requiring two *b-jets* with the compound trigger (100(d)). In each case a sliding window fit was used with the function and window half width identified by the procedure and noted in Table 18. The blue vertical lines indicate the region of greatest excess in each case; no observed excess is statistically significant.

The unblinding procedure specified in Section 7.9.3, selects a nominal and alternate fit function and a SWIFT window half-width above the specified minimum value. The alternate function was defined as the function with the worst χ^2 $p-value$in each channel which passes the requirements for an acceptable fit.

The starting location for the fits in the compound trigger channels was adjusted from the first optimistic minimum of 303 GeVto a final value of 335 GeV in accordance with the unblinding procedure,to work around a residual effect of the trigger

Channel	Nominal function	Alternate function	Fit low edge	Fit high edge	SWIFT whw	BH $p-value$	χ^2 $p-value$
Single γ trigger, inclusive	`our5param`	`our4param`	169 GeV	1200 GeV	19	0.74	0.11
Compound trigger, inclusive	`our4param`	`UA2`	335 GeV	1200 GeV	23	0.60	0.23
Single γ trigger, 2 *b-jets*	`our4param`	`our3param`	169 GeV	1200 GeV	23	0.97	0.75
Compound trigger, 2 *b-jets*	`our3param`	`our5param`	335 GeV	1200 GeV	23	0.63	0.53

Table 18: The BumpHunter $p-value$ for the four channels range from 0.59 to 0.97

turn-on present in the first two bins.

Figure 101 shows the final sizes of the fit uncertainty and fit function choice uncertainty, derived from the unblinded data as described in the previous section. Since no evidence of new physics was observed, the same nominal and alternate functions selected in each spectrum are used in the limit setting procedure described in the following two sections.

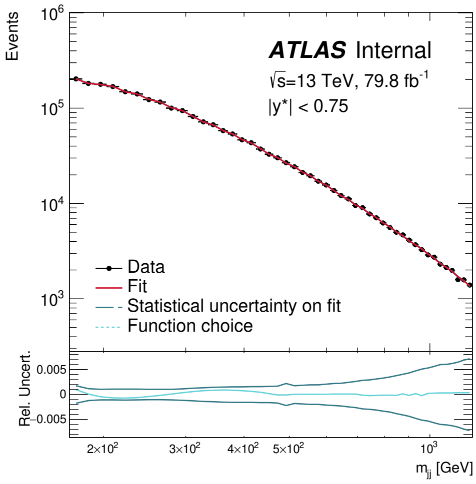

(a) Inclusive, single photon trigger

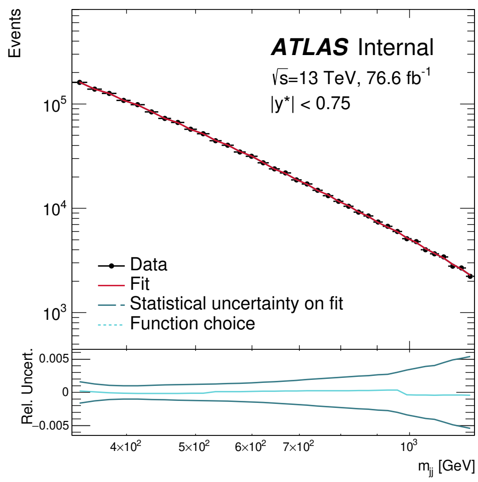

(b) Inclusive, compound trigger

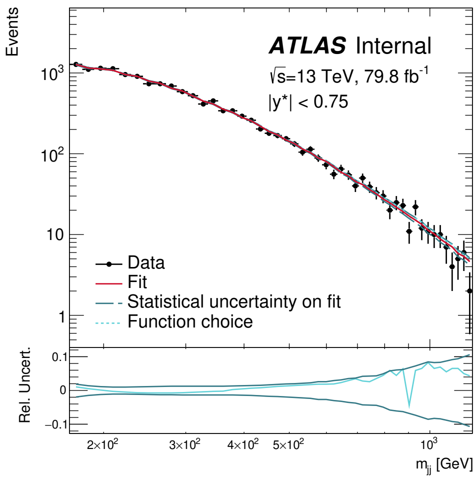

(c) 2 *b-jets* , single photon trigger

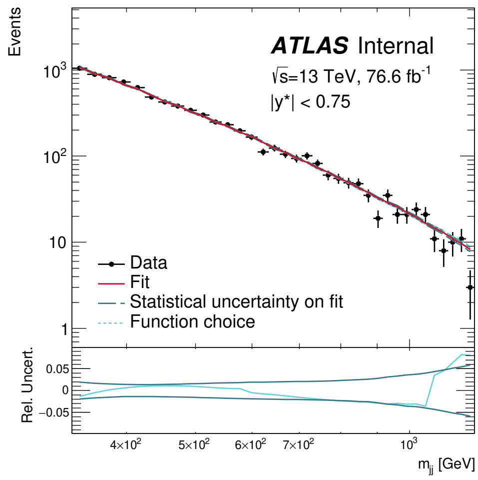

(d) 2 *b-jets* , compound trigger

Figure 101: Fit uncertainty and function choice uncertainty determined from unblinded data in each of the four channels: inclusive using the single photon trigger (101(a)), inclusive using the compound trigger (101(b)), requiring two *b-jets* with the single photon trigger (101(c)), and requiring two *b-jets* with the compound trigger (101(d)).

7.11.1 Limit setting procedure

In absence of signal, the limits on the possible number of events from resonant new physics processes must be set.

The Bayesian method documented in ref. [30] is applied to data at these same mass points to set a 95% CL limit on the cross-section times acceptance, $\sigma \times \mathcal{A}$, for the new phenomenal (NP) signal as a function of m_{NP}, using a prior constant in signal strength. The limit on $\sigma \times \mathcal{A}$ from data is interpolated logarithmically (that is, linearly in the log of the cross-section) between mass, points to create a continuous curve versus M_{jj} . The exclusion limit on the mass (or energy scale) of the given NP signal occurs at the value of M_{jj} where the limit on $\sigma \times \mathcal{A}$ from data is the same as the theoretical value, which is derived by interpolation between the generated mass values.

Also, the limits for the generic signal are approximated using a Gaussian line shape. This provides a limit on the cross-section times acceptance times efficiency times branching ratio which can be applied to any model which would approximate this shape after the analysis selection [38].

This form of analysis applies to all resonant phenomena where the NP couplings are strong compared to the scale of perturbative QCD at the signal mass, so that interference with QCD terms can be neglected.

7.11.2 Model dependent limits

This section shows the limits set on the benchmark Z' model following a Bayesian procedure. All uncertainties discussed in Section 7.10 have been accounted for when calculating these results, and the signal samples were generated in both mc16a and mc16d weighted according to the proportion of luminosity made up by each year of data taking. The limits as a function of Z' mass are calculated independently for the two values of the SM quark coupling g_{SM} which are above and below the theoretical excluded cross section. These limits are shown in Figures 102–105.

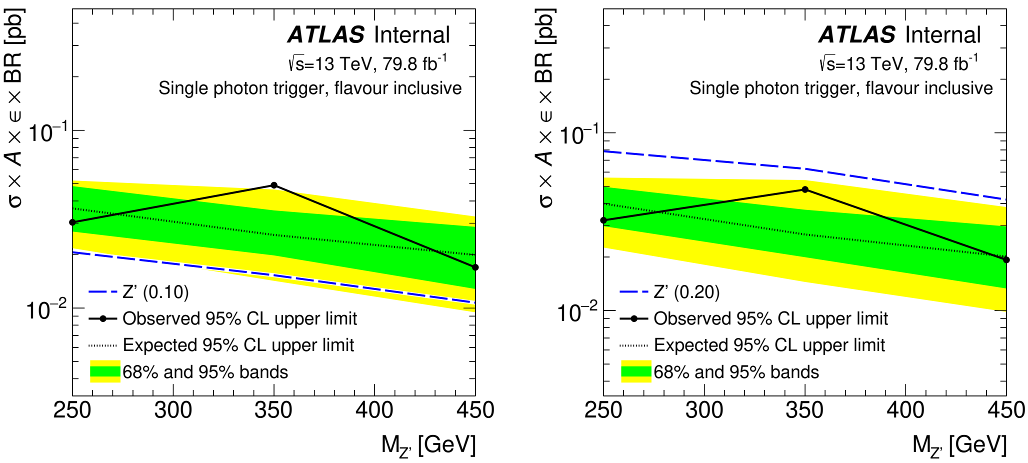

(a) $g_{SM} = 0.1$

(b) $g_{SM} = 0.2$

Figure 102: Limits set using Z' benchmark model using the single photon trigger and the inclusive selection. All uncertainties are applied. The two coupling values relevant for the model exclusion are shown. All samples use the photon filter at 100 GeV.

A single summary exclusion across all coupling values is presented combining the results from the single and compound triggers in each channel to produce a single plot. The different coupling possibilities are combined by interpolating the limit

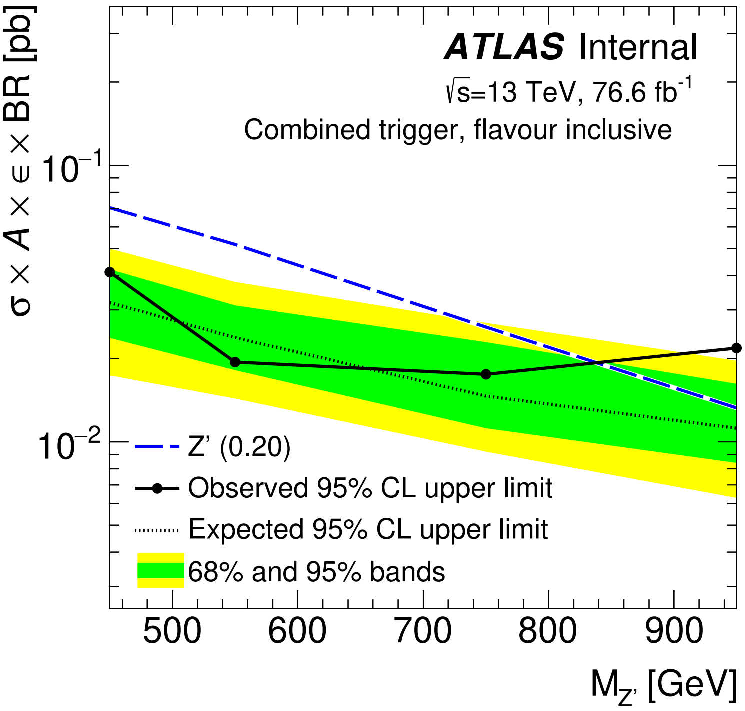

Figure 103: Limits set using Z' benchmark model using the compound trigger and the inclusive selection. All uncertainties are applied. Only the $g_q = SM = 0.2$ coupling was generated for the samples with photon filter at 50 GeV, so only this coupling is shown.

results across coupling as well as mass. The final result is a single two-dimensional plot of limit versus coupling and M_{jj} for each of the inclusive and two *b-tag* selections. The limits from the plots shown above, with couplings of $g_q = 0.1$ and $g_1 = 0.2$, are used as inputs. These final plots are shown in Figures 106 and 107.

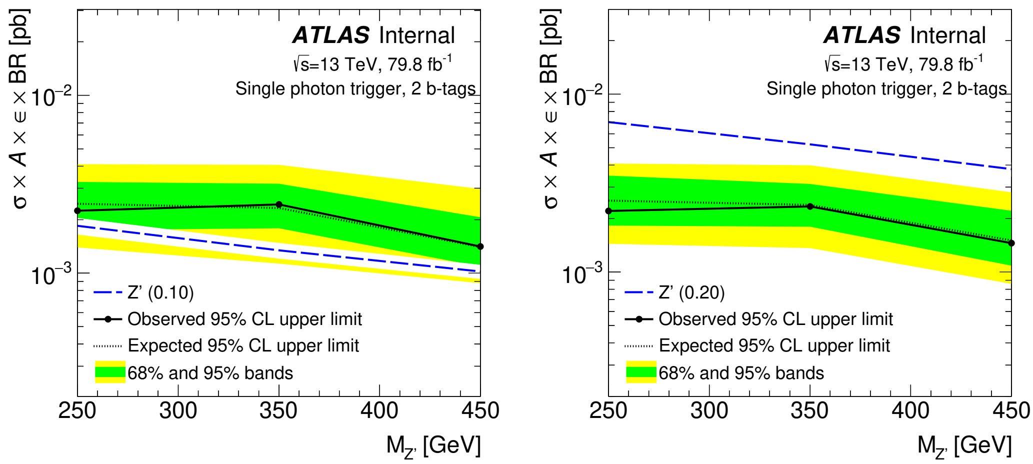

(a) $g_{SM} = 0.1$ (b) $g_{SM} = 0.2$

Figure 104: Limits set using Z' benchmark models using the single photon trigger and the 2 *b-tag* selection. All uncertainties are applied. The two coupling values relevant for the model exclusion are shown. All samples use the photon filter at 100 GeV.

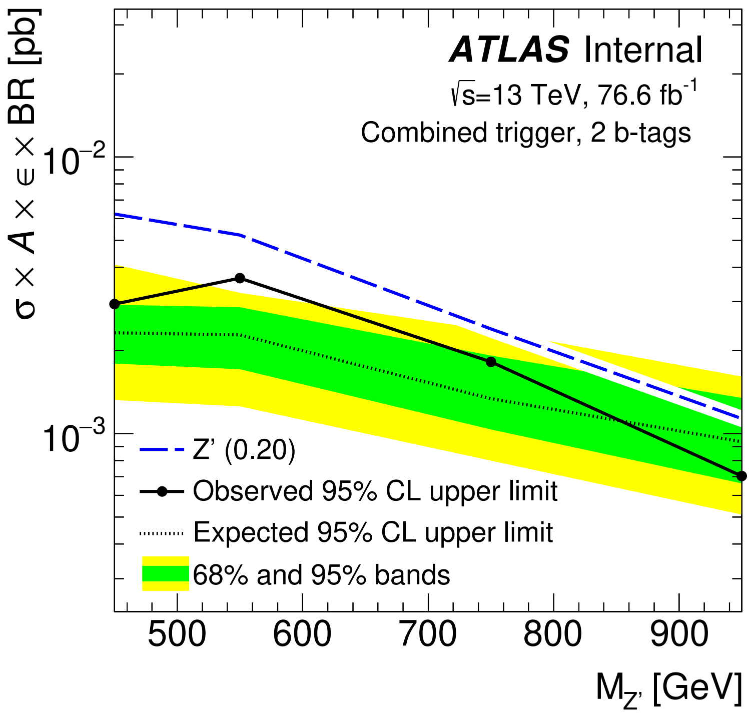

Figure 105: Limits set using Z' benchmark models using the compound trigger and the 2 *b-tag* selection. All uncertainties are applied. Only the $g_q = SM = 0.2$ coupling was generated for the samples with photon filter at 50 GeV, so only this coupling is shown.

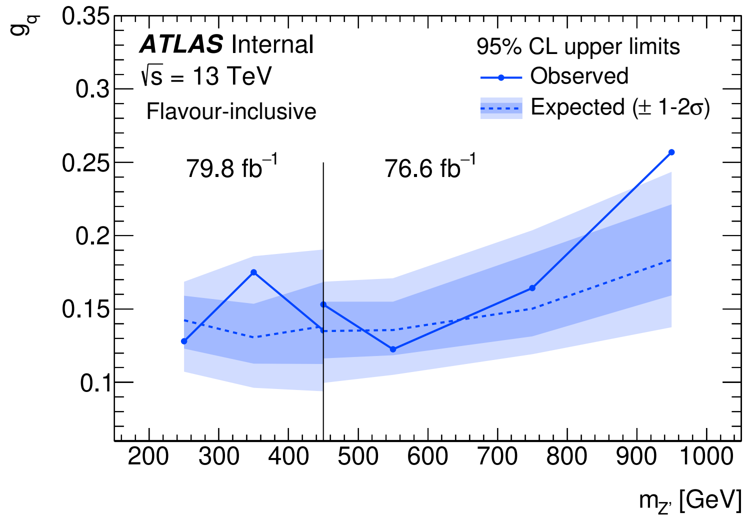

Figure 106: Limits on Z' mediators as a function of coupling and mass, using the inclusive selection. Limits up to masses of 450 GeVare set using the single photon trigger; above this mass the compound trigger is used. All uncertainties are applied.

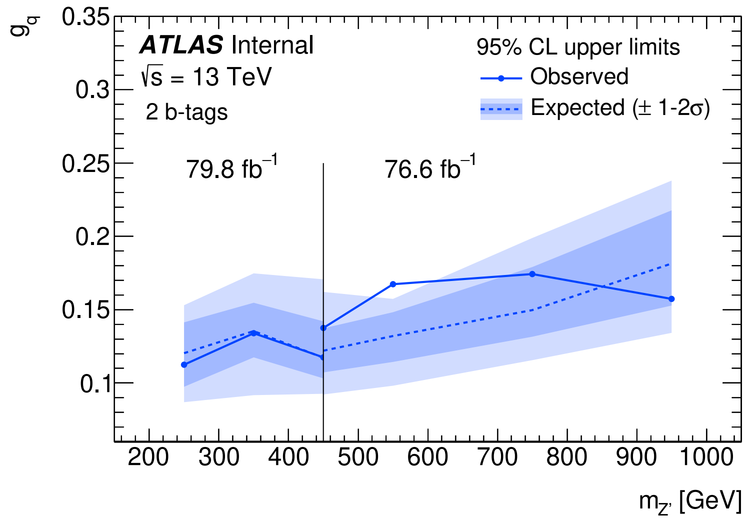

Figure 107: Limits on Z' mediators as a function of coupling and mass, using the 2 *b-tag* selection. Limits up to masses of 450 GeVare set using the single photon trigger; above this mass the compound trigger is used. All uncertainties are applied.

7.11.3 Model independent limits

The model-independent limits are set using Gaussian template shapes. These represent the maximum cross-section times analysis acceptance times efficiency times branching ratio for any process which, after application of the analysis selection, has a shape that can be approximated as a Gaussian. Signal-related uncertainties are equivalent to those used for the model-dependent limits. Figure 108 shows the Gaussian limits with no systematic uncertainties considered. Figure 109 shows the Gaussian limits including all relevant uncertainties in each channel, as described in Table 17. The systematic shift is dominated by the b-tagging scale factor uncertainty in the channels with 2 *b-jets* , and even in the inclusive channel the addition of another small scale factor to the existing combination of luminosity $\oplus$ photon E/R $\oplus$ JER $\oplus$ PDF should be negligible.

As for the model-dependent limits, only one limit value is reported at each mass point, so the two plots in Figures 110 and 111 will be shown. While the y-axis is shared between the two selections in these plots, the signal acceptance varies, and thus the two sets of limit points relate to two different interpretations of $\sigma \times A \times \epsilon \times$ BR. For example, after accounting for the difference in filter efficiency between the samples used for the two triggers, the acceptance for a Z' of mass 550 GeVis about twice as large for the compound trigger as for the single-photon trigger. This is also illustrated in Figure 90. When comparing to an actual theoretical prediction, this acceptance must be taken into account.

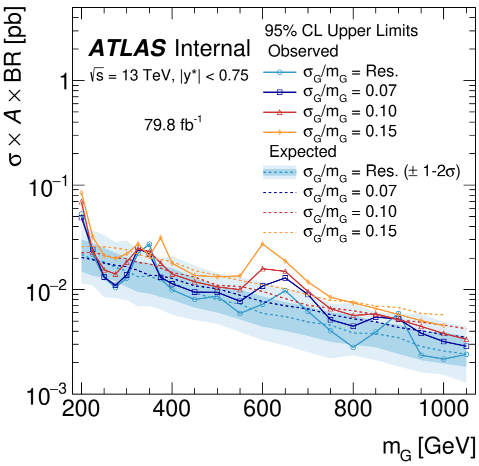

(a) Inclusive, single photon trigger

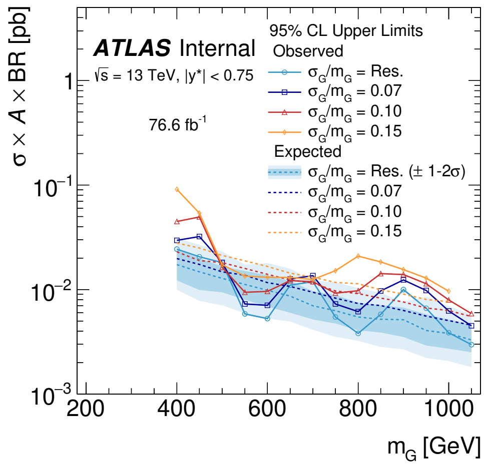

(b) Inclusive, compound trigger

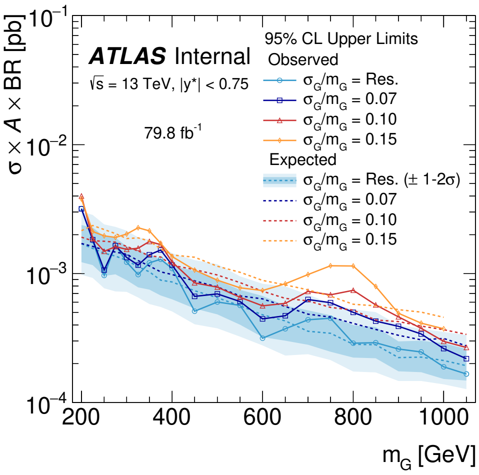

(c) 2 *b-jets* , single photon trigger

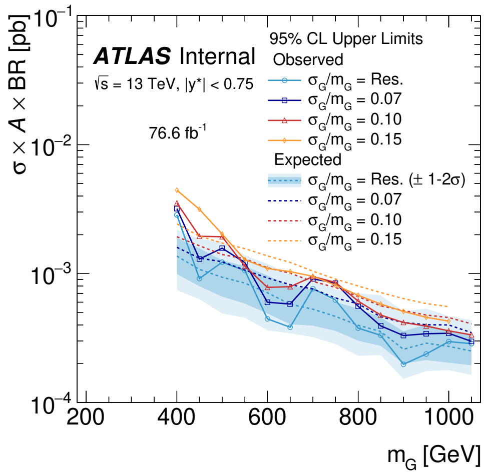

(d) 2 *b-jets* , compound trigger

Figure 108: Limits on generic Gaussian shaped signals of 15%, 10%, 7% or M_{jj} resolution width in each of the four channels. No uncertainties are applied; the limit at each point is strongly determined by the statistics in the relevant portion of the data spectra.

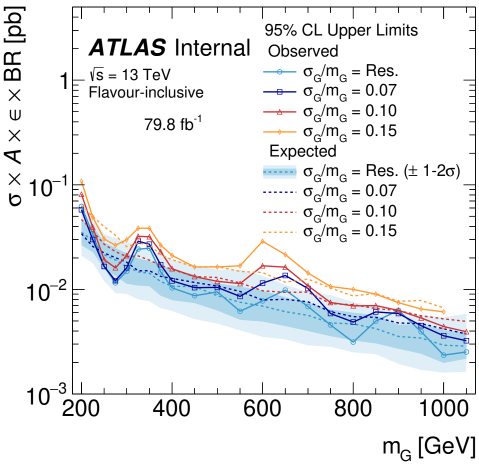

(a) Inclusive, single photon trigger

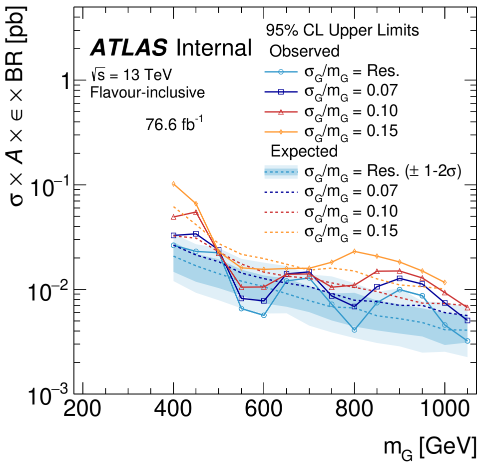

(b) Inclusive, compound trigger

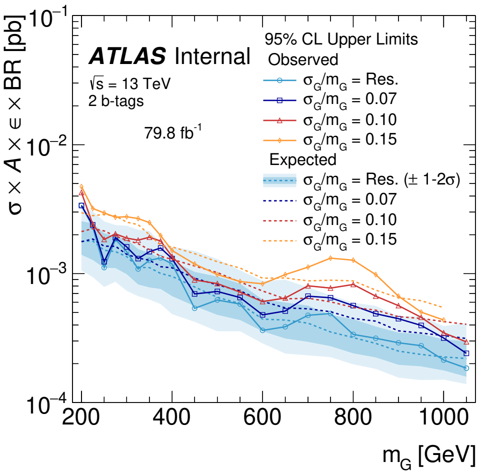

(c) 2 *b-jets* , single photon trigger

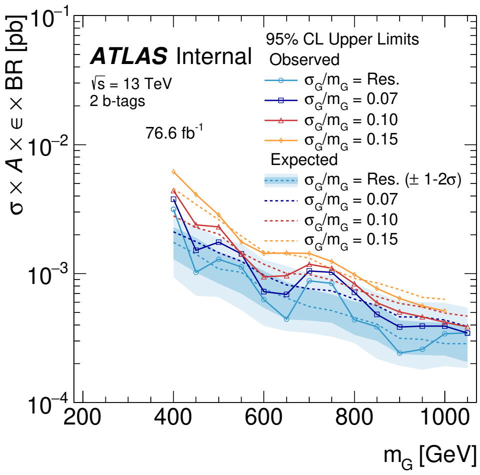

(d) 2 *b-jets* , compound trigger

Figure 109: Limits on generic Gaussian shaped signals of 15%, 10%, 7% or M_{jj} resolution width in each of the four channels. All uncertainties are applied.

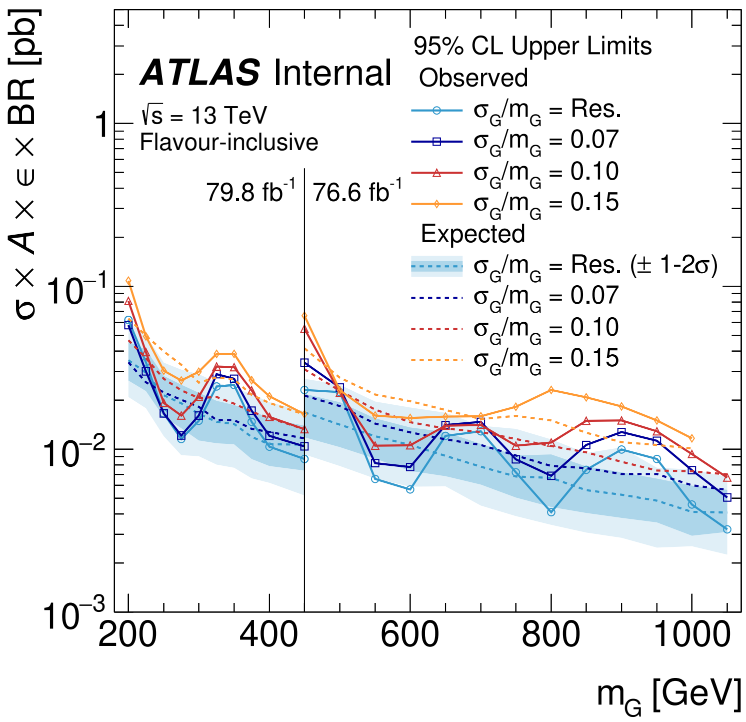

Figure 110: Limits on generic Gaussian shaped signals of 15%, 10%, 7% or M_{jj} resolution width using the inclusive selection. Limits up to masses of 450 GeV are set using the single photon trigger; above this mass the compound trigger is used due to its greater sensitivity. All uncertainties are applied. The acceptances of the two selections shown are different and must be accounted for when comparing the sensitivity.

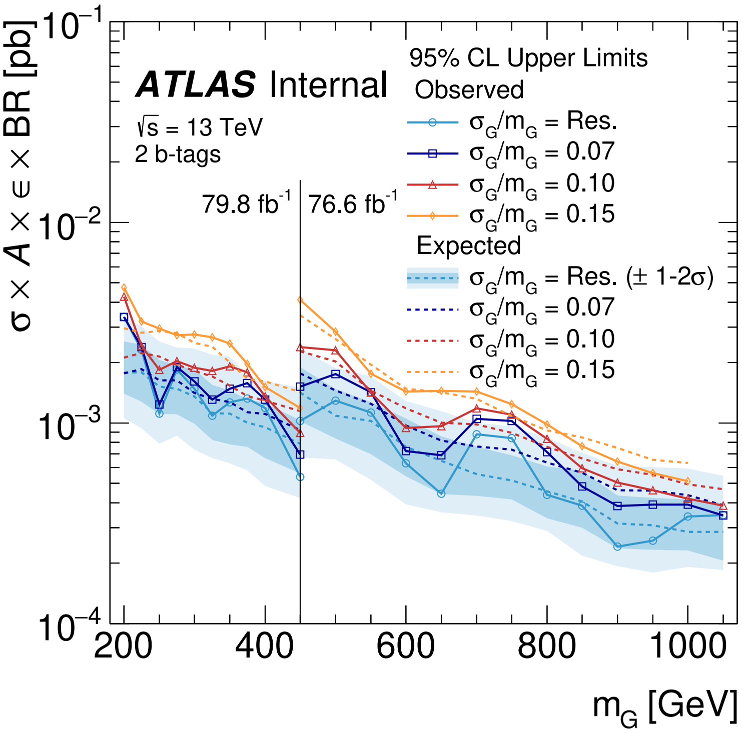

Figure 111: Limits on generic Gaussian shaped signals of 15%, 10%, 7% or M_{jj} resolution width using the 2 *b-tag* selection. Limits up to masses of 450 GeV are set using the single photon trigger; above this mass the compound trigger is used due to its greater sensitivity. All uncertainties are applied. The acceptances of the two selections shown are different and must be accounted for when comparing the sensitivity.

8 Conclusions

The work presented throughout this thesis belongs within the framework of the experimental high energy physics and was carried out in the ATLAS experiment at CERN. It includes two different analyses that involve different physics processes and uses the measurements of two of the main components of the ATLAS detector: the inner detector and the calorimeters. The first analysis is a study of the distributions of charged primary particle distributions, that are important to reflect the strong interaction with low momentum transfer and are essential to constrain free parameters of Monte Carlo event generators allowing to get an accurate description of *pp* interactions. In addition, this study explores a new phase-space in the low momentum region of the tracks, that are the experimental observation of the passage of charged particles throught the detector.

The second analysis is a search for new physics. Since any strongly interacting new particle produced in *pp* collision will mostly decay into a pair of quarks, and reconstructed later as a pair of jets. Searches of localized excess in the dijet mass distributions are an important tool for the quest of new physics.

The first analysis is based on the *"Charged-particle distributions at low transverse momentum in $\sqrt{s}$ =13 TeV pp interactions measured with the ATLAS detector at the LHC"* paper [41]. The aim is to study the charged-particle density as a function of the pseudorapidity and the transverse momentum of the tracks. It also studied the average value of the transverse momentum as a function of the number of charged particles. All these distributions are important because they provide a data-driven correction to the simulation-based track-reconstruction, and allow us to reduce the systematic uncertainty and to obtain better results to be used in the tuning of Monte Carlo event generators.

The selected data was corrected with an event and a track weight, taking into account the inefficiencies in the reconstruction processes and the contributions of non-primary particles. Then it was unfolded using a Bayesian method to deconvolute the effects of the detector resolution. Lastly, the data was compared to the predictions of PYTHIA 2, PYTHIA *Monash*, EPOS LHC and QGSJET-II Monte Carlo event generators.

The results show that the density distribution of the number of particles in an event as a function of the number of charged particles is not properly described by the different MC generators, but the best agreement comes from EPOS LHC generator. As well as for the case of the transverse momentum distribution the best description comes from the EPOS LHC generator. For the density of the number of charged particle density distribution as a function of the pseudorapidity, there is good agreement except for PYTHIA 2. The average of the transverse momentum as a function of the number of charge particles is well described by EPOS LHC and PYTHIA 2 while PYTHIA *Monash* present larges differences.

To compare the mean particle density with previous measurements, it was computed for the central value of the pseudorapidity resulting equal to 6.500±0.002(stat.)± 0.099(syst.), which is compatible with previous analysis.QGSJET-II and EPOS LHC presents the best description even when they have problems for other distributions as the mean transverse momentum distribution.

The second analysis presented relates to the *"Search for low-mass resonances decaying into two jets and produced in association with a photon using pp collisions at $\sqrt{s}$ =13 TeV with the ATLAS detector"* paper [49]. This is a search of Dark Matter particles, in a scenario where a dark matter mediator particle interacts with the particles of the Standard Model. In this study, the Dark Matter mass is fixed at 10 TeV, which is inaccessible at current colliders. Nevertheless, a dijet search can probe a dark matter interaction via the interaction with the particles of the Standard Model. Even when ATLAS has been performed several dijet searches before, at low values of the mass range, they are very limited by the prescaled triggers used to reduce the high rate of the large multi-jet background. The presented analysis uses a different approach. It utilizes dijet events in association with a high transverse momentum photon produced as initial-state radiation which is used for triggering, allowing then to reconstruct the resonance mass from jets with lower transverse momentum. Thus the final state of this analysis is 2 jets and a photon. The signal significance can be improved by requiring that the two jets come from a b quark. So, two final states were analyzed: 2 *b-tag* jets and an ISR photon, and two inclusive jets and an ISR photon. Besides, two triggers were implemented to get to low mass ranges while not loosing sensitivity. The single-photon trigger allows us to reach lower masses range (below 303GeV) and the compound trigger increases the sensitivity for higher mass values. Then, a study was performed to get a discriminant variable from which an optimal cut value can be extracted to increase the significance. For the 2 *b-jet* case a tagging study was performed to chose the optimal tagger and working points to increase the sensitivity and to control the miss-tagging rate.

The analysis searches for resonances scanning a smoothly falling background distribution, thus it must be properly fit. To get the best fit function a study was performed over non-sensitive samples. As the amount of stats in the background Monte Carlo distributions available was not enough for this study, a fraction of the collected data during 2015-2017 was used instead since it gave a null- result. The fit procedure starts with a global fit. But, for the cases in which it is not sufficient flexible, a SWIFt fit is performed using a sliding window fit. This means that a maximum and a minimum window fit needs to be defined. The former is the maximum value that allows a good adjustment of the fit function. The second, the minimum width is such that a small value would lose sensitivity to the possible signal.

Finally, the invariant mass distribution was analyzed using a frequentist approach. Unfortunately, no evidence of new physics was observed so limits were set for the possible number of events from resonant new physics processes applying a 95% CL limit on the cross-section times acceptance for new phenomena signal, and a limit on the cross-section times acceptance times efficiency times branching ratio which can be applied to any model which would be approximated by a gaussian signal shape. These limits extend the current ATLAS constraints on dijet resonances to the mass range between 225 and 1100 GeV that was unexplored before.

A Studies for Charged-primary particles distributions

A.1 Backgrounds estimation studies

Secondary tracks may pass the selection cuts due to different processes, ranging from electron and positron tracks from converted photons to tracks from long-lived hadron decays and fake tracks. Due to their broader impact parameter distribution, the fraction of secondaries can be fitted in the control region of the d_0 distribution, i.e. in side-bands defined as $|d_0| >$ some value which is 4 mm in the default case. The upper cut on the transverse impact parameter is 9.5 mm and defined by the size of the search window in the pattern recognition.

The template distributions are taken from the simulation and the fractions are fitted in the side-bands. The data is fitted using normalized MC templates for primaries $p(x)$ and secondaries $s(x)$ in side-bands, keeping the normalization to the full range so that to obtain secondaries yield for full range. The fit formula used is

$$Fit(d_0) \equiv D^{full}\left[\left(1-(B^{SB}_{sec}-1)\cdot\frac{S^{full}_{MC}}{P^{full}_{MC}}\right)\cdot p(d_0)+B^{SB}_{sec}\cdot s(d_0)\right] \tag{49}$$

where B^{SB}_{sec} is the secondaries scaling factor fitted in side-bands, D^{full} is the number of tracks in data, and S^{full}_{MC} and P^{full}_{MC} are the secondaries and the primaries rates in MC, respectively.

The fitted scale factor was evaluated for the default MC as a function of the side-band region size. A scale factor of 1.3738 ± 0.0056 was fitted for the $p_{\mathrm{T}} > 500$ MeV bin which means that the tails of the transverse impact parameter allow about 40% more secondaries than in the Monte Carlo. This is consistent with a secondary track fraction of 0.0228 ± 0.0056 in the signal $|d_0| < 1.5$ mm range. For the lower p_{T}bins, the template was splitted further into an electron and a non-electron template.

To study the systematic error on the fit method the scale factor was fitted in different side-band regions. The choice of the fit window is arbitrary and a variation of $^{+2}_{-1}$ mm leads to a change of 4.5% w.r.t. the default value in the 100 MeV $< p_{\mathrm{T}} <$ 150 MeV bin. The window choice was verified to be in a reasonable interval based on ensuring that the side-band region is well dominated by secondaries. For estimating the effects of different material assumptions, varied samples were used.

Variations as large as 6.8% in the 100 MeV $< p_{\mathrm{T}} <$ 150 MeV bin using the different material samples were observed and taken as a systematics, not dividing by a factor of two. The secondaries fraction could be different in data and Monte Carlo because most of the secondary tracks are produced in the material of the detector, depending on η. The variation in the scale factor is small and leads to a systematic error of 2.1% on the scale factor, in the 100 MeV $< p_{\mathrm{T}} <$ 150 MeV bin. Much larger uncertainties are expected from the interpolation of the fitted value in the side-band into the core region. Here the generator dependence was studied. The transfer function, defined as the ratio of secondaries fraction in the analysis phase-space of $|d_0| < 1.5$ mm and the side-band region of $|d_0| > 4$ mm. The full difference between EPOS and Pythia8 was used as systematic uncertainty which leads to an uncertainty of 5.2% in the 100 MeV $< p_{\mathrm{T}} <$ 150 MeV bin.

Next, the dependence of the transfer-function on the slope in the transverse impact-parameter distribution between data and Monte Carlo was used. The method is expecting a flat ratio between data and Monte Carlo. The slope can be interpolated with a straight line to the core and it was estimated that integrated over the transverse impact parameter range in the signal region up to 13.7% more secondaries could be filled in. All systematic errors added in quadrature lead to a total error of 17% on the secondary estimate in the $100\,\mathrm{MeV} < p_{\mathrm{T}} < 150\,\mathrm{MeV}$ bin.

B Studies for resolved dijet resonances

B.1 Monte Carlo samples for the dijet search

The simulated Z' signals are in Tables 19 and 20.

Generator	DSID	Mass [GeV]	g_{SM}	σ [pb]	$\epsilon_{\mathrm{filter}}$
Madgraph+pythia	305161	300	0.3	1.381300e+01	6.537400e-02
Madgraph+pythia	305162	400	0.3	6.405000e+00	8.757300e-02
Madgraph+pythia	305163	500	0.3	3.292000e+00	1.055600e-01
Madgraph+pythia	305465	250	0.3	2.146000e+01	5.373200e-02
Madgraph+pythia	305466	250	0.2	9.563800e+00	5.312200e-02
Madgraph+pythia	305467	250	0.1	2.389000e+00	5.425300e-02
Madgraph+pythia	305468	350	0.3	9.329000e+00	7.718300e-02
Madgraph+pythia	305469	350	0.2	4.154500e+00	7.701000e-02
Madgraph+pythia	305470	350	0.1	1.039500e+00	7.658100e-02
Madgraph+pythia	305471	450	0.3	4.527500e+00	9.710500e-02
Madgraph+pythia	305472	450	0.2	2.013800e+00	9.784300e-02
Madgraph+pythia	305473	450	0.1	5.032000e-01	9.874600e-02
Madgraph+pythia	305474	550	0.3	2.454000e+00	1.143400e-01
Madgraph+pythia	305475	550	0.2	1.089800e+00	1.144700e-01
Madgraph+pythia	305476	550	0.1	2.725300e-01	1.144000e-01
Madgraph+pythia	305477	750	0.4	1.608300e+00	1.418700e-01
Madgraph+pythia	305478	750	0.3	9.062000e-01	1.408600e-01
Madgraph+pythia	305479	750	0.2	4.016500e-01	1.428800e-01
Madgraph+pythia	305481	950	0.3	4.018800e-01	1.656600e-01
Madgraph+pythia	305482	1050	0.4	1.238500e-01	1.996100e-01
Madgraph+pythia	305483	1050	0.3	6.846500e-02	2.040100e-01

Table 19: Signal samples with a photon filter cut at $p_{\mathrm{T}} = 100$ GeV. All samples are FullSim.

Generator	DSID	Mass [GeV]	g_{SM}	σ [pb]	$\epsilon_{\mathrm{filter}}$
Madgraph+pythia	308967	250	0.2	9.5670e+00	1.8690e-01
Madgraph+pythia	308968	350	0.2	4.1526e+00	2.2809e-01
Madgraph+pythia	308969	450	0.2	2.0142e+00	2.5954e-01
Madgraph+pythia	308970	550	0.2	1.0913e+00	2.8470e-01
Madgraph+pythia	308971	750	0.2	4.0150e-01	3.2058e-01
Madgraph+pythia	308972	950	0.2	1.7771e-01	3.4522e-01
Madgraph+pythia	308973	1050	0.2	3.0000e-01	3.9196e-01

Table 20: Signal samples with a photon filter cut at $p_{\mathrm{T}} = 50$ GeV. All samples are FullSim.

B.2 Cutflow tables for MC

Cutflow for mc16a (Table 21) and mc16d (Table 23) with samples weighted and normalised to 1 pb^{-1}.

	Single photon trigger		Compound trigger	
Cut	Events remaining	% remaining	Events remaining	% remaining
Total	38056.414	–	38056.414	–
Trigger	233.465	0.6%	341.779	0.9%
Cleaning	233.242	99.9%	341.394	99.9%
$n_{jets} \geq 2$	171.403	73.5%	327.592	96.0%
$n_{\gamma} \geq 1$	133.912	78.1%	283.683	86.6%
Lead γ p_{T} cut	98.513	73.6%	174.196	61.4%
Lead jet p_{T}cut	98.513	100%	164.344	94.3%
Sublead jet p_{T}cut	98.513	100%	103.115	62.7%
$\lvert y^{*}\rvert < 0.75$	60.377	61.3%	60.742	58.9%

Table 21: Cutflow for mc16a with samples weighted and normalised to 1 pb^{-1}. Percentages remaining are relative to the previous cut, and all values are relative to the objects remaining in the ntuple: thus all jets pass the leading and subleading jet cut, since only jets above 25 GeV are kept in the ntuple.

Cutflow for data 2015+2016 in Table22 and for data 2017 in Table24.

	Single photon trigger		Compound trigger	
Cut	Events remaining	% remaining	Events remaining	% remaining
Total	6443085312	–	5227867136	–
GRL	111929303	1.7%	103846024	2.0%
Trigger	93589345	83.6%	34203232	32.9%
Cleaning	93424536	99.8%	34149788	99.8%
$n_{jets} \geq 2$	89115138	95.4%	33409444	97.8%
$n_{\gamma} \geq 1$	19199687	21.5%	16350066	48.9%
Lead γ p_{T} cut	5249652	27.3%	9174245	56.1%
Lead jet p_{T}cut	5249652	100%	8712658	95.0%
Sublead jet p_{T}cut	5249652	100%	5633026	64.7%
$\lvert y^{*}\rvert$ <0.75	3093280	58.9%	3478528	61.8%

Table 22: Cutflow for data 2015+2016. Percentages remaining are relative to the previous cut, and all values are relative to the objects remaining in the ntuple: thus all jets pass the leading and subleading jet cut, since only jets above 25 GeV are kept in the ntuple. Please note that there was not compound trigger used in 2015, so all events there originate in the 2016 dataset.

Cut	Single photon trigger		Compound trigger	
	Events remaining	% remaining	Events remaining	% remaining
Total	38578.586	–	38578.586	–
Trigger	232.885	0.6%	286.231	0.7%
Cleaning	232.695	99.9%	285.971	99.9%
$n_{jets} \geq 2$	176.678	75.9%	274.149	95.9%
$n_{\gamma} \geq 1$	135.919	76.9%	233.471	85.2%
Lead γ p_{T} cut	97.943	72.1%	178.433	76.4%
Lead jet p_{T}cut	97.943	100%	167.308	93.8%
Sublead jet p_{T}cut	97.943	100%	101.788	60.8%
$\lvert y^{*}\rvert < 0.75$	59.605	60.9%	59.960	58.9%

Table 23: Cutflow for mc16d with samples weighted and normalised to 1 pb^{-1}. Percentages remaining are relative to the previous cut, and all values are relative to the objects remaining in the ntuple: thus all jets pass the leading and subleading jet cut, since only jets above 25 GeV are kept in the ntuple.

Cut	Single photon trigger		Compound trigger	
	Events remaining	% remaining	Events remaining	% remaining
Total	5002680320	–	5002680320	–
GRL	139551621	2.8%	139551621	2.8%
Trigger	109049835	78.1%	42646980	30.6%
Cleaning	108878354	99.8%	42593952	99.9%
$n_{jets} \geq 2$	104090372	95.6%	41596064	97.7%
$n_{\gamma} \geq 1$	24898568	23.9%	20861906	50.2%
Lead γ p_{T} cut	6325551	25.4%	12916492	61.9%
Lead jet p_{T}cut	6325551	100%	12125213	93.9%
Sublead jet p_{T}cut	6325551	100%	7380192	60.9%
$\lvert y^{*}\rvert < 0.75$	4014393	63.5%	4552562	61.7%

Table 24: Cutflow for data 2017. Percentages remaining are relative to the previous cut, and all values are relative to the objects remaining in the ntuple: thus all jets pass the leading and subleading jet cut, since only jets above 25 GeV are kept in the ntuple.

B.3 MC-Data comparison

Various kinematic quantities were examined to ensure that the data was well understood. Comparisons for the most important quantities of both 2016 and 2017 datasets are given here.

Comparing data to simulation, analysis selection

Inclusive channel

The following figures compare data taken in 2016 (and 2015, for the single photon trigger) to mc16a. Data taken in 2017 is compared to mc16d. Appropriate pileup reweighting is applied to MC in all cases. All MC samples are generated using Sherpa.

No significant discrepancies are observed between the data and MC distributions.

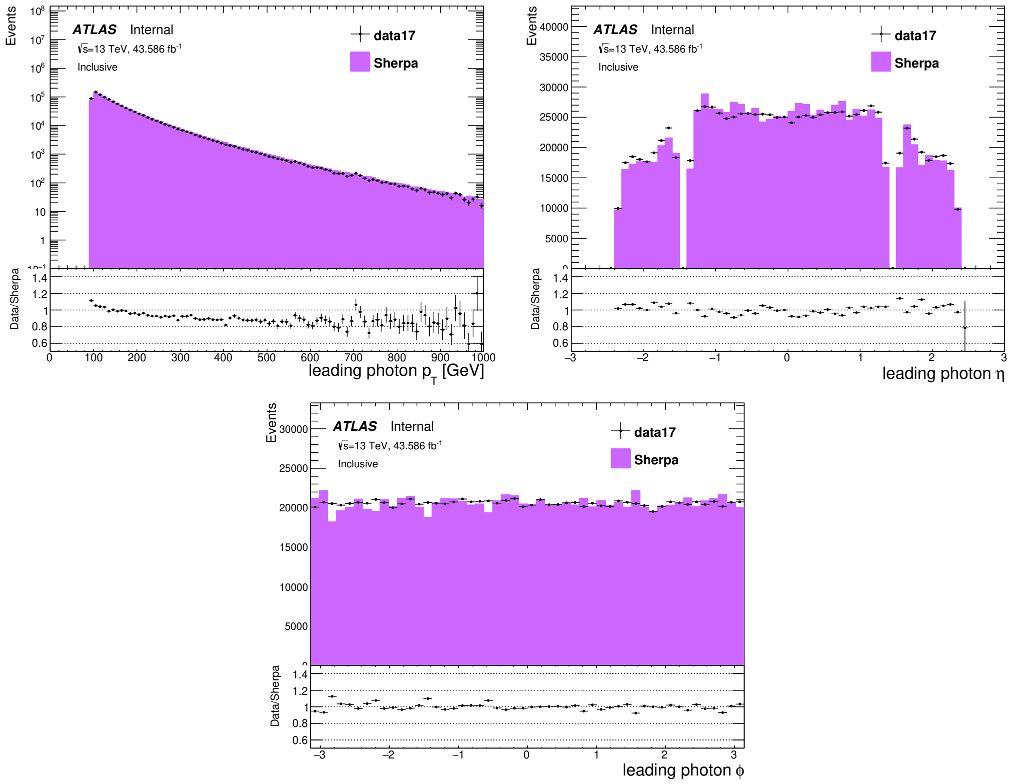

Figure 112: Comparison of photon kinematic quantities in data 2017 to mc16d for the inclusive channel with the compound trigger. The analysis selection is used.

The largest differences are observed in the photon p_{T} spectrum for the compound trigger and in the subleading jet p_{T} spectrum for the single photon trigger. Since the photon does not enter the final analysis observable, differences of the magnitude observed in its p_{T} are not overly concerning. For the subleading jet $p_{\mathrm{T}}$with the single photon trigger, the data/MC difference is smooth and changes slowly, indicating that it will not be able to introduce an M_{jj} -dependent feature into the final result. Distributions of the vector sum $p_{\mathrm{T}}$of the two relevant jets also show very good agreement. For these reasons the team is satisfied that the analysis kinematics in the inclusive channel are sufficiently well understood in both the 2015–2016 and 2017 datasets. Similar tests were performed for the *b-tag* channel: these can be found in the next section.

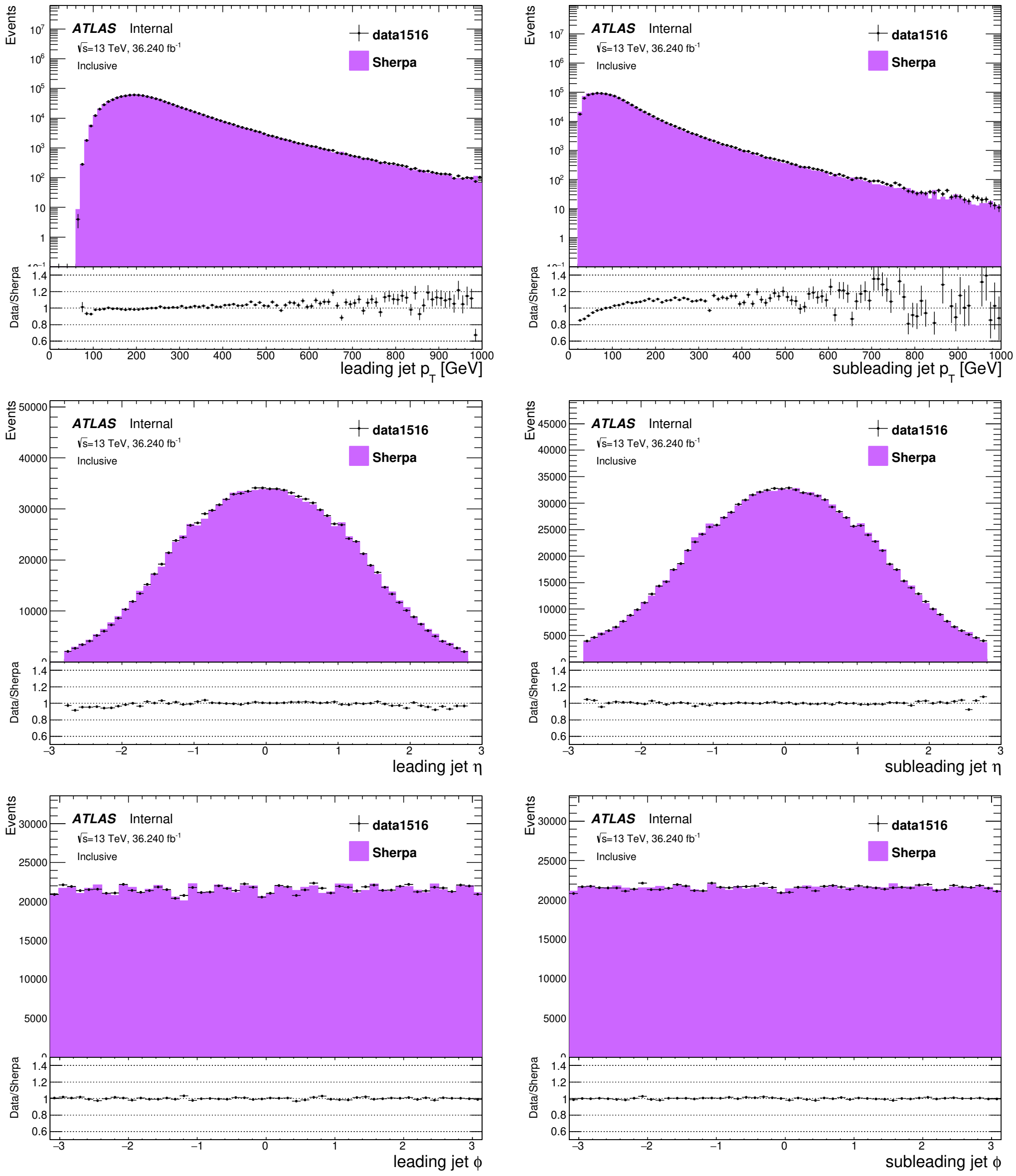

Figure 113: Comparison of jet kinematic quantities in data 2015+2016 to mc16a for the inclusive channel with the single photon trigger. The analysis selection is used.

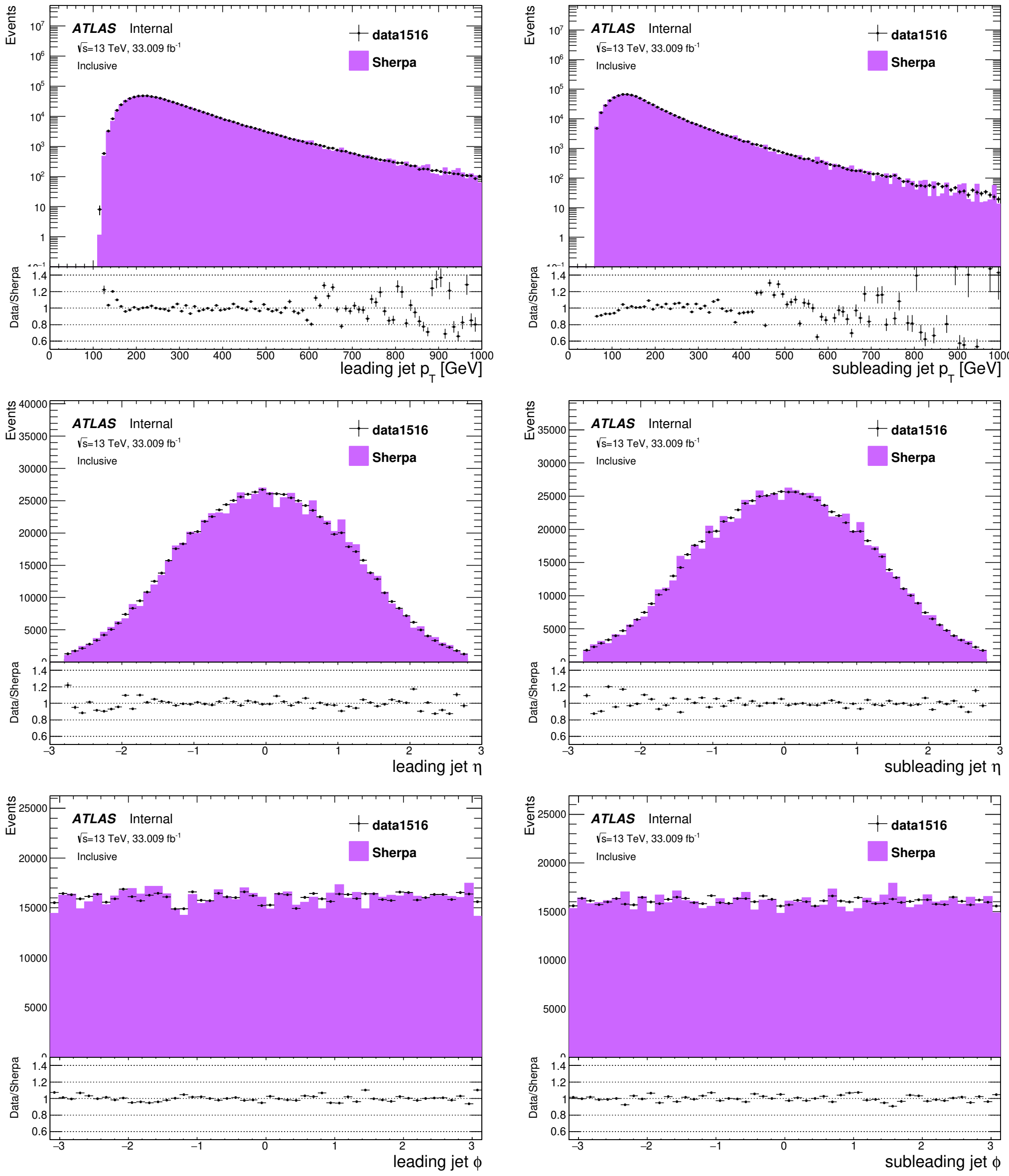

Figure 114: Comparison of jet kinematic quantities in data 2015+2016 to mc16a for the inclusive channel with the dijet+photon trigger. The analysis selection is used.

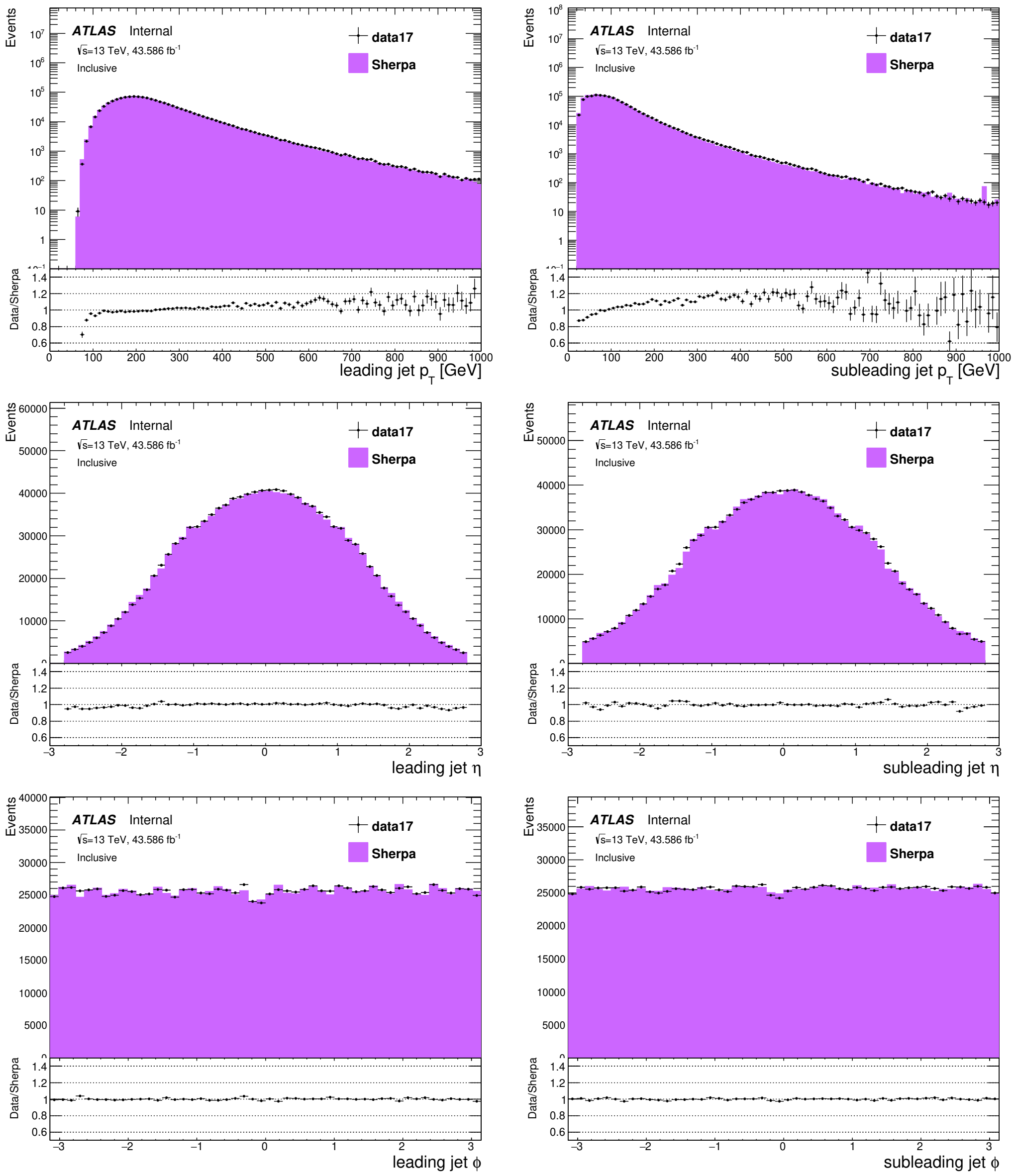

Figure 115: Comparison of jet kinematic quantities in data 2017 to mc16d for the inclusive channel with the single photon trigger. The analysis selection is used.

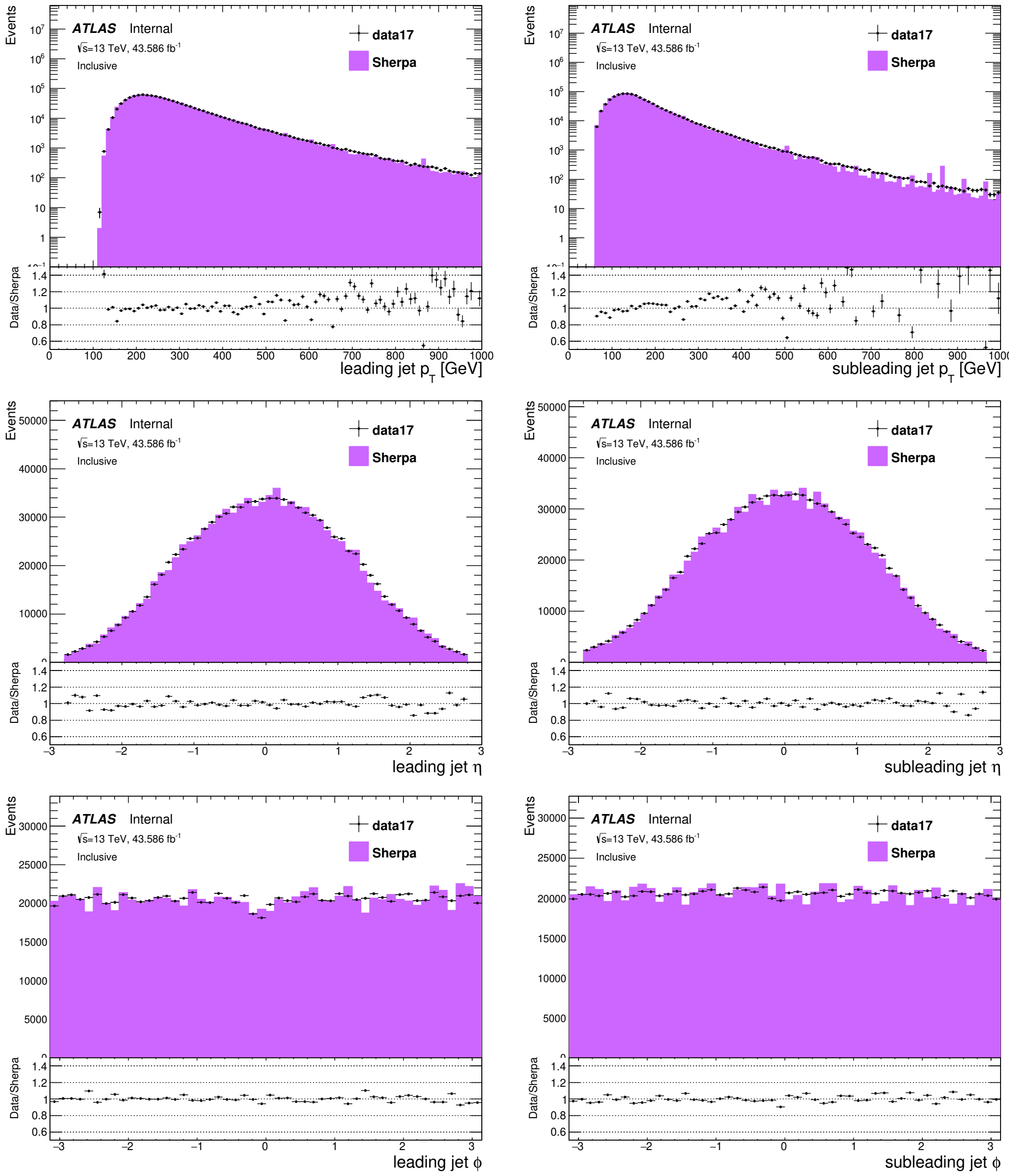

Figure 116: Comparison of jet kinematic quantities in data 2017 to mc16d for the inclusive channel with the compound trigger. The analysis selection is used.

B-tagged channel Data to Monte Carlo plots comparing key kinematic quantities for events passing the 2-*b-tag* selection are shown for 2017 data in Figures 117, 118, 119 and 120.

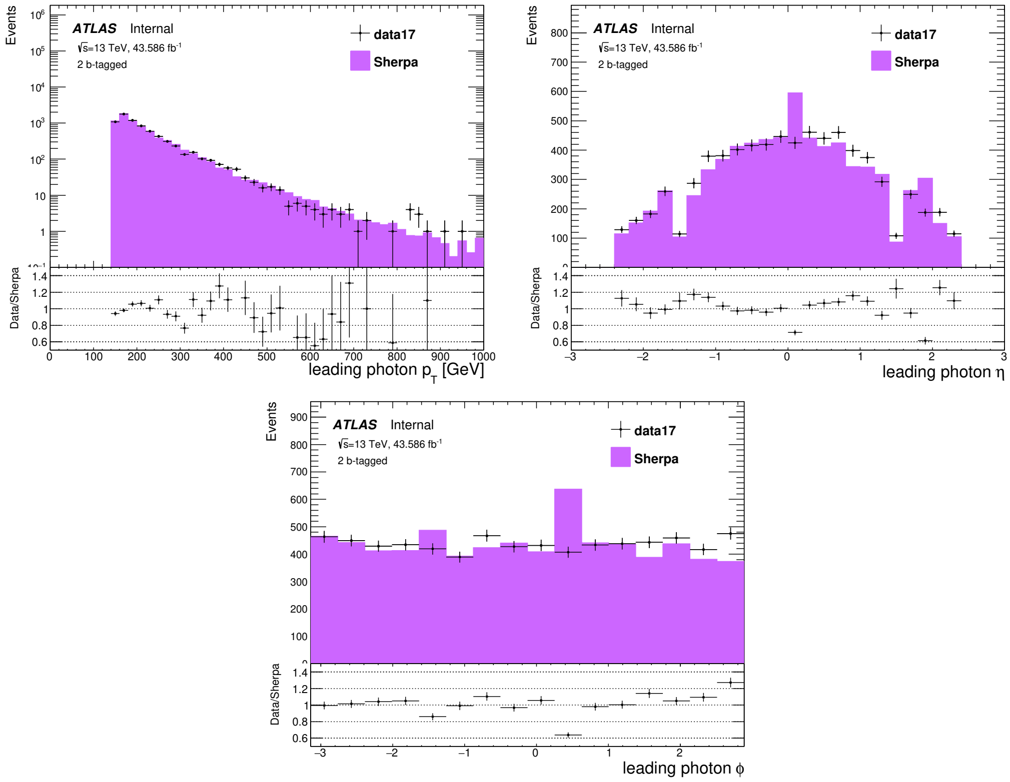

Figure 117: Comparison of photon kinematic quantities in data 2017 to mc16d for the b-tagged channel with the single-photon trigger. The analysis selection is used.

Insofar as the low statistics in the 2-tagged channel allow meaningful comparisons, no problems are seen in these comparison plots.

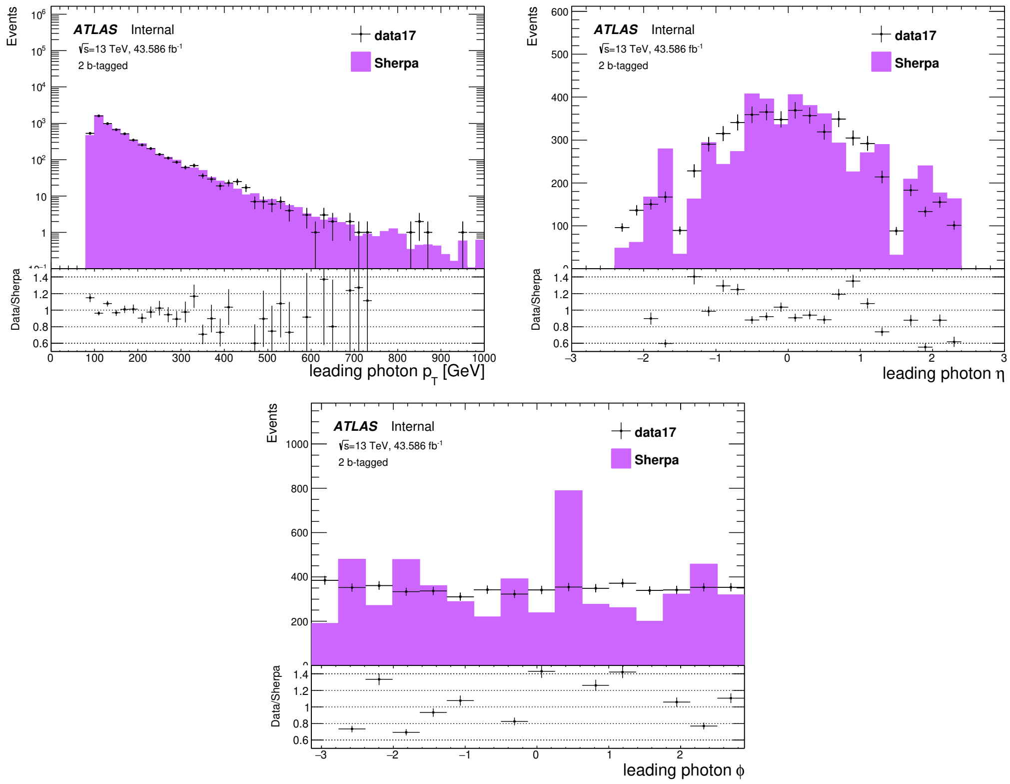

Figure 118: Comparison of photon kinematic quantities in data 2017 to mc16d for the b-tagged channel with the compound trigger. The analysis selection is used.

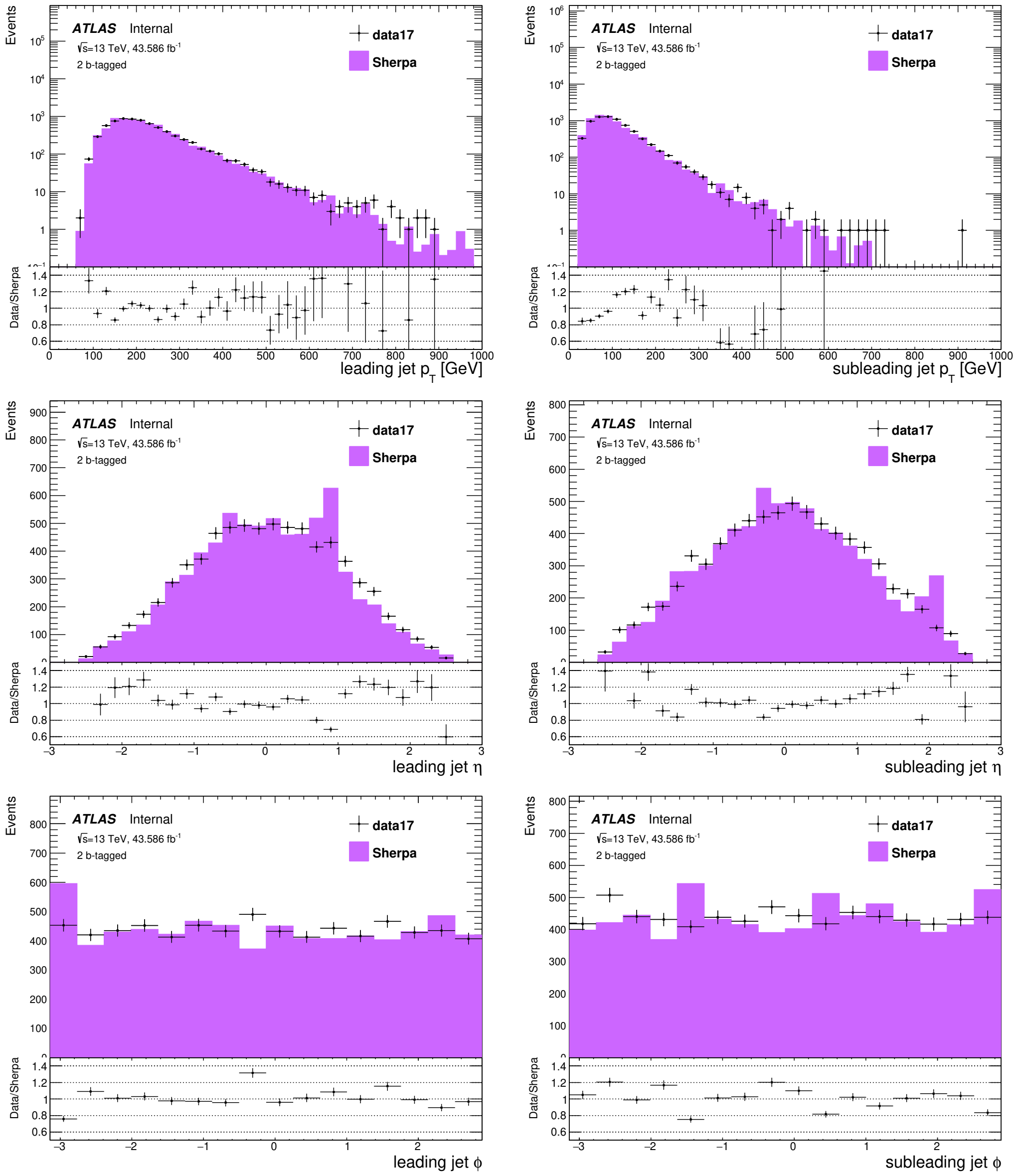

Figure 119: Comparison of jet kinematic quantities in data 2017 to mc16d for the 2-*b*-*tag* channel with the single photon trigger. The analysis selection is used.

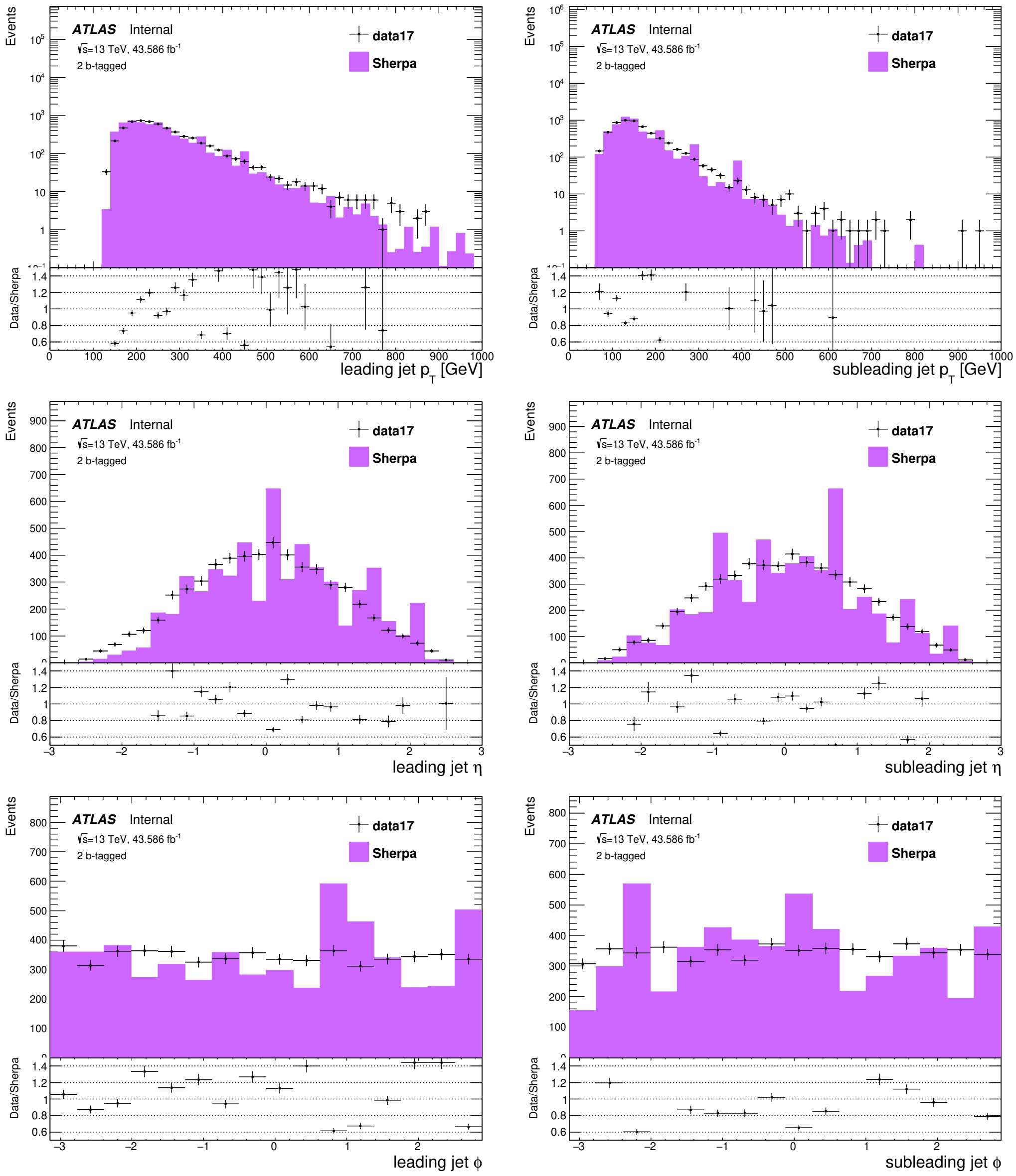

Figure 120: Comparison of jet kinematic quantities in data 2017 to mc16d for the 2-*b-tag* channel with the compound trigger. The analysis selection is used.

B.3.1 Checks for tagging performance inconsistency or alignment issues

The di-b analysis encountered complications in the 2016 dataset in Release 20.7 due to mis-alignment of the detector. These issues manifested as unexpected features in the jet ϕ distributions during several run periods, and caused localised issues in the spectrum which in turn posed challenges to background fitting. Figures 121 and 122 show the pt, eta, and phi of the leading and subleading jets in the event, for the inclusive selection with both triggers, divided by 2017 data period.

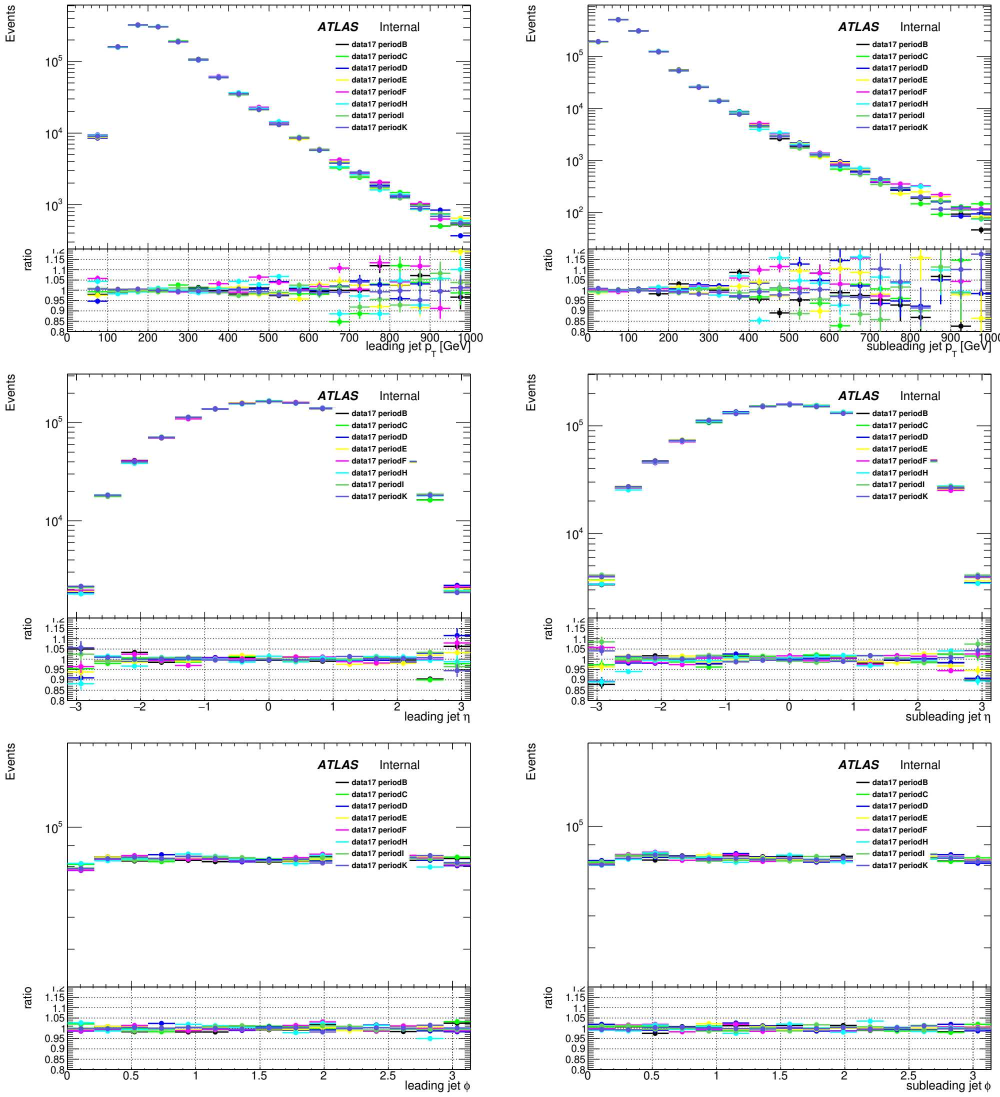

Figure 121: Distributions of leading and subleading jet p_{T}, η, and ϕ divided by 2017 data-taking period. The full analysis selection and single photon trigger are used to obtain these datasets.

Small discrepancies around η $1.2 - 1.4$ can be attributed to changes in pileup conditions between periods. There are no significantly worrisome discrepancies in the full dataset.

Equivalent distributions for only events which pass the 2-b-*tag* requirements are

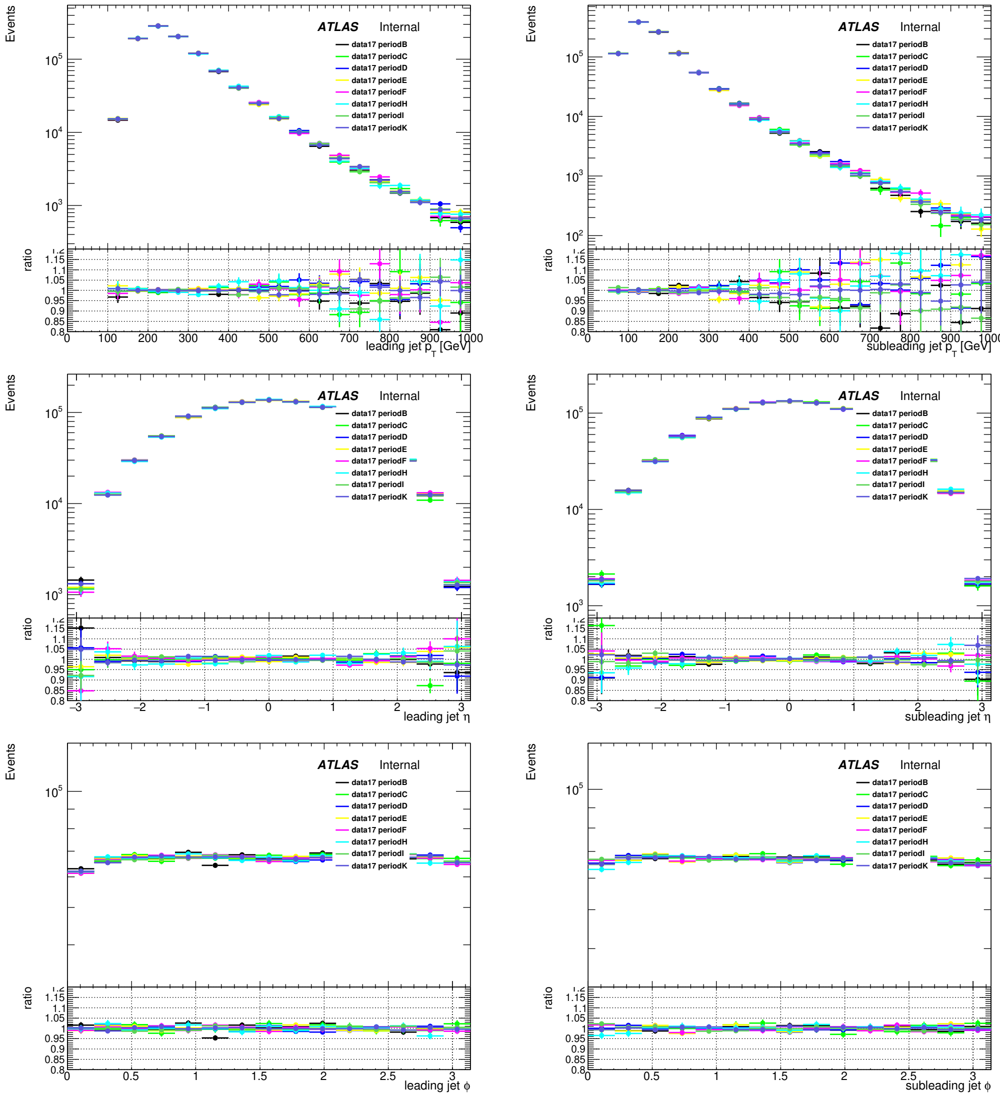

Figure 122: Distributions of leading and subleading jet p_{T}, η, and ϕ divided by 2017 data-taking period. The full analysis selection and compound trigger are used to obtain these datasets.

shown in Figures 123 and 124. 2017 data is shown. The observed distributions agree well within the large statistical uncertainties.

No significant discrepancies are observable in the phi distributions. Recall that this is one of the distributions in which 2016 detector alignment issues manifested for the di-b analysis. This agreement therefore gives tentative confidence in the 2017 dataset to not introduce similar problems. To increase this confidence, another key plot was made: the difference in phi between the two signal jets. If this quantity changed from one data period to another, it could be a similar indicator of detector problems which could ultimately impact the analysis. That plot showed no discrepancies and is displayed in Figure 125.

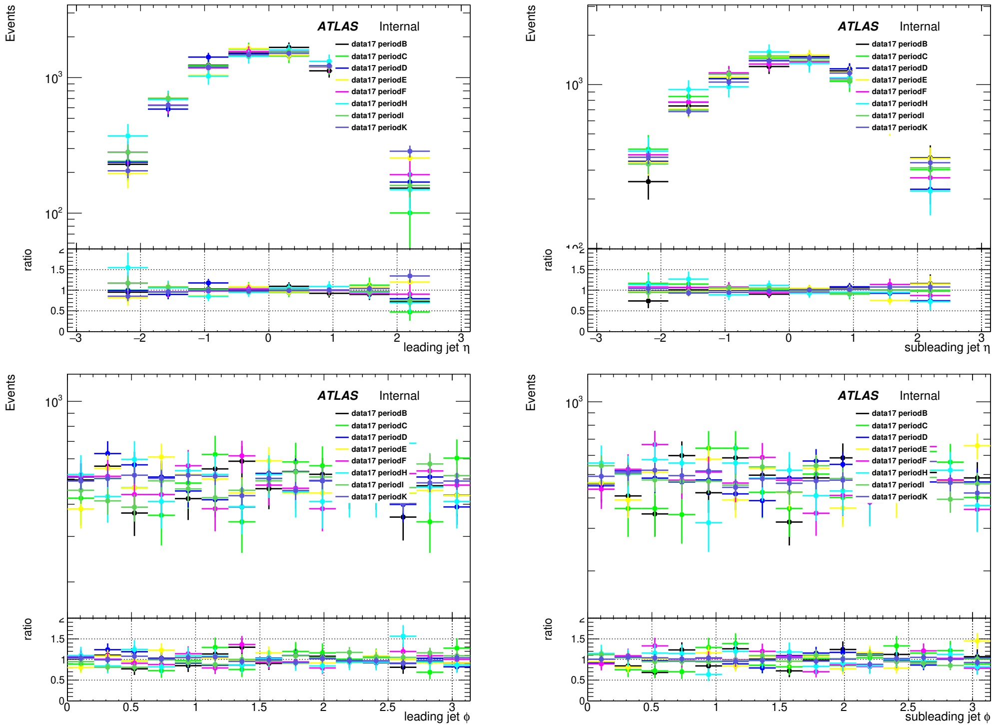

Figure 123: Distributions of signal jet η and ϕ divided by 2017 data-taking period. The analysis selection with single photon trigger is used to obtain these datasets and both jets are required to pass a *b-tag* requirement based on the DL1 tagger and fixed 77% working point.

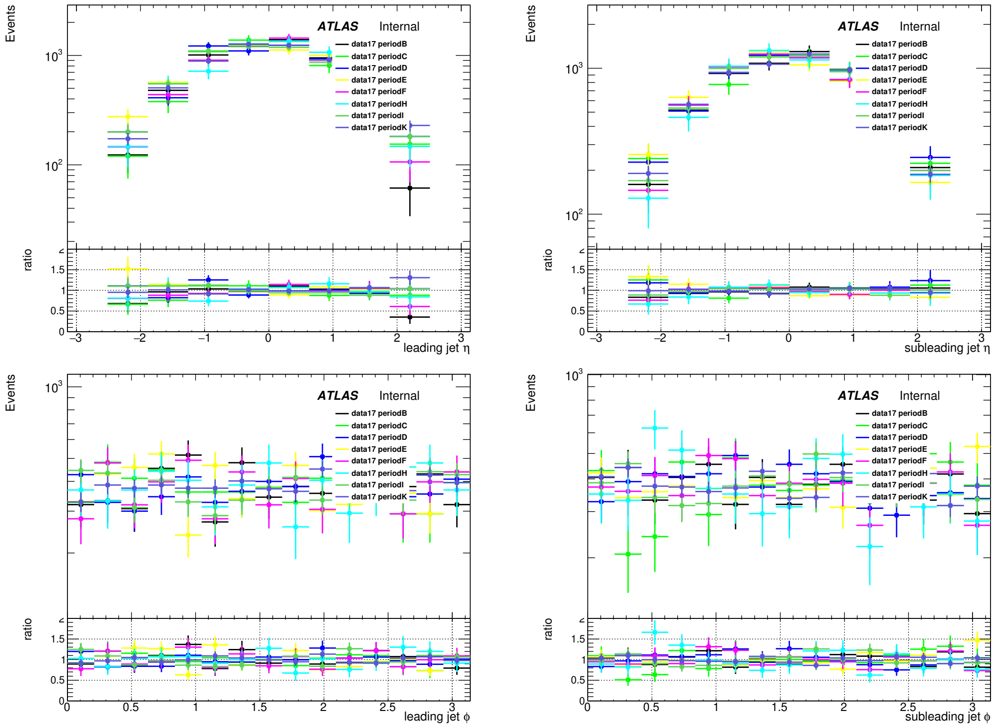

Figure 124: Distributions of signal jet η and ϕ divided by 2017 data-taking period. The analysis selection with single photon trigger is used to obtain these datasets and both jets are required to pass a *b-tag* requirement based on the DL1 tagger and fixed 77% working point.

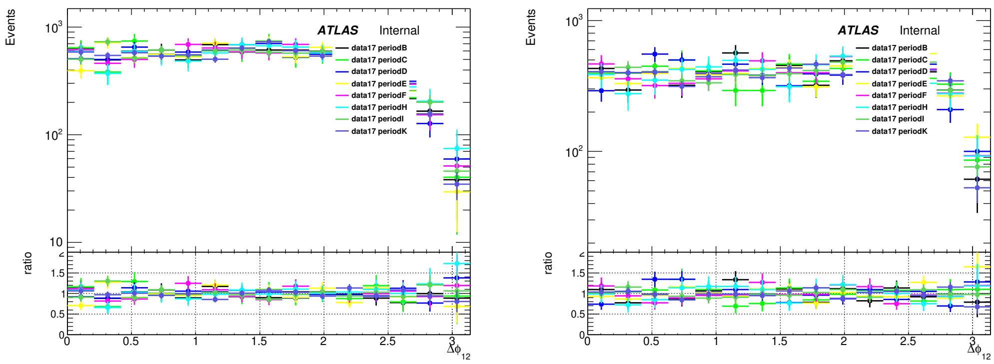

Figure 125: $\Delta\phi$ between the two signal jets for each data period in 2017 data. The full analysis selection is shown, with the single photon trigger and compound trigger. Both jets are required to pass a *b-tag* requirement based on the DL1 tagger and fixed 77% working point.

B.3.2 Checks of kinematic agreement between years

Additional checks compared kinematic distributions between the full 2016 and 2017 datasets and can be found in Figures 126 to 129. These checks were used to ensure that unblinding tests done in portions of 2016 data would be consistent with expected results in 2017 data.

While some differences were found at very low p_{T}in for the jets and photons, there are few other differences and those which exist are understood. Slight discrepancies in jets around $\pm\eta 1.4$ are due to changing pileup conditions between the years. Differences in the jet ϕ distributions are due to different dead tiles in the two years; these are accounted for properly in the signal MC samples. The distributions of di-jet quantities shown in Figures 130 and 131 show very good agreement. Overall, these kinematic checks are therefore taken as confirmation that a subset of the 2016 data is sufficiently consistent with the 2017 data as to provide adequate unblinding checks.

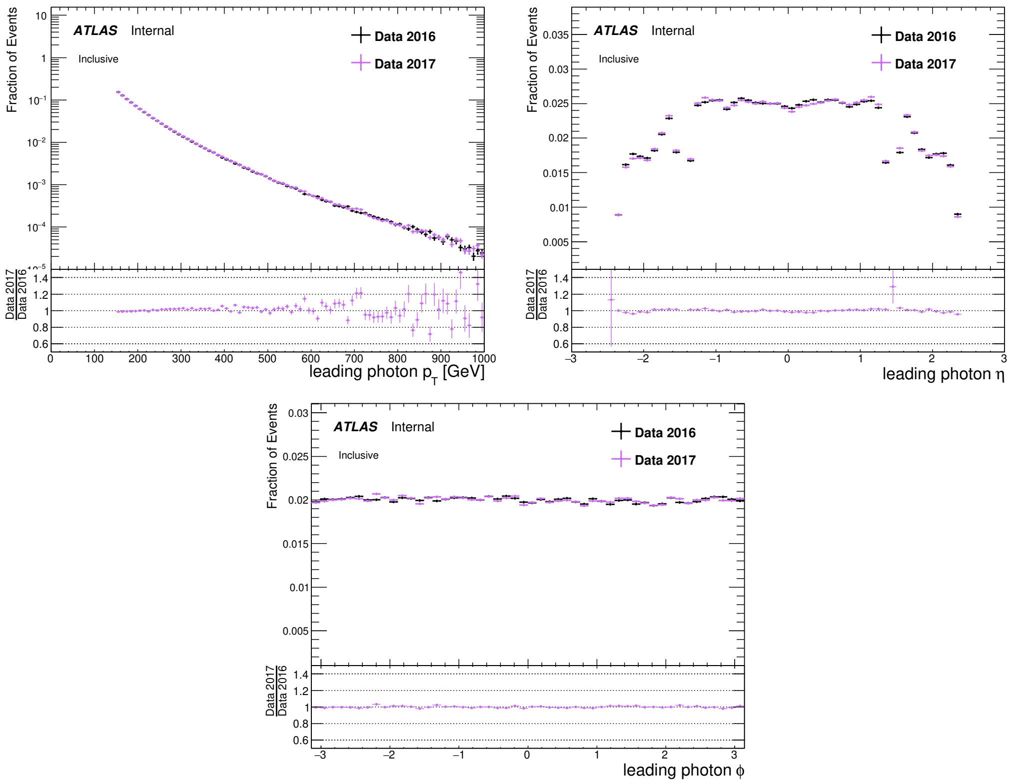

Figure 126: Comparison of photon kinematic quantities in data 2016 to data 2017 for the inclusive channel with the single photon trigger. The analysis selection is used.

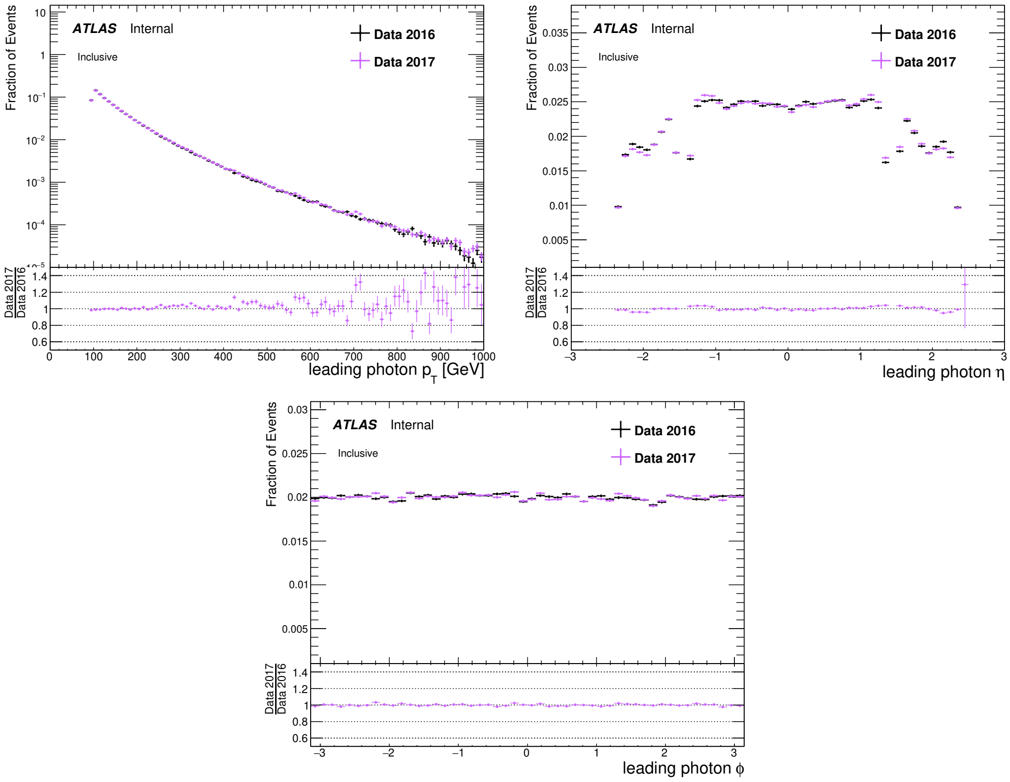

Figure 127: Comparison of photon kinematic quantities in data 2015+2016 to mc16a for the inclusive channel with the compound trigger. The analysis selection is used.

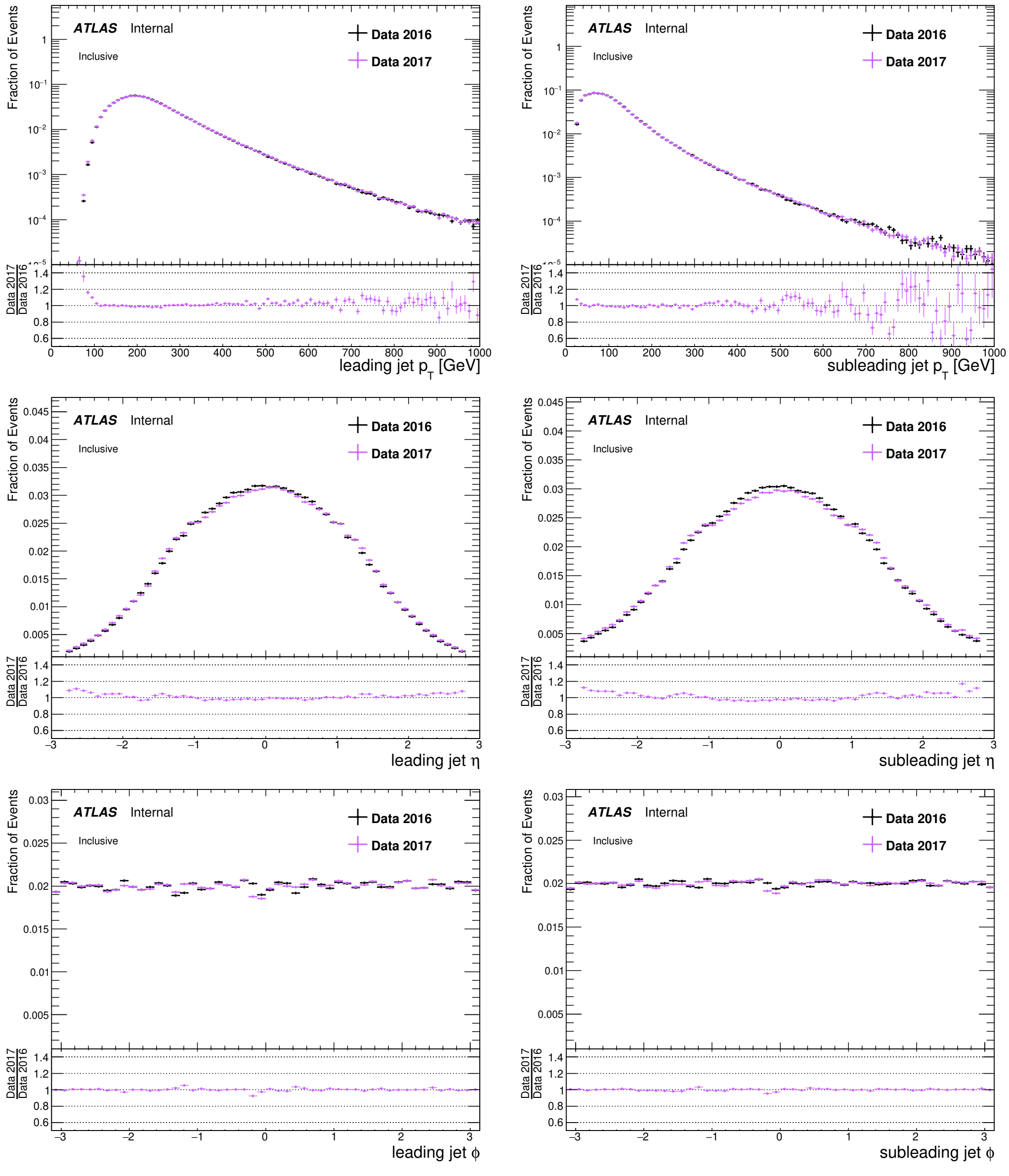

Figure 128: Comparison of jet kinematic quantities in data 2016 to data 2017 for the inclusive channel with the single photon trigger. The analysis selection is used.

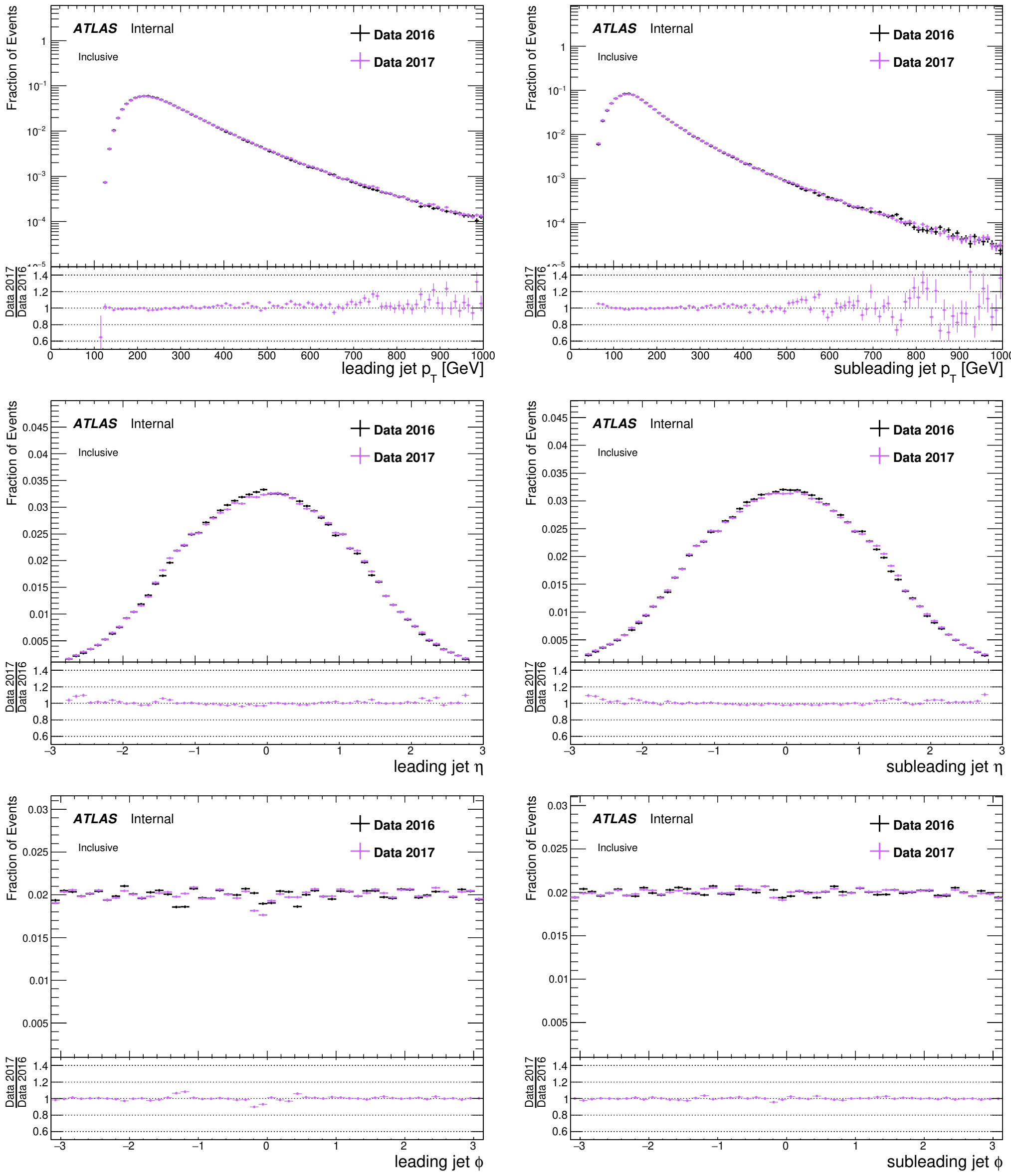

Figure 129: Comparison of jet kinematic quantities in data 2016 to data 2017 for the inclusive channel with the compound trigger. The analysis selection is used.

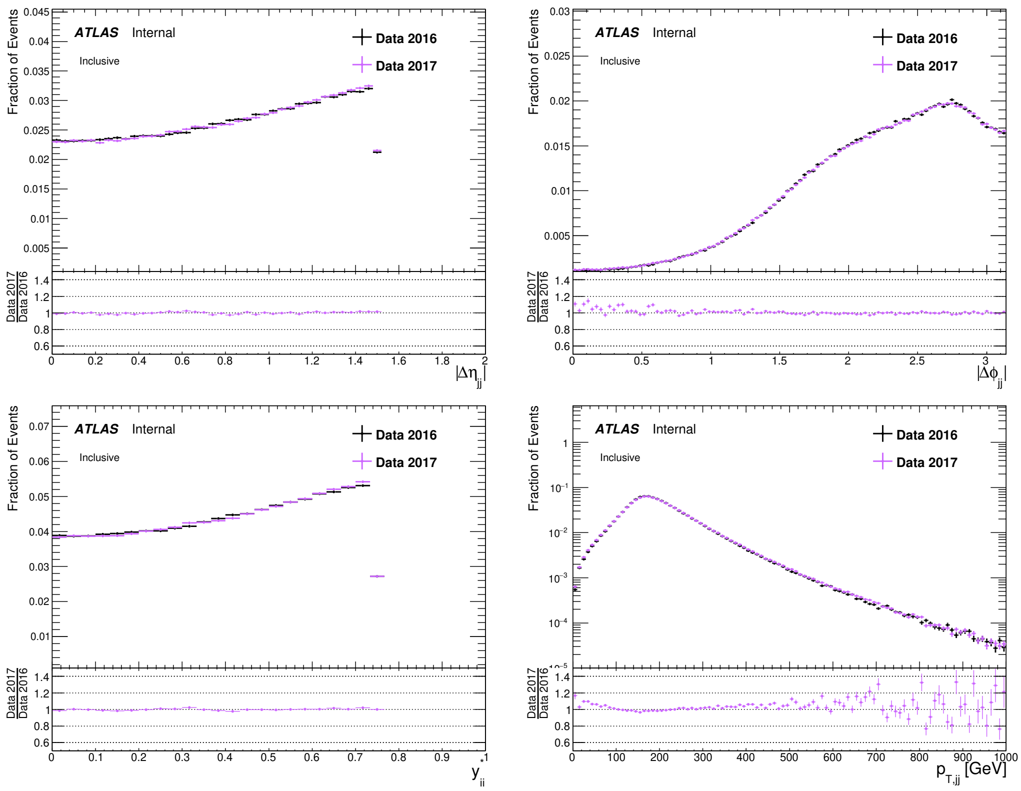

Figure 130: Various dijet kinematic quantities for the inclusive selection and the single photon trigger. The figures show $\Delta\eta$ between the two leading jets , Δphi between the two leading jets , the rapidity difference y^* between the two leading jets , and the vector sum $p_{\mathrm{T}}$of the two leading jets.

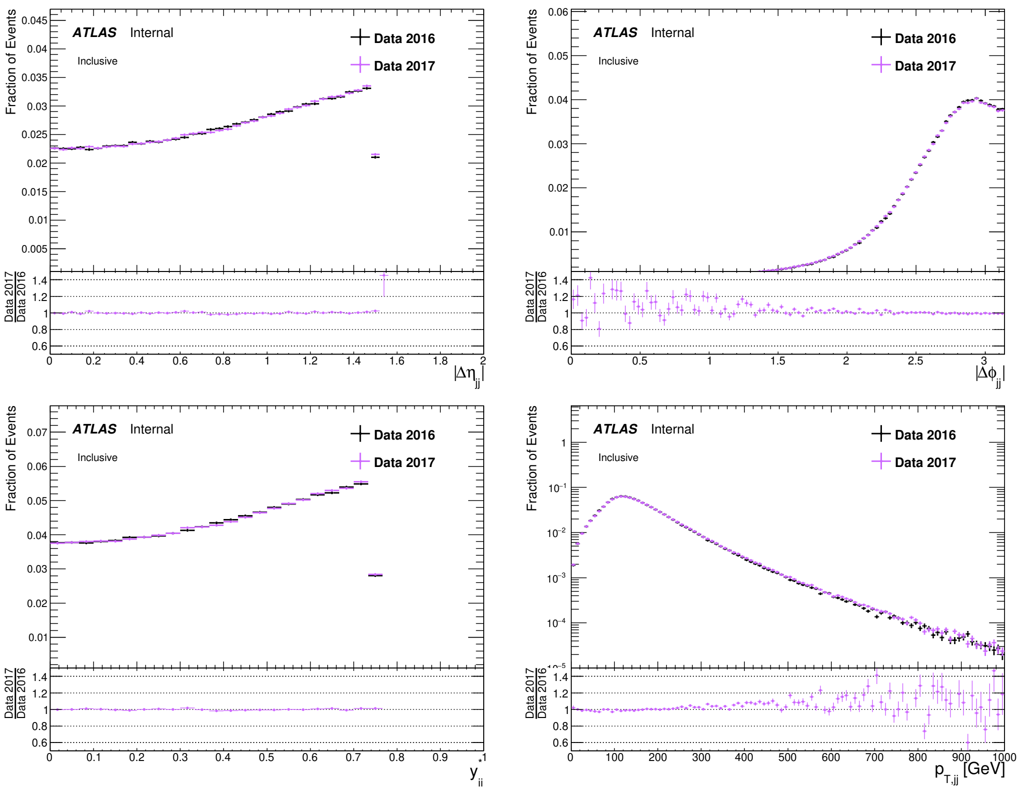

Figure 131: Various dijet kinematic quantities for the inclusive selection and the compound trigger. The figures show $\Delta\eta$ between the two leading jets , Δphi between the two leading jets, the rapidity difference y^* between the two leading jets, and the vector sum $p_{\mathrm{T}}$of the two leading jets.

Checks of kinematic agreement between years (*b-tag* channel)

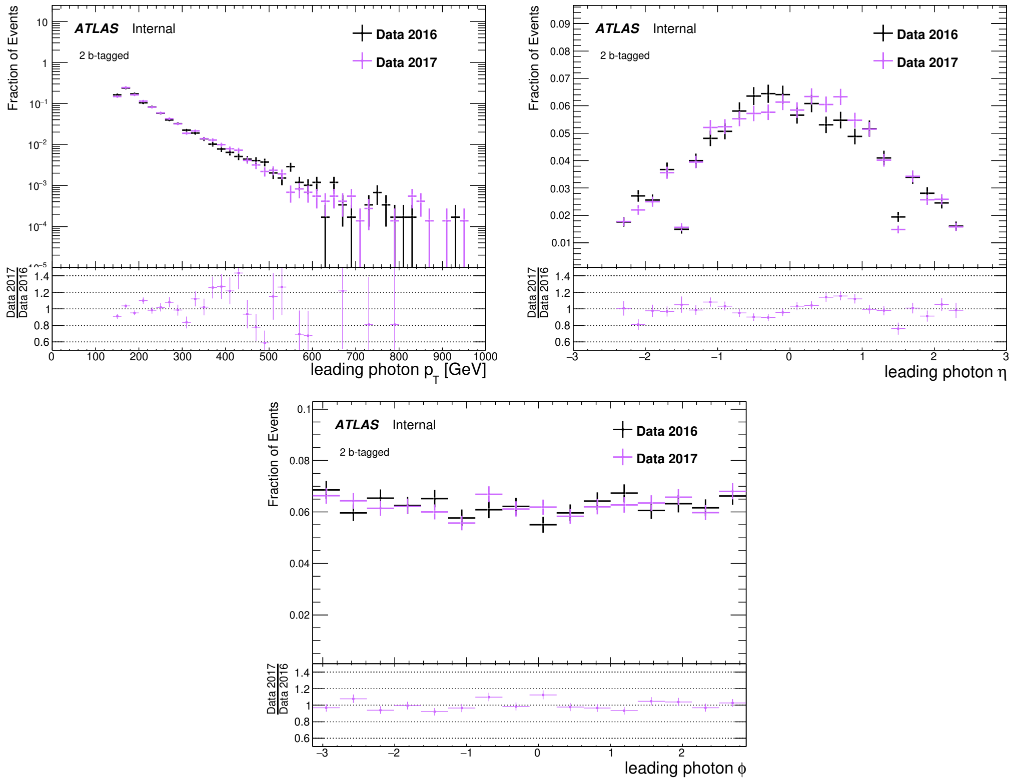

Figure 132: Comparison of photon kinematic quantities in data 2016 to data 2017 for the inclusive channel with the single photon trigger.

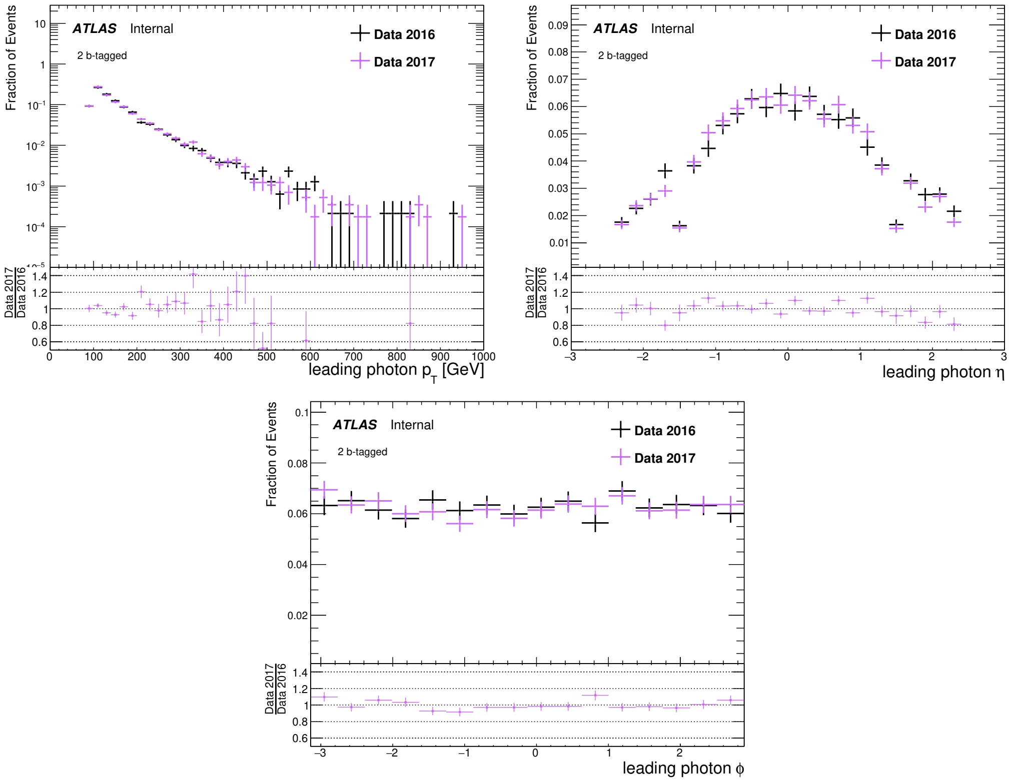

Figure 133: Comparison of photon kinematic quantities in data 2015+2016 to mc16a for the inclusive channel with the compound trigger.

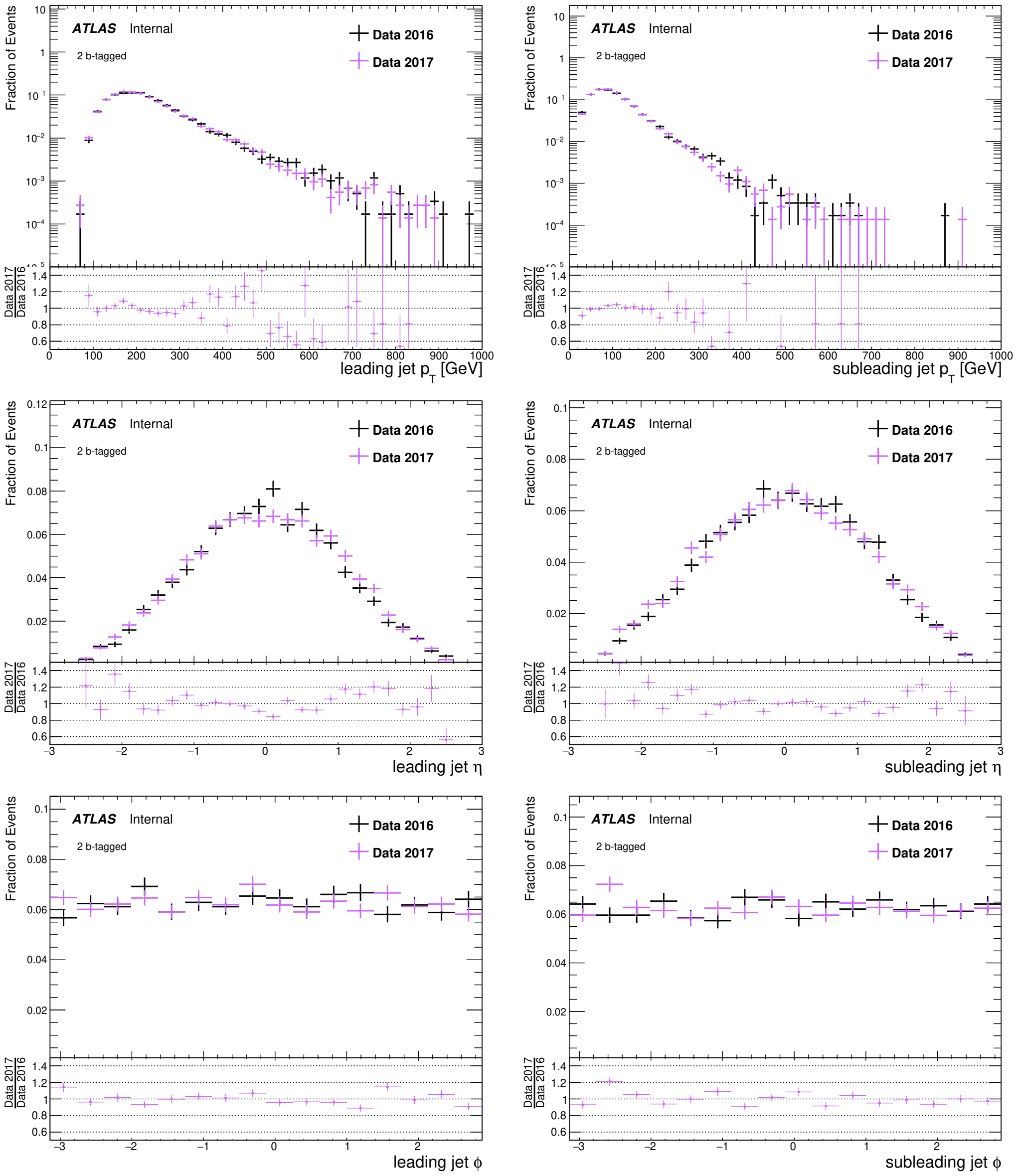

Figure 134: Comparison of jet kinematic quantities in data 2016 to data 2017 for the inclusive channel with the single photon trigger.

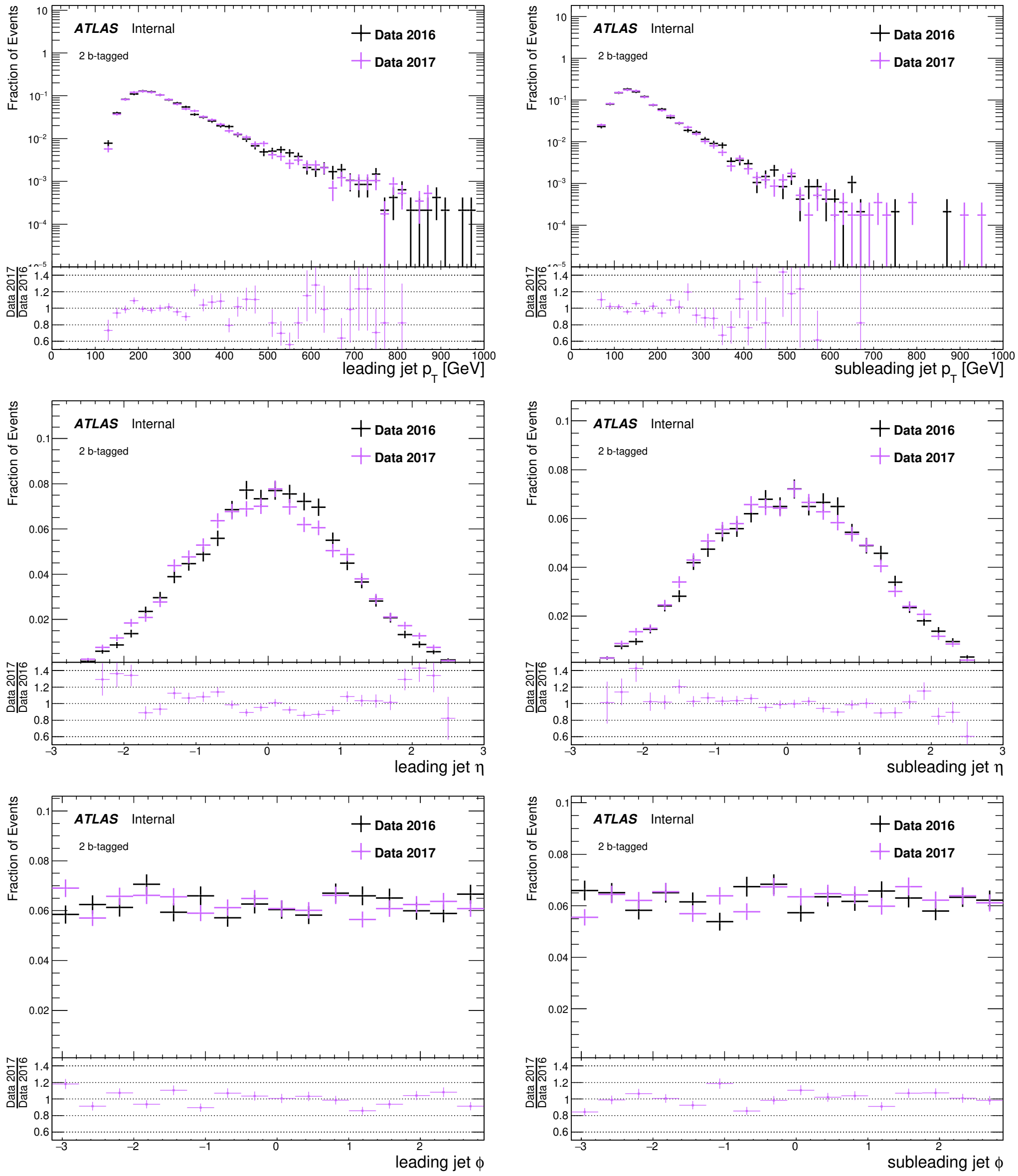

Figure 135: Comparison of jet kinematic quantities in data 2016 to data 2017 for the inclusive channel with the compound trigger.

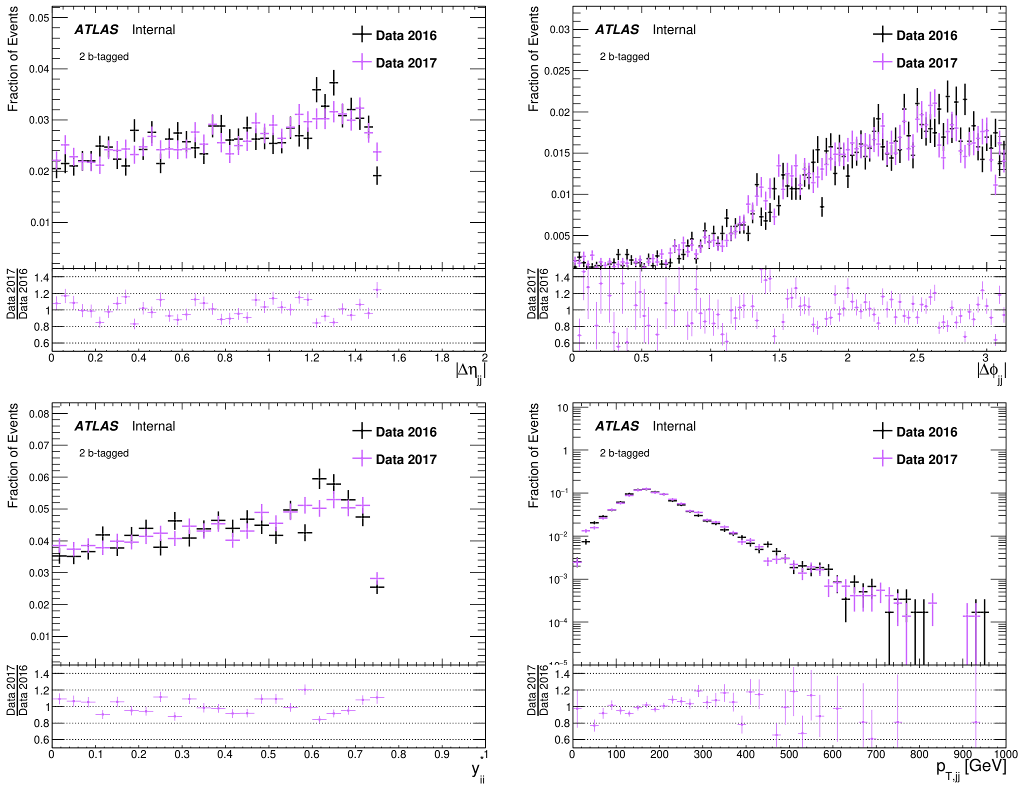

Figure 136: Various dijet kinematic quantities for the inclusive selection and the single photon trigger.

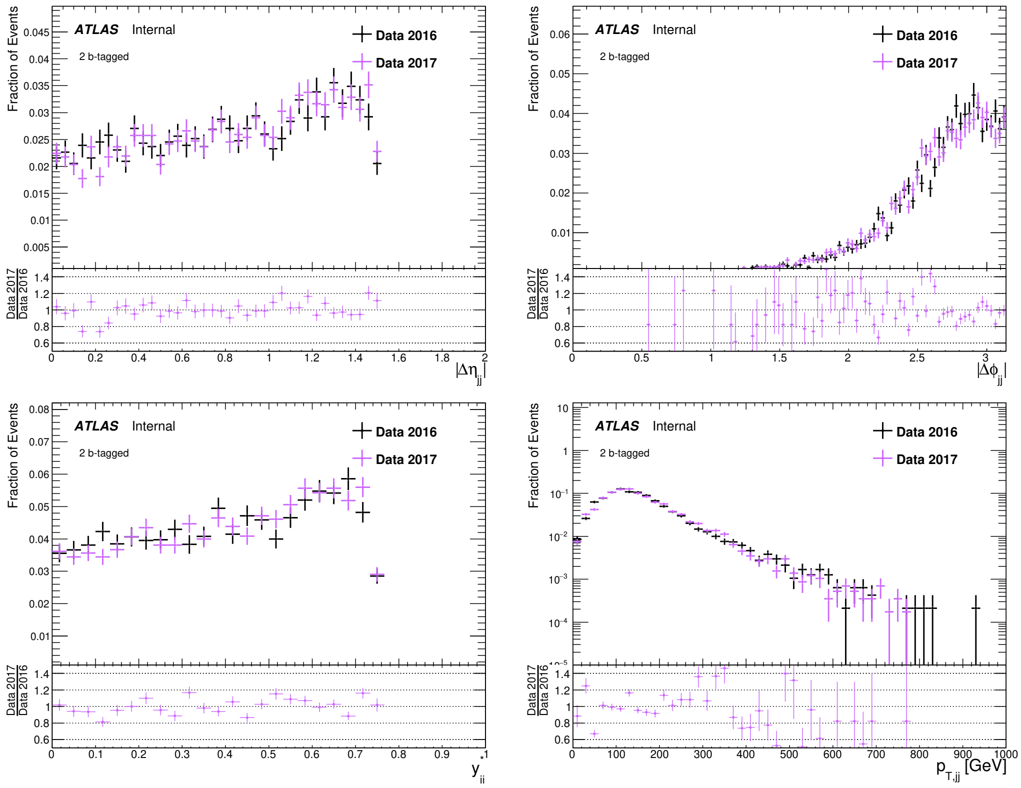

Figure 137: Various dijet kinematic quantities for the inclusive selection and the compound trigger.

B.4 Trigger studies

As it was mention before two kind of triggers were analized in detail: single-object and multi-object triggers. For the last one, two HLT triggers was used: `HLT_g75_tight_3j50noL1_L1EM22VHI`, running unprescaled in 2016, and `HLT_g85_tight_L1EM22VHI_3` running unprescaled in 2017. Both are seeded by the L1 trigger `L1_EM22VHI`, which ran unprescaled in both years.

These triggers require the presence of at least three jets with $p_T > 50$ GeV and at least one photon with $p_T > 75$ or 85 GeV, respectively, passing the tight identification criteria.

The efficiency of the trigger with respect to the offline reconstruction is studied by bootstrapping from the `HLT_g60_loose` trigger, which is fully efficient for the full set of events passing the multi-object ("compound") trigger.

Left side of Figure 138 shows the efficiency of `HLT_g75_tight_3j50noL1_L1EM22VHI` in 2016 data with no kinematic selection. The trigger reaches a plateau for subleading jets with $p_T > 65$ GeV, and the right side shows the efficiency after requiring that the subleading jet has flat efficiency. It demonstrates that full efficiency is reached by additionally requiring photon $p_T > 85$ GeV. The same conclusion can be reached by reversing the selection. The result of first applying a photon $p_T > 85$ GeV cut without a selection on the subleading jet p_T cut is shown in figure 139. There the trigger becomes fully efficient for subleading jet with $p_T > 65$ GeV. This demonstrates that the multi-object dijet+γ trigger for 2016 is fully efficient for events with an offline isolated photon of $p_T > 85$ GeV passing tight identification and two jets of $p_T > 65$ GeV. Additionally, no issues are seen with the HLT approximation of the photon-jet overlap removal where every photon is assumed to fake a jet.

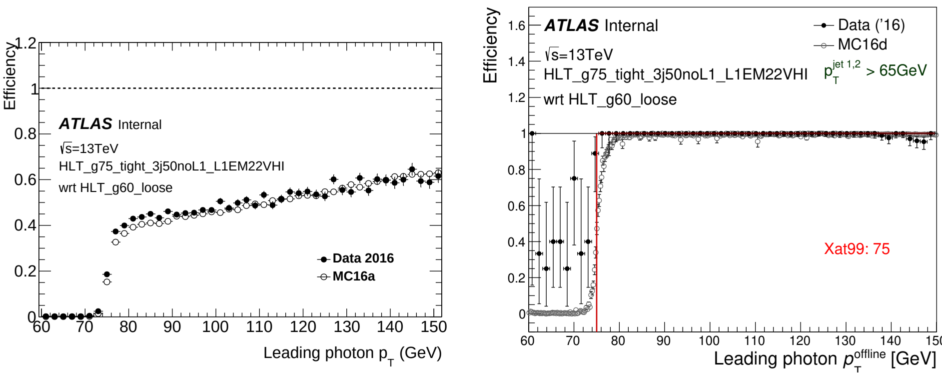

Figure 138: The efficiency of the dijet+γ trigger as a function of leading isolated photon passing tight identification criteria without any kinematic selection (left). Same, but after requaring that the subleading jet p_T >65 GeV.

A similar behaviour is observed with the `HLT_g85_tight_L1EM22VHI_3j50noL1` trigger in the 2017 dataset. Figure 140 shows the efficiency of this trigger without (left) and with (right) kinematic selection. Once again, the efficiency of the trigger with respect to the offline reconstruction is studied by bootstrapping from the `HLT_g60_loose` trigger. Figure 141 shows the efficiency vs. subleading jet p_T when photon $p_T > 95$ GeV (full efficiency for the photon term).

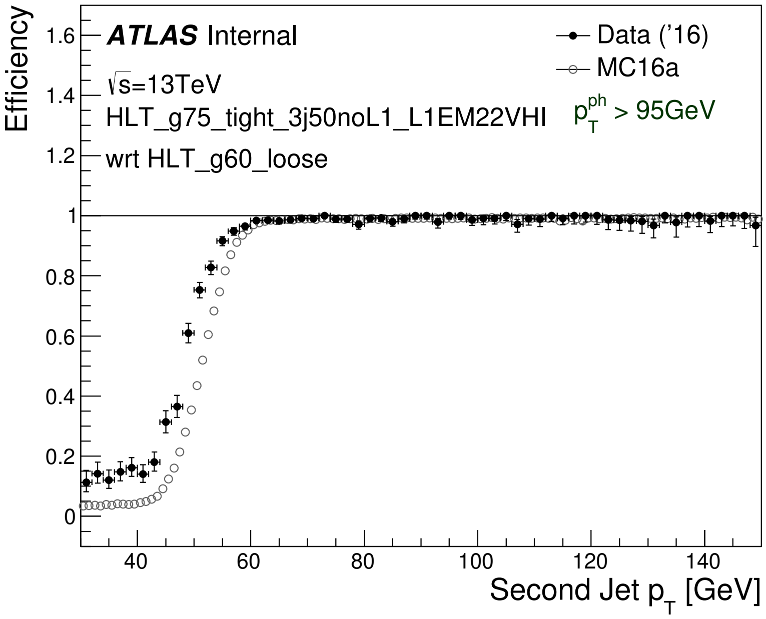

Figure 139: The efficiency of the dijet+γ trigger as a function of subleading jet p_{T} after overlap removal. The leading photon p_{T} is required to be above 95 GeV. The efficiencies in 2016 data and mc16a are shown.

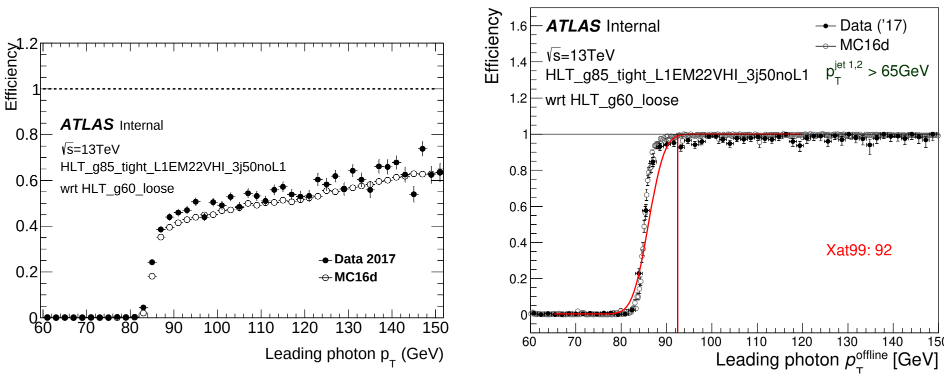

Figure 140: The efficiency of the dijet+γ trigger as a function of leading isolated photon passing tight identification criteria without any kinematic selection. Same for the right plot but after requiring the subleading jet p_{T} >65 GeV.

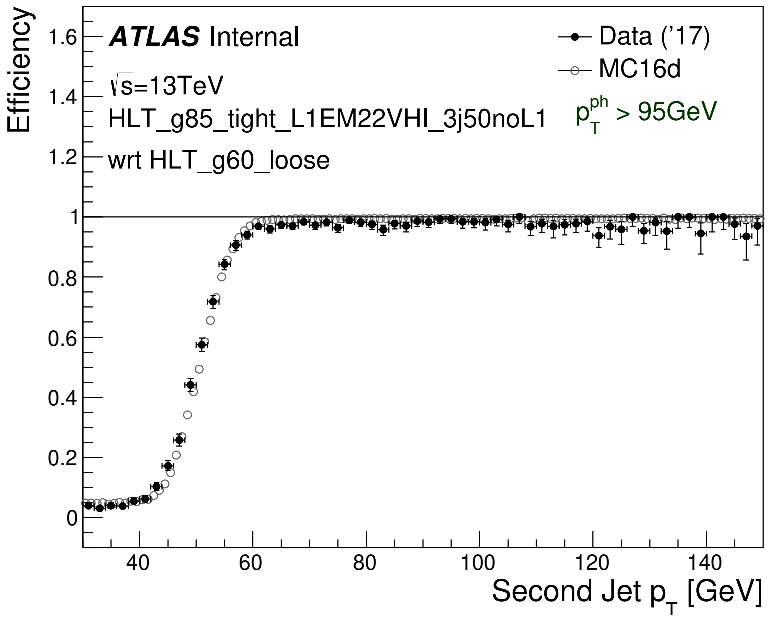

Figure 141: The efficiency of the dijet+γ trigger as a function of subleading jet p_{T} after overlap removal. The leading photon p_{T} is required to be above 95 GeV. The efficiencies in 2017 data and mc16d are shown.

B.5 Optimization cuts studies

A brief description of the discriminant variables studied.

***Asymmetry* :** The asymmetry in p_T between the two signal jets: $A = \frac{(|p_{T,1}|-|p_{T,2}|)}{(|p_{T,1}|+|p_{T,2}|)}$.

***AsymmetryISR* :** The asymmetry in p_T between the ISR object and the reconstructed Z.

ΔR : The difference in η,ϕ location between the ISR object and the nearest signal jet. In a signal event with a reasonably boosted resonance these are expected to be roughly back-to-back.

$\Delta R_{M_{jj}}$: Same as before but with respect to the invariant jet mass.

y^* : A key discriminating variable for dijet analyses, y^* is a measure of rapidity difference between the two signal jets.

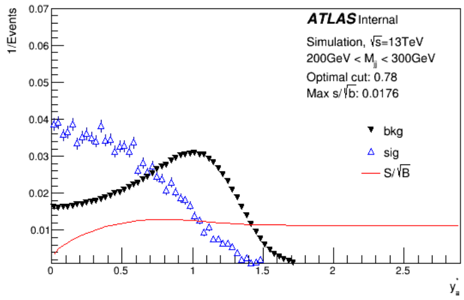

(a) y^*

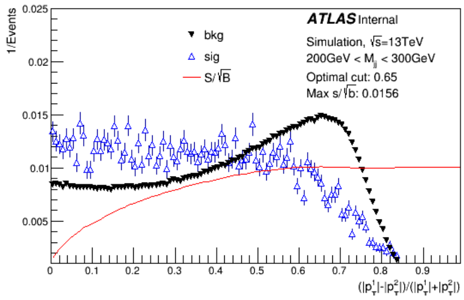

(b) Asymmetry between two resolved jets

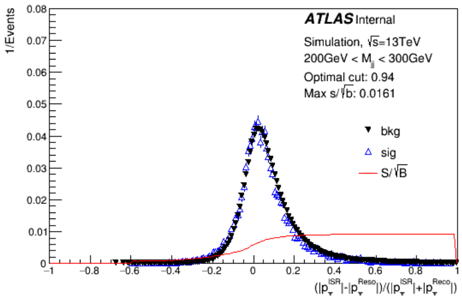

(c) Asymmetry between ISR and reconstructed jet

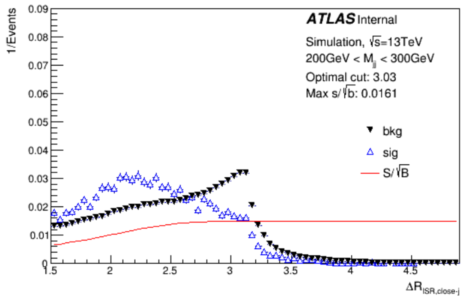

(d) ΔR distance between the ISR and the closest jet

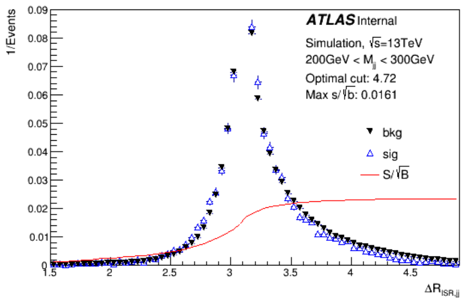

(e) ΔR distance between the ISR and the reconstructed jet

Figure 142: Signal (s) and background (b) distributions of the significant variables , along with the function $s/\sqrt{b}$. Photon ISR channel with HLT_g140_loose trigger, mass range 200GeV to 300GeV.

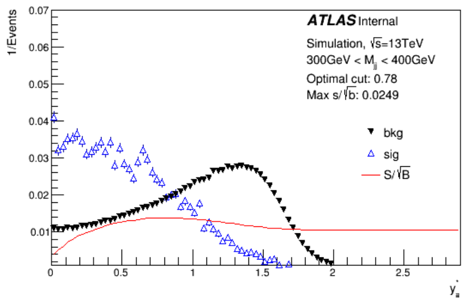

(a) y^*

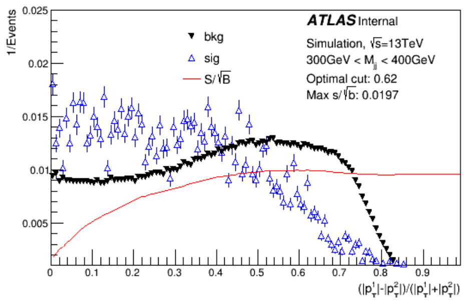

(b) Asymmetry between two resolved jets

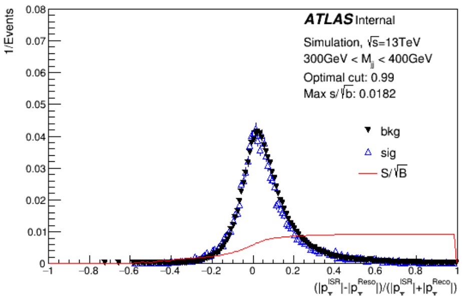

(c) Asymmetry between ISR and reconstructed jet

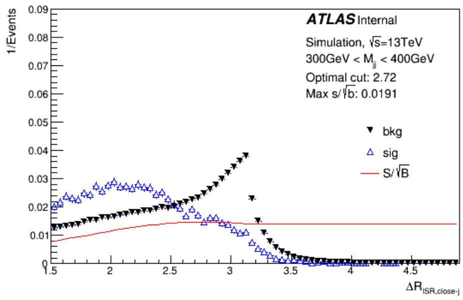

(d) ΔR distance between the ISR and the closest jet

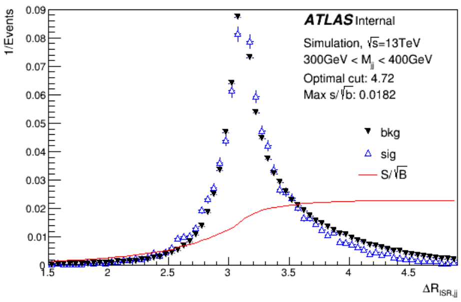

(e) ΔR distance between the ISR and the reconstructed jet

Figure 143: Signal (s) and background (b) distributions of the significant variables , along with the function $s/\sqrt{b}$. Photon ISR channel with HLT_g140_loose trigger, mass range 300GeV to 400GeV.

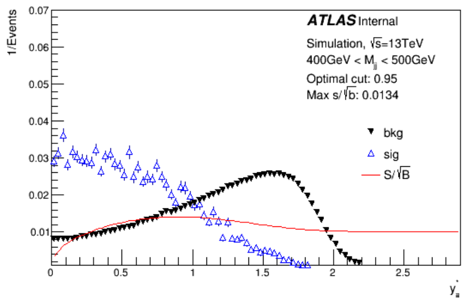

(a) y^*

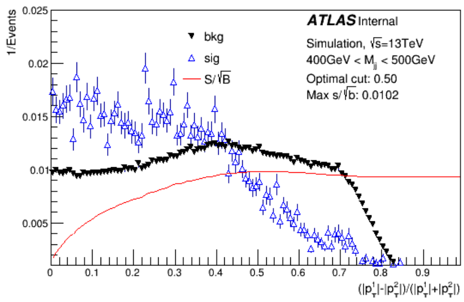

(b) Asymmetry between two resolved jets

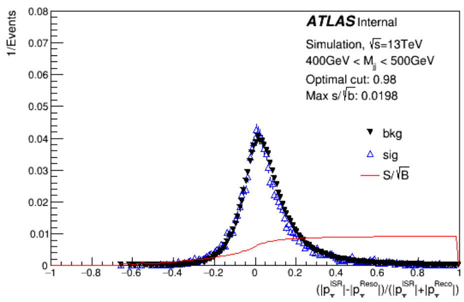

(c) Asymmetry between ISR and reconstructed jet

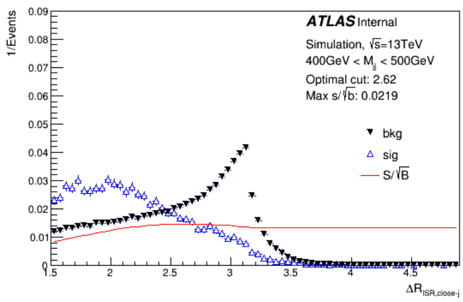

(d) ΔR distance between the ISR and the closest jet

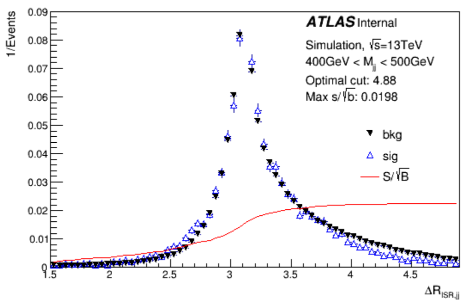

(e) ΔR distance between the ISR and the reconstructed jet

Figure 144: Signal (s) and background (b) distributions of the significant variables , along with the function $s/\sqrt{b}$. Photon ISR channel with HLT_g140_loose trigger, mass range 400GeV to 500GeV.

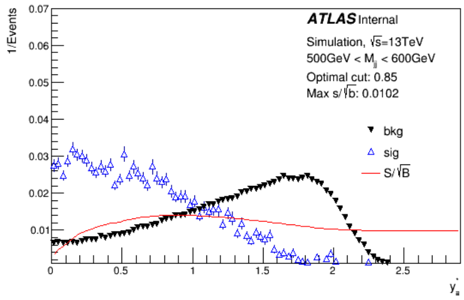

(a) y^*

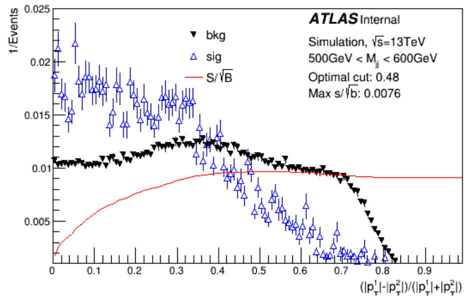

(b) Asymmetry between two resolved jets

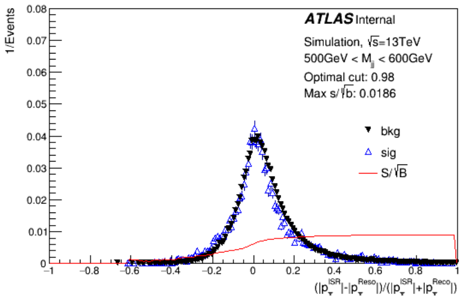

(c) Asymmetry between ISR and reconstructed jet

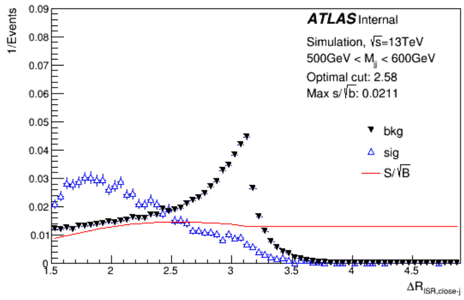

(d) ΔR distance between the ISR and the closest jet

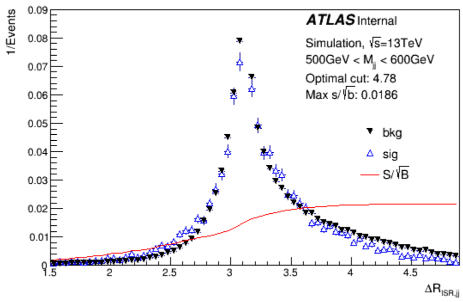

(e) ΔR distance between the ISR and the reconstructed jet

Figure 145: Signal (s) and background (b) distributions of the significant variables , along with the function $s/\sqrt{b}$. Photon ISR channel with HLT_g140_loose trigger, mass range 500GeV to 600GeV.

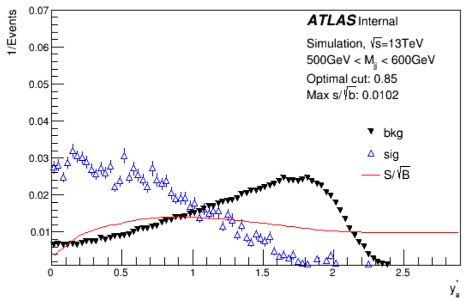

(a) y^*

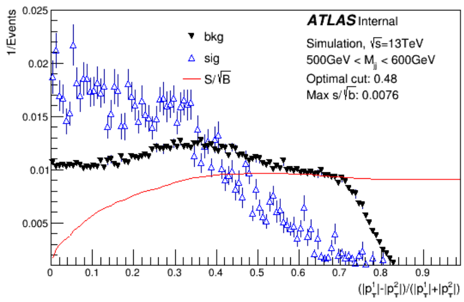

(b) Asymmetry between two resolved jets

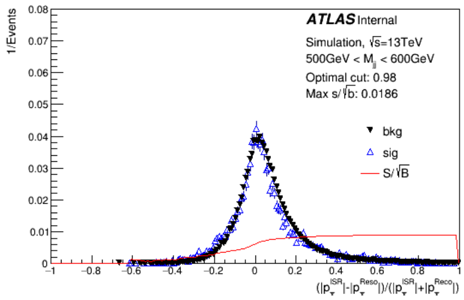

(c) Asymmetry between ISR and reconstructed jet

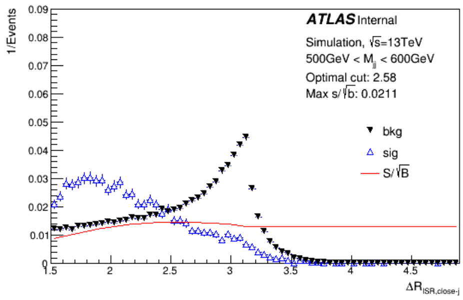

(d) ΔR distance between the ISR and the closest jet

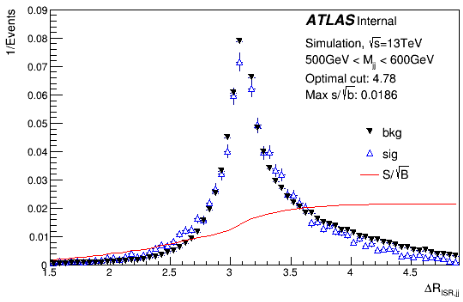

(e) ΔR distance between the ISR and the reconstructed jet

Figure 146: Signal (s) and background (b) distributions of the significant variables , along with the function $s/\sqrt{b}$. Photon ISR channel with HLT_g140_loose trigger, mass range 500GeV to 600GeV.

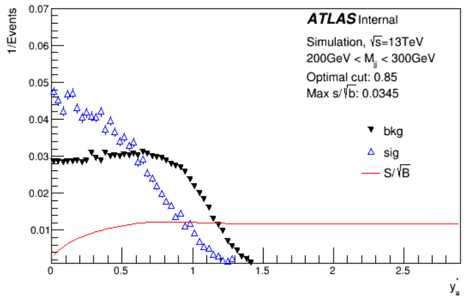

(a) y^*

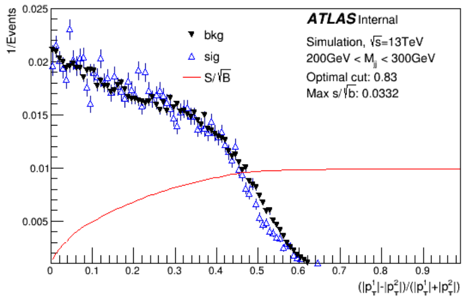

(b) Asymmetry between two resolved jets

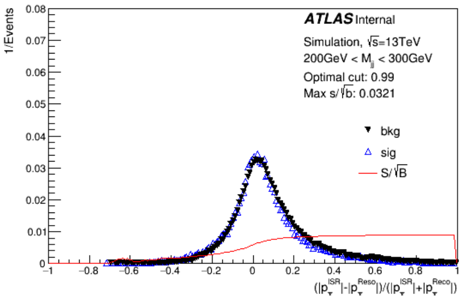

(c) Asymmetry between ISR and reconstructed jet

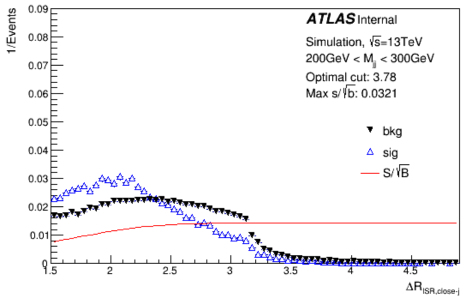

(d) ΔR distance between the ISR and the closest jet

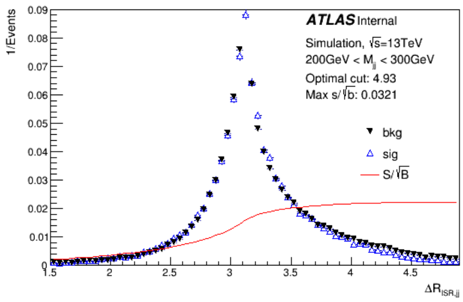

(e) ΔR distance between the ISR and the reconstructed jet

Figure 147: Signal (s) and background (b) distributions of the significant variables, along with the function $s/\sqrt{b}$. Photon ISR channel with HLT_g75_tight_3j50noL1_L1EM22VHI trigger, mass range 200GeV to 300GeV.

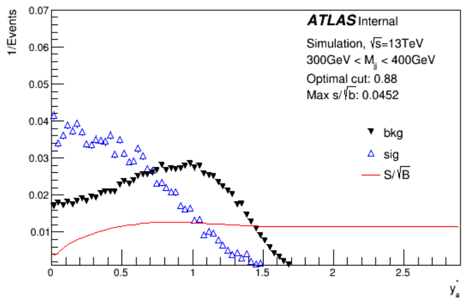

(a) y^*

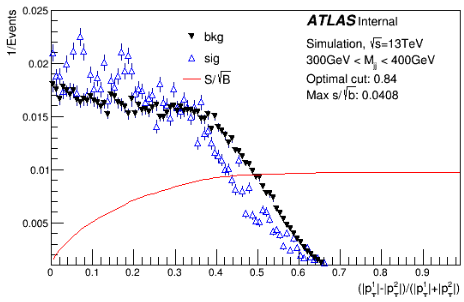

(b) Asymmetry between two resolved jets

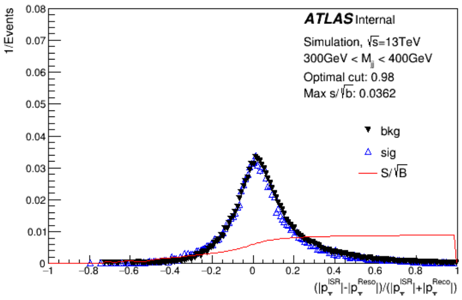

(c) Asymmetry between ISR and reconstructed jet

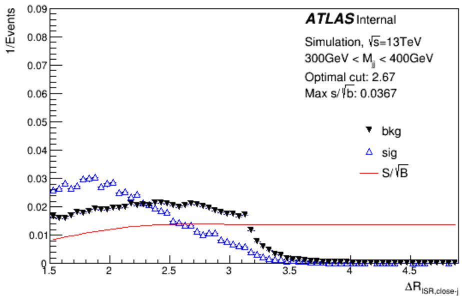

(d) ΔR distance between the ISR and the closest jet

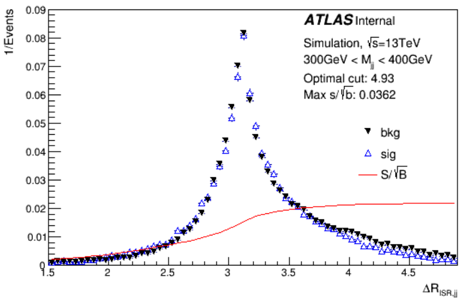

(e) ΔR distance between the ISR and the reconstructed jet

Figure 148: Signal (s) and background (b) distributions of the significant variables, along with the function $s/\sqrt{b}$. Photon ISR channel with HLT_g75_tight_3j50noL1_L1EM22VHI trigger, mass range 300GeV to 400GeV.

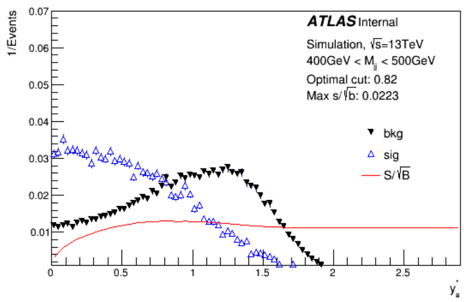

(a) y^*

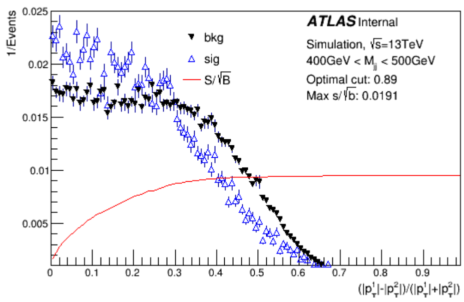

(b) Asymmetry between two resolved jets

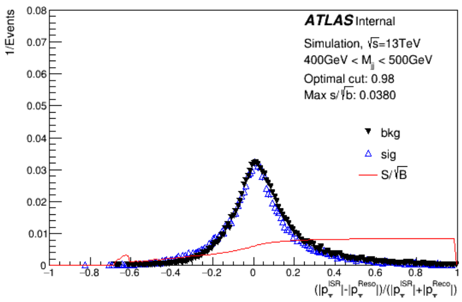

(c) Asymmetry between ISR and reconstructed jet

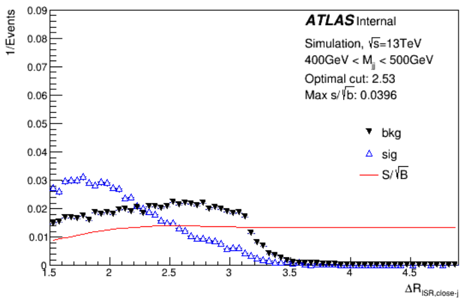

(d) ΔR distance between the ISR and the closest jet

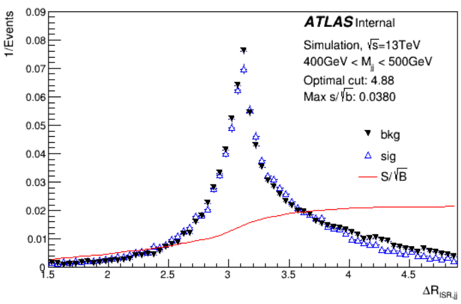

(e) ΔR distance between the ISR and the reconstructed jet

Figure 149: Signal (s) and background (b) distributions of the significant variables , along with the function $s/\sqrt{b}$. Photon ISR channel with HLT_g75_tight_3j50noL1_L1EM22VHI trigger, mass range 400GeV to 500GeV.

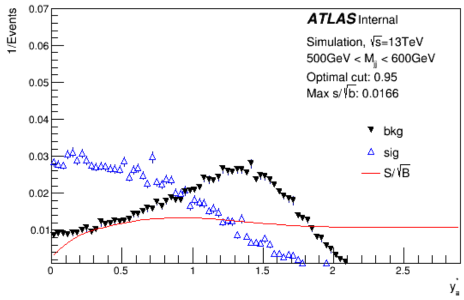

(a) y^*

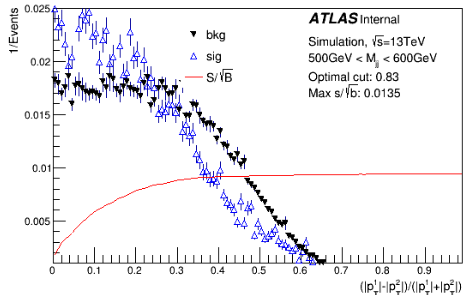

(b) Asymmetry between two resolved jets

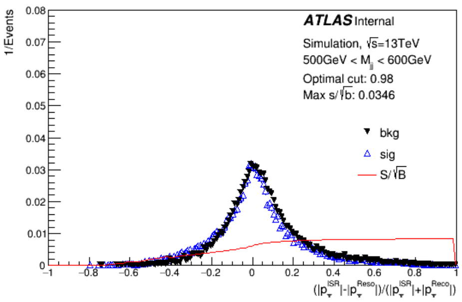

(c) Asymmetry between ISR and reconstructed jet

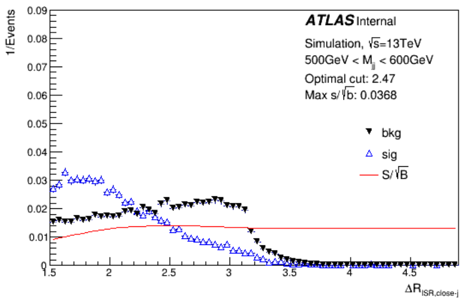

(d) ΔR distance between the ISR and the closest jet

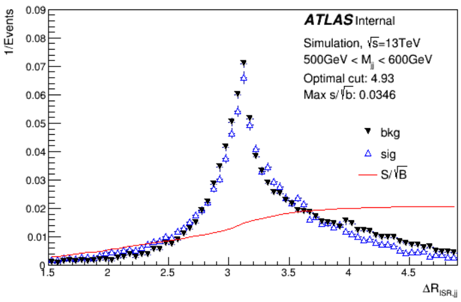

(e) ΔR distance between the ISR and the reconstructed jet

Figure 150: Signal (s) and background (b) distributions of the significant variables , along with the function $s/\sqrt{b}$. Photon ISR channel with HLT_g75_tight_3j50noL1_L1EM22VHI trigger, mass range 500GeV to 600GeV.

B.6 Composition of kinematic distributions after tagging

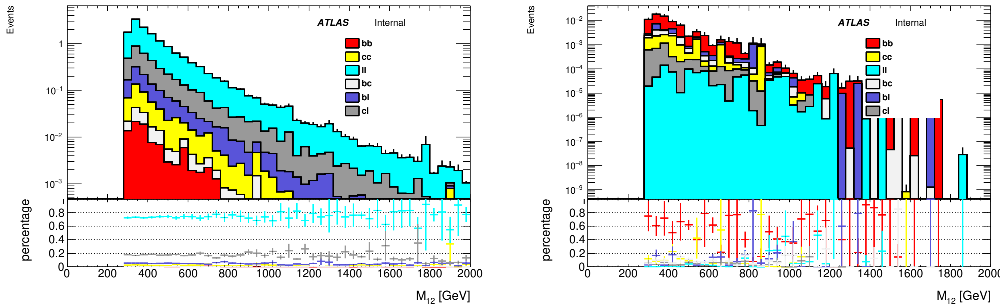

Figure 151: Flavour composition breakdown of M_{jj} spectrum in Sherpa mc16d for the inclusive selection on the left and for the 2-tagged selection on the right . The fraction represented by each flavour pairing is shown in the ratio plot. The compound signal region is used.

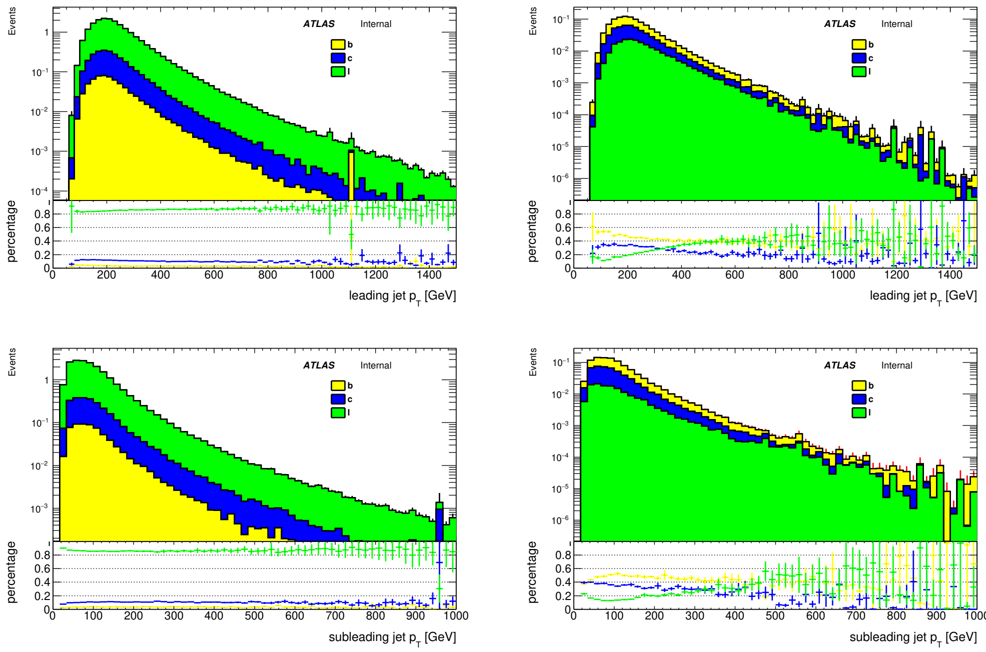

Figure 152: Composition of the leading and subleading jet distributions for the single photon trigger, before and after the application of *b-tag* . The plots use Sherpa mc16d.

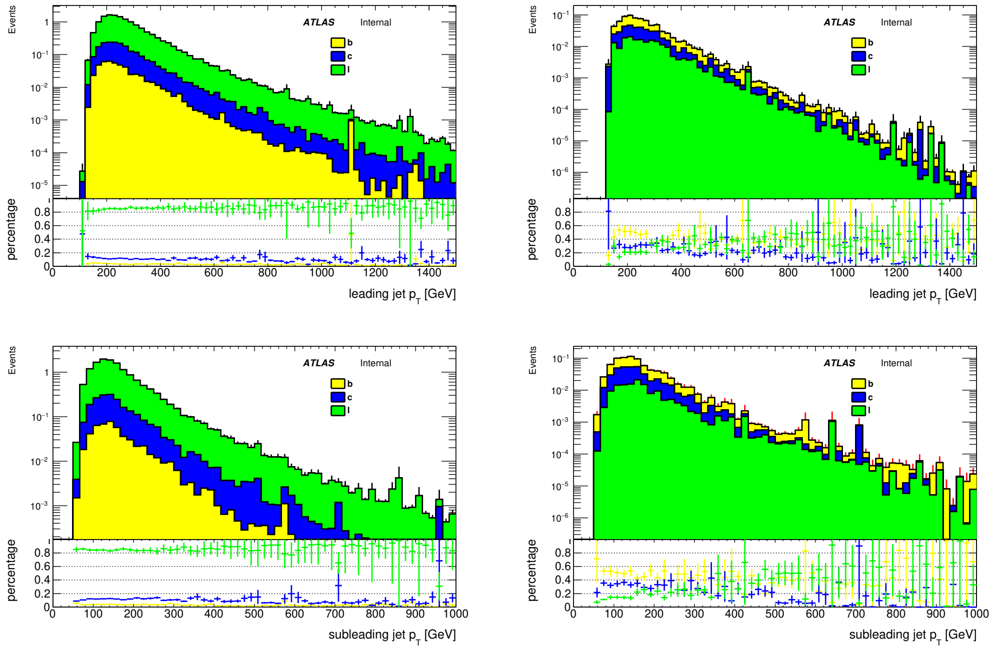

Figure 153: Composition of the leading and subleading jet distributions for the compound trigger, before and after the application of *b-tag* . The plots use Sherpa mc16d.

B.7 Significance plots for different tagger and working point selections

The following figures compare all working points for a specific tagger, and all taggers at a specific working point. Wherever possible, results are shown across values of g_q ranging from 0.1 to 0.4. Since smaller values of g_q are of more interest to the analysis, with larger values already being effectively probed by earlier results, the optimal choices for smaller couplings are given preference in cases where different choices dominate for different coupling values.

Figures 154 and 155 compare signal efficiencies for various taggers at the 77% hybrid efficiency working point and 77% fixed efficiency working points respectively. `DL1` is seen to out-perform `MV2c10` across the relevant mass range for small values of g_q in the photon ISR channel and for all values of g_q in the jet ISR channel. It is thus concluded that `DL1` should be the preferred tagging algorithm.

Selection of a hybrid working point for the `DL1` tagger uses the information shown in Figures 156, while selection of a fixed efficiency working point uses the information in Figures 157 and 158. For the hybrid working points, both photon ISR and jet ISR results are shown, and it can be seen that tagging offers an advantage over the inclusive selection in the photon ISR channel with no further combination, but that in the jet ISR channel the inclusive selection performs best. This preference for an inclusive result in the jet ISR channel then leads to improved performance from more inclusive taggers. Since the photon ISR channel benefits most from tagging and shows differences between WPs which correspond not only to degree of inclusiveness,

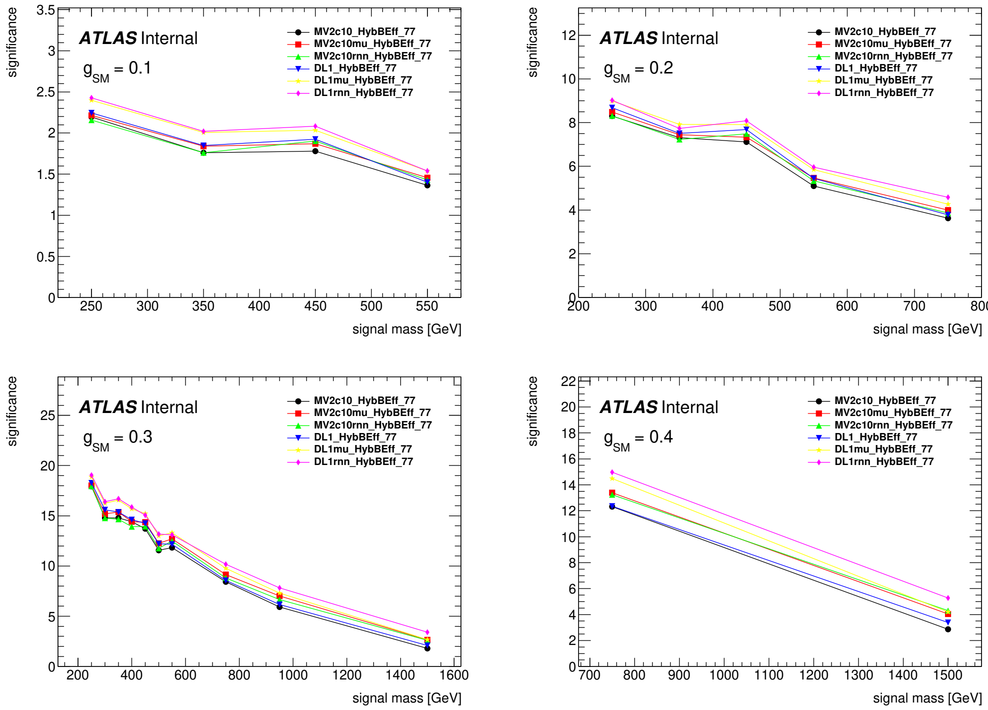

Figure 154: Comparison of taggers at the 77% hybrid efficiency working point for signal samples of different couplings. The photon ISR channel is shown with the single photon trigger and corresponding analysis selection.

it is the photon ISR channel which is used to determine the optimal selection. The photon ISR channel plots then show that the optimal hybrid efficiency WP and fixed efficiency WP are both 77%, and that those two options give quite comparable performance to one another. The choice between them is therefore left to other analysis factors, in particular the expected smoothness of the spectrum.

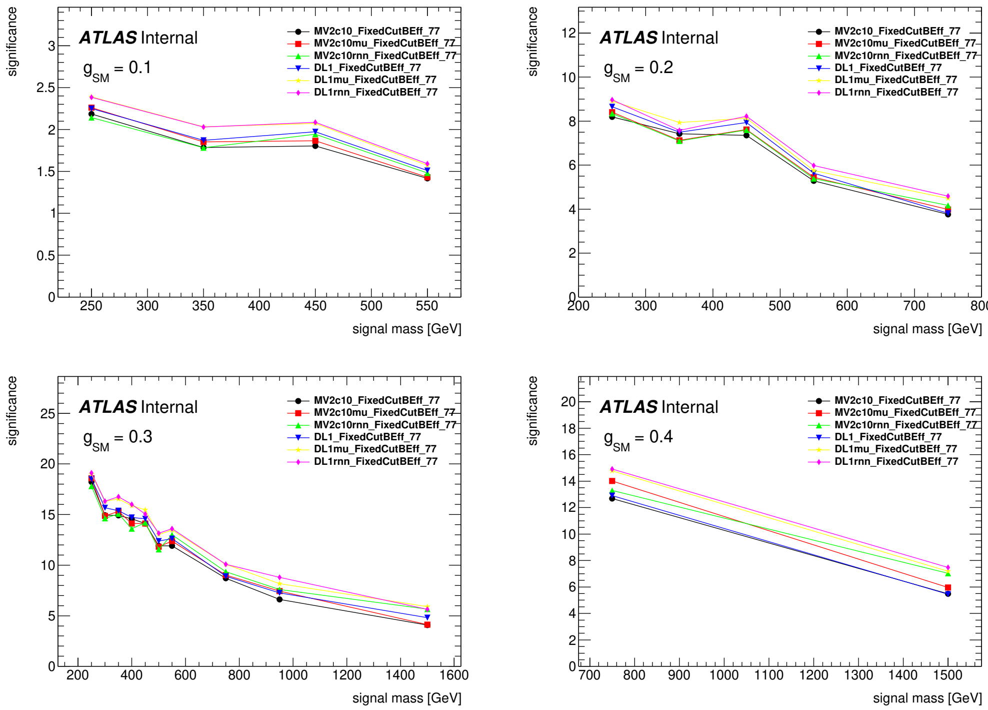

Figure 155: Comparison of taggers at the 77% fixed efficiency working point for signal samples of different couplings. The photon ISR channel is shown with the single photon trigger and corresponding analysis selection.

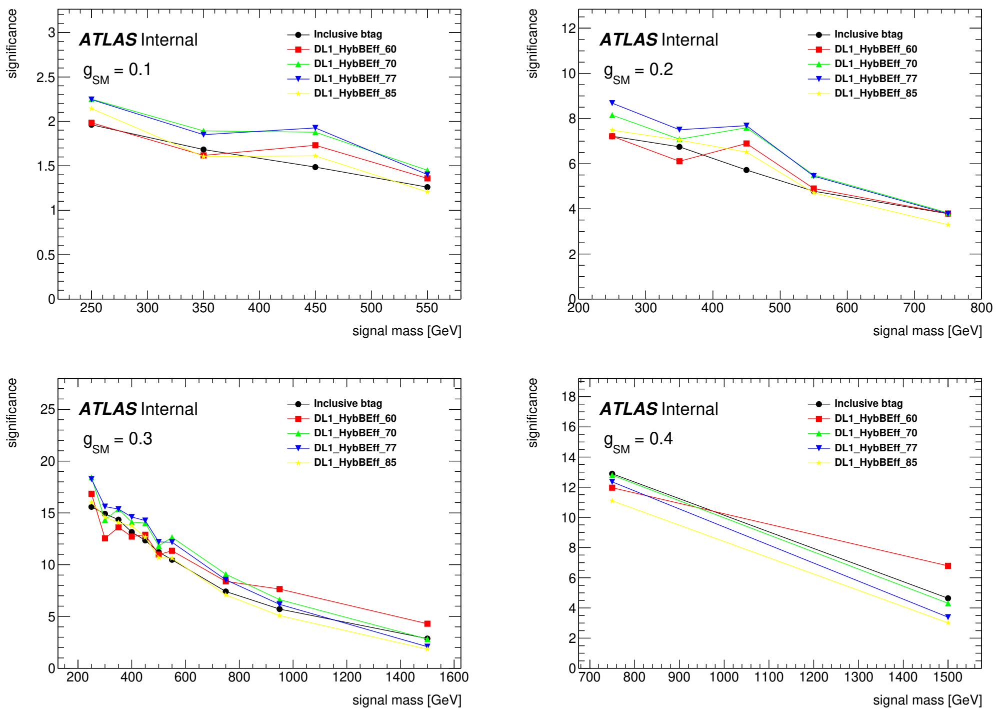

Figure 156: Comparison of `DL1` hybrid efficiency working points for signal samples of different couplings. The photon ISR channel is shown with the single photon trigger and corresponding analysis selection.

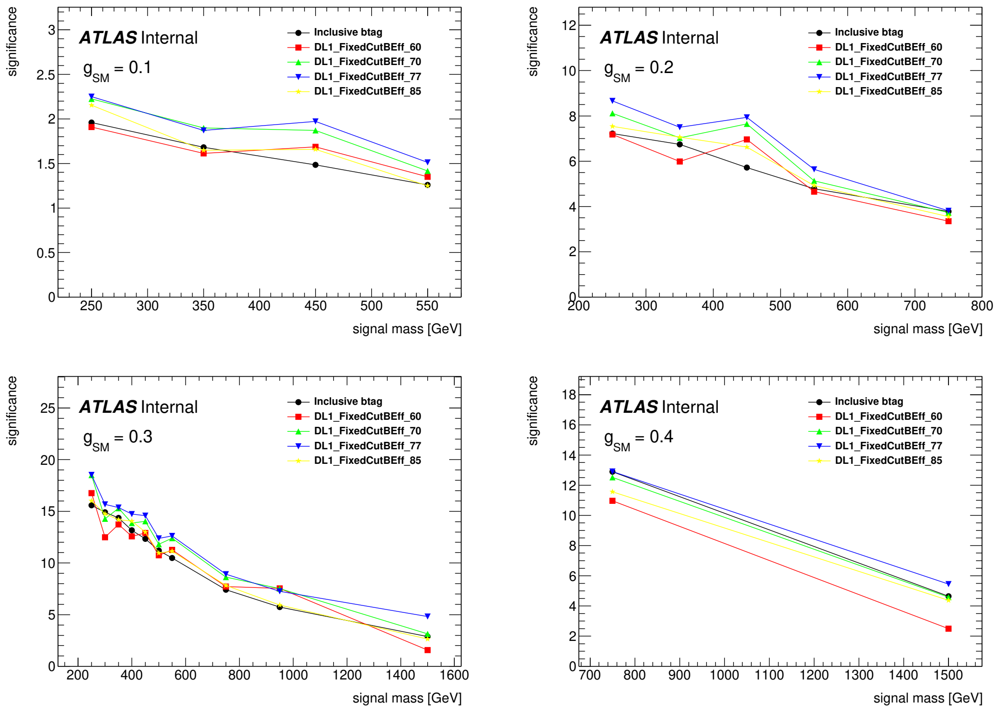

Figure 157: Comparison of `DL1` fixed efficiency working points for signal samples of different couplings. The photon ISR channel is shown with the single photon trigger and corresponding analysis selection.

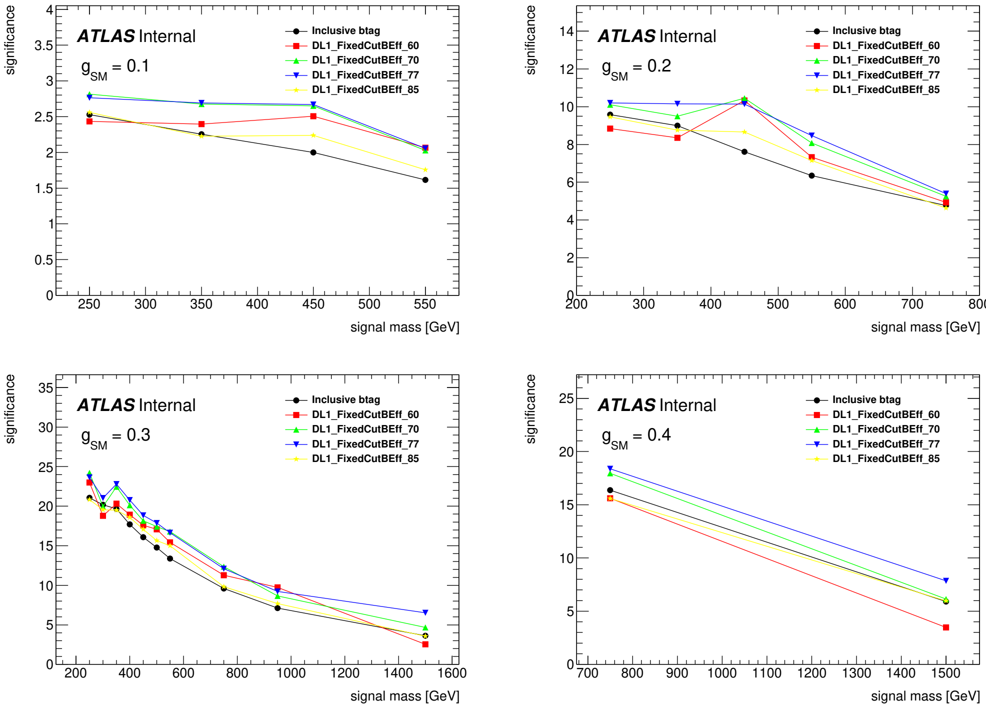

Figure 158: Comparison of DL1 fixed efficiency working points for signal samples of different couplings. The photon ISR channel is shown with the combined trigger and corresponding analysis selection.

B.8 Smoothness of the 2 b-tagged M_{jj} spectrum

The di-jet analyses are based on the assumption that the QCD background distribution is a smoothly falling spectrum. Any process, (such as selection) that leads to structures in the background spectrum, may cause spurious signals. Previous studies [9] showed that if the *b-tag* efficiency as a function of the transverse momentum causes some structures in the M_{jj} spectrum, the fitting M_{jj} spectrum may fail. This analysis showed the existence of some features in the *b-tag* efficiency distributions (Figure 81-83) in Section. 7.7.1, such as the features in the low jet p_{T}region for *b*-jet and *c*-jet tagging efficiencies using hybrid working points and for light-jet tagging efficiency using fixed working points. In this section, we will study how these features sculpt the 2 *b-tag* M_{jj} spectra.

The reweighting method is used to obtain the 2 *b-tag* M_{jj} spectra. The strategy is as follows: First, the 3D histograms for leading jet p_{T}, subleading jet p_{T}, and M_{jj} are made. Each jet could have a different truth flavor type, *b*-jet, *c*-jet or light-jet, there are 9 different flavor categories for the 3D histograms. Then, the *b-tag* efficiency is set as a function of each jet p_{T}(*b*-jet, *c*-jet and light-jet) Finally, the 2 *b-tag* M_{jj} spectrum is obtained by reweighting these histograms using Equation 50. In Eqution 50, $N(m_{jj})$ is the number of events in each bin of 2 *b-tag* M_{jj} spectrum. $N_{mn}(p_{T,j1}, p_{T,j2}, m_{jj})$ is bin content of the 3D histogram in which the truth flavors of the 2 selected jets are m and n respectively. ϵ_m and ϵ_n are the *b-tag* efficiency of corresponding truth flavor we set before, and they are both functions of jet p_{T}.

$$N(m_{jj}) = \sum_{\substack{m=b,c,l \\ n=b,c,l}} \int N_{mn}(p_{T,j1}, p_{T,j2}, m_{jj}) \times \epsilon_m(p_{T,j1}) \times \epsilon_n(p_{T,j2})\, dp_{T,j1} dp_{T,j2} \quad (50)$$

To visualize the possible structures in the 2 *b-tag* M_{jj} spectra obtained by reweighting, rough fit is done for these spectra. As the statistic of data goes higher and higher, it is hard to fit the M_{jj} spectrum globally. Instead, SWIFT will be used to fit the M_{jj} spectra formally in di-jet ISR analysis. In this study, the 2 *b-tag* M_{jj} spetra are fitted in three different region (160 GeV,300 GeV), (300 GeV,700 GeV) and (700 GeV,1200 GeV) seperately. The fit function shows in Equation 51, where $z = m_{jj}/\sqrt{s}$.

$$f(z) = c_1(1-z)^{c_2} z^{c_3 + c_4 \ln z} \quad (51)$$

Figure 159 show the 2 *b-tag* M_{jj} spectrum obtained by reweighting 3D histograms according to flat *b-tag* efficiencies and the fit result. This provides a baseline for this study. Some reasonable features are set on these flat *b-tag* efficiency distributions, as showed in Figure 160, 161, 162 and 163. Reasonable features mean these features have comparable shape and size with the realistic features in *b-tag* efficiency of DL1 hybrid 77% and fixed 77% working point. Comparing the fit results of the 2 *b-tag* spectra obtained by reweighting 3D histograms according to these *b-tag* efficiency distribution we set with the fit result of flat efficiency case, no obvious structures is observed. However, if the features are more extreme, the 2 *b-tag* spectra will be sculpted, as showed in Figure 164.

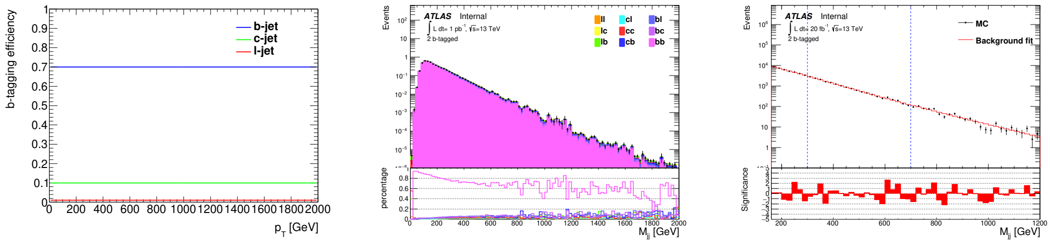

(a) B-tagging efficiency (b) Composition of M_{jj} spectrum (c) Fitting result

Figure 159: The *b-tag* efficiencies are set as flat distributions with values coinsiding with fixed DL1 70% working point(159(a)). Reweight the 3D histograms according to these *b-tag* efficiencies to get the 2 *b-tag* M_{jj} spetrum with 9 composition(159(b)). 159(c) shows the fit result of this 2 *b-tag* M_{jj} spetrum.

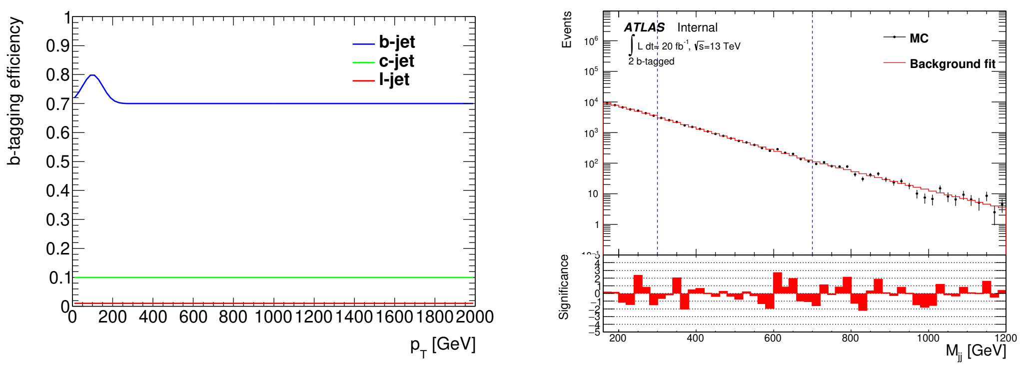

(a) B-tagging efficiency (b) Fitting result

Figure 160: A reasonable feature, which is comparable with the realistic feature in the b-jet *b-tag* efficiency distribution of DL1 hybrid 77% working point, is set on the flat b-jet tagging efficiency distribution(160(a)). 160(b) shows the fit result of the 2 *b-tag* M_{jj} spetrum.

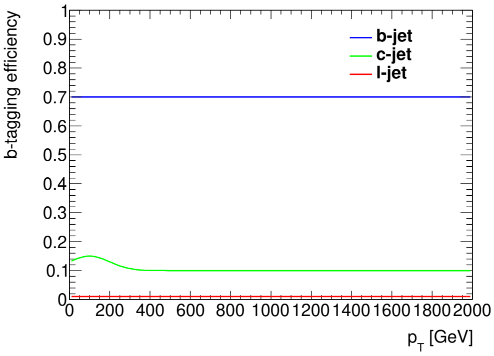

(a) B-tagging efficiency

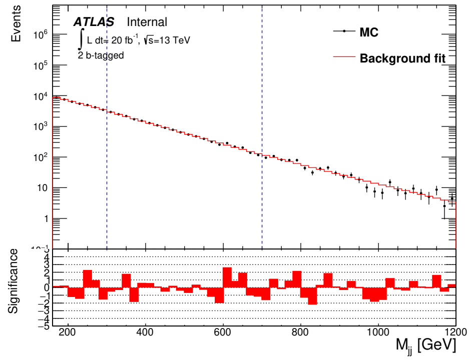

(b) Fitting result

Figure 161: A reasonable feature, which is comparable with the realistic feature in the c-jet b-tag efficiency distribution of DL1 hybrid 77% working point, is set on the flat c-jet tagging efficiency distribution(161(a)). 161(b) shows the fit result of the 2 b-tag M_{jj} spetrum.

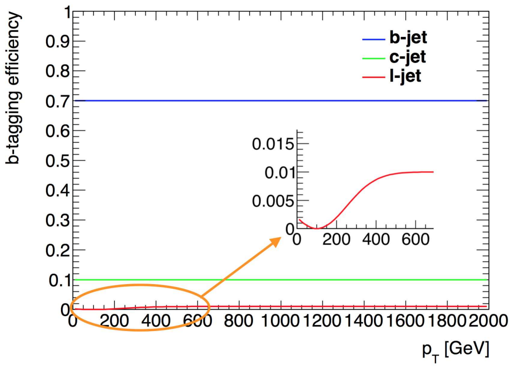

(a) B-tagging efficiency

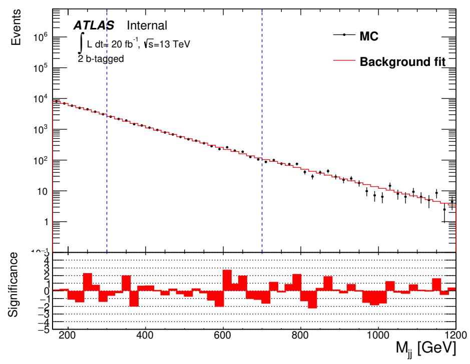

(b) Fitting result

Figure 162: A reasonable feature, which is comparable with the realistic feature in the light-jet b-tag efficiency distribution of DL1 fixed 77% working point, is set on the flat light-jet tagging efficiency distribution(162(a)). 162(b) shows the fit result of the 2 b-tag M_{jj} spetrum.

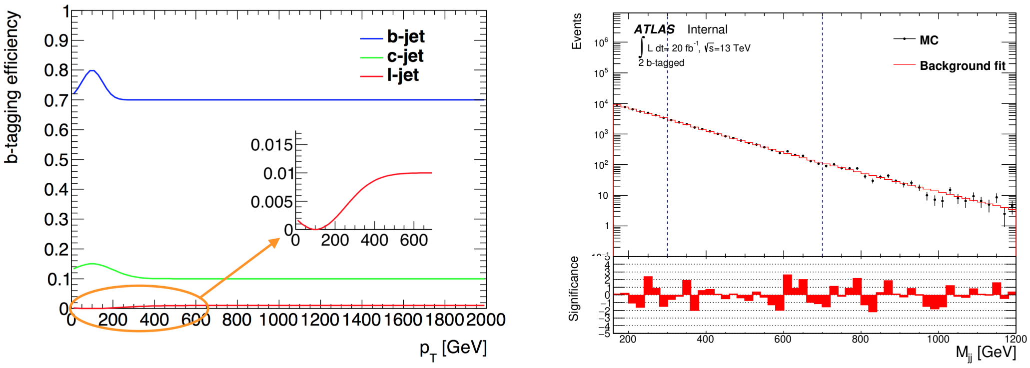

(a) B-tagging efficiency (b) Fitting result

Figure 163: Set the reasonable features on the flat b-jet, c-jet and light-jet tagging efficiency distribution at the same time(163(a)). 163(b) shows the fit result of the 2 b-*tag* M_{jj} spetrum.

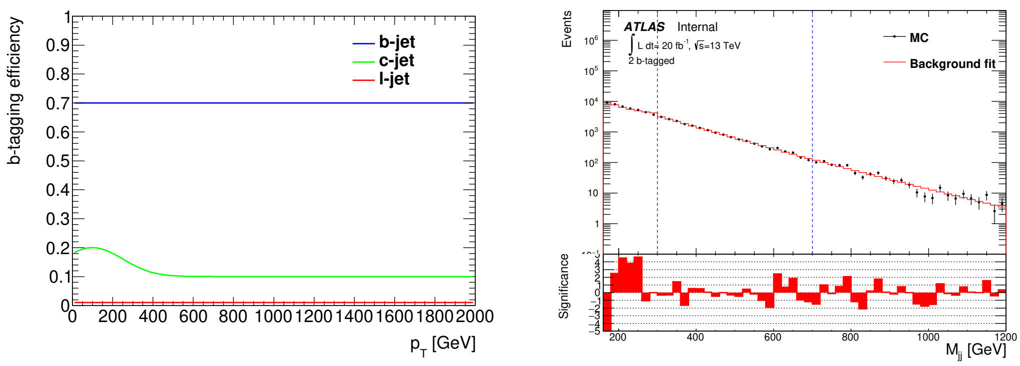

(a) B-tagging efficiency (b) Fitting result

Figure 164: An extreme feature is set on the flat c-jet tagging efficiency distribution(164(a)). 164(b) shows such feature cause some structure in the low mass region of the 2 b-*tag* M_{jj} spetrum.

B.9 Fitting tests on MC spectra

Even when large datasets available in Run2 are unable to reach the expected statistics available in data, all fits should be tested in MC spectra. Their success is not guaranteed of success in data, but any failures could indicate a failure in data. In fact, for the doubly b-tagged spectra, the MC provides a pre-unblinding look at changes in spectrum shape and smoothness which can be expected as a result of the tagging requirement. These tests can also indicate the widest sliding window widths likely to succeed on the unblinded spectra.

Three fits are shown to the inclusive mc16a+mc16d spectra for each of the single-photon trigger (Figure 165) and compound trigger (Figure 166). The MC samples are normalized to the luminosities expected in the full 2015–2017 dataset (79.8 $fb^{-1}$for the single-photon trigger and 76.6 $fb^{-1}$for the compound trigger). These use the five-parameter dijet function as a global fit and with two different SWIFT window half-widths. For the single-photon trigger, these are 20 and 16 bins; for the compound trigger where the M_{jj} spectrum turns on later the widest available window is 18 bins across, so 18 and 16 are shown. The UA2 and four-parameter functions were also tested. In the single-photon trigger case, the UA2 function does not yield an acceptable χ^2 $p-value$with a half-window width above 14 bins so if data looked like MC it would have been discarded. These results are not considered a problem, given that the tests of fitting on the more realistic data shape from a dataset corresponding to 15fb^{-1}show that all three functions chosen yield acceptable χ^2 $p-value$for window width above 14, and some even using the global fit. The summary of the χ^2 $p-value$in MC for the two inclusive channels is shown in Table 25.

Functional form	Channel (inclusive)	Fit type	χ^2 p-value
`our4param`	Single photon trigger	global	0.0
`our4param`	Single photon trigger	SWiFt, whw=22	0.002
`our4param`	Single photon trigger	SWiFt, whw=18	< 0.012
`our4param`	Single photon trigger	SWiFt, whw=16	< 0.019
`our4param`	Single photon trigger	SWiFt, whw=14	< 0.061
`our5param`	Single photon trigger	global	0.042
`our5param`	Single photon trigger	SWiFt, whw=22	0.132
`our5param`	Single photon trigger	SWiFt, whw=18	0.148
`our5param`	Single photon trigger	SWiFt, whw=16	0.171
`UA2`	Single photon trigger	global	< 0.01
`UA2`	Single photon trigger	SWiFt, whw=18	< 0.01
`UA2`	Single photon trigger	SWiFt, whw=16	< 0.01
`UA2`	Single photon trigger	SWiFt, whw=9	0.48
`our4param`	Compound trigger	global	0.852
`our5param`	Single photon trigger	global	0.856
`UA2`	Single photon trigger	global	0.079

Table 25: Summary of the MC-based fitting tests, showing the χ^2 p-value for different fitting configurations.

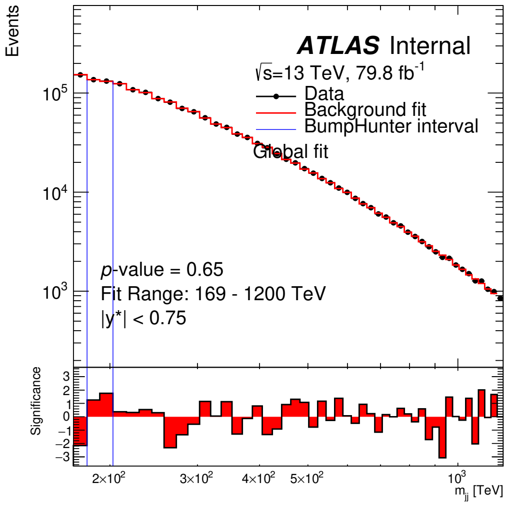

(a) Global

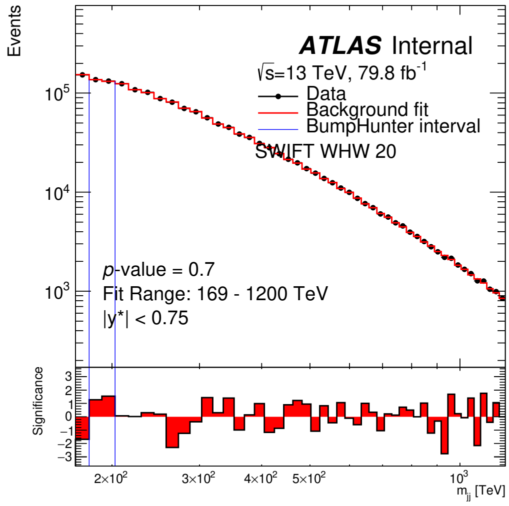

(b) SWIFT whw 20

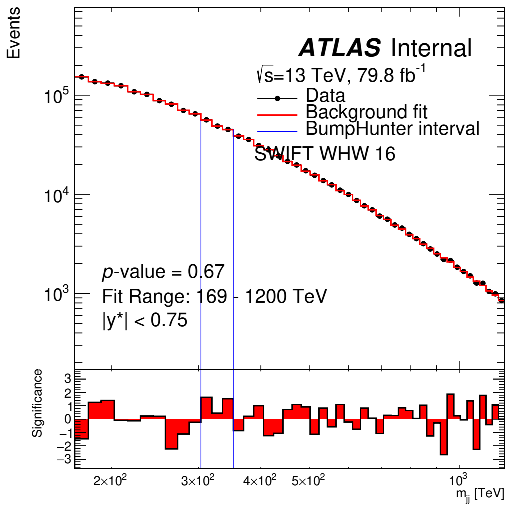

(c) SWIFT whw 16

Figure 165: Fits to the inclusive selection with the single photon trigger in Sherpa Monte Carlo. Samples are normalised to the full analysis luminosity. A fit using the five-parameter dijet function is shown for global (165(a)), SWIFT whw 20 (165(b)), and SWIFT whw 16 (165(c)) settings.

A similar test was done for the doubly b-tagged channel. In this case the equivalent MC statistics are even worse than in the inclusive case. Only limited conclusions can be drawn from the plots, which are challenging to fit or evaluate due to the presence of sporadic high-weight MC events. Figure 167 shows two fits to the b-tagged spectrum in the single photon trigger selection (167(a),167(b)) and two fits to the b-tagged spectrum in the compound trigger selection (167(c),167(d)). A global fit and a SWIFT fit with window half-width 16 are shown in each case. All fits are acceptable given the MC statistics.

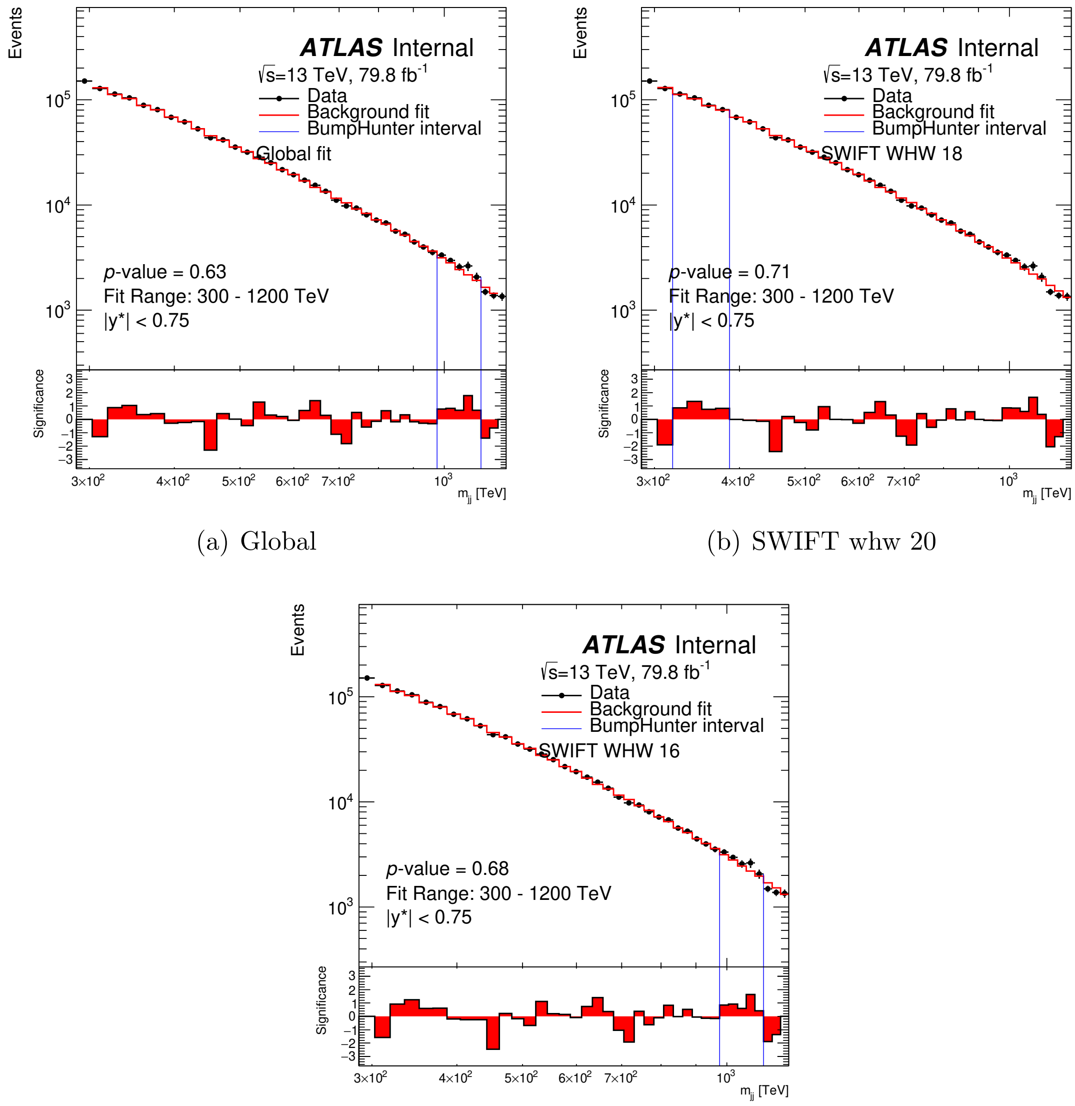

(a) Global

(b) SWIFT whw 20

(c) SWIFT whw 16

Figure 166: Fits to the inclusive selection with the compound trigger trigger in Sherpa Monte Carlo. Samples are normalised to the full analysis luminosity. A fit using the five-parameter dijet function is shown for global (166(a)), SWIFT whw 18 (166(b)), and SWIFT whw 16 (166(c)) settings.

B.10 Systematic uncertainties plots

B.10.1 Uncertainties applied to the signal

Jet energy scale and resolution

JES

following the JetEtMiss group recommendations, the number of uncertanties is the strongly-reduced 4 nuisance parameters

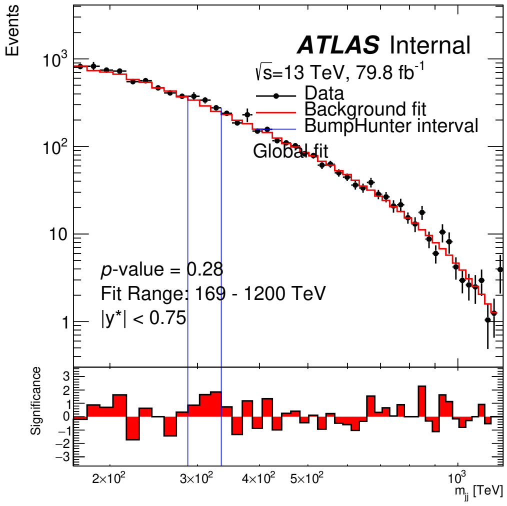

(a) Single photon trigger, global fit

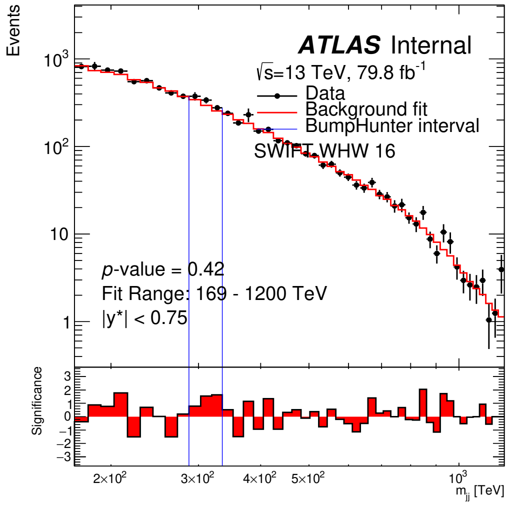

(b) Single photon trigger, SWIFT whw 16

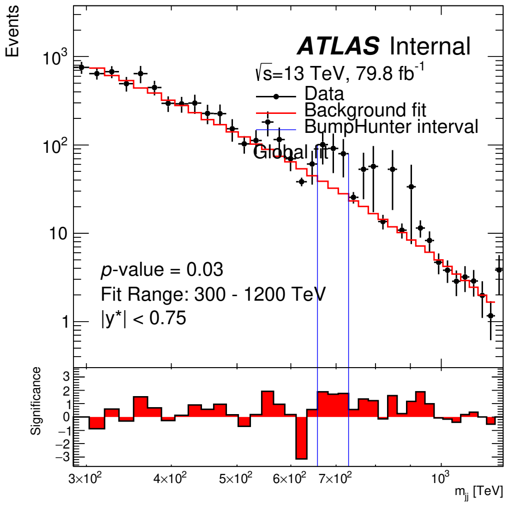

(c) Photon + dijet trigger, global fit

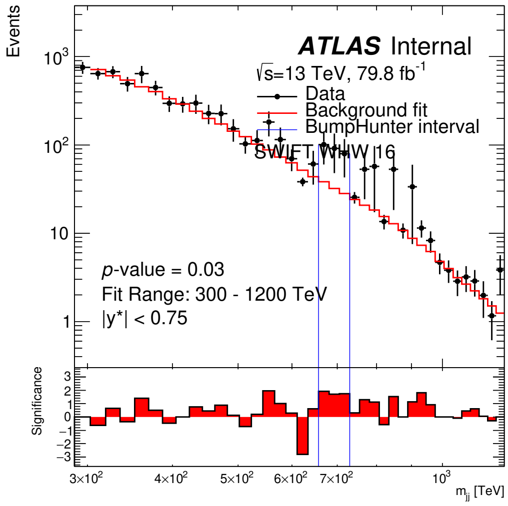

(d) Photon + dijet trigger, SWIFT whw 16

Figure 167: Fits to the doubly *b-tag* selection with the single photon trigger (167(a),167(b)) and the compound trigger (167(c),167(d)) in Sherpa Monte Carlo. Samples are normalised to the full analysis luminosity. A fit using the five-parameter dijet function is shown for global (167(a),167(c)) and SWIFT whw 16 (167(b),167(d)) settings.

A variation due to each nuisance parameter is given in Figures 168 and 169, for the inclusive and the 2 *b-tag* cases. All the uncertainties act not on the acceptance but rather on the peak location, moving it to higher or lower M_{jj} as events move between bins.

JER

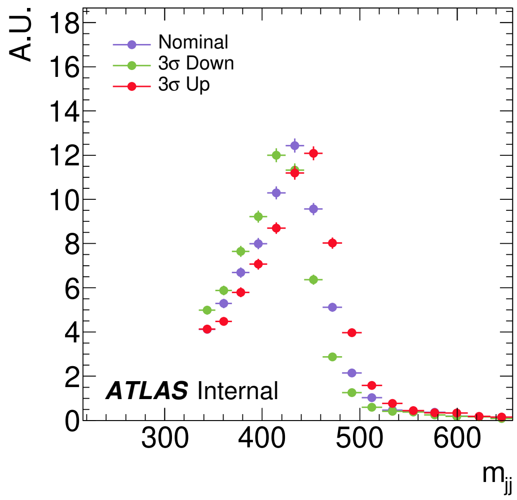

(a) GroupedNP 1

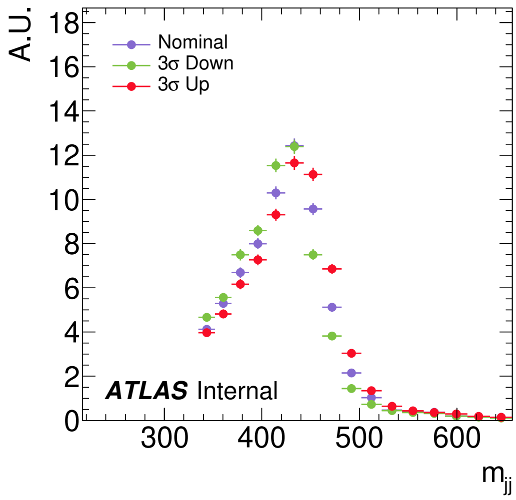

(b) GroupedNP 2

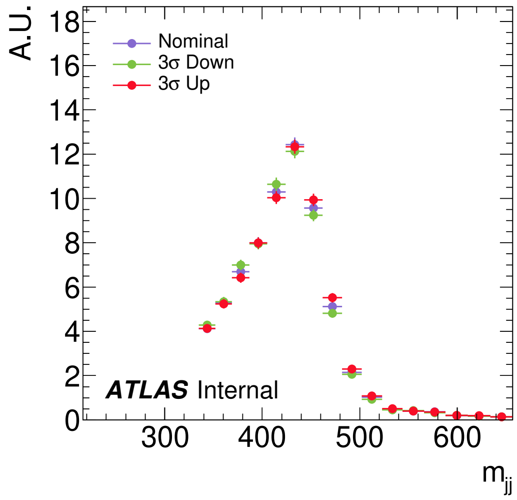

(c) GroupedNP 3

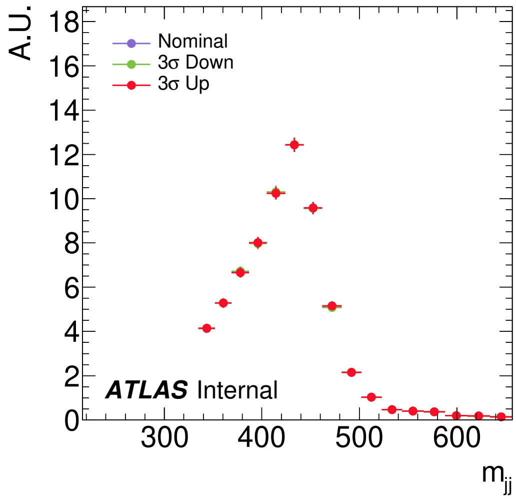

(d) η intercalib. non-closure

Figure 168: Impact of $\pm 3\sigma$ variation in each of the four strongly reduced JES systematics. The Z' point with mass 450 GeVand coupling $g_q = 0.2$ is used as an illustrative example. The compound trigger and inclusive selection are applied.

Photon ID resolution

B.10.1.1 Trigger efficiency

B.10.1.2 b-tagging

Figure 179 shows the impact of the two largest scale factor uncertainties (`FT_EFF_Eigen_B_0` and `FT_EFF_Eigen_B_1`) on a representative signal sample with mass 450 GeVand $g_q = 0.2$. The single photon trigger is used and the 2 *b-tag* selection applied.

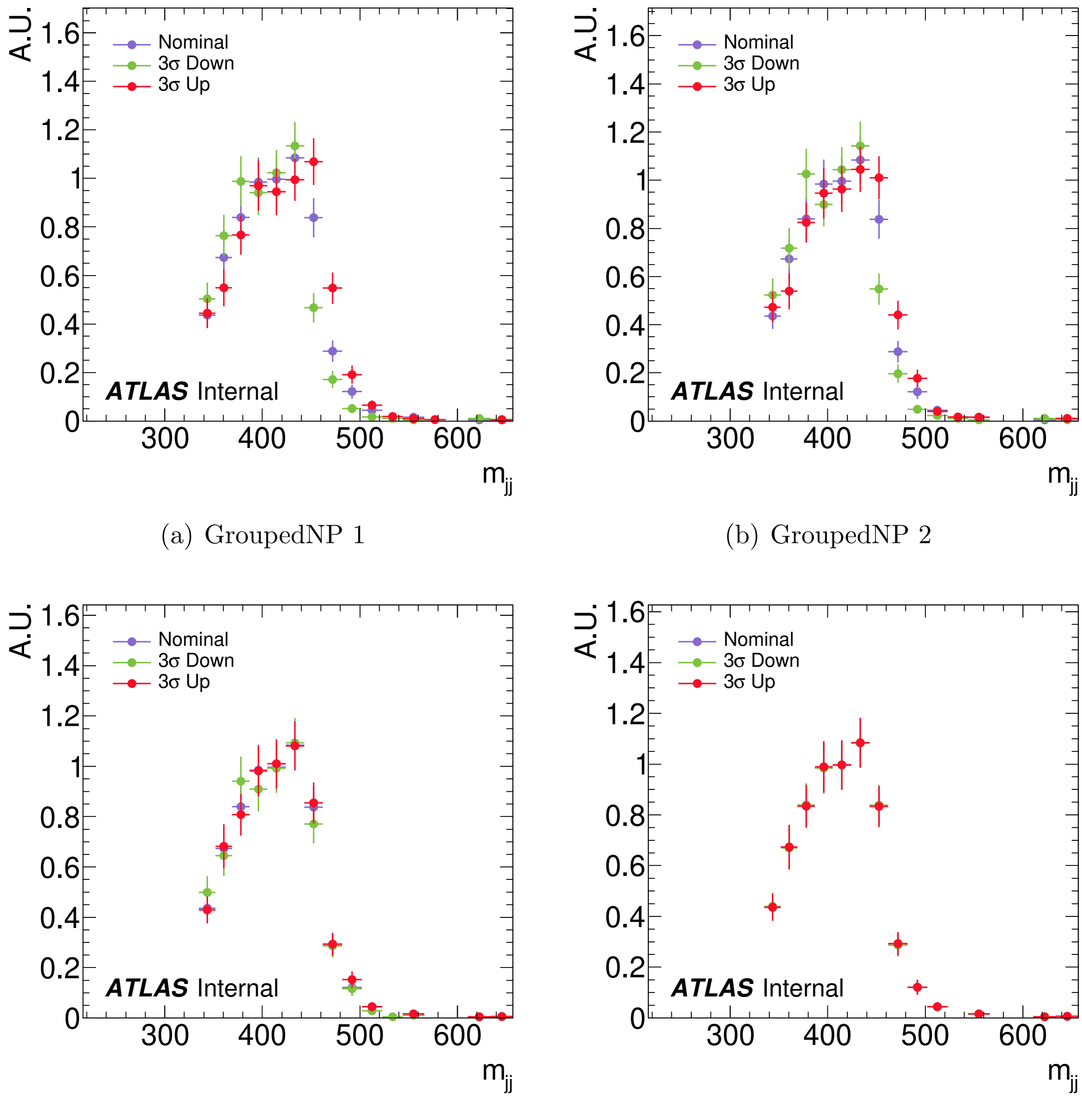

(a) GroupedNP 1

(b) GroupedNP 2

(c) GroupedNP 3

(d) η intercalib. non-closure

Figure 169: Impact of $\pm 3\sigma$ variation in each of the four strongly reduced JES systematics. The Z' point with mass 450 GeVand coupling $g_q = 0.2$ is used as an illustrative example. The compound trigger and 2 *b-tag* selection are applied.

B.10.1.3 PDF

B.10.1.4 JES for model independent

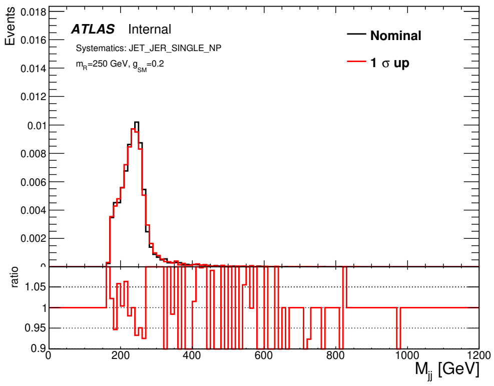

(a) 250 GeV Z', $g_q = 0.2$

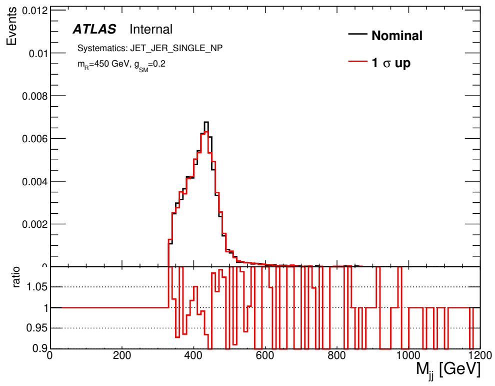

(b) 450 GeV Z', $g_q = 0.2$

Figure 170: Impact of JER variation on two representative signal samples. The impact of the uncertainty is, on average, to widen the peak somewhat, but the statistical effects are substantial.

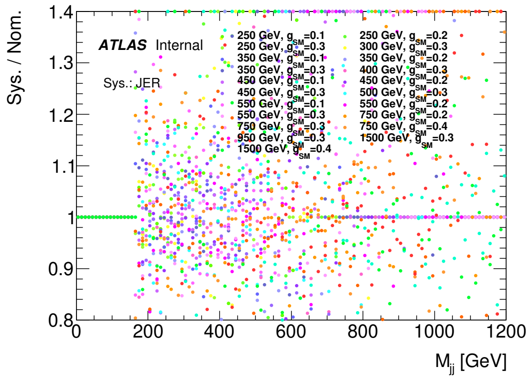

(a) Single photon trigger

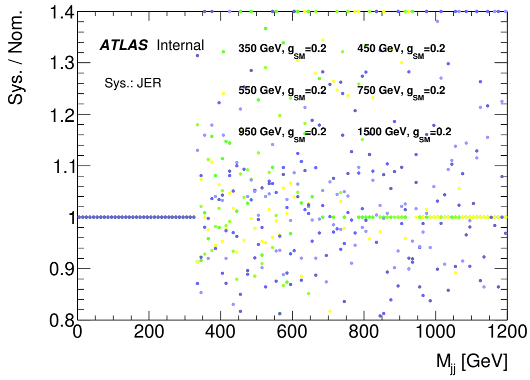

(b) Compound trigger

Figure 171: Impact of JER variation on all signal samples for the single photon trigger (171(a)) and compound trigger (171(b)). Statistical fluctuations in this fine binning make patterns hard to distinguish.

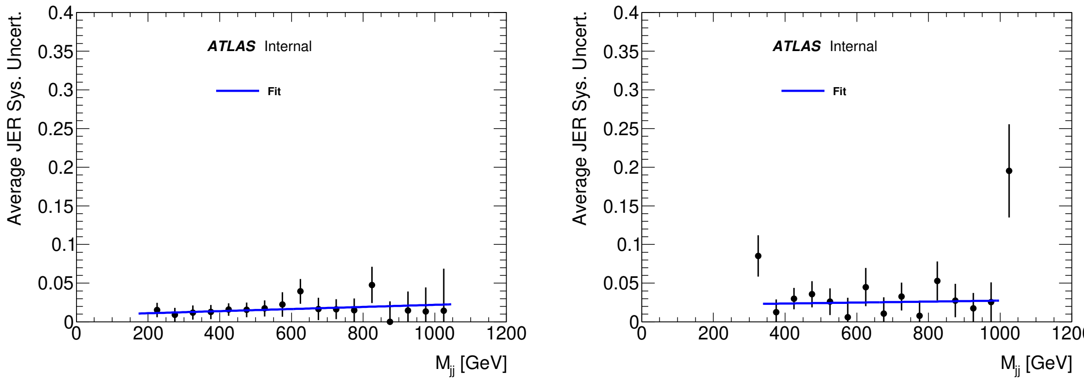

(a) Single photon trigger

(b) Compound trigger

Figure 172: Impact of JER variation on the bin-by-bin average of all signal samples for the single photon trigger (172(a)) and compound trigger (172(b)). By rebinning to 50 GeVbins, statistical fluctuations are suppressed, and the resulting points show a simple linear dependence on M_{jj} . A linear fit to each is shown. These plots support the use of a 3% flat uncertainty on JER in both channels.

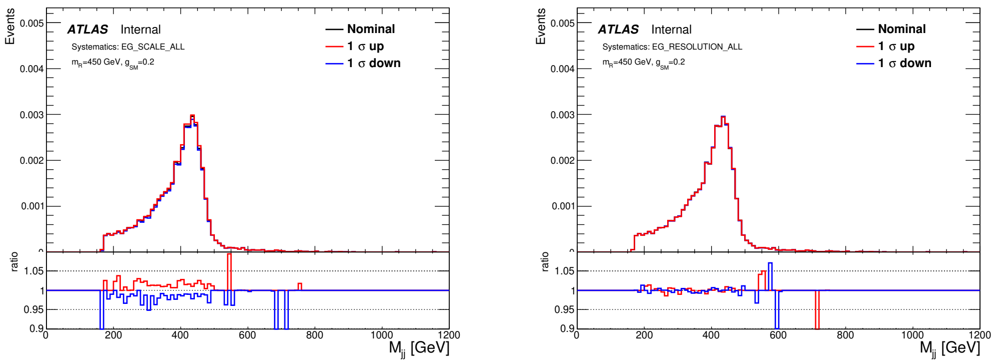

(a) Photon energy scale

(b) Photon energy resolution

Figure 173: Impact on a representative Z'signal MC sample of $\pm1\sigma$ variations in the the photon energy scale (173(a)) and photon energy resolution (173(b)) uncertainties. The selected sample has mass 450 GeVand $g_q = 0.2$ and the single photon trigger inclusive selection is applied. The uncertainties are not found to have a meaningful effect on signal shape or peak location, but instead change the signal normalisation (equivalent to the acceptance).

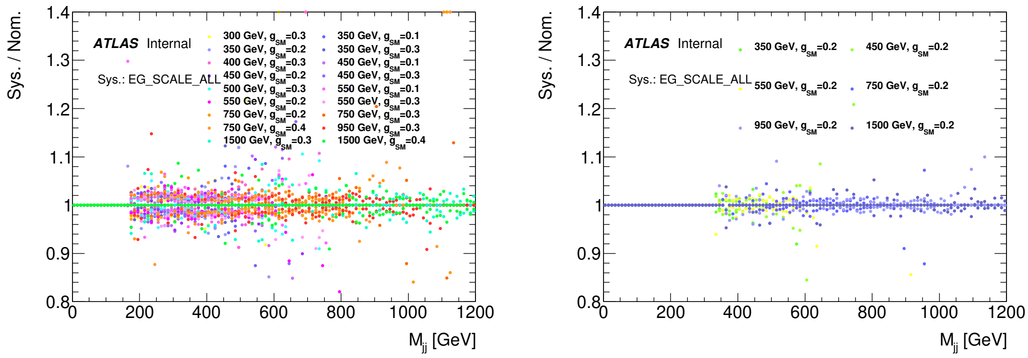

(a) Single photon trigger

(b) Compound trigger

Figure 174: Overlay of the photon energy scale uncertainties for all signal samples using the inclusive selection with the single photon trigger (174(a)) and compound trigger (174(b)).

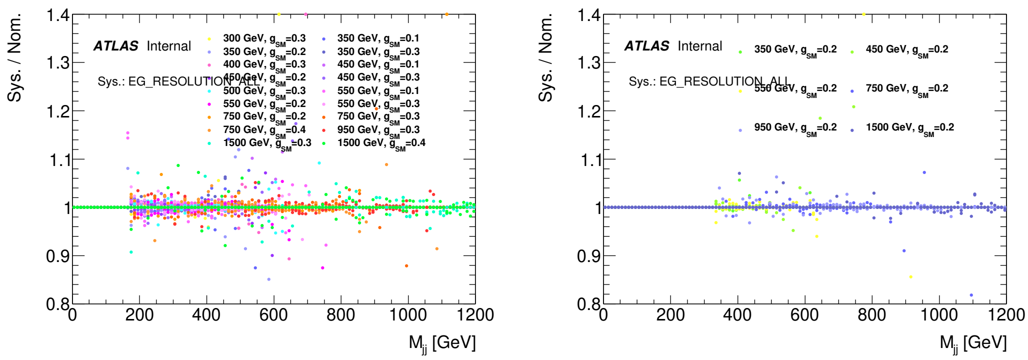

(a) Single photon trigger

(b) Compound trigger

Figure 175: Overlay of the photon energy resolution uncertainties for all signal samples using the inclusive selection with the single photon trigger (175(a)) and compound trigger (175(b)).

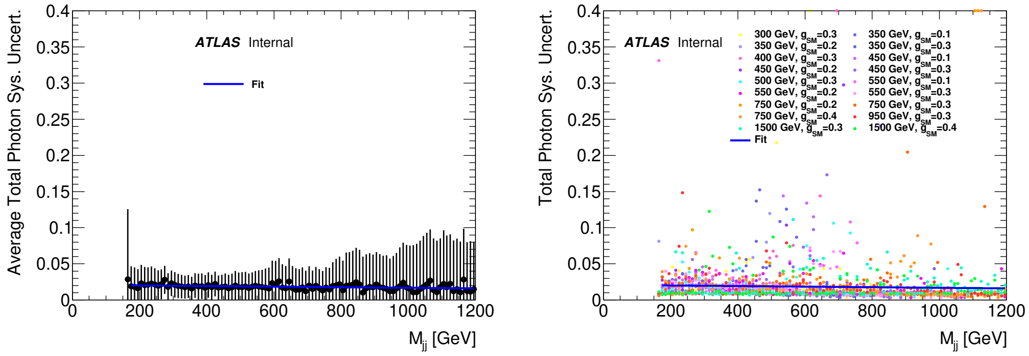

(a) Fit to total photon energy uncertainty (b) Fit overlaid on total uncertainty per sample

Figure 176: The total photon energy uncertainty is obtained by summing the energy scale, energy resolution, and ID scale factor uncertainties in quadrature, for all signal samples using the single photon trigger and inclusive selection. A weighted average of the results in each bin across the various signal samples is then fitted and shown in 176(a). The resulting fit is overlaid on the total uncertainty for each signal separately in 176(b). This demonstrates that a 2% uncertainty, flat as a function of M_{jj} , is appropriate for the photon related uncertainties.

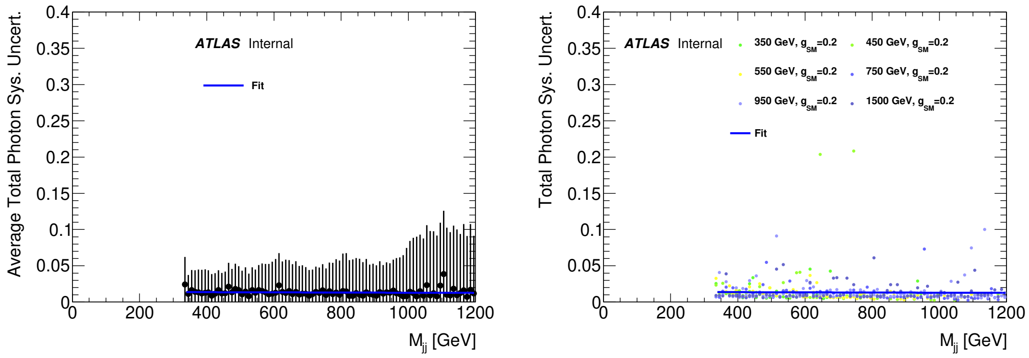

(a) Fit to total photon energy uncertainty (b) Fit overlaid on total uncertainty per sample

Figure 177: The total photon energy uncertainty is obtained by summing the energy scale, energy resolution, and ID scale factor uncertainties in quadrature, for all signal samples using the compound trigger and inclusive selection. A weighted average of the results in each bin across the various signal samples is then fitted and shown in 177(a). The resulting fit is overlaid on the total uncertainty for each signal separately in 177(b). This demonstrates that a 1.4% uncertainty, flat as a function of M_{jj} , is appropriate for the photon related uncertainties.

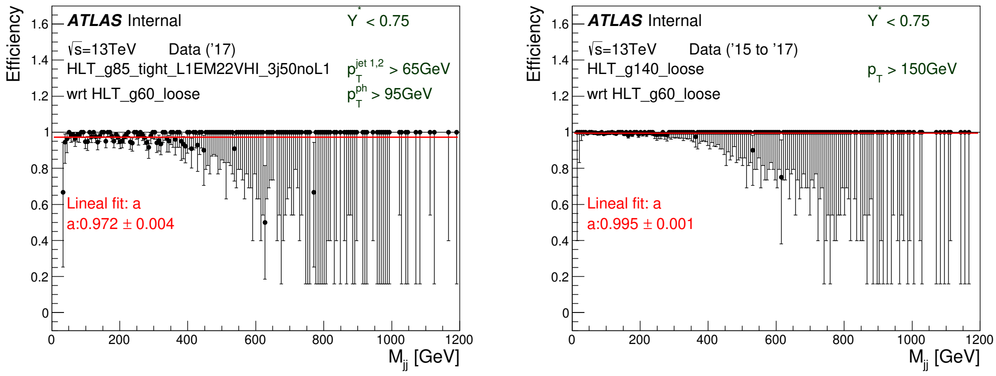

Figure 178: Trigger efficiency as a function of M_{jj} for the compound trigger (left) and for the single photon trigger (right). This trigger achieves only $\sim 97\%$ efficiency across the entire observable mass range. A 3% uncertainty is therefore applied to the compound trigger channels to account for this inefficiency.

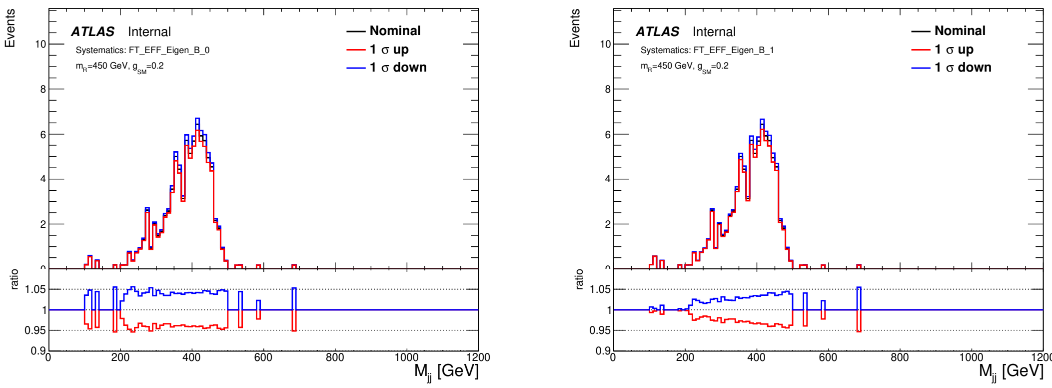

(a) `FT_EFF_Eigen_B_0` (b) `FT_EFF_Eigen_B_1`

Figure 179: Impact on a representative Z'signal MC sample of $\pm 1 sigma$ variations in the the `FT_EFF_Eigen_B_0` (179(a)) and `FT_EFF_Eigen_B_1` (179(b)) *b-tag* scale factor uncertainties. The selected sample has mass 450 GeVand $g_q = 0.2$. The uncertainties are not found to have a meaningful effect on signal shape or peak location, but instead change the signal normalisation (equivalent to the acceptance).

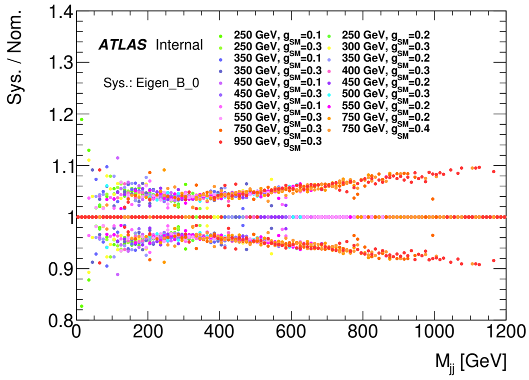

(a) `FT_EFF_Eigen_B_0`

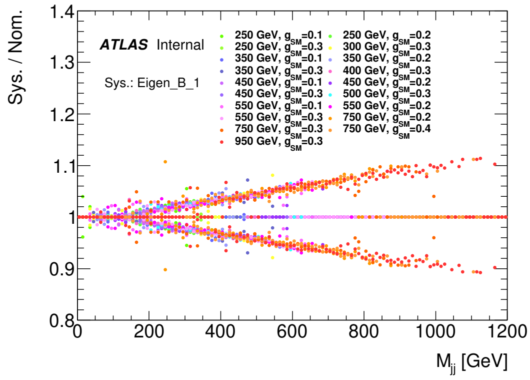

(b) `FT_EFF_Eigen_B_1`

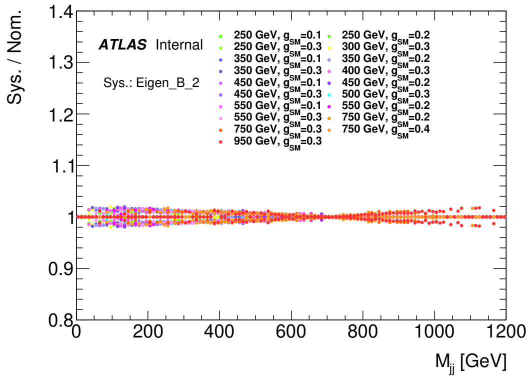

(c) `FT_EFF_Eigen_B_2`

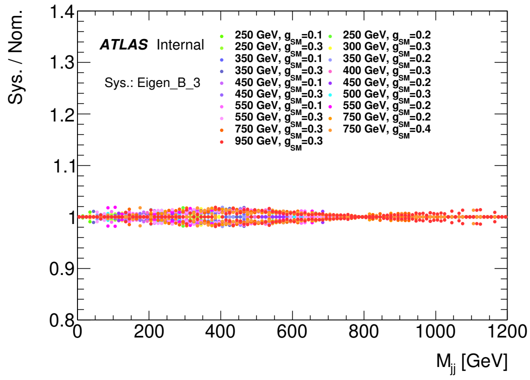

(d) `FT_EFF_Eigen_B_3`

Figure 180: Overlay of the four largest *b-tag* scale factor uncertainties for all signal samples using the single photon trigger and the 2 *b-tag* selection.

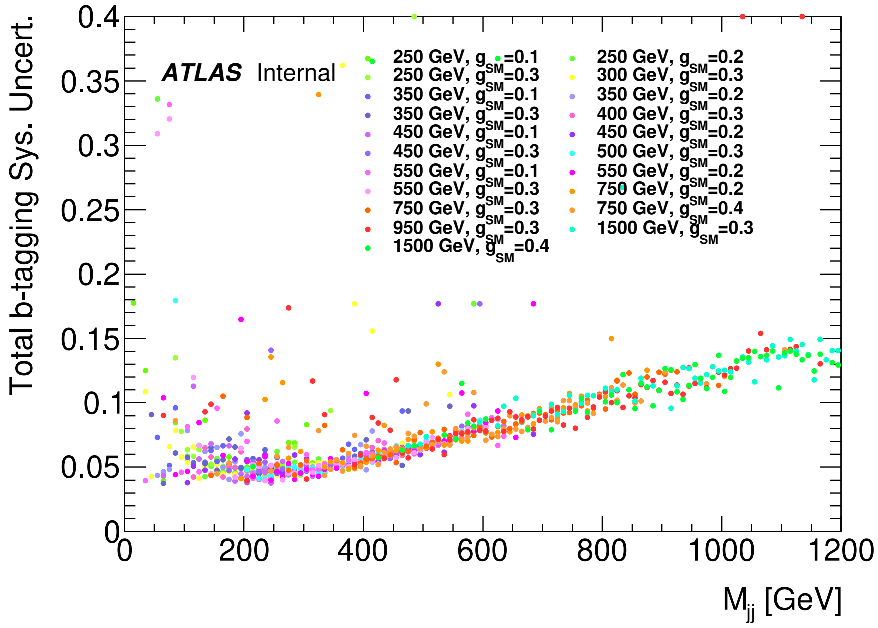

Figure 181: Sum in quadrature of the 25 *b-tag* scale factor uncertainties for every signal sample using the single photon trigger and 2 *b-tag* selection. The total uncertainty is relatively flat as a function of M_{jj} until roughly 300 GeV, then increases to a maximum size of approximately 15%.

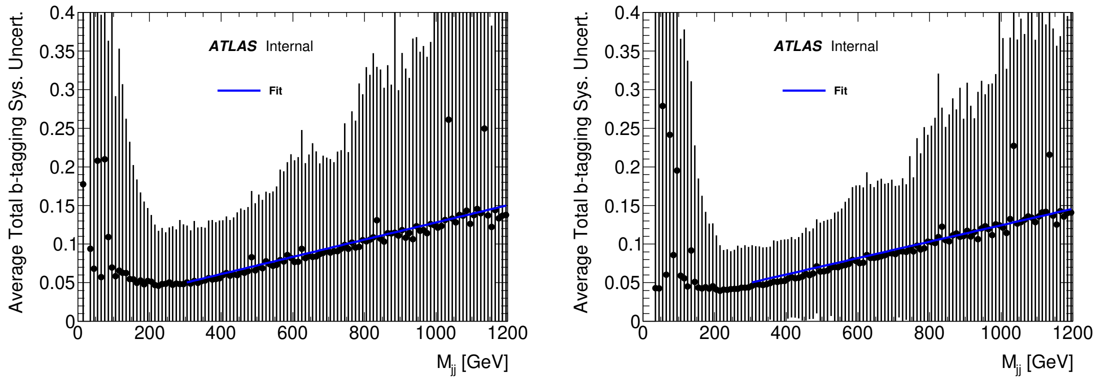

(a) Single photon trigger

(b) Compound trigger

Figure 182: Weighted average of the total *b-tag* scale factor uncertainty across all signal samples in each M_{jj} bin. A linear fit is made to the total uncertainty for 300 GeV $< M_{jj} <$ 1200 GeV. The lower edge of the fit is fixed to 5% to match the flat uncertainty which will be used below 300 GeV. The fit is performed in the single photon trigger 2 *b-tag* channel (182(a)) and is compared to the compound trigger 2 *b-tag* channel to validate its use in both cases (182(b)).

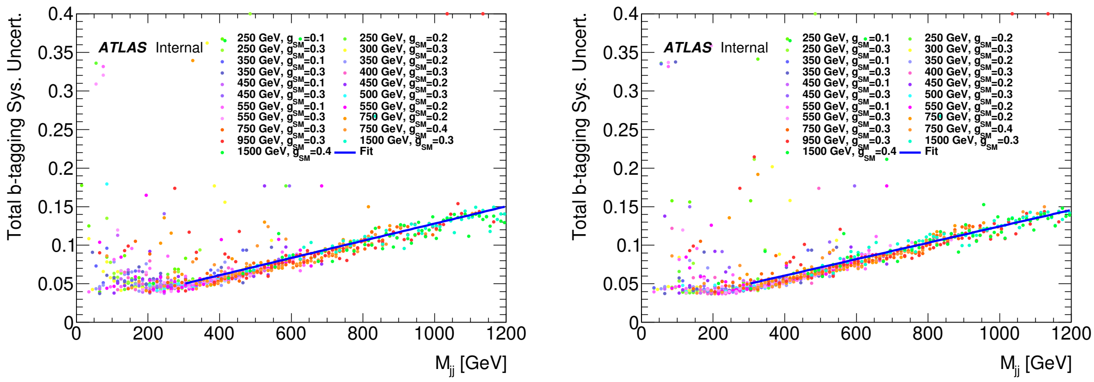

(a) Single photon trigger

(b) Compound trigger

Figure 183: The fit result calculated from the weighted average across all signal samples is overlaid on the total uncertainty separated by signal sample. The single photon trigger result is given in 183(a) and the compound trigger result is in 183(b).

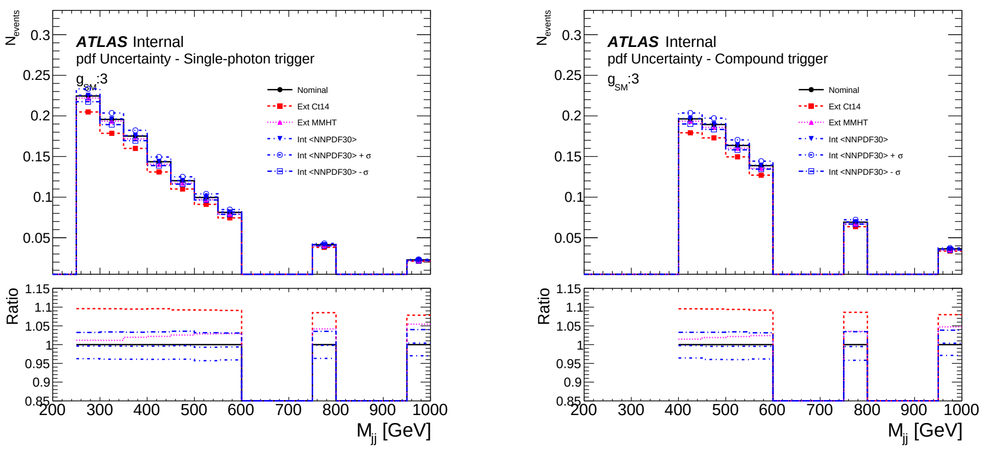

(a) Single photon trigger

(b) Compound trigger

Figure 184: The mass distribution after the analysis selection as a function of mediator mass for each PDF variation. Z'samples with coupling $g_q = 0.3$ are shown. The compound trigger selection is on the right and the single trigger selection is on the left; in each case the inclusive selection is used for the sake of statistics.

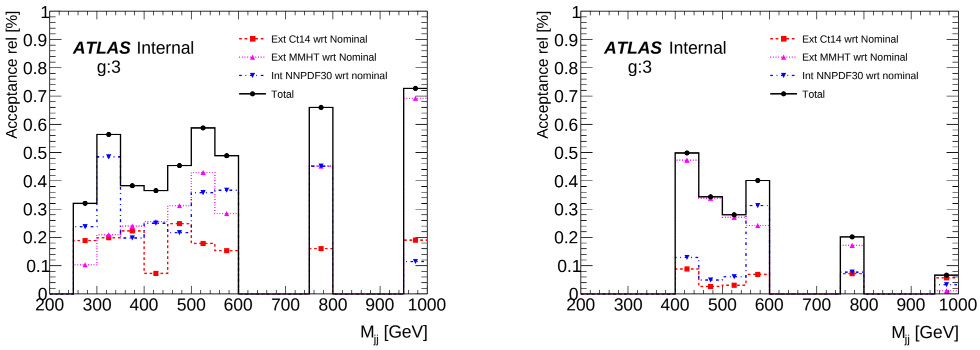

(a) Single photon trigger

(b) Compound trigger

Figure 185: The relative acceptance for each PDF variation with respect to the nominal PDF choices. Z'samples with coupling $g_q = 0.3$ are shown. The compound trigger selection is on the right and the single trigger selection is on the left; in each case the inclusive selection is used for the sake of statistics.

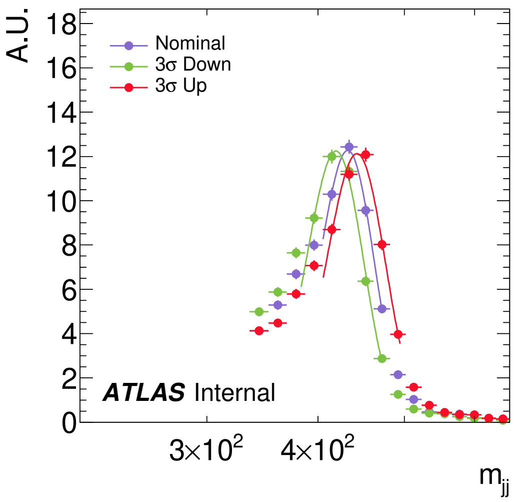

(a) GroupedNP 1

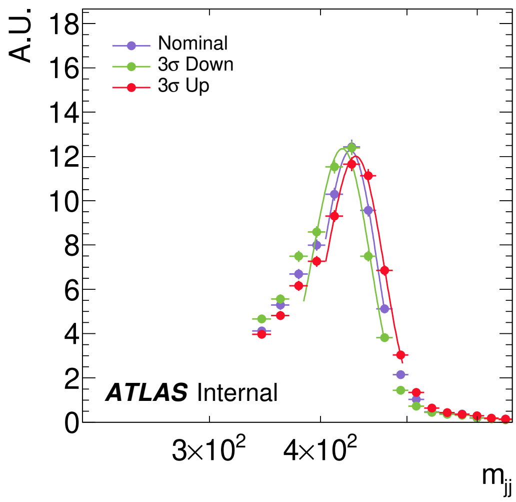

(b) GroupedNP 2

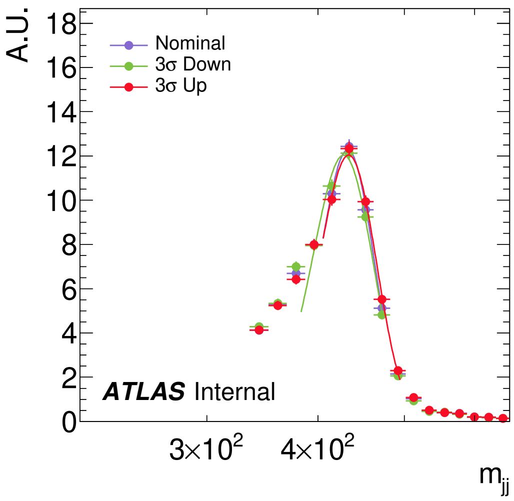

(c) GroupedNP 3

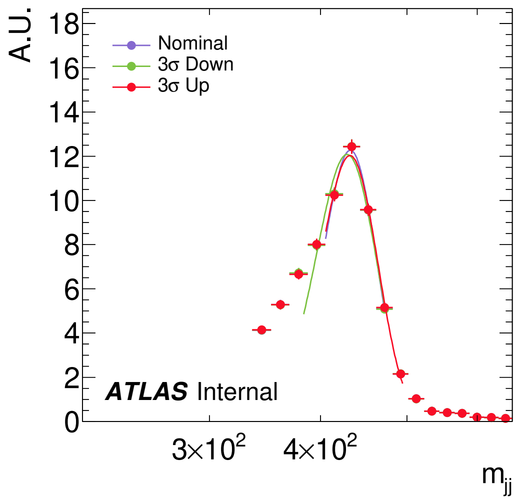

(d) η intercalib. non-closure

Figure 186: Fits to the nominal and $\pm 3\sigma$ variations in each of the four strongly reduced JES systematics. The Z' point with mass 450 GeVand coupling $g_q = 0.2$ is used as an illustrative example. The compound trigger and inclusive selection are applied. The impact on the mean of the Gaussians is seen to be relatively small.

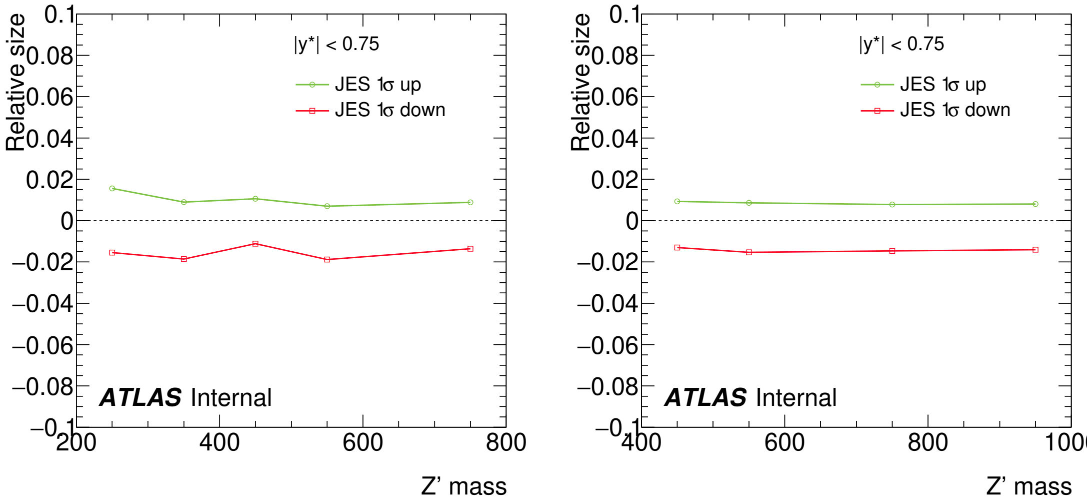

(a) Single photon trigger

(b) Compound trigger

Figure 187: Impact of $\pm 1\sigma$ in the total JES on the mean location of a Z'signal peak. The inclusive selection is used.

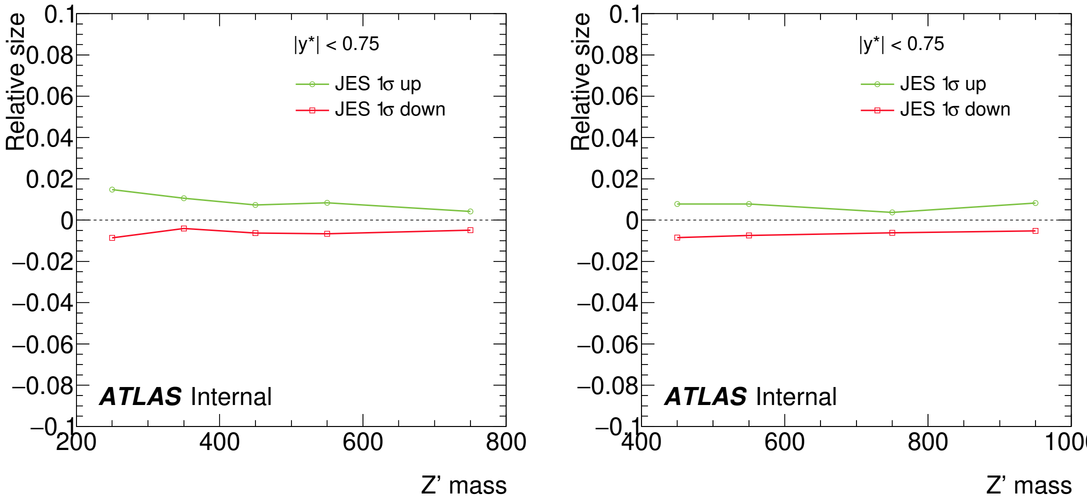

(a) Single photon trigger

(b) Compound trigger

Figure 188: Impact of $\pm 1\sigma$ in the total JES on the mean location of a Z'signal peak. The 2 *b-tag* selection is used. The fits, particularly to the upward variations, suffer from low statistics and therefore the inclusive channel provides a better measure of the JES impact.

B.11 Background estimation by ABCD method

Since the statistics in the 2 *b-tag* MC spectra is low compared with Run II data, the ABCD method is applied to provide the background only for the 2 *b-tag* samples, for fitting tests. It is created by reweighting the inclusive events using tagging efficiencies of the two selected jets from the candidate resonance. The four regions are defined below:

- `Region A`: The two selected jets with $|y^*| < 0.75$, both are *b-tag*
- `Region B`: The two selected jets with $|y^*| > 0.75$,
  - `B1`: The jet with higher $p_{\mathrm{T}}$is *b-tag*
  - `B2`: Both are *b-tag*
- `Region C`: The two selected jets with $|y^*| < 0.75$
- `Region D`: The two selected jets with $|y^*| > 0.75$

Region A is our signal region, and the tagging efficiencies can be derived from Regions B and D. By inverting the $|y^*|$ cut in Regions B and D, the signal contamination can be ignored. Since the *b-tag* performance depends on the $p_{\mathrm{T}}$and η of the jets, the *b-tag* efficiencies are parametrized by these two kinematic variables. To avoid the correlation of the jets flavors in the di-jet process, the independent efficiency of the jet with higher p_{T}(j1) and conditional efficiency of another jet (j2) are calculated. Independent efficiency means we just require j1 is *b-tag* , thus the efficiency $\epsilon_{j1,independent}$ is:

$$\epsilon_{j1,independent}(p_{\mathrm{T}}(j1), \eta(j1)) = \frac{N_{B1}(p_{\mathrm{T}}(j1), \eta(j1))}{N_D(p_{\mathrm{T}}(j1), \eta(j1))} \tag{52}$$

where $N_{B1}(p_{\mathrm{T}}(j1), \eta(j1))$ and $N_D(p_{\mathrm{T}}(j1), \eta(j1))$ are number of events in Region B and D binned in j1 $p_{\mathrm{T}}$and j1 η respectively. Conditional efficiency is calculated by requiring j1 and j2 are both *b-tag* with the condition that j1 is *b-tag* :

$$\epsilon_{j2,conditional}(p_{\mathrm{T}}(j2), \eta(j2)) = \frac{N_{B2}(p_{\mathrm{T}}(j2), \eta(j2))}{N_{B1}(p_{\mathrm{T}}(j2), \eta(j2))} \tag{53}$$

the complete *b-tag* efficiency is as Equation 54. Each of the components are shown in Figure 189.

$$\epsilon(p_{\mathrm{T}}(j1), \eta(j1), p_{\mathrm{T}}(j2), \eta(j2)) = \epsilon_{j1,independent}(p_{\mathrm{T}}(j1), \eta(j1)) \times \epsilon_{j2,conditional}(p_{\mathrm{T}}(j2), \eta(j2)) \tag{54}$$

Actually, $|y^*|$ and *b-tag* are not perfectly uncorrelated, which will influnce the ABCD method significantly. Thus, some correction factors are necessary to be introduced in ABCD method. As the *b-tag* performance depends on $p_{\mathrm{T}}$and η of the two selected jets, four corresponding correction factors can be introduced. However, studies show the most useful factor is the one to correct the distribution of j1 p_{T}. Therefore, only the factor derived from the j1 p_{T}shape is used to correct the *b-tag* efficiency. The different shapes of the j1 p_{T}bias the *b-tag* efficiency in $|y^*| > 0.75$

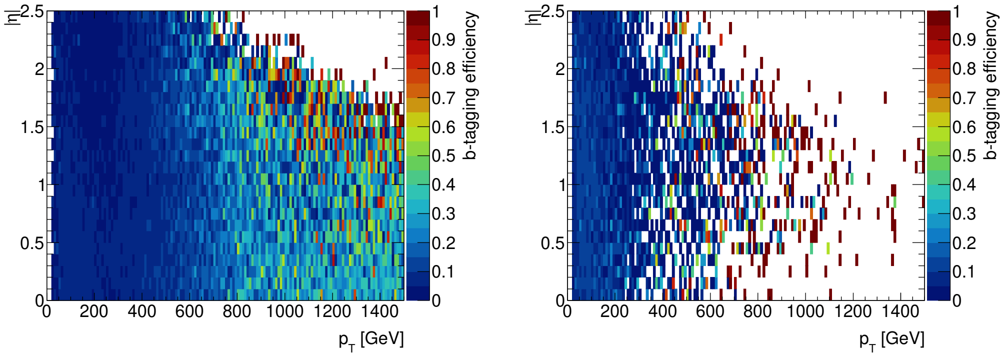

Figure 189: Independent *b-tag* efficiency map (left) for jet with higher $p_{\mathrm{T}}$and conditional *b-tag* efficiency map (right) for another jet. The efficiencies are parametrized in p_{T}-η space.

compared with the *b-tag* efficiency in $|y^*| < 0.75$. The correction factor is defined as follows:

$$f(p_{\mathrm{T}}(j1)) = \frac{f_{2btag}(p_{\mathrm{T}}(j1))}{f_{incl}(p_{\mathrm{T}}(j1))} \tag{55}$$

where $f_{incl}(p_{\mathrm{T}}(j1))$ is obtained by taking the ratio of normalized distributions of j1 p_{T} in Region C and D (Figure 190). As $f_{incl}(p_{\mathrm{T}}(j1))$ is a function of p_{T} of j1, this factor should be calculated in each bin:

$$f_{incl}(p_{\mathrm{T}}(j1)) = \frac{N_{incl,|y^*|<0.75}(p_{\mathrm{T}}(j1))}{N_{incl,|y^*|>0.75}(p_{\mathrm{T}}(j1))} \tag{56}$$

where $N_{incl,|y^*|<0.75}$ and $N_{incl,|y^*|>0.75}$ are the number of events in the corresponding bins of j1 p_{T} distributions in Region C and D respectively. Likewise,

$$f_{2btag}(p_{\mathrm{T}}(j1)) = \frac{N_{2btag,|y^*|<0.75}(p_{\mathrm{T}}(j1))}{N_{2btag,|y^*|>0.75}(p_{\mathrm{T}}(j1))} \tag{57}$$

$N_{2btag,|y^*|<0.75}$ and $N_{2btag,|y^*|>0.75}$ correspond to the number of events in each bin of j1 p_{T} distribution in Region A and B. The ultimate *b-tag* efficiency just need to by multiply the factor $f(p_{\mathrm{T}}(j1))$ to get the correction.

Figure 191 shows the closure test of the ABCD method using Monte Carlo samples.

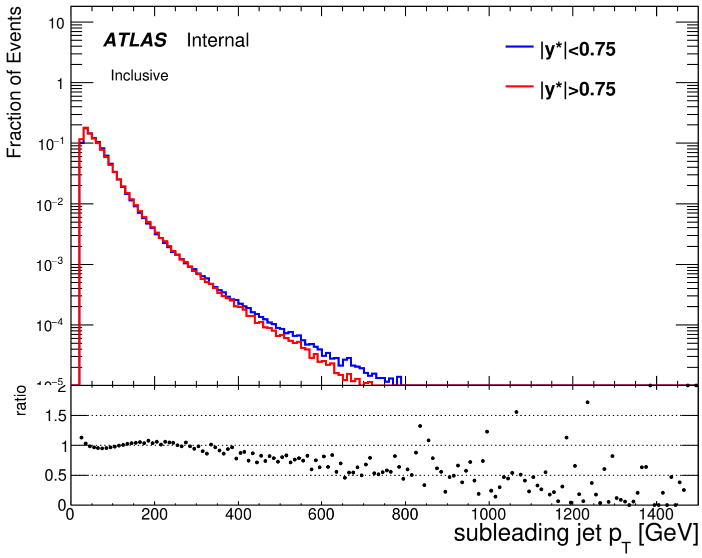

Figure 190: Comparison of j1 p_{T} distributions for inclusive using Monte Carlo smaples. Both distributions are normalized to 1 to just compare shape. The correction factors are derived from this distributions.

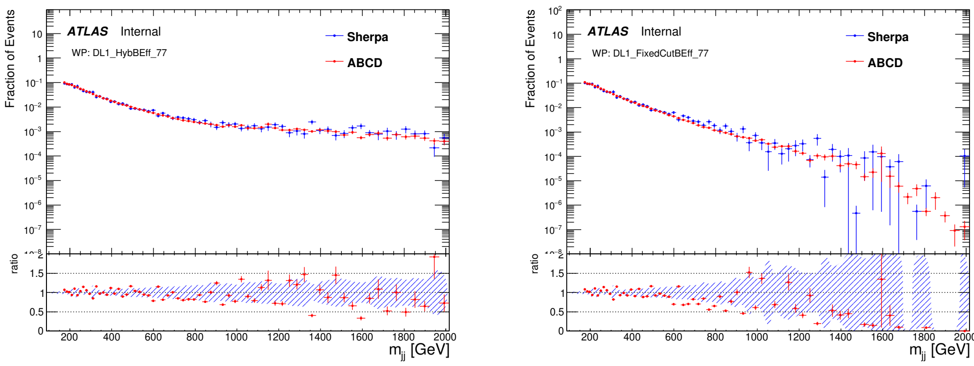

Figure 191: Closure results of the ABCD method using sherpa samples. All spectra are normalized to 1 to compare the shapes. Left plot is 2 *b-tag* M_{jj} spectra using DL1 77% hybrid working point and right plot using DL1 77% fixed efficiency working point.

References

[1] A. Salam. Elementary Particle Theory. Stockholm . 1969.

[2] A. Salam. Gauge unification of fudamental forces . *Rev. Mod. Phys.*, pages 525–538, 1980.

[3] A. Salzburger. Track Simulation and Reconstruction in the ATLAS Experiment. 2008.

[4] Daniel Abercrombie et al. Dark Matter Benchmark Models for Early LHC Run-2 Searches: Report of the ATLAS/CMS Dark Matter Forum. 2015.

[5] Tim Adye. Unfolding algorithms and tests using RooUnfold. *arXiv:1105.1160*, 2008.

[6] S. Agostinelli et al. GEANT4: a simulation toolkit. *Nucl. Instrum. Meth.*, A506:250–303, 2003.

[7] A.K. Salzburger. Track Simulation and Reconstruction in the ATLAS Experiment. *PhD thesis, Innsbruck University, 2008.*

[8] ALICE Collaboration. The ALICE Experiment at the CERN LHC, 2008.

[9] John Alison, Francesco Armando Di Bello, Sergei Chekanov, Andrea Coccaro, Tobias Golling, Gabriel Facini, Andreas Korn, Marie Christine Lanfermann, Thomas LeCompte, Bingxuan Liu, Jeremy Love, Laurie McClymont, Olaf Nackenhorst, Nishu Nishu, James Proudfoot, Soo Ryu, Rui Wang, Ning Zhou, Karishma Sekhon, Ryan Christopher Edgar, Dante Amidei, and Jinlong Zhang. Search for resonances in the di-jet mass distribution with one or two jets identified as b-jets in proton-proton collisions at $\sqrt{s}$=13 TeVwith the ATLAS detector. (ATL-COM-PHYS-2016-1561), Nov 2016.

[10] Johan Alwall et al. MadGraph 5: going beyond. *JHEP*, 06:128, 2011.

[11] Christos Anastopoulos, Ludovica Aperio Bella, Martin Florian Bessner, Phillip George Hamnett, Giovanni Marchiori, Simone Michele Mazza, Fernando Monticelli, Elisabeth Petit, Michael Pitt, Kerstin Tackmann, and Guillaume Unal. Photon identification pre-recommendations for run 2. (ATL-COM-PHYS-2015-496), Jun 2015.

[12] A Ashkenazi, G Bella, H S Bawa, A Boveia, C Doglioni, O Endner, F Guescini, T Huelsing, A Korn, C J Meyer, F Ruehr, K E Pachal, A Picazio, M Shupe, T Sumida, and J Tseng. ATLAS search in 2012 data for new phenomena in dijet mass distributions using pp collisions at $\sqrt{s}$ = 8 TeV. (ATL-COM-PHYS-2013-1518), Nov 2013.

[13] ATLAS Collaboraion. ATLAS liquid-argon calorimeter. *Technical Desing Report.*, 1996.

[14] ATLAS Collaboraion. The ATLAS Experiment at the CERN Large Hadron Collider. *JINST*, 3, 2008.

[15] ATLAS Collaboraion. The ATLAS Experiment at the CERN Large Hadron Collider. *JINST 3*, 2008.

[16] ATLAS Collaboration. ATLAS Insertable B-Layer Technical Design Report. *ATLAS-TDR-19*.

[17] ATLAS Collaboration. ATLAS pixel detector: Technical Design Report. `https://cds.cern.ch/record/381263`.

[18] ATLAS Collaboration. Charged particle multiplicities in pp interactions for track $p_{\mathrm{T}} > 100$ MeV at $\sqrt{s} = 0.9$ and 7 TeV measured with the ATLAS detector at the LHC.

[19] ATLAS Collaboration. Further ATLAS tunes of Pythia 6 and Pythia 8.

[20] ATLAS Collaboration. Improved luminosity determination in pp collisions at 7 TeV using the ATLAS detector at the LHC. *Eur.Phys.J.*

[21] ATLAS Collaboration. Jet energy resolution in 2017 data and simulation . `https://atlas.web.cern.ch/Atlas/GROUPS/PHYSICS/PLOTS/JETM-2018-005/`.

[22] ATLAS Collaboration. Luminosity Public Results for Run2 in ATLAS. `https://twiki.cern.ch/twiki/bin/view/AtlasPublic/LuminosityPublicResultsRun2`.

[23] ATLAS Collaboration. Supporting note for the Minimum Bias publication: Charge particle multiplicity in pp interactions at 13 TeV measured with the ATLAS detector. `https://cds.cern.ch/record/2011604`.

[24] ATLAS Collaboration. ATLAS tile calorimeter: Technical Design Report. Technical Design Report ATLAS. 1996.

[25] ATLAS Collaboration. The ATLAS Experiment at the CERN Large Hadron Col- lider. *Journal of Instrumentation*, 2008.

[26] ATLAS Collaboration. The ATLAS Experiment at the CERN Large Hadron Collider. *JINST*, 2008.

[27] ATLAS Collaboration. Charged-particle multiplicities in pp interactions at $\sqrt{s} = 900$ GeV measured with the ATLAS detector at the LHC. *Phys. Lett.*, B688:21–42, 2010.

[28] ATLAS Collaboration. Performance of Jet Algorithms in the ATLAS Detector. ATL-PHYS-INT-2010-129, 2010.

[29] ATLAS Collaboration. Charged-particle multiplicities in pp interactions measured with the ATLAS detector at the LHC. *New J.Phys.*, 13:053033, 2011.

[30] ATLAS Collaboration. Search for new physics in dijet mass and angular distributions in pp collisions at $\sqrt{s} = 7$ TeVmeasured with the ATLAS detector. *New J. Phys.*, 13:053044, 2011.

[31] ATLAS Collaboration. Summary of ATLAS Pythia 8 tunes. `https://cds.cern.ch/record/1474107`, 2012.

[32] ATLAS Collaboration. Summary of ATLAS Pythia 8 tunes. `ATL-PHYS-PUB-2012-003`, 2012.

[33] ATLAS Collaboration. Jet energy measurement with the ATLAS detector in proton-proton collisions at $\sqrt{s} = 7$ TeV. `http://arxiv.org/abs/1112.6426`, (2013).

[34] ATLAS Collaboration. Jet energy scale and its systematic uncertainty in proton-proton collisions at $\sqrt{s} = 7$TeV with ATLAS 2011 data. (2013).

[35] ATLAS Collaboration. ATLAS Pythia 8 tunes to 7 TeV data. `https://cds.cern.ch/record/1966419`, 2014.

[36] ATLAS Collaboration. Tagging and suppression of pileup jets with the ATLAS detector. ATLAS-CONF-2014-018, 2014.

[37] ATLAS Collaboration. Studies of the ATLAS Inner Detector material using s = 13 TeV pp collision data. *ATL-PHYS-PUB-2015-050*, 2015.

[38] ATLAS Collaboration. Search for new phenomena in the dijet mass distribution using pp collision data at $\sqrt{s} = 8$ TeV with the ATLAS detector. *Phys. Rev. D*, 91:052007, 2015.

[39] ATLAS Collaboration. Selection of jets produced in 13 TeV proton–proton collisions with the ATLAS detector. ATLAS-CONF-2015-029, 2015.

[40] ATLAS Collaboration. Track Reconstruction Performance of the ATLAS Inner Detector at s = 13 TeV. *ATL-PHYS-PUB-2015-018*, 2015.

[41] ATLAS Collaboration. Charged-particle distributions at low transverse momentum in $\sqrt{s}$ =13 TeV p-p interactions measured with the ATLAS detector at the LHC. `https://arxiv.org/abs/1606.011336`, (2016).

[42] ATLAS Collaboration. Charged-particle distributions in $\sqrt{s} = 13$ TeV pp interactions measured with the ATLAS detector at the LHC, 2016.

[43] ATLAS Collaboration. Search for light dijet resonances with the ATLAS detector using a Trigger-object Level Analysis in LHC pp collisions at $\sqrt{s} =$ 13 TeV. ATLAS-CONF-2016-030, 2016.

[44] ATLAS Collaboration. Search for low-mass dijet resonances in 2016 data with Trigger-object-Level Analysis. (ATL-COM-PHYS-2016-1498), Oct 2016.

[45] ATLAS Collaboration. Search for new light resonances decaying to jet pairs and produced in association with a photon or a jet in proton–proton collisions at $\sqrt{s} = 13$ TeV with the ATLAS detector. ATLAS-CONF-2016-070, 2016.

[46] ATLAS Collaboration. Search for New Phenomena in Dijet Mass and Angular Distributions from pp Collisions at $\sqrt{s} = 13$ TeV with the ATLAS Detector. *Phys. Lett. B*, 754:302, 2016.

[47] ATLAS Collaboration. Search for new phenomena in dijet events using 37 fb^{-1} of pp collision data collected at $\sqrt{s}$ =13 TeV with the ATLAS detector. 2017.

[48] ATLAS Collaboration. Search for dijet resonances in events with an isolated lepton using $\sqrt{13}$ TeV proton–proton collision data collected by the ATLAS detector. ATLAS-CONF-2018-015, 2018.

[49] ATLAS Collaboration. Search for low-mass resonances decaying into two jets and produced in association with a photon using pp collisions at $\sqrt{s}$ =13 TeV with the ATLAS detector. `https://arxiv.org/abs/1901.10917`, (2018).

[50] B. Andersson et al. Parton Fragmentation and String Dynamics.

[51] Richard D. Ball, Valerio Bertone, Stefano Carrazza, Christopher S. Deans, Luigi Del Debbio, et al. Parton distributions with LHC data. *Nucl.Phys.*, B867:244–289, 2013.

[52] Richard D. Ball et al. Parton distributions with LHC data. *Nucl. Phys.*, B867:244–289, 2013.

[53] U. Baur, I. Hinchliffe, and D. Zeppenfeld. Excited Quark Production at Hadron Colliders. *Int. J. Mod. Phys.*, A2:1285, 1987.

[54] U. Baur, M. Spira, and P. M. Zerwas. Excited-quark and -lepton production at hadron colliders. *Phys. Rev. D*, 42:815–824, Aug 1990.

[55] Bruning, O. S. et al. The LHC Main Ring. *CERN-2004-003-V1, CERN-2004-003, CERN-2004-003-V-1*, 2004.

[56] A. D. Bukin. Fitting function for asymmetric peaks. (0711.4449), Feb 2008.

[57] Mikael Chala, Felix Kahlhoefer, Matthew McCullough, Germano Nardini, and Kai Schmidt-Hoberg. Constraining Dark Sectors with Monojets and Dijets. *JHEP*, 07:089, 2015.

[58] Georgios Choudalaki. On hypothesis testing, trials factor, hypertests and the BumpHunter.

[59] G. Choudalakis and D. Casadei. Plotting the differences between data and expectation. *European Physical Journal Plus*, 127:25, February 2012.

[60] CMS Collaboration. The CMS experiment at the CERN LHC, 2008.

[61] Glen Cowan, Kyle Cranmer, Eilam Gross, and Ofer Vitells. Asymptotic formulae for likelihood-based tests of new physics. *The European Physical Journal C*, 71(2):1554, Feb 2011.

[62] D. Abercrombie et al. Dark Matter Benchmark Models for Early LHC Run-2 Searches: Report of the ATLAS/CMS Dark Matter Forum. *Phys. Rev. D.*

[63] D. Abercrombie et al. Dark Matter Benchmark Models for Early LHC Run-2 Searches: Report of the ATLAS/CMS Dark Matter Forum. `http://arxiv.org/abs/1507.00966`, 2015.

[64] D. Wicke and P. Z. Skands. Non-Perturbative QCD Effects and the Top Mass at the Tevatron. *Nuovo Cim..*, 132, 2008.

[65] S. D. Ellis and D. E. Soper. Successive combination jet algorithm for hadron collisions. *Phys. Rev. D*, 48:3160–3166, Oct 1993.

[66] Ellis, J. The superstring - Theory of everything or of nothing. *Nature.*, 323:595–598, 1986.

[67] Englert, F. and Brout, R. Broken Symmetry and the Mass of Gauge Vector Mesons. *Phys. Rev. Lett.*, 13:321323, 1964.

[68] F. Englert and R. Brout. Broken symmetry and the mass of gauge vector mesons. *Physical Review Letters*, 13:321–323, 1964.

[69] F. Marcastel. CERN's Accelerator Complex. La chaîne des accélérateurs du CERN. `https://cds.cern.ch/record/1621583`, 2013.

[70] G. F. Knoll. Radiation detection and measurement. *Wiley*, 2010.

[71] G. S. Guralnik, C. R. Hagen, and T. W. B. Kibble. Global Conservation Laws and Massless Particles. *Phys. Rev. Lett*, 13:585–587, 1964.

[72] G. Zweig. An SU3 model for strong interactions symmetry and its breaking . *Tech. Rep. CERN-TH-401*, pages 5,6, 1964.

[73] D. J. Gross and F. Wilczek. Ultraviolet behavior of non-abelian gauge theories. *Phys. Rev. Lett.*, 30:1343–1346, 1973.

[74] Particle Data Group. Review of particle physics. *Phys. Rev. D*, 86:010001, 2012.

[75] Robert M. Harris and Konstantinos Kousouris. Searches for Dijet Resonances at Hadron Colliders. *Int. J. Mod. Phys.*, A26:5005–5055, 2011.

[76] Heather M. Gray. The Charged Particle Multiplicity at Center of Mass Energies from 900 GeV to 7 TeV measured with the ATLAS Experiment at the Large Hadron Collider. *ATLAS-THESES.*

[77] J. C. Collins and D. E. Soper. The Theorems of Perturbative QCD. *Ann.Rev.Nucl.Part.Sci*, 37, 1987.

[78] J. E. Nuth, N.Wainer, K. Meier, N. Hadley, F. Aversa, et al. Toward a standardization of the jet definitions.

[79] J. M. Campbell, J. Huston, and W. Stirling. Hard Interactions of Quarks and Gluons: A Primer for LHC Physics. *Rept.Prog.Phys.*, 70, 2007.

[80] Jonathan David Bossio Sola. Measurement of inclusive jet cross-sections and search for resonances decaying into a photon and a jet.

[81] Katherine Pachal. earch for new physics in the dijet invariant mass spectrum at 8 TeV.

[82] Paul Langacker. The physics of heavy Z' gauge bosons. *Rev. Mod. Phys.*, 81:1199–1228, Aug 2009.

[83] LHCb Collaboration. The LHCb Detector at the LHC, 2008.

[84] M. Cacciari, G. P. Salam, and G. Soyez. The anti-k t jet clustering algorithm. *JHEP, arXiv:0802.1189*, B406:187–224, 1993.

[85] M. Delmastro, S. Gleyzer, C. Hengler, M. Jimenez, T. Koffas, M. Kuna, K. Liu, Y. Liu, G. Marchiori, E. Petit, M. Pitt, E. Soldatov, y K. Tackmann,. Photon identification efficiency measurements with the ATLAS detector using LHC Run 1 data, Aug 2014.

[86] M Gell-Mann. A schematic model ob baryons and mesons. *Phys. Lett.*, 8:214–215, 1964.

[87] M. Koboyashi and T. Maskawa. C-P Violation in the Renormalizable Theory of Weak Interaction. *Progress of Theoretical Physics*, 49:652–657, 1973.

[88] M. Markevitch, A. Gonzalez, D. Clowe, et al. Direct constraints on the dark matter self-interaction cross-section from the merging galaxy cluster. *Astrophys.J.*, 606:819–824, 2004.

[89] M. Wobisch and T. Wengler. Hadronization corrections to jet cross sections indeep- inelastic scattering. *arXiv:hep-ph/9907280.*

[90] N. Cabibbo. Unitary Symmetry and Leptonic Decays. *Phys Rev. Lett.*, 10:531–533, 1963.

[91] S. Ostapchenko. Monte carlo treatment of hadronic interactions in enhanced pomeron scheme: Qgsjet-ii model. *Phys. Rev. D*, 83:014018, Jan 2011.

[92] Particle Data Group Collaboraion, J BEringer et al. . Review of Particle Physics. *Phys. Rev.*, 86:1,5,6,12,13,22,121, 2012.

[93] H. D. Politzer. Reliable Perturbative Results for Strong Interactions. *Phys. Rev. Lett.*, 30:1346–1349, 1973.

[94] S. Porteboeuf, T. Pierog, and K. Werner. Producing Hard Processes Regarding the Complete Event: The EPOS Event Generator. 2010.

[95] R. Fruhwirth, W. Waltenberger, and P. Vanlaer. Adaptive vertex fitting. `http://dx.doi.org/10.1088/0954-3899/34/12/N01`, 2007.

[96] R. Frhwirth. Application of Kalman Filtering to Track and Vertex Fitting. *Nucl. Instr. Meth*, 1987.

[97] S. Agostinelli et al. GEANT4: A Simulation toolkit. *Nucl. Instrum. Meth. A*, 506:250–303, 2003.

[98] S. Bethke, G. Dissertori, and G. P. Salam. Quantum chromodynamics. *Particle Data Group Review.*

[99] S. Catani et al. Longitudinally invariant K_t clustering algorithms for hadron hadron collisions. *Nucl. Phys. B*, 406:187–224, 1993.

[100] S. Catani, Y. L. Dokshitzer, M. Seymour, and B. Webber. Longitudinally invariant Kt clustering algorithms fot hadronization collisions. *Nucl. Phys.*, B406:187–224, 1993.

[101] S L. Glashow. Partial-symmetries of weak interactions. *Nuclear Physics*, 22:579–588, 1961.

[102] S. Weinberg. A model of leptons. *Phys. Rev. Lett.*, pages 1264–1266, 1967.

[103] Karishma Sekhon, Ryan Christopher Edgar, and Dante Amidei. SWiFt: Sliding Window Fit Method for Resonance Searches. (ATL-COM-PHYS-2018-161), Feb 2018.

[104] A. Sherstnev and R.S. Thorne. Parton Distributions for LO Generators. *Eur.Phys.J.*, C55:553–575, 2008.

[105] Torbjorn Sjostrand, Stephen Mrenna, and Peter Z. Skands. A Brief Introduction to PYTHIA 8.1. *Comput. Phys. Commun.*, 178:852–867, 2008.

[106] Peter Skands, Stefano Carrazza, and Juan Rojo. Tuning PYTHIA 8.1: the Monash 2013 Tune. *Eur.Phys.J.*, C74(8):3024, 2014.

[107] S.L.Glashow. Partial-symmetries of weak interactions. *Nuclear Physics.*, 22:579–588, 1961.

[108] T. Cornelissen et al. Concepts, Design and Implementation of the ATLAS New Tracking. *ATL-SOFT-PUB-2007-007*, 2007.

[109] T. H. Gleisberg et al. Event generation with SHERPA 1.1. *JHEP*, 02:007, 2009.

[110] T. H. Gleisberg et al. Event generation with SHERPA 1.1. *JHEP*, 02:007, 2009.

[111] T. Kibble. Symmetry breaking in nonAbelian gauge theories. *Phys.Rev.*, 155:1554–1561, 1967.

[112] T. S. van Albada, J. N. Bahcall, K. Begeman, and R. Sancisi. Distribution of dark matter in the spiral galaxy NGC 3198. *ApJ*, 295:305-313, 1985.

[113] S. Mrenna T. Sjostrand and P. Skands. Brief introduction to pythia 8.1. *Comput. Phys. Comm.*, 178, 2008.

[114] T. Sjostrand, S. Mrenna and P. Z. Skands. PYTHIA 6.4 Physics and Manual. *JHEP*, 05:026, 2006.

[115] U. Sarkar. Particle and Astroparticle Physics. Series in High Energy Physics, Cosmology and Gravitation. https://books.google.ch/books?id=t-qL07MSvxEC, (2007).

[116] UA2 Collaboration, J. Alitti et al. A Measurement of two jet decays of the W and Z bosons at the CERN $\bar{p}p$ collider. *Z.Phys.*, C49:17–28, 1991.

[117] V. C. Rubin and J. Ford, W. Kent. Rotation of the Andromeda Nebula from a Spectroscopic Survey of Emission Regions. *Astrophys.J.*, 159:379–403, 1970.

[118] Valentina Cairo. Charged-paticle distributions and material meansurements in $\sqrt{s}$ =13TeV pp collisions with the ATLAS Inner Detector. *PhD thesis, Universita della calabria, Italy*, 2017.

[119] W. Lampl, S. Laplace, D. Lelas, P. Loch, H. Ma, S. Menke, S. Rajagopalan, D. Rousseau, S. Snyder, and G. Unal. Calorimeter Clustering Algorithms: Description and Performance. *Tech. Rep. ATL-LARG-PUB-2008-002*, 2008.

[120] Y. L. Dokshitzer, G. Leder, S. Moretti, and B. Webber. Better jet clustering algorithms. *JHEP 08, arXiv:hep-ph/9707323*, B406, 1997.